UNIVERSITE PARIS 7 - DENIS DIDEROT
UFR de PHYSIQUE

Doctorat
Physique et Technologie des Grands-Instruments

MARC DOLEANS

ETUDES DANS LES CAVITES SUPRACONDUCTRICES ELLIPTIQUES A BETA-REDUIT

(Considérations Générales de leur Design, Variation Dynamique de leur Fréquence, et Dynamique Longitudinale)

Thèse dirigée par Sang-ho Kim

Soutenue le 22 Septembre 2003

JURY

François VANNUCCI	, Président
Joël LE DUFF	, Directeur de thèse
Alban MOSNIER	, Rapporteur
François MEOT	, Rapporteur
Terry GARVEY	

A la mémoire de mon père Bernard Doléans,

à ma mère Marie-Thérèse Doléans,

et à mes frères et soeur, Philippe, Anne, et Laurent.

Acknowledgments

The three and a half years I have spent at the Oak Ridge National Laboratory (ORNL), working for the Spallation Neutron Source (SNS) project, were very fruitful for me on a professional level as well as on a personal level. I would therefore want to warmly thank the people who made this great opportunity possible: My thesis advisor Dr. Joël Le Duff, and Dr. Yang Lai Cho and Dr. Marion White from the SNS. I am grateful to my advisor for his support through the years, and though the distance did not facilitate our exchanges, I benefited from his interest and useful comments at key moments. I would especially want to express my gratitude to him for his efforts and patience when reading my thesis dissertation. As for Dr. Yang Lai Cho and Dr. Marion White, I've been deeply touched by their commitment to create opportunities for a young scientist like myself and by their continuous kindness and concern regarding my accomodations in Oak Ridge.
I would like to express my deepest gratitude to Dr. Sang-ho Kim who accepted to become my practical mentor at the SNS and invested so much of his precious time. Since day one, he was always there to help me out on every level and to support my work. His broad knowledge, highly diversified skills, pedagogy, experience, organization, patience, and kindness are all outstanding, and to have been under his supervision was a true privilege.
Of course, I would like to thank the successive Associate directors, Dr. D. Moncton and Dr. T. Mason, and division directors Dr. B. Kustom , and Dr. N. Holtkamp, to have supported my stay at the SNS.

As a student, I had the chance to be employed through the remarkable Oak Ridge Associated Universities (ORAU) organization. I was the lucky beneficiary of the highly professional and organized people working there, and I would like to express sincere collective thanks to them, and in particular to Linda Holmes, Linda McCamant, Debbie Alcorn, Marlene Mayton, Jeannie Robinson, Cheryl Guthrie, Angela Kelly, Martha Hammond, Bonnie DeJarnette, Norma Patterson, and Debbie Shanks. I also want to emphasize my deep appreciation for the tremendous work and help I received from the fantastic Brenda Goodman!
The link between ORAU and the SNS was done through my two successive mentors, David Olsen and John Galambos. I would hereby like to express my gratitude to them for their willingness to fulfill this role.

Working within the physics group has been a real pleasure, thanks to the professional and human skills of the people belonging to it. I feel priviledged to have been able to work within such a group of people, and I am giving warm thanks to the two successive group leaders Jei Wei and Stuart Henderson, and all the physics group team members: Sang-ho Kim, Eugène Tanke, Sarah Cousineau, John Galambos, Jeff Holmes, Slava Danilov, Dong-o Jeon, Yoishi Sato, Tom Pelaia, C. Paul Chu, Sasha Aleksandrov, Leonid Kravchuk, Andrei Shishlo, Mike Plum, J. Stovall, Wolf-Dieter Klotz, and also to Jian-Guang Wang and Weishi Wan that were once part of it.

I would like to thank many of them on a more personal level. I express candid thanks to Sang-ho and Eugène, for all their help and for the intense joy of our morning coffee and daily lunch. Eugène was an extremely enjoyable person to work with. His straightforwardness, amazing ability to come with simple solutions for any type of complicated problems, open mind, experience, multilingual skills, and sense of humor have been constant source of refreshment, inspiration, and energy. I also express him my gratitude for helping me with editing of my thesis and articles. I am thankful to Sarah, my old office mate, for her friendship, her quick mind and constant dynamism, our sharing of excitations and frustrations during our respective Ph.D., and all the great time playing volleyball! I have friendly thoughts for Sasha, for his various comments and advice that were always useful, and for his great skills on the volleyball court. I shared very enjoyable time with Slava, who besides giving me invaluable advice or feedback in my work, was also a great soccer teammate and a tough table tennis opponent! I owe lots of thanks to Paul who was always ready to give up some of his time to help me on numerous computer related problems, therefore preventing me to turn insane on many occasions! I would like to express my very truthful appreciation to Dong-o who always showed interest in my work and my plans. John is a fabulous person that I felt very lucky to meet and work with. Beside many other things, I would like to show him my sincere gratitude for his help on editing my thesis. Leonid is another person I would like to express warm thanks to, for his extraordinary openness toward a young scientist as myself, for his beneficial comments, and for the sharing of his extremelly valuable experience. One crucial area during a Ph.D. is the access to information. In this regard, I feel deeply thankful to Jeff who gave me full access to his collection of books and who shared many great stories from his work and his life experiences, which always enlightened my days. Being far from my country, I was delighted to speak french with Wolf-Dieter and Eugène Tanke (and also Marion!) who are perfectly fluent in my native language and were always kind to offer me this simple pleasure.
I would like to value the hard work of the three successive secretaries of the physics group that have made our lives so much easier: Jackie Smith, Muriel Tate, and Myra Fultz. Without them we would just be totally lost! I am also expressing my sympathy to the various visitors that I shared my office with: Sasha Zhukov, Sasha Feschenko, etc...

Working at the SNS gave me the unique opportunity to be in contact with people with many different professional and cultural backgrounds. Though I mainly worked with the people from the physics group, I would like to give sincere and sounding thanks to all the other people I had the chance to interact with, including people from the other laboratories collaborating with the SNS, in particular my colleagues from Jefferson Laboratory (JLAB): Peter Kneisel, Ricky Campisi, Jean Delayen, Kirk Davis, Ronald Sundelin, and Haipeng Wang, for their collaboration and help during my various visits there. I also express my appreciation to these ORNL colleagues: Yoon Kang, Daniel Stout, and An Sun, for all their friendly help.

I would like to show my sincere appreciation to the members of my jury, François

Vannuci, Joël Le Duff, François Méot, Alban Mosnier, and Terry Garvey. I want to give special thanks to François Vannucci and Joël Le Duff who were of great help in the preparation of the defense of my thesis. In this matter, I also want to express sincere thanks to Lucième Guenot from the administrative department of my University who made many efforts and considerably eased the fullfilement of the administrative requirements. I am extremely grateful to my two thesis reviewers, Alban Mosnier and François Méot, who generously accepted to perform this heavy task and provided me great feedback to improve my dissertation. I would finally want to thank Saby Valero with all my heart, for his friendship and his invaluable help, particularly in the preparation of my defense.
I would like to seize the opportunity to thank some of my teachers and professors. My middle school math and english teachers, respectively Mr Lainé and Ms. Jayez, who played a crucial role in my education. More recently, my University professors, Galliano Valent, Alain Laverne, Luc Valentin, Pascal David, François Amiranoff, François Vannucci, Joël Le Duff, André Tkatchenko, and Nicolas Pichoff, have all offered high quality and entertaining classes.

If the brightest of us stand on the shoulders of giants, as greatly worded by Isaac Newton, I, more humbly but as proudly, stand on the shoulders of my friends. I would like to express my very sincere gratitude to the people that helped me when I arrived in the US: Cathy, Franck, and Kristin. I would like to mention few of the people with whom I hanged out and had a lot of fun through my Ph.D. years: Sangho and Jean, Eugène and Diana, Sarah and Jeff, David and Valérie, Laura and Tim, Dale and Sarah, Hugh and Sandra. I would also like to take the opportunity to greet many friends. Some from my college years: Vincent Serrière, Guillaume Olry, Olivier Dadoun, Gilles Castillon, Franck Letendu, Murat Yasar, José Belda. Others who are long time friends: Lahoucine Agourram, Sylvain Goulet, Alexandre Talasi, Hervé Loste, Stéphane Mauduit, and Benjamin Terrier. And finally a few friends from my childhood: Yvan le Texier, Jérôme Nourri, Marc Maisons, and Frédéric Matthieu.
I am delighted to have shared these three particular years of my life with my finacée Kimberly, who has always been there to support and believe in me; WE made it! I also want to thank her fantastic family, composed of people with great heart.
And for my family: Je veux remercier mes parents et mes frères et soeur. Les années passent, les choses changent, seul l'amour que je vous porte reste intact.

Résumé

Marc Doleans

ETUDES DANS LES CAVITES SUPRACONDUCTRICES ELLIPTIQUES A BETA-REDUIT

(Considérations générales de leur design, variation dynamique de leur fréquence, et dynamique longitudinale)

Les cavités elliptiques supraconductrices radio-fréquences (SRF) sont choisies dans de nombreux linacs à cause de leur capacité à opérer avec une grande efficacité RF, de leur large rayon de bore, etc... Ces cavités mûrissent à de nombreux égards mais la constante évolution de leurs gradients accélérateurs requière des études complémentaires. Par exemple, la variation dynamique de la fréquence des cavités par rapport à celle de la RF les excitant, dûe à la pression de radiation changeante dans le temps pour des cavités opérées en mode pulsé, comme dans le projet SNS, devient plus sévère avec l'augmentation du champ accélérateur. Comme autre exemple, l'approximation usuelle d'une vitesse de faisceau constante à l'intérieur d'une cavité peut devenir imprécise pour des particules passant dans des cavités à beta-réduit et subissant un large gain d'énergie. Il est alors intéressant de developer une approche plus générale pour la dynamique longitudinale prenant en compte ces variations de vitesse.

Avant de présenter les études sur ces deux exemples, une introduction générale des cavités SRF elliptiques est donnée en présentant les considérations du design des cavités moyen et haut beta du SNS ($\beta = 0.61$ and $\beta = 0.81$). Dans cette optique, l'espace des paramètres géométriques de la cavité est exploré pour trouver une géométrie satisfaisante. Pour guider cette investigation, différents aspects de la performance des cavités peuvent être calculés pour chaque ensemble de paramètres géométriques. Pour trouver une géométrie candidate, des critères de design sur les aspects qui peuvent être facilement estimés sont posés. Une région dans l'espace des paramètres géométrique satisfaisant tous les critères de design peut finalement être déterminée. Les géométries des cavités SNS sont dans ces régions. Une fois que les paramètres géométriques de base de la cavité sont connus, d'autres aspects requérant des calculs plus conséquents peuvent être étudiés.

Pour des cavités SRF elliptiques, opérant avec des hauts gradients accélérateurs, le detuning de Lorentz est un problème majeur. Dûe à leur faiblesse mécanique intrinsèque, les cavités SRF elliptiques subissent une variation dynamique de leur fréquence de résonance à cause des forces de Lorentz changeantes dans le temps qui s'appliquent sur leurs surfaces. La variation de fréquence produite par ces forces peut être du même ordre que la bande passante de la cavité et donc sérieusement affecter l'amplitude et la phase du champ accélérateur. Pour contrebalancer le changement en fréquence créé par les forces de Lorentz, une compensation active à l'aide de tuners piézoélectriques est possible. Dans la thèse, un modèle du problème est présenté. Ce modèle vise à

mieux comprendre le problème dans ces aspects dynamiques et finalement à établir un processus de compensation à l'aide des tuners piézoélectriques. La modélisation est décomposée en deux parties: La première est liée à l'évolution du voltage RF de la cavité, la seconde est liée aux déformations mécaniques de la cavité, et aux changements de fréquences associés, produits par les deux sources de vibrations, pression de radiation et tuner piézoélectrique. Grâce a l'effort de modélisation, la différence de couplage entre l'action des forces de Lorentz et l'action des tuners piézoélectriques sur la cavité est mieux comprise. Les résultats de la modélisation sont comparés à des résultats expérimentaux et l'accord est satisfaisant. Les simulations sont alors utilisées pour extraire les paramètres mécaniques de la cavité d'après les résultats de mesures expérimentales. Ces paramètres permettent d'avoir un modèle réaliste de cavité qui est ensuite utilisé pour illustrer un processus de compensation du detuning de Lorentz. Ce processus est basé sur une analyse harmonique du problème.
Pour des cavités opérées avec des hauts gradients accélérateurs, un autre possible problème est lié au changement de vitesse des particules lors de leurs passages à l'intérieur d'un élément (problème similaire à la dynamique longitudinale des faisceaux basses énergies). Dans cette thèse, une approche analytique de ce problème est proposée. Quand la vitesse des particules change significativement dans l'élément, l'assomption usuelle d'une évolution de phase linéaire devient imprécise. Au lieu de fragmenter l'élément accélérateur, une méthode alternative prenant en compte les non-linéarités de l'évolution de la phase est développée. Cette méthode montre que le jeu d'équations de Panofsky est la simplification d'une formulation plus générale. La méthode utilisant l'approximation d'une loi de phase linéaire est d'abord rappelée pour des gaps accélérateurs avec des champs symmetriques par rapport a leurs milieux géométriques, et ensuite étendue pour les cas non symmetriques. Les limitations inhérentes à cette méthode sont illustrées. Une méthode de calcul plus générale est alors développée et se base sur des itérations analytiques. Les calculs sont menées pour trois itérations, ce qui est suffisant pour couvrir les cas où la partie non-linéaire de l'évolution de la phase est en dessous d'une certaine limite. Les résultats obtenus par le processus itératif suggère une formulation plus générale pour la solution du problème. Dans cette formulation, les dépendances pour certaines variables sont explicites (charge électrique et masse des particules, phase d'entrée des particules par rapport au champ accélérateur, et amplitude de ce champ), et implicites pour d'autres (béta d'entrée des particules et profil normalisé du champ). De cette formulation, une méthode semi-analytique est déduite pour traiter les cas où la non-linéarité de l'évolution de la phase est trop large.
Dans la mesure où la plupart des exemples et illustrations proposés dans cette thèse proviennent d'études réalisées pour le projet SNS, une brève présentation de ce projet et de son système accélérateur est proposée dans le chapitre 0.

Abstract

Marc Doleans

STUDIES IN REDUCED-BETA ELLIPTICAL SUPERCONDUCTING CAVITIES

(General Design Considerations , Dynamic Detuning, and Longitudinal Dynamics)

Elliptical superconducting radio-frequency (SRF) cavities have been chosen as a preferred structure for many linacs because of their capacity to operate with high RF efficiency, their large bore radius, etc... Such cavities reach maturity in many regards but the continual increase in their accelerating gradients prompt further studies. For example, the dynamic detuning of a cavity with respect to the RF source feeding it, originating from the time varying radiation pressure in cavities operated in pulsed mode, like those in the Spallation Neutron Source (SNS) project, becomes more of an issue as the amplitude of the accelerating field increases. As another example, the usual assumption of a constant velocity of the beam within the cavity can become inaccurate for particles passing through reduced-beta SRF cavities and experiencing large energy gain. As a consequence, it is interesting to develop a more general approach taking the variations of the particle's velocity within the accelerating element into account.

Before presenting studies on both of those examples, a general introduction of elliptical SRF cavities is given, focusing on the design considerations for the SNS medium and high betas cavities ($\beta = 0.61$ and $\beta = 0.81$). The cavity geometrical parameter space is explored to find proper cavity shapes. To guide this investigation, various aspects of the the cavity performance can be calculated for different sets of geometrical parameters. To find a candidate for the cavity geometry, design criteria are set on those aspects which can easily be integrated in the investigation process. A region in the geometrical parameter space satisfying all the design criteria can eventually be found. The SNS cavity geometries are in such regions. Once some basic parameters of the cavity are found, other aspects requiring more involved computations are considered.

For elliptical SRF cavities, operating with high accelerating gradients, the Lorentz detuning is a major concern. Due to their intrinsic weak mechanical properties, elliptical SRF cavities operated in pulsed mode experience a dynamic variation of their resonant frequency due to the time varying Lorentz forces to which their surface is exposed. The detuning generated by these forces can be of the same order as the electromagnetic bandwidth of the cavity and consequently strongly affect the amplitude and the phase of the accelerating field during the beam pulse. To counteract the detuning action of the dynamic Lorentz forces, an active compensating scheme using piezoelectric tuners may be used. The proposed model focuses on improving

the understanding of the problem in its dynamical aspects and eventually leads to the establishment of a compensation scheme using piezoelectric tuners. The modeling is divided into two aspects: One related to the evolution of the RF cavity voltage, and an other related to the mechanical deformations and the corresponding detuning generated by the two sources of mechanical vibrations, radiation pressure and piezoelectric tuners. From the modeling, the difference in the coupling between the Lorentz forces action and the action of the piezoelectric tuner forces to the cavity structure is better understood. The results from the modeling are compared to experimental results and their agreement is found to be satisfying. Simulations are then used to extract values for the parameters pertaining to the mechanical aspect from the measurements. Those parameters allow to have a realistic model of the cavity, which is used to illustrate a compensating scheme of the Lorentz detuning using piezoelectric tuners. The scheme itself is based on a harmonic analysis of the problem.
For a cavity operated with high accelerating gradients, one other possible issue is the non negligible change of the particle's velocity within the accelerating element (not unlike the longitudinal dynamics of low energy beams). An analytical approach of the problem is presented. When the particle's velocity changes significantly within the element, the usual assumption of a linear phase law becomes inaccurate. Instead of fractioning the accelerating element into smaller pieces, an alternative method taking into account the non linearity of the phase law is developed. This method shows that the usual set of Panofsky equations is a simplification of a more general formulation for the longitudinal dynamics of accelerated particles. The thin lens approximation method is first reviewed for gaps with symmetric field with respect to their geometrical middle, and then extended to non symmetric cases. Furthermore, the inherent limits of this method are illustrated. Subsequently, a more general method based on a solution of the problem by analytical iterations is developed. Calculations are made up to three iterations, which is sufficient to cover cases where the non linearity of the phase law is below a certain limit. The results suggest a general form for the solution of the problem. In this form, dependencies upon certain variables are explicit (electrical charge, mass, and entrance phase of the particle with respect to the accelerating field, and amplitude of the accelerating field), and implicit for others (entrance beta of the particle and normalized profile of the field). From this formulation a semi-analytical method is derived to treat cases with stronger non linearity of the phase law.
Since most of the examples and illustrations in this thesis are based on studies developed for the SNS project, a basic presentation of this project and its accelerator system is proposed in chapter 0.

Contents

Chapter 0

SNS overview

In this chapter, a basic presentation of the SNS project and its accelerator system is given. This overview and much more material about the SNS can be found on the project website (http://www.sns.gov). The latest status of the SNS project can be found in [46].

0.1 The SNS Partnership

The SNS project is a partnership involving six DOE national laboratories (Argonne, Brookhaven, Jefferson, Lawrence Berkeley, Los Alamos, and Oak Ridge) in the design and construction of what will be the most powerful spallation source in the world for neutron-scattering R&D. The baseline design calls for an accelerator system consisting of an ion source, full-energy linear accelerator (linac), and an accumulator ring that combine to produce short, powerful pulses of protons. These proton pulses impinge onto a mercury target to produce neutrons through the spallation nuclear reaction process. The SNS site plan with these systems marked out is presented in Fig. 1. The SNS will deliver 1.4 million watts (1.4 MW) of beam power onto the target (other basic design technical parameters of the SNS are summarized in Table 1).

0.2 The Ion Source

Lawrence Berkeley National Laboratory (LBNL) is responsible for designing and building the SNSs front-end system, which includes an ion source, beam formation and control hardware, and low energy beam transport and acceleration systems. The ion source produces negative hydrogen (H-) ions — hydrogen with an additional electron attached — that are formed into a pulsed beam and accelerated to an energy of 2.5 million electron volts (MeV). This beam is delivered to a large linear accelerator.

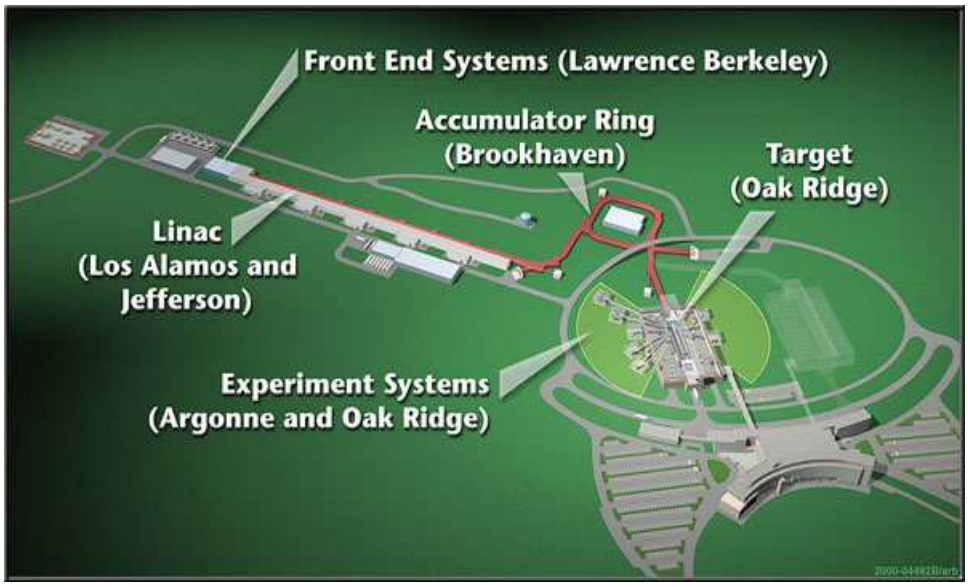

Figure 1: SNS site plan.

0.3 The Linac

Los Alamos National Laboratory (LANL) is responsible for the linear accelerator, which accelerates the H - beam from 2.5 to 1000 MeV, or 1 GeV. The linac is a superposition of normal conducting and super-conducting radio-frequency cavities that accelerate the beam and a magnetic lattice that provides focusing and steering. Three different types of accelerators are used. The first two, the drift tube linac and the coupled-cavity linac are made of copper, operate at room temperature, and accelerate the beam to about 200 MeV. The remainder of the acceleration is accomplished by superconducting niobium cavities, which are the responsibility of Thomas Jefferson National Accelerator Facility (JLab). These cavities are cooled with liquid helium to an operating temperature of 2 K. A schematic layout of the SNS linac is presented in Fig. 2. Diagnostic elements provide information about the beam current, shape, and timing, as well as other information necessary to ensure that the beam is suitable for injection into the accumulator ring and to allow the high-power beam to be controlled safely.

0.4 The Accumulator Ring

Brookhaven National Laboratory (BNL) is responsible for the accumulator ring structure, which bunches and intensifies the ion beam for delivery onto the mercury target to produce the pulsed neutron beams. The intense H- beam from the linac must be sharpened more than 1000 times to produce the extremely short, sharp bunch of neutrons needed for optimal neutron-scattering research. To accomplish this goal, the H- pulse from the linac is wrapped into the ring through a stripper foil that strips the electrons from the negatively charged hydrogen ions to produce the protons (H+)

Table 1: Basic Design Technical Parameters

Proton beam power on target	1.4 MW
Proton beam kinetic energy on target	1.0 Gev
Average beam current on target	1.4 mA
Pulse repetition rate	60 Hz
Protons per pulse on target	1.5×10^{14}
Charge per pulse on target	24 μC
Energy per pulse on target	24 kJ
Proton pulse length on target	695 ns
Ion type (Front end, Linac, HEBT)	H-
Ion type (Ring, RTBT, Target)	H+
Average linac macropulse H- current	26 mA
Linac beam macro pulse duty factor	6 %
Front end length	7.5 m
Linac length	331 m
HEBT length	170 m
Ring circumference	248 m
RTBT length	150 m
Ring filling time	1.0 ms
Ring revolution frequency	1.058 Mhz
Number of injected turns	1060
Ring filling fraction	68 %
Ring extraction beam gap	250 ns
Maximum uncontrolled beam loss	1 W/m
Target material	Hg
Initial number of Instruments	5

that circulate in the ring. Approximately 1200 turns are accumulated, and then all these protons are kicked out at once, producing a pulse less than 1 millionth of a second (10^{-6} seconds) in duration that is delivered to the target. In this way, short, intense proton pulses are produced, stored, and extracted at a rate of 60 times a second to bombard the target. A schematic layout of the SNS ring is given in Fig. 3.

0.5 The Target

ORNL is responsible for the design and construction of the liquid mercury target. Because of the enormous amount of energy that the short, powerful pulses of the incoming 1 GeV proton beam will deposit in the spallation target, it was decided to use a liquid mercury target rather than a solid target such as tantalum or tungsten. The SNS will be the first scientific facility to use pure mercury as a target for a proton beam. Mercury was chosen for the target for several reasons: (1) it is not damaged by radiation, as are solids; (2) it has a high atomic number, making it a

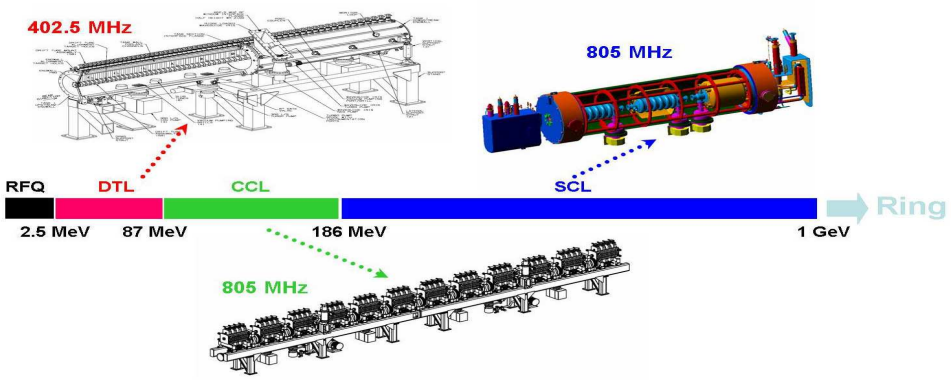

Figure 2: Schematic layout of the SNS linac.

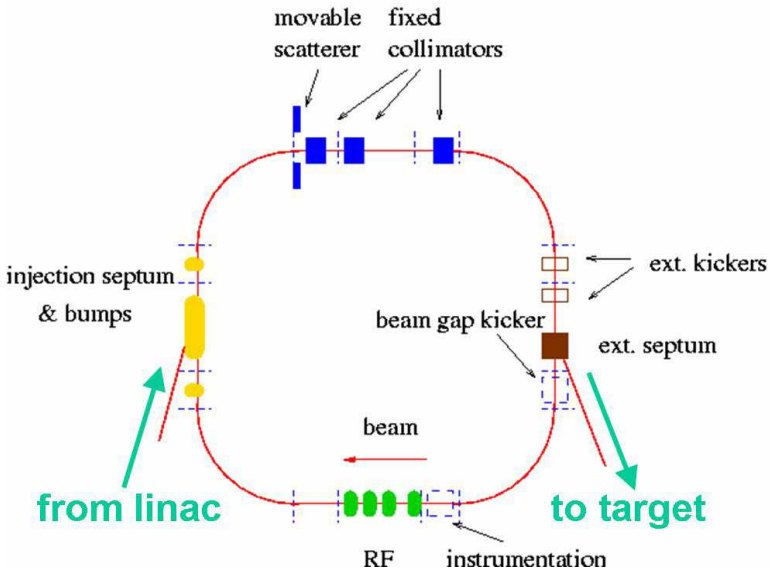

Figure 3: Schematic layout of the SNS ring.

source of numerous neutrons (the average mercury nucleus has 120 neutrons and 80 protons); and (3), because it is liquid at room temperature, it is better able than a solid target to dissipate the large, rapid rise in temperature and withstand the shock effects arising from the rapid high-energy pulses. The neutrons coming out of the target must be turned into low-energy neutrons suitable for research — that is, they must be moderated to room temperature or colder. The neutrons emerging from the target are slowed down by passing them through cells filled with water (to produce room-temperature neutrons) or through containers of liquid hydrogen at a temperature of 20 K (to produce cold neutrons). These moderators are located above and below the target. Cold neutrons are especially useful for research on polymers and proteins.

Chapter 1

Design considerations of elliptical superconducting cavities

Elliptical shape SC cavities have become a technology of choice in many accelerator applications. Achieving the highest accelerating gradient and RF efficiency possible are usually primary goals common to all the applications where elliptical SRF are chosen as accelerating structures. Other aspects such as high order modes (HOM), Lorentz force detuning, field flatness, thermal stability and multipacting have also to be considered at the design stage and can influence the choice for the geometric parameters of the cavity. Because these different concerns can interfere with one an other, the design of a cavity is usually a matter of compromises. To help finding a satisfying cavity shape, it is beneficial to define a global design scheme where particular design criteria are targeted. Once such requirements are set, a systematic investigation in the cavity geometrical parameter space provides a convenient manner to converge toward an adequate cell shape. Such a procedure was developed in the design of the SRF cavities at the SNS [2]. Areas in the cavity geometrical parameter space were identified and the final cavity shapes [3] are consistent with them. In the following, the main results of this procedure are reviewed. The basic parameters of the SNS cavities, the parametrization of the cavity geometry, and the design criteria are presented first. The results of the geometry optimization procedure are then shown. Finally, further studies with the chosen geometries are reported.

1.1 Basic parameters

SRF elliptical cavities are typically designed to operate with frequencies from a few hundreds of megahertz to a couple of gigahertz. The choice of the frequency is the first step of the design and can be determined considering basic scaling laws for the frequencies [1]. It is for example known that whereas high frequencies relate to smaller cavities and are therefore efficient in terms of building cost, low frequencies lead to lower surface heat dissipation and are consequently efficient in terms of cryogenic operating cost. Practically, the exact choice for the operating frequency is not an isolated issue and it can heavily be influenced by other components of the accelerator.

Other main parameters of an elliptical SRF cavity are the length and the number of its cells. Contrary to some other accelerating structures such as DTL cavities, elliptical SRF cavities, operated in pi mode, do not have drift tubes between consecutive cells to insure synchronicity between the particles and the RF accelerating field. Instead, a particle with a matched beta crosses a cell in half an RF period and therefore sees an accelerating field in each consecutive gap. For this reason, the cavity is usually identified by a "geometrical" beta, which corresponds to the particle's velocity for which perfect synchronicity occures. Even though the acceleration is maximum for particles having their beta equal to the cavity's geometrical beta, the acceleration can remain efficient enough over a broad range of velocities. This efficiency is strongly influenced by the number of cells in the cavity. Depending on the energy range the particles have to be accelerated and on the achievable accelerating gradient, an optimum value for the geometrical beta and for the number of cells of a cavity can be determined (physics of the longitudinal dynamics are developed in chapter 3). In the SNS for example, two different 6-cell elliptical SRF cavities are designed with geometrical beta equal to 0.61 and 0.81. The first type is used to accelerate H^- ions from $\beta = 0.55$ to $\beta = 0.7$ and the second from $\beta = 0.7$ to $\beta = 0.88$. The basic parameters of the SNS SRF cavities are summarized in Table 1.1.

Table 1.1: Basic parameters for the SNS elliptical SRF cavtities

Frequency	805 MHz
Geometrical betas	0.61 and 0.81
Number of cells	6
Section 1, Number of 0.61 cavities	33
Section 2, Number of 0.81 cavities	48
Accelerated particles	H^-
Repetition rate	60 Hz
Peak beam current	26 mA
Average beam current	1.56 mA
Energy Range	185-1000 Mev
Energy at the transition	390 Mev
Beta Range	0.55-0.88
Beta at the transition	0.7

1.2 Cavity geometrical parameter space

After choosing the frequency and the number of cells, the geometrical parameters of SRF cavities can be investigated. A multicell SRF cavity is usually designed to have identical inner-cells; the end-cells need to be designed separately due to their connection to the beam pipes. The main results of the design scheme presented in [2] are shown in this section.

An inner cell is usually composed of two identical half-cells. Each half cell can be

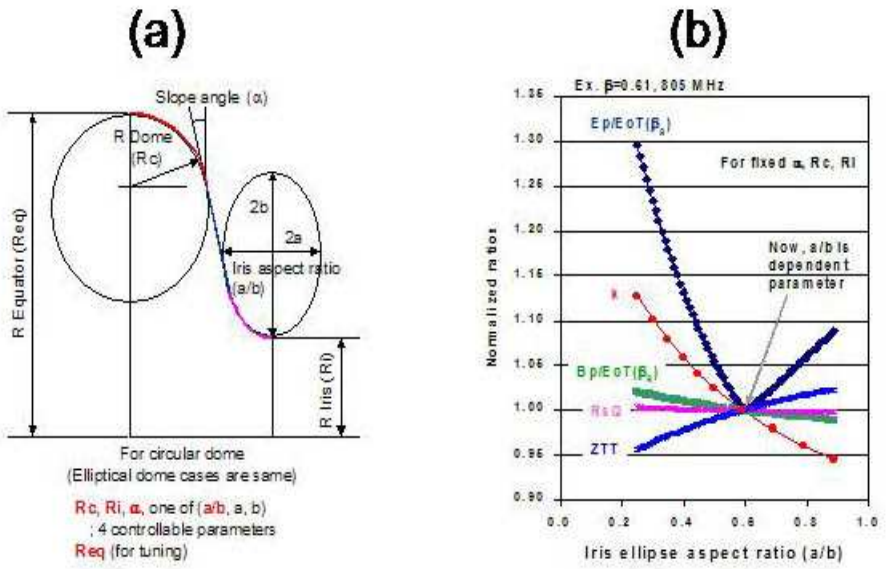

Figure 1.1: (a) Geometrical parametrization for a cell of an elliptical SRF cavity using five variables Req, Rc, α, a/b, Ri. (b) For a given set of geometrical parameters there exists an optimal value for a/b such that the quantity Ep/E_0T is minimized. In the design process this value for a/b is used making it a quantity dependent on the other geometrical parameters.

designed using a cicular dome, a straight line, and an elliptical iris as displayed in Fig. 1.1. The cell shape can be described using five geometrical parameters: The Equator radius Req, the radius of the circular dome Rc, the slope angle of the straight line α, the ratio of the iris ellipse half axis a/b, and the radius of the iris Ri (Superfish [4] notations). Because the length of the cell is already determined from the choice of the geometrical beta of the cell, these parameters are in fact not totally independent. The value of the equator radius Req is used for tuning only since its effect on the resonance frequency is large but its influence on the cavity performance is negligible. Only four variables constitute the geometrical parameter space of the cavity. To determin a cavity shape, some design criteria can first be defined.

1.3 Qualitative aspects of the cavity performance

The cavity performance depends on many different aspects, and the design is a matter of compromises. Whereas some aspects and their tendancies (R/Q, ratio of peak surface field to on-axis field, intercell coupling coefficient...) can be estimated when exploring the geometrical parameter space , some others (HOM properties, multipacting, thermal stability...) are difficult to consider or control at such stage . As a consequence it is necessary to proceed in two phases. First, optimizing the cell shape

with respect to aspects which can easily be calculated. Secondly, estimate the overall performance of the cavity, including the aspects overlooked during the first phase, and possibly alter the design if the results are not satisfying.

Table 1.2: Aspects for the first phase of the design of the cavity shape

Inner cell	Minimize the peak surface fields Maximize the R/Q Achieve reasonable inter-cell coupling coefficient Provide a reasonable mechanical stiffness
End cell	Equal or lower peak surface fields than for the inner cells Achieve a reasonable Qex Obtain a good field flatness

Controllable aspects considered during the design of the inner-cells and end-cells are listed in Table 1.2. For the inner cell, a basic criteria is to minimize the peak surface fields, since field emission increases with larger surface electric field, and because high magnetic fields can lead to a quench of the superconducting state of the cavity (the theoritical limit is approximately 200 mT but quenching is possible below such a value due to material defects). Surface fields are linearly proportional to the accelerating gradient and are therefore limiting factors for the performance of the cavity. The upper limit for the peak surface electric field, located in the iris region of the cell, is strongly dependent on the condition of the cavity surface. To enhance this limit, many surface treatment processes have been developed over the years (helium processing [5], high pressure rinsing [6], electro-polishing [7], baking [8], chemical processing [9]...). Combinations of these surface processes have so far allowed to reach peak surface electric fields around 40 MV/m in a reliable manner [10]. Surface electric fields as high as 100 MV/m have already been reached but are not reliable yet for machine operation.
An other desired aspect for the design of a cavity is to maximize the R/Q parameter, which is proportional to the ratio of the stored energy in the cavity over the on-axis accelerating voltage (this last quantity depends on the beta of the particle). Maximizing the R/Q allows to optimize the accelerating efficiency of the structure. This parameter is usually quoted as a "geometrical" parameter because its value depends on the shape of the cavity but not on the amplitude of the field.
A third aspect of the design is to achieve a reasonable amount of coupling between cells. A large coupling allows to have a good field flatness for the entire cavity and lower the risk of having trapped HOMs.
A fourth aspect is to obtain a mechanical stiffness such as to limit the effect of the mechanical deformations/vibrations induced in SRF cavities by microphonics and Lorentz forces. In pulsed operation, the dynamic detuning generated by the Lorentz forces is a major concern in elliptical SRF cavities. It is then of great interest to design a cavity shape that would intrinsically be stiff. Supplementary methods, for example the addition of stiffening rings between cells, are usually applied to further enhance

the stiffness of the structure. Even if calculations using simulation codes are not precise enough to estimate all the aspects of this problem, they are useful to obtain relative tendencies among different cell shapes (issues relative to dynamic detuning in SRF cavities and its compensation are presented in chapter 2). The design of the

Table 1.3: Aspects for the second phase of the design of the cavity shape

For chosen cavity shape	High Order Modes related issues Multipacting Static and dynamic lorentz detuning Thermal stability

end cells must be different from the design of the inner cells due to the connections to the beam pipes. Both end cells can also be different from one an other, for example to accomodate for the connection to the fundamental power coupler (FPC). A first aspect of the end cell design is to obtain equal or lower surface fields than in the inner cells in order to avoid deteriorating the overall cavity performance in terms of accelerating gradient. A second aspect is the external Q (Qex) of a cavity which is mainly determined from the end cell geometry and its connection to the FPC. The Qex measures the amount of coupling between the cavity and the RF feeding source. Depending on the nominal accelerating gradient and on the beam current, an optimum value for the Qex can be determined (see details in section A.5). A third aspect when determining the shape of the end cells is the field flatness.

1.4 Optimization of the cavity geometry

1.4.1 Inner cell case

All the aspects enumerated in the previous section should be considered when desiging a cavity. As a concrete example, the case of the SNS medium beta ($\beta = 0.61$) is presented. It was mentioned before that only four geometrical parameters can be considered for the design of the cell shape. These parameters are, the dome radius Rc, the bore radius Ri, the slope angle α, and the ellipse ratio a/b. For an elliptical SRF cavity of geometrical beta 0.61, the cell is rather weak mechanically and it is found that the slope angle should be smaller than 8 degrees to insure minimum stiffness. At the same time, to insure effective chemical and HPR surface processings, the slope angle of the cavity should be larger than 6 degrees. As a consequence, the value for the slope angle is here constrained in the small region $6° \leq \alpha \leq 8°$. As a trade off, α can be fixed to 7 degrees. The three remaining parameters are Rc, Ri and a/b. The various aspects presented in Table 1.2 can be scanned for different values of these variables. In the following, four different quantities are estimated for each cell geometry and quantitative design criteria are set for each of them. The first of these quantities is E_p/E_{acc}, where E_p is the peak surface electric field and $E_{acc} = E_0 T$ is the accelerating gradient taken for particles with beta equal to the

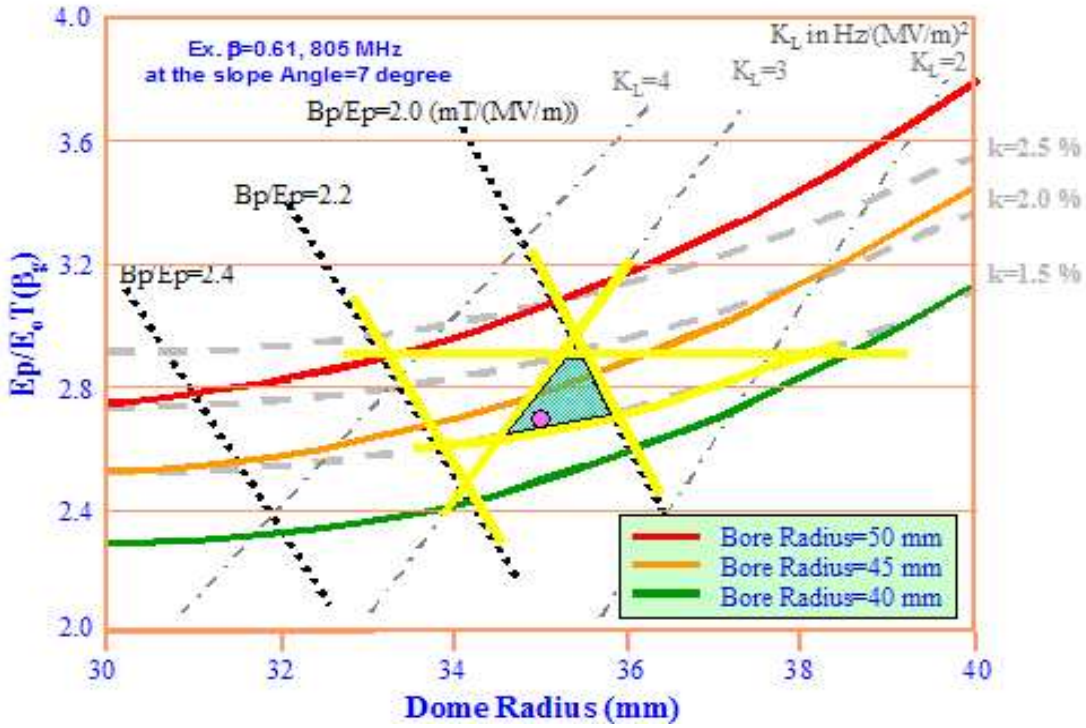

Figure 1.2: Inner cell shape optimization in the SNS medium beta cavity. Four quantities E_p/E_0T, B_p/E_p, k, and K_L are estimated for different values of the geometrical parameters Rc and Ri. Design criteria over the four plotted parameters define an acceptable region where the cell shape can be designed. The final cell design is indicated with a pink dot.

geometrical beta of the cavity β_g. For a given E_p it is of interest to have this ratio as small as possible. In the SNS medium beta cavity, the accelerating gradient is desired to be larger than 10 MV/m and a peak surface electric field of 27.5 MV/m is fixed as nominal value. Adding a 10% margin gives as a first design criteria $E_p/E_{acc} \leq 2.9$. The second quantity is the ratio B_p/E_p where B_p is the peak surface magnetic field. As a design criteria, B_p is pursued to be less than 60 mT for the nominal value of E_p. This translates to a design criteria $B_p/E_p \leq 2.2$ $[mT/MV/m]$. Investigating existing elliptical cavities, it is observed that a ratio lower than 2 seems to translate to lower cavity performance. This empirical observation is used to set an additional criteria $B_p/E_p \geq 2$ $[mT/MV/m]$. The third quantity is the intercell coupling coefficient k calculated from the fundamental passband frequencies as in [1]. The criteria is set to be $k \geq 1.5\%$. Finally, the fourth quantity is the Loretnz force detuning coefficient K_L which relates the amount of static detuning Δf to the accelerating gradient E_{acc} as $\Delta f = -K_L E_{acc}^2$. The criteria for the static Lorentz detuning coefficient is set to be $K_L \leq 3$ $[Hz/MV^2/m^2]$. During the scanning of the geometrical parameters space, it is found that for each values of Rc and Ri, an optimum value of the iris ratio a/b

can be found such that the ratio Ep/E_{acc} is miminized, as illustrated in Fig. 1.1 (the influence over the other parameters can be discarded). As a consequence, the geometrical space can be explored for the two variables Rc and Ri only, by setting the ratio a/b to its optimum value in every case. Different values for Rc and Ri are scanned and the four previous quantities Ep/E_{acc}, Bp/Ep, k and K_L are calculated for each case. The results are presented in Fig. 1.2. The design criteria define a region where the values of Rc and Ri lead to acceptable cavity performance. The final choice is a matter of strategy. In the SNS case for example, the geometry minimizes E_p/E_{acc}. The same approach has also been applied to the SNS high beta case where the nominal surface peak electric field is equal to 35 MV/m and similar results were obtained.

1.4.2 End cell case

Due to the attached beam pipes, the end cell should be designed separately. The aspects related to the end cell shape are listed in Table 1.3. As a first concern, the nominal Qex value should be approximately achieved. In the SNS, the fundamental power coupler is of coaxial type and the Qex is therefore influenced by the level of the electric field at the inner conductor tip position. Because the nominal Qex is large ($Qex = 7.3\ 10^5$ in the SNS medium beta case), the coupler must be positioned in low field region, here a few centimeters away from the end cell of the cavity, in the beam pipe region, as displayed in Fig. 1.3. Because the shape of the end cell influences the electric field (mainly the bore radius or BPR parameter in Fig. 1.3), its design allows to control the value of the Qex. But other parameters shown in Fig. 1.3 must be considered as well. Particularly, the dependence on the vertical position of the inner conductor tip is strong and permits to efficiently control the value of the Qex with other parameters fixed. The Qex was estimated using the calculation scheme proposed in [11] and the agreement with the measurements performed by JLAB on the SNS medium beta cryomodule is satisfying as illustrated in Fig. 1.4. Other aspects of the end cell design are the surface peak fields and the field flatness. The shape of the end cells can be controlled to achieve good results. For example in Fig. 1.5, the on axis longitudinal electric field profile is presented for three different end cell geometries for the SNS high beta case. The field flatness varies roughly from a percent to five percents in this example. The computed field flatness for the final SNS cavity geometries is below the three percents design criteria (Tuning and flattening of a cavity are still required after the assembly of the cavity [12]). The peak surface electric fields are lower in the end cells than in the inner cells which also satisfies the design criteris listed in Table 1.3 (Surface field profiles are shown in chapter 2).

1.5 Further studies with chosen geometry

The design of the inner cells and of the end cells focuses on the general performance of the cavity. As listed in Table 1.3, other particular issues have to be addressed.

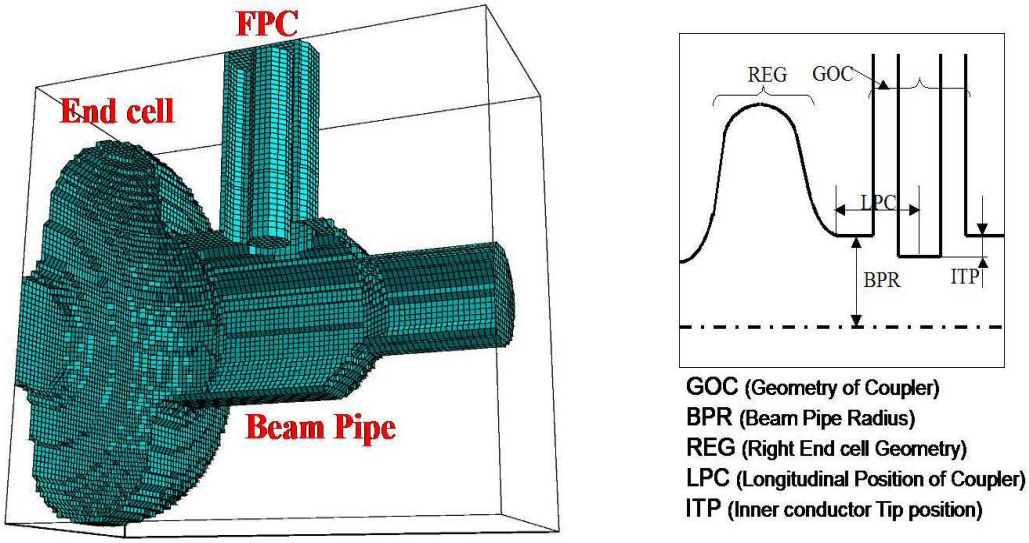

Figure 1.3: End cell and fundamental power coupler. To achieve the nominal Qex, the end cell geometry and the parameters of the FPC can be varied.

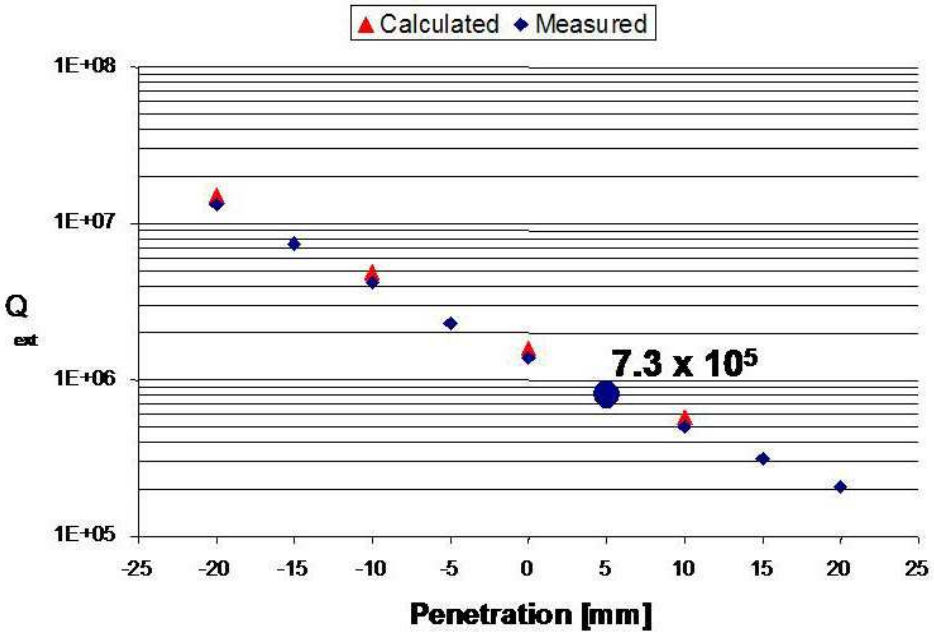

Figure 1.4: Calculated and measured variation of the Qex with respect to the FPC inner conductor tip position (Measurement performed by I. Campisi at JLAB).

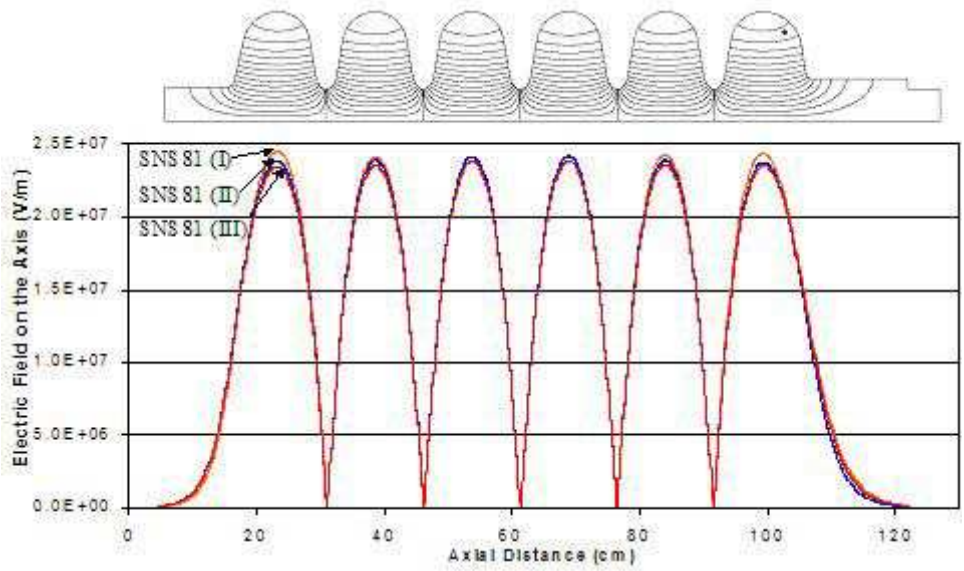

Figure 1.5: On axis longitudinal electric field amplitude with respect to the longitudinal position. The field flatness can be varied by adjusting the end cell geometry.

1.5.1 High Order Modes

As the beam passes through the cavity it deposes energy in the fundamental mode (usual beam loading) but also in all the other modes of the resonator (other fundamental passband modes and HOM). Large excitations of HOM can lead to unacceptable additional power dissipation in the cryogenic system or generate beam instabilities. The amplitude of the excitation for each HOM depends on the HOM's frequency, field profile and level of damping, and on the current, velocity, and time structure of the beam. The characteristics of the HOMs depend on the cavity geometry. Particular attention has to be paid on modes with frequencies close to Fourier components of the beam time structure and on possible trapped modes (modes with large field amplitude in the inner cells and small field amplitude in the end cells). The risk of possible trapped modes increases with the number of cells of the cavity. Such modes have high external Q and can therefore be largely excited by the beam. Study of the HOM related issues in the SNS showed that beam instabilities are not a main concern [13] due to the relatively large mass of the H^-. Inversely, the complex time structure of the SNS beam increases the probability to excite non negligible amount of HOM power [14]. As a consequence, HOM couplers are installed at both end of each SRF cavity to increase the damping of the HOMs and to limit the amplitude of the HOM power deposited in the cryogenic system (The design of the HOM dampers for the SNS was derived from the TESLA HOM couplers [15]).

1.5.2 Microphonics and Lorentz detuning

For high Q resonator such as superconducting cavities, the narrow electromagnetic bandwidth $\omega_{1/2} = \frac{\omega}{2Q_e x}$ makes the coupling between the cavity and the RF feeding source sensitive to rather small amount of detuning (in the same order as the cavity half-bandiwidth $\omega_{1/2}$). As a result, small mechanical deformations due for example to the surronding vibration noise (microphonics) or Lorentz forces (due to the radiation pressure), are a source of concern. Whereas microphonics are usually critical for CW operation, the dynamic detuning associated to Lorentz forces is the main issue for pulsed operation as in the SNS. The shape of the cavity determins its intrinsic stiffeness and relative comparison between different geometries can gives useful tendencies during the desgin of the cells. For example, it is found that in the case of elliptical cavities, smaller α helps increasing the mechanical stability of the cavity. Because the design must take many other issues into considerations, the cavity shape is not solely considered from the mechanical point of view, and the intrinsic stiffness of an elliptical cavity is usually not sufficient. The amplitude of the mechanical deformations can be further limited by increasing the stiffness of the accelerating structure, for example by the addition of stiffening rings between the cavity cells. Calculations using a code simulating mechanical system, as ANSYS [16] for example, allows to find efficient positionning of such stiffening element. Because the cavity needs to be tuned after assembly, the strength of the stiffening must be kept below a certain limit (related to the strength of the tuning system). Generally, the allowable additional stiffening helps reducing the amplitude of the induced vibrations but is not sufficient to make the associated detuning negligible compare to the electromagnetic half-bandwidth. Therefore, the study of an elliptical SRF cavity under dynamic detuning is needed after the design stage. An extensive effort for such a study has been carried in the case of the SNS (see Chapter 2).

1.5.3 Multipacting

The multipacting is a general issue for many RF structures and a global introduction of this phenomenon can be found in [1]. Basically, an electron can be accelerated by the RF field, collide with the wall of the structure and produce secondary electrons. These secondary electrons can in turn produce more electrons and so on. Eventually, a large number of electrons can be generated and, in SRF cavities, absorb a non negligible part of the RF energy or dissipate enough heat through collision to the cavity surface to provoke a thermal breakdown. In both cases, multipacting limits the achievable accelerating gradient of the cavity. The multipacting depends strongly on the cavity geometry (which affects the resonant trajectories of the electrons) and on its surface condition (which affects the secondary electron emission coefficient). After a geometry is considered it is important to look for possible multipacting process. Different codes, such as MultiP [17], exist to study multipacting. 3-D calculations using this code were done for the SNS medium beta cavities [18] and showed good agreement with experimental results and previous calculations performed at the University of Helsinki [19]. In conclusion, the multipacting issue can be investigated using

simulation codes and included in the second phase of the design stage of an elliptical SRF cavity. If strong multipacting is expected, the cavity geometry can eventually be modified.

1.5.4 Thermal stability

For SRF cavities, the thermal stability is a crucial aspect. Many different phenomenons such as thermal breakdown, multipacting, field emission, can affect the thermal stability of a superconducting cavity. Some of them depend directly on the geometry. For example, thermal breakdown can occur in high magnetic field region where a material defect is present [1]. Therefore, limiting the peak surface magnetic field Bp during the design is of direct benefit. Also, the multipacting is a resonant phenomenon related to the cavity geometry and can generate untolerable amount of heat. As a last example of thermal stability issue, it is interesting to mention the case of the SNS cavities where both sides of beam pipes are not actively cooled (the helium vessel ends at the connections of the end cells and the beam pipes). Also, the RRR of the beam pipes was chosen lower than the RRR of the cavity for economical reasons. Using a map of the magnetic field in the end cell regions, a study of thermal stability was done [20] from which the dependence on the beam pipe's RRR values and acceptable defect size was found (the RRR of the beam pipe has been increased from 25 to 50 according to the results). In conclusion, some thermal stability issues are directly related to the cavity geometry and various studies can be valuable to show if the chosen geometry would lead to thermal instabilities.

1.6 Conclusion

The design of a superconducting cavity is a compromise effort that must take various issues into account. To find a satisfying geometry, different aspects governing the cavity performance can be listed. Whereas some aspects can easily be quantified and considered at the early phase of the design, some others necessitating more elaborate studies are generally only addressed in a second phase. In the first phase, a set of criteria for the performance of a cavity can be set and the geometrical parameter space investigated. Eventually, a region in the parameter space satisfying all the design criteria can be found. In the second phase, remaining aspects of the cavity performance can be studied using the chosen cavity geometry. If particular problems are discovered, the cavity shape can possibly be altered.

Chapter 2

Dynamic detuning in SRF cavities

In many designs and real applications for pulsed mode linacs, elliptical SRF cavities have been chosen because of their capacity to operate at high accelerating gradient with high RF efficiency, large bore radius, etc. These elliptical cavities have, however, intrinsic weak mechanical properties. In pulsed mode operation the cavities will experience dynamic detuning, for example due to the time varying Lorentz forces acting on the cavity walls. Since SRF cavities have high Q values in comparison with normal conducting cavities, the matching to the RF generator is sensitive even to small amounts of detuning. To minimize the amplitude of the dynamic detuning, the mechanical strength of the cavity stucture can be enhanced, for example by adding some stiffening rings between the cells [15], by copper deposition on the cavity outer surface [39], or by increasing the mechanical stiffeness of the helium vessel attached to the cavity. These passive schemes help to reduce the amplitude of the dynamic detuning but are usually not sufficient to reduce the detuning to negligible levels compared to the cavity electromagnetic bandwidth. To compensate for the detuning mismatch and to keep the voltage ratings constant during the beam pulse, the RF input power amplitude and phase must be adjusted. For this, a RF control system is needed. Various RF control systems exist to handle such problems, and some high performance digital systems operating mutltiple cavities with a single klystron source, even in presence of dynamic detuning, have already been succefully designed and implemented [25]. In this latest case, particular instabilities for the RF system have nevertheless been identified [26]. Compensating the dynamic detuning effects with the RF system requires providing additional RF power. To avoid wasting RF power, some other active compensative approaches have been proposed [27, 28]. The scheme based on a dynamic tuning of the cavity frequency by piezoelectric tuners has been proven to be a viable choice [33, 29]. To optimize the frequency compensation scheme by a piezoelectric tuner, a clear understanding and modeling of the full detuning dynamics is desirable. Such modeling should combine the calculation of the voltage when the cavity is under a dynamic detuning and the calculation of this detuning, mainly created by the Lorentz forces and by the piezoelectric tuner action. In Section 2.1, the sources of dynamic detuning in SRF cavities will first be presented. In Section 2.2, the dynamic response of the voltage for a cavity under dynamic detuning will be developed and illustrated. In Section 2.3, the modeling for the detuning itself

will be shown. In Section 2.4, both aspects of the modeling will be compared to experimental measurements done on the SNS medium beta prototype cryomodule. Particular emphasis will be made on the calculation of cavity mechanical parameters using simulations and experimental data. With these parameters, the modeling of a cavity can become a valuable tool not only for the understanding but also for practical applications. For example in the last Section 2.5, a study on the compensation of the detuning using a piezoelectric tuner is presented and applied to the SNS case to find adequate piezoelectric input voltage waveforms.

2.1 Sources of the dynamic detuning

To minimize the required RF power consumption, the cavity resonance frequency can be intentionaly detuned with a step tuner, for example when the beam is not accelerated on crest or when the cavity is operated in CW and experiences a static Lorentz force detuning. In such a case, the cavity has a constant resonance frequency offset compared to its nominal value which corresponds to a static detuning situation. In contrast, a dynamic detuning refers to a time dependent variation of the cavity frequency. Three different sources of dynamic detuning will be presented next: the radiation pressure, the piezoelectric active tuner, and the microphonics.

2.1.1 Radiation pressure

The radiation pressure is due the transfer of momentum from the electromagnetic wave to the cavity surface. The pressure is applied normal to the surface and its amplitude, after averaging on the fast RF oscillations of the fields, is given by

$$P_{rad} = \frac{1}{4}\{\mu_0|H|^2 - \epsilon_0|E|^2\} \tag{2.1}$$

where $|H|$ and $|E|$ are the field amplitudes on the cavity surface. The pressure is directed outward when this quantity is positive and directed inward when it is negative. Calculating the field distribution at the surface of the cavity with a code like SUPERFISH [4] shows that in the equator region of the cells where the magnetic field is large, the radiation pressure is positive and pushes the cavity wall outward whereas in the iris region, where the electric field is large, the pressure is directed inward. Applying Eq. (2.1) to the cases of the SNS medium and high beta cavities gives a pressure in the order of 1000 Pa in the equator region where the maximum magnetic field is around 60mT for the nominal accelerating field gradients, and -2000 Pa at the iris region where the nominal peak surface electric fields are around 30 MV/m in both cases. The details of the surface magnetic and electric field distributions and of the radiation pressure distribution, in the SNS medium beta cavity and high beta cavity are displayed in Fig. 2.1 and Fig. 2.2 respectively. In pulsed operation, the cavity is filled and emptied of electromagnetic energy at the operation repetition rate (60 Hz in the SNS). As a consequence the radiation pressure is not constant in time but follows the RF field build-up and decay cycle which produces a dynamic

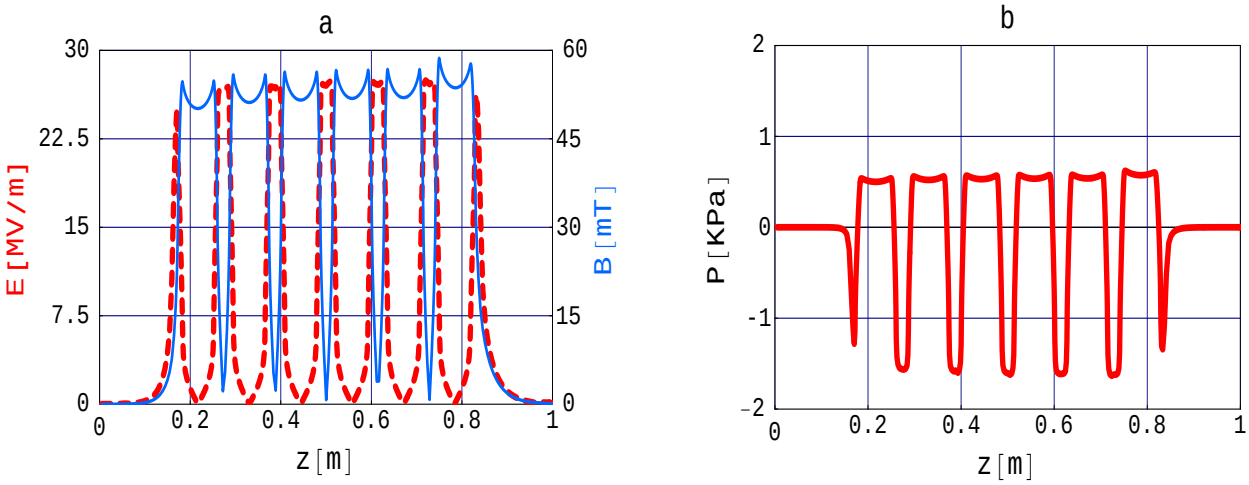

Figure 2.1: (a) Amplitude of the surface magnetic field and surface electric field versus the longitudinal position in the SNS medium beta cavity. The peak surface electric field is set to its nominal value of 27.5 MV/m. (b) Radiation Pressure versus the longitudinal position in the SNS medium beta cavity.

detuning. Due to the inertia of the cavity structure, the mechanical deformations of the cavity surface do not exactly follow in time the variations of the radiation pressure. As a direct consequence, the Lorentz detuning in pulsed operation is usually not constant within the beam pulse, even if the voltage amplitude is maintained constant during this period of time. This raises some issues for the RF control system which should provide a stable voltage amplitude and phase when the beam is on. If the detuning is dynamic during an RF cycle it is nevertheless, after reaching its steady state behavior, repetitive from one pulse to an other because the voltage pulse profile repeats with such a period (see Section 2.3.2). Due to the repetitive nature of the Lorentz detuning, an optimization of the cavity operation by proper feedforward and/or by compensation of the detuning using piezoelectric tuners is possible.

2.1.2 Piezoelectric tuner

Here to fore, the piezoelectric tuner will sometimes simply be refered to as the piezoelectric. When the detuning is dynamic within the beam pulse, the matching condition between the RF source and the cavity is also dynamically varying. To keep the voltage ratings constant, the RF forward power and its phase need to be controled. Compensating for the effect of the detuning requires consumming additional RF power (as shown in Section 2.2.3). Thus, it is desirable to minimize the amplitude of the detuning itself. Some passive methods exist to increase the cavity mechanical strength and minimize the deformations but their application is limited because too rigid a structure would initially be difficult or impossible to tune. An active scheme, first introduced at TESLA, uses a piezoelectric device to dynamically tune the cavity. The physical principle of piezoelectric devices is based on the property of certain crys-

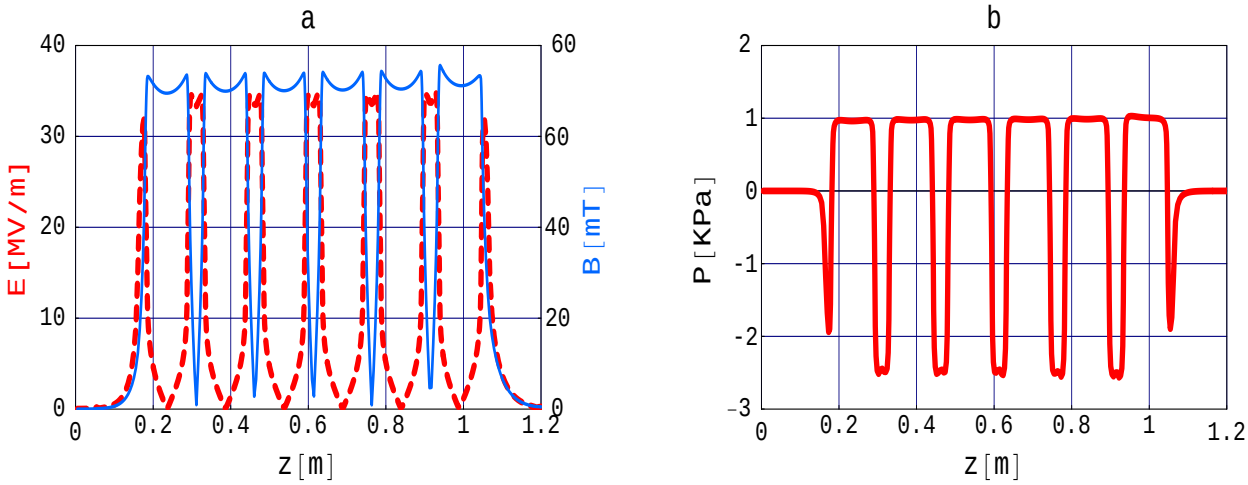

Figure 2.2: (a) Amplitude of the surface magnetic field and surface electric field versus the longitudinal position in the SNS high beta cavity. The peak surface electric field is set to its nominal value of 35 MV/m. (b) Radiation Pressure versus the longitudinal position in the SNS high beta cavity.

tals to mechanically deform when a voltage is applied. The mechanical movement of the piezoelectric transducer can be transmitted to the cavity to deform its surface and therefore to change its frequency. Ideally, the piezoelectric should create a frequency variation exactly opposite to the Lorentz detuning during the beam pulse (and possibly during the RF turn on transient). If the Lorentz detuning is properly cancelled by the piezoelectric tuner action, the cavity frequency remains stable during the beam pulse and the cavity operation is optimal. The piezoelectric is installed outside of the helium vessel but inside of the cryomodule and is consequently operated at cryogenic temperature (see Fig. 2.3). The range of motion of a piezoelectric device is severly reduced when the temperature is lowered from room temperature to cryogenic temperature. It is therefore necessary to choose a piezoelectric tuner with enough stroke margin to insure proper tuning capability at low operating temperatures. In the SNS for example, the desired static tuning range for the piezoelectric is approximately 2 Khz. Some concerns exist about the lifetime of a piezoelectric transducer operating in a radiative environement such as a SRF cavity where gamma-radiation from field emission and possible beam-loss exist. Encouraging results from tests performed by the DESY group showed that the expected lifetime will cover their twenty years machine operation [31]. Similar tests were done at JLAB for the piezoelectric that will be used in the SNS medium beta cavities and there also, no degradation of performances were observed for an equivalent lifetime radiation dose [29]. In conclusion, it appears that the radiations damage is not a limit to the use of piezoelectrics. For the active compensation, the input voltage profile of the piezoelectric needs to be controled in order to generate a dynamic detuning approximately equal and opposite to the Lorentz detuning. Because the detuning generated by the Lorentz forces will be repetitive in steady state, it is in principle possible to optimize the input voltage

profile of the piezoelectric (see Section 2.5). The coupling of the piezoelectric to the cavity is inherently different than the coupling of the Lorentz forces because the action of the piezoelectric is local whereas the action of the radiation pressure is distributed along the structure. For example, the piezoelectric mounted in the SNS medium beta cavities are coupling to the longitudinal modes but not to the transverse modes. To study the optimization of the piezoelectric input voltage waveform, modeling of the cavity system is needed and should include such considerations.

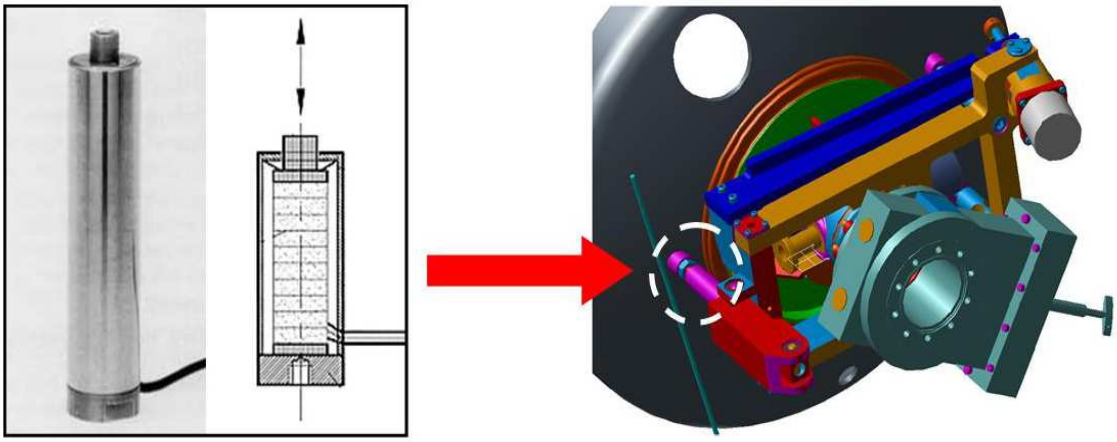

Figure 2.3: Piezoelectric tuner installed in the SNS medium beta cryomodule. The piezoelectric device (left) is installed at one of the cavity end cells (right).

2.1.3 Microphonics

Microphonics characterize any random source of vibrations. They can originate for example from the ground vibrations, from the cryogenic system (variation of the helium pressure...), or from the surrounding equipement (vaccum pumps, water pumps...). At high accelerating gradient, the amplitude of the microphonics detuning is usually much smaller than the detuning created by the radiation pressure. Nevertheless, for cavities with low beam loading and high Q_{ex}, the microphonics are a concern, especially if the cavities are operated in CW. The microphonics are caused by unpredictable sources of mechanical vibrations but their main spectrum components are of low frequencies, it is possible to compensate microphonics detuning by automized piezoelectric tuners [40]. In the cryomodule tests carried by JLAB on the SNS medium beta prototype cryomodule, measurements of the detuning associated to microphomics have been performed and found to be small compared to the half-bandwidth of the cavity $\omega_{1/2}$. For this cavity, the nominal Q_{ex} is equal to 7.10^5 which corresponds to a half-bandwidth of $f_{1/2} = 575Hz$. For the microphonics detuning, the measured σ of the density probability distribution is inferior to 10Hz [29]. Therefore the impact of the microphonics is small, but further measurements will be needed in

the linac tunnel where the cavities will be installed, because the microphonics depend on the local environment.

2.2 Modeling for the cavity RF voltage

The modeling of a cavity dynamics includes two distinct and coupled models. The first concerns the electromagnetic aspect of the problem and is the modeling of the cavity voltage behavior when the cavity is dynamically detuned. This aspect will be studied in this section. The second is the modeling of the detuning itself and is related to the mechanical aspect of the problem which will be studied in Section 2.3. For the electromagnetic part, the cavity is usually represented by a parallel resonant circuit model [21, 22]. In this representation it is possible to have a relation between the RF and beam current source amplitudes and phases, the dynamic detuning, and the cavity voltage amplitude and phase. This relation provides a better understanding of the cavity voltage behavior under dynamic detuning, and can be useful for the optimization of the cavity operation. First, the general analytic expression of the cavity voltage envelope as a function of the current sources and the detuning is derived in an integral form. This general expression includes dynamic detuning of the cavity and time-varying amplitudes and phases of any current sources. Second, different cases where the integral can be analytically solved are presented. The voltage behavior is shown for different types of dynamic detuning functions and RF current functions either in the time domain or as a complex mapping of the complex frequency (see Annex A.2 for explanations). Third, a simple semi-analytical scheme is introduced to calculate the cavity voltage envelope in any practical case. Fourth, the general analytical expression for the voltage envelope as a function of the source current is reinterpreted in two other usefull manners. The first one is to express the source current as a function of the voltage envelope and of the dynamic detuning. With such an interpretation it is for example possible to find various RF control schemes for the build up of the voltage during the turn on transient period for a cavity under dynamic detuning. These schemes will be illustrated in the case of a simple dynamic detuning function. The second reinterpretation is to have the dynamic detuning as a function of the cavity voltage and the source current. From this formulation, it is possible to deduce the dynamic detuning by measuring the voltage and the RF forward power. This could be of practical use for the estimation of the dynamic detuning during the cavity operation.

2.2.1 Integral formulation for the voltage of a cavity under dynamic detuning

In the usual parallel resonant circuit model and in absence of dynamic detuning, the parameters of the resonant circuit are constant through time. In a more general case when the capacitance $C(t)$ and the inductance $L(t)$ are slowly varying in time and when the loaded shunt impedance R_L is constant, the differential equation for the

accelerating mode voltage is

$$C(t)\ddot{V}(t) + \frac{1}{R_L}\dot{V}(t) + \frac{1}{L(t)}V(t) = \dot{I}(t) \tag{2.2}$$

where V is the voltage of the accelerating mode along the cavity axis and where I is the excitation current given by the linear composition of the RF source current I_{RF} and the beam current I_b. Dividing Eq. (2.2) by $C(t)$ and introducing usual cavity parameters gives

$$\ddot{V} + \frac{\omega_c}{Q_L}\dot{V} + \omega_c^2 V = \omega_c \frac{R_L}{Q_L}\dot{I} \tag{2.3}$$

where the angular frequency of the cavity $\omega_c = \sqrt{\frac{1}{LC}}$ and the loaded Q of the cavity $Q_L = R_L\sqrt{\frac{C}{L}}$ are time dependent. Introducing the time dependent frequency detuning parameter $\Delta\omega = \omega_c - \omega$, using the half bandwidth of the cavity $\omega_{1/2} = \frac{\omega_c}{2Q_L}$, and writing the current and the voltage as the products of a complex envelope and an oscillating term following the RF frequency ω as $I = \tilde{I}(t)e^{j\omega t}$ and $V = \tilde{V}(t)e^{j\omega t}$, Eq. (2.3) can be rewritten as

$$\ddot{\tilde{V}} + 2(\omega_{1/2} + j\omega)\dot{\tilde{V}} + (2\omega(\Delta\omega + j\omega_{1/2}) + \Delta\omega^2)\tilde{V} = 2R_L\omega_{1/2}(\dot{\tilde{I}} + j\omega\tilde{I})$$

For systems with loaded Q much larger than the unity, $Q_L >> 1$, the half bandwidth is much smaller than the oscillation frequency, $\omega_{1/2} << \omega$. Considering only the case where the cavity detuning is small compare to the RF frequency, $\Delta\omega << \omega$, and where the source current envelope contains only slow frequency components compared to the RF frequency, $|\dot{\tilde{I}}| << |\omega\tilde{I}|$, the previous equation can be approximated by

$$\frac{1}{2j\omega}\ddot{\tilde{V}} + \dot{\tilde{V}} - j\tilde{\omega}\tilde{V} = R_L\omega_{1/2}\tilde{I} \tag{2.4}$$

with the complex frequency $\tilde{\omega} = \Delta\omega + j\omega_{1/2}$. Under the previous assumptions and considering the case where the detuning frequency contains only slow frequency components compared to the RF frequency, $|\dot{\Delta\omega}| << |\omega\Delta\omega|$, the second order term can be assumed negligible and Eq. (2.4) approximated by the first order equation

$$\dot{\tilde{V}} - j\tilde{\omega}\tilde{V} = R_L\omega_{1/2}\tilde{I} \tag{2.5}$$

The solution of Eq. (2.5) will be shown to be, in good approximation, a solution of Eq. (2.4). In Eq. (2.5), the term $R_L\omega_{1/2}$ can be approximated constant through time because its variations are negligible compared to its initial value. Therefore the complex frequency $\tilde{\omega}$ can be considered as the only time varying parameter. As shown in [25] the RF current and the beam current are explicitely given by $I_{RF} = \sqrt{\frac{8P_{RF}}{R_L}}$, where P_{RF} is the forward power from the RF source, and $I_b = 2I_{DC}$, where I_{DC} is the DC component of the beam (In the case of a cavity in pulsed operation, the DC current is only calculated during the beam-on time). The solution of Eq. (2.5) is the

sum of the source free voltage $\tilde{V}_{SF}$, solution of the homogenous equation, and the driven voltage solution $\tilde{V}_I$, particular solution.

$$\tilde{V} = \tilde{V}_{SF} + \tilde{V}_I \tag{2.6}$$

Separating the variables for the homogenous part of Eq. (2.5) leads to

$$\frac{d\tilde{V}_{SF}}{\tilde{V}_{SF}} = j\tilde{\omega}dt$$

Integrating each side gives the expression for the source free voltage in the case of a time varying frequency

$$\tilde{V}_{SF} = \tilde{V}_0\, e^{j\int_0^t \tilde{\omega}(t')dt'} \tag{2.7}$$

where $\tilde{V}_0$ is the initial state of the cavity voltage envelope. When the driving current is applied for a small amount of time dt' , the derivative of the driven voltage solution is equal to $R_L\omega_{1/2}\tilde{I}$. As a result the driven voltage envelope is changed by an amount

$$d\tilde{V}_I = R_L\omega_{1/2}\tilde{I}dt' \tag{2.8}$$

This constitutes the immediate response of a cavity to a sudden impulse. The evolution of the voltage created by a sudden impulse is equivalent to the evolution of a voltage initially present in the cavity as stated in Eq. (2.7). Using the superposition principle, the current source is seen as a succession of impulses in time and the driven voltage is expressed by a convolution integral.

$$\tilde{V}_I = R_L\omega_{1/2}\int_0^t \tilde{I}(t')\, e^{j\int_{t'}^t \tilde{\omega}(t'')dt''}dt' \tag{2.9}$$

Using Eq. (2.6), Eq. (2.7) and Eq. (2.9), the total cavity voltage can therefore be written as

$$\tilde{V} = \tilde{V}_0\, e^{j\int_0^t \tilde{\omega}(t')dt'} + R_L\omega_{1/2}\int_0^t \tilde{I}(t')\, e^{j\int_{t'}^t \tilde{\omega}(t'')dt''}dt' \tag{2.10}$$

This expression can be used in order to confirm that the second order derivative term of Eq. (2.4), under the stated assumptions, plays a negligible role, see Section A.1. Eq. (2.10) constitutes the integral formulation of the cavity voltage solution in the case of a time varying complex frequency and a time varying complex source current envelope. The first term concerns the behavior of the voltage initially present in the cavity. The real part of the integral under the exponent represents the overall rotation angle due to the detuning and the imaginary part corresponds to the decay of the voltage amplitude. The second term is the voltage induced by the current. It is the sum of all the induced successive voltage impulses. Since the current is assumed non constant in time it remains under the integral. The rotation angle and amplitude decay of an induced voltage impulse are evolving from the time the impulse originates. This fact is included in the boundaries of the integral for the complex frequency.

2.2.2 Application to different cases of dynamic detuning and RF current functions

The Eq. (2.10) is the general integral formulation for the cavity voltage envelope in presence of dynamic detuning and a time varying driving current. Obtaining a more explicit analytical expression for a given set of current and detuning functions $\{\tilde{I}, \tilde{\omega}\}$ is a matter of solving the integrals. Some examples where the integrals can be solved are presented and illustrated. The behavior of the complex voltage envelope will be presented in the time domain and as a complex mapping of the complex frequency, see Annex A.2.

I Constant detuning and constant current envelope

$$\begin{aligned} \tilde{\omega}(t) &= \tilde{\omega}_0 \\ \tilde{I}(t) &= \tilde{I}_0 \\ \tilde{V}(t) &= \tilde{V}_0\, e^{j\tilde{\omega}_0 t} + jR_L\tilde{I}_0\frac{\omega_{1/2}}{\tilde{\omega}_0}\{1 - e^{j\tilde{\omega}_0 t}\} \end{aligned} \tag{2.11}$$

This is the simplest situation, the driving current and the detuning are constant through time. When the detuning is constant it is usually called static detuning. This situation is also a good approximation when the dynamic detuning is negligible compared to the half bandwidth of the cavity. As a first illustration, the development of the voltage amplitude and phase can be presented in time for a few detuning values (see Fig. 2.4). The results for the amplitude are normalized with respect to the value of the voltage in steady state for the on resonance case. After a few $\tau_{1/2}$, the voltage reaches its steady value. The profile of the cavity voltage amplitude and phase in steady state with respect to the detuning are presented in Fig. 2.5. The previous results can also be presented as a mapping of the initial frequency line, see Annex A.2. The normalized mapping is obtained from Eq. (2.11) and illustrated in Figure 2.6 for four different instants in time. Since the phase of the driving current is constant and since no detuning occurs, the point corresponding to $\Delta\omega_0 = 0$ always remains on the real axis. As expected from the analytical solution of Eq.(2.11), the real axis is a line of symmetry for the positive and negative values of the detuning. In steady state the map forms a circle figure equivalent to the well-known impedance figure for a narrow bandwidth resonator. In the first picture of Fig. 2.6, corresponding to $t = 0.7\tau_{1/2}$, the point $\Delta\omega_0 = 0$ is halfway between the origin and its position in steady state. This is consistent with the expected value, since $1 - e^{-\omega_{1/2}t} = 1 - e^{-0.7} \approx 0.5$. This gives an insight on how the mapping can easily give some graphical representation and estimation of the considered case.

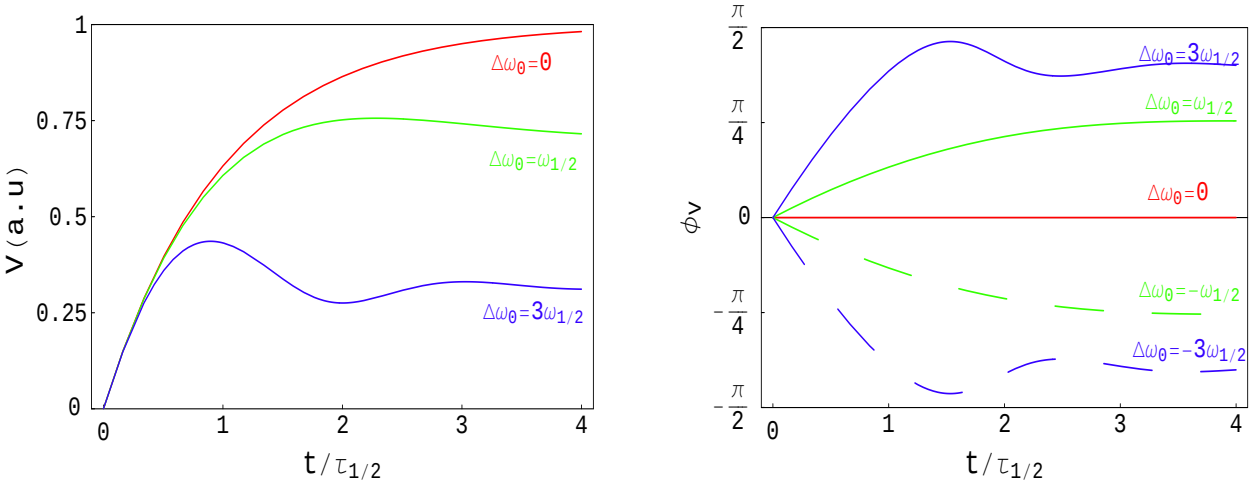

Figure 2.4: development of the voltage amplitude (normalized) and phase (rad) through time for few cases of static detuning. The time unit is equal to the inverse of the half-bandwidth, $\tau_{1/2} = \frac{1}{\omega_{1/2}}$. $\tau_{1/2}$ is a measure of the time needed to reach the steady state value.

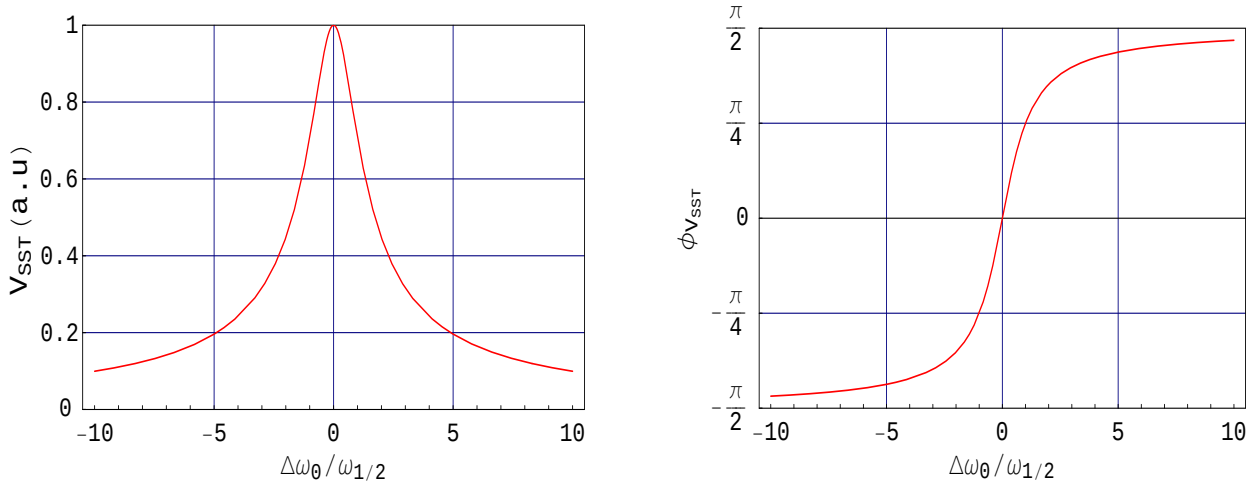

Figure 2.5: voltage amplitude (normalized) and phase (rad) in steady state as function of the value of the static detuning. The amplitude is normalized with respect to the on resonance case and $\omega_{1/2}$ is used for the unit of the detuning axis.

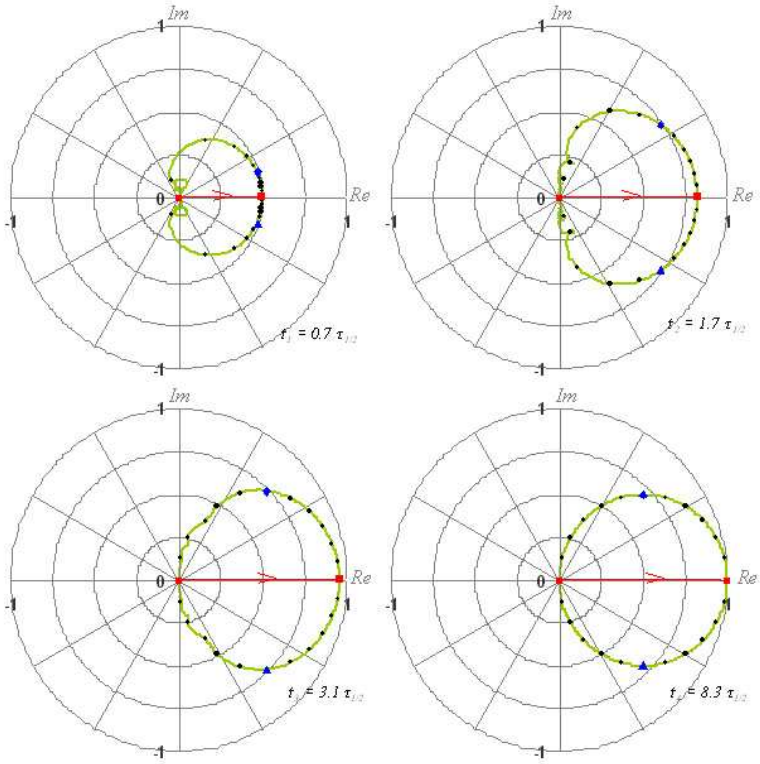

Figure 2.6: Mapping of the normalized quantity $\frac{\tilde{V}(t)}{R_L \tilde{I}_0}$, at four different times for the case of a constant frequency, $\tilde{\omega}(t) = \tilde{\omega}_0$, and a constant current envelope, $\tilde{I}(t) = \tilde{I}_0$.

II Constant detuning and exponential current envelope

$$\begin{aligned} \tilde{\omega}(t) &= \tilde{\omega}_0 \\ \tilde{I}(t) &= \tilde{I}_0\, e^{j\tilde{\omega}_I t} \\ \tilde{V}(t) &= \tilde{V}_0\, e^{j\tilde{\omega}_0 t} + jR_L\tilde{I}_0 \frac{\omega_{1/2}}{\tilde{\omega}_0 - \tilde{\omega}_I}\{1 - e^{j\{\tilde{\omega}_0 - \tilde{\omega}_I\}t}\} \end{aligned} \tag{2.12}$$

As before, such a case can occur if the dynamic detuning is negligible compared to the half bandwidth. The frequency $\tilde{\omega}_I$ of the current function $\tilde{I}$ is complex so that amplitude variations and phase variations are both included. The phase here is varying linearly whereas the amplitude is varying exponentially. Both cases can be of practical interest. From the exponential variation it is easy to derive the case of linear amplitude variation. The mapping is obtained from Eq. (2.12). The result is largely related to the previous mapping. For the frequency $\tilde{\omega}_I = \Re(\tilde{\omega}_I) + j\Im(\tilde{\omega}_I)$ the new mapping can be obtained by translating the frequency domain by $-\tilde{\omega}_I$, performing the previous mapping, then rotating it by an angle equal to $\Re(\tilde{\omega}_I)t$ and finally expanding it by a factor equal to $e^{-\Im(\tilde{\omega}_I)t}$. As an example, the case $\tilde{\omega}_I = \omega_{1/2}$ is displayed in Figure 2.7. The mapping is the same as in the previous case but rotated. For $t = 3.1\tau_{1/2}$ the rotation angle is expected to be $\Re(\tilde{\omega}_I)t = \omega_{1/2}\frac{3.1}{\omega_{1/2}} \approx \pi$, as shown

in the third picture. For the illustrated example, the amplitude of the mapping is unchanged because the frequency $\tilde{\omega}_I$ is purely real. Beside the global rotation of the figure, the reference points have moved along the mapping line. For example the detuning $\Delta\omega_0 = \omega_{1/2}$ occupies the same position on the map as the point $\Delta\omega_0 = 0$ on the previous map. This is consistent with the translation of the frequency domain by $-\tilde{\omega}_I = -\omega_{1/2}$.

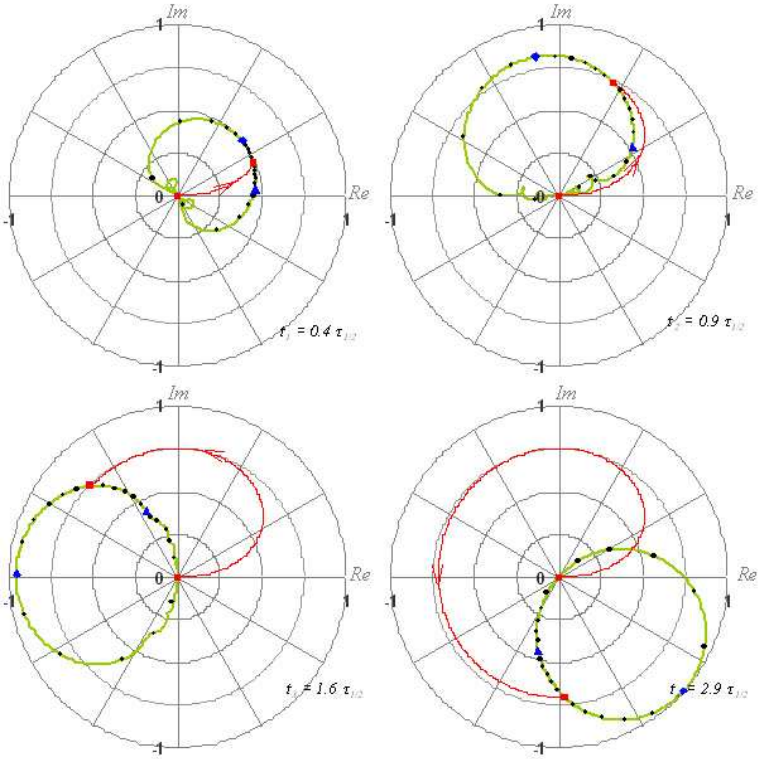

Figure 2.7: Mapping of the normalized quantity $\frac{\tilde{V}(t)}{R_L \tilde{I}_0}$, at four different times for the case of a constant frequency, $\tilde{\omega}(t) = \tilde{\omega}_0$, and an exponential current envelope, $\tilde{I}(t) = \tilde{I}_0\, e^{j\tilde{\omega}_I t}$. For the displayed case $\tilde{\omega}_I = \omega_{1/2}$.

III Linear detuning and constant current envelope

$$
\begin{aligned}
\tilde{\omega}(t) &= \tilde{\omega}_0 + \dot{\omega}_0 t \\
\tilde{I}(t) &= \tilde{I}_0 \\
\tilde{V}(t) &= \tilde{V}_0\, e^{j\{\tilde{\omega}_0 + \frac{\dot{\omega}_0 t}{2}\}t} \\
&\quad - R_L \omega_{1/2} \tilde{I}_0 \sqrt{\frac{\pi}{2}} \left\{ \frac{j}{\dot{\omega}_0} \right\}^{1/2} e^{j\frac{\tilde{\omega}_0^2}{2\dot{\omega}_0}}\, e^{j\{\tilde{\omega}_0 + \frac{\dot{\omega}_0 t}{2}\}t} \left\{ \mathrm{Erfi}\left(\frac{j^{3/2}}{\sqrt{2\dot{\omega}_0}} \omega(\tilde{t}') \right) \right\}_{t'=0}^{t'=t}
\end{aligned}
\tag{2.13}
$$

In the case of linear dynamic detuning, the integral of the complex frequency in Eq. (2.13) leads to a phase varying as the second power of time. Therefore the

integral for the voltage can be expressed with the error function. As in the case of constant detuning an expression for the case of an exponential current function is also possible. Because the linear detuning case can be solved analytically, it is a tool of interest to benchmark a numerical routine used to solve more complicated cases. The mapping function, obtained from Eq. (2.13), is much more complex than in the cases of a constant frequency, but nevertheless the mapping leads to a rather simple interpretation. The case $\dot{\omega}_0 = -0.5\omega_{1/2}^2$ is illustrated in Figure 2.8. The first picture is the mapping at an early time. This mapping looks very similar to the previous ones because the linear dynamic detuning effect is still small. On the second and third pictures the detuning effect appears and the maps seem to be distorted when compared to the maps for no dynamic detuning. Particularly the symmetry with respect to the real axis is broken. This is understandable because the linear dynamic detuning function is not acting symmetrically on the frequency domain. Since the chosen value for $\dot{\omega}_0$ is negative, the points are migrating clockwise on the mapping line. After a long time the pattern of the map freezes. It eventually becomes the equivalent of the trajectory for the values of $\Delta\omega_0$ positive and large compare to $\omega_{1/2}$. All the reference points on the map are migrating towards the origin since in the case of linear dynamic detuning all the frequencies are moving towards an infinite value. The map is totally related with the manner that the dynamic detuning function is affecting the initial detuning values with respect to the resonance region.

IV Sinusoidal detuning and constant current envelope

$$\begin{aligned}
\tilde{\omega}(t) &= \tilde{\omega}_0 + \Delta\omega_{osc}\sin(\omega_{osc}t + \theta_{osc}) \\
\tilde{I}(t) &= \tilde{I}_0 \\
\tilde{V}(t) &= \omega_{1/2}R_L\tilde{I}_0\int_0^t e^{j\frac{\Delta\omega_{osc}}{\omega_{osc}}\{\cos(\omega_{osc}t'+\theta_{osc})-\cos(\omega_{osc}t+\theta_{osc})\}}e^{j\tilde{\omega}_0\{t-t'\}}dt'
\end{aligned} \tag{2.14}$$

Because the detuning in SC cavities originates from mechanical vibrations of the structure, the case of a sinusoidal detuning function is of direct interest. In Eq. (2.14), $\Delta\omega_{osc}$ is the amplitude of the sinusoidal detuning and ω_{osc} is the frequency of its oscillations. No straightforward solution for the voltage envelope can be obtained but an approximation of the solution is developed in Annex A.3. In steady state and for the case with no initial detuning ($\Delta\omega 0 = 0$), it writes

$$\tilde{V}_{SST}(\theta) = R_L\tilde{I}_0 e^{-j\sigma\cos(\theta+\theta_{osc})}\sum_n \tilde{P}_n(\sigma)\cos\theta_n\cos(n\{\theta+\theta_{osc}\}-\theta_n) \tag{2.15}$$

with $\theta = \omega_{osc}t$, $\psi_i = \frac{\omega_{1/2}}{\omega_{osc}}$, $\sigma = \frac{\Delta\omega_{osc}}{\omega_{osc}}$, $\tilde{P}_n(\sigma)$ polynomes of σ with complex coefficients given in Annex A.3,and $\tan\theta_n = \frac{n}{\psi_i}$. As an example, the case $\omega_{osc} = 4\omega_{1/2}$, $\Delta\omega_{osc} = \omega_{1/2}$, and $\theta_{osc} = 0$ is illustrated in Fig. 2.9. Since this dynamic detuning is a pure sine function, the mapping shows reference points migrating counter clockwise and clockwise alternatively. Because the voltage in steady state is a periodic function of frequency ω_{osc}, the mapping eventually becomes periodic in time. The periodicity is visible in the fourth picture of the Fig. 2.9, where the closed trajectories for few

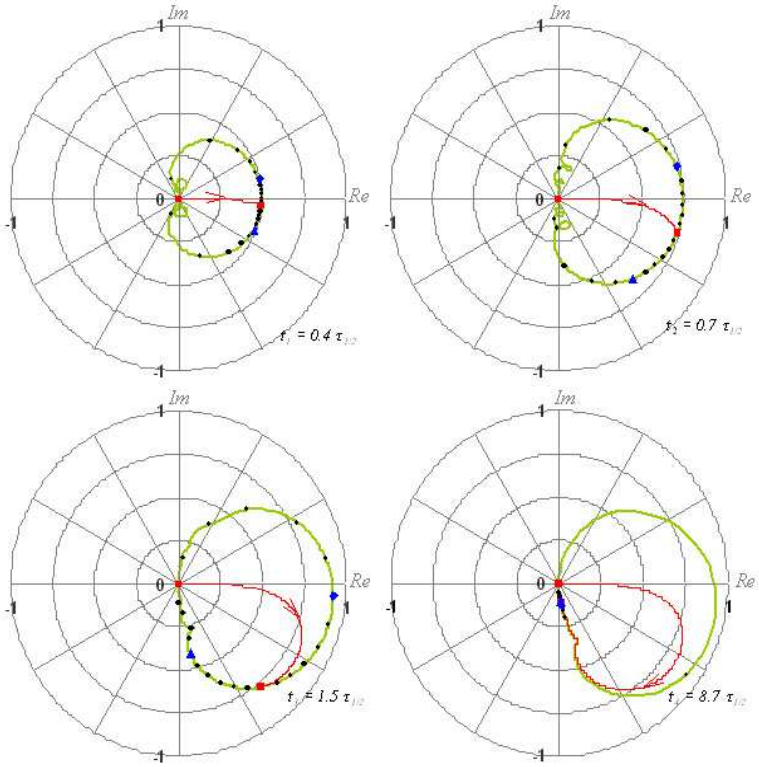

Figure 2.8: Mapping of the normalized quantity $\frac{\tilde{V}(t)}{R_L \tilde{I}_0}$, at four different times for the case of a linear dynamic detuning, $\tilde{\omega}(t) = \tilde{\omega}_0 + \dot{\omega}_0 t$, and a constant current envelope, $\tilde{I}(t) = \tilde{I}_0$. For the case displayed $\Delta\dot{\omega}_0 = -0.5\omega_{1/2}^2$.

reference detuning points are drawn on top of the map. The sense of rotation for these trajectories is noted with plus and minus signs. The symmetry of these trajectories with respect to the real axis is linked to the symmetry property of the sinusoidal dynamic detuning function. The extension of a trajectory depends on the amplitude and on the frequency of the sine detuning function. Faster oscillations or smaller amplitude generally mean smaller extensions.

These facts are illustrated in Fig. 2.10. On the first picture, four closed trajectories of the voltage in the steady state are presented in the case of no initial detuning $\Delta\omega_0 = 0$, a constant frequency of the detuning function $\omega_{osc} = 0.5\omega_{1/2}$, and for a few values of the amplitude of the oscillations $\Delta\omega_{osc}$. As stated, the extension of the voltage trajectory enlarges with the amplitude of the detuning function. On the second picture, four closed trajectories of the voltage are shown for the case of, no initial detuning $\Delta\omega_0 = 0$, a constant amplitude of the detuning function $\Delta\omega_{osc} = \omega_{1/2}$, and four different frequency of oscillations ω_{osc}. As explained, the extension of the voltage trajectories shrink as the frequency of the oscillations increases. When the variations of the detuning are very slow compare to the cavity half-bandwidth, $\omega_{osc} << \omega_{1/2}$, the voltage envelope has time to reach its steady state for every value of the detuning. In this case, the voltage moves approximately on the static detuning

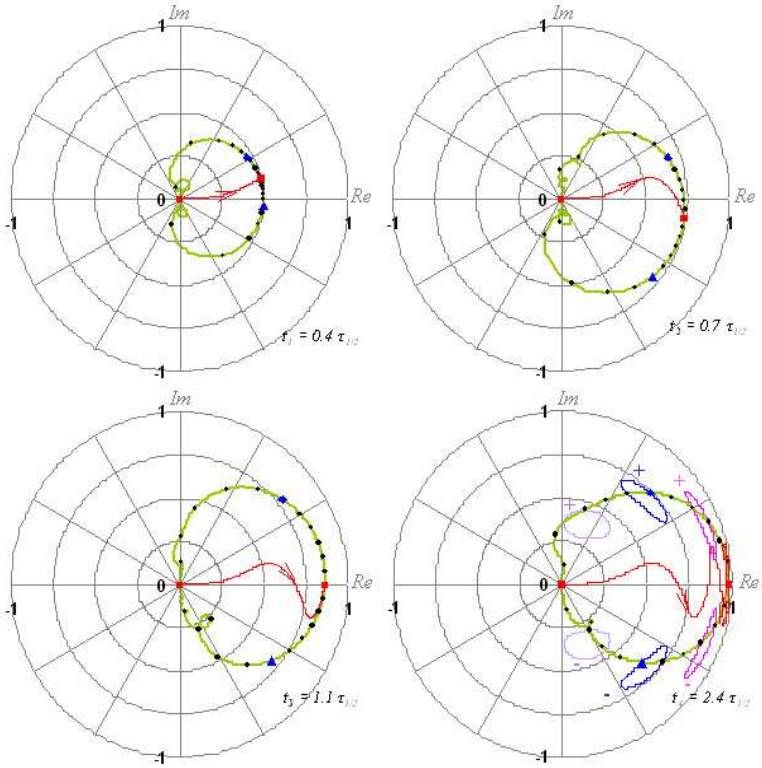

Figure 2.9: Mapping of the normalized quantity $\frac{\tilde{V}(t)}{R_L \tilde{I}_0}$, at four different times for the case of a sinusoidal dynamic detuning, $\tilde{\omega}(t) = \tilde{\omega}_0 + \Delta\omega_{osc}\sin(\omega_{osc}t + \theta_{osc})$, and a constant current envelope, $\tilde{I}(t) = \tilde{I}_0$. On the last picture the closed loops drawn on top of the map are the steady state periodic orbits of a few points. The signs correspond to the sense of rotation of these orbits. For the case displayed, $\psi_i = 1/4$, $\sigma = 1/4$, and $\theta_{osc} = 0$.

circle. As the variations of the detuning becomes faster than the time required for the voltage to reach its steady state, the trajectory of the voltage becomes more complicated. Eventually when the frequency of the detuning is much larger than the half-bandwidth, $\omega_{osc} >> \omega_{1/2}$, the voltage does not have time to vary much during a period of the detuning function and the extension of the voltage trajectory becomes very small.

For each detuning frequency case, it is possible to calculate the minimum and the maximum of the voltage amplitude and of the voltage phase closed trajectory. The results are illustrated in Fig. 2.11. In this picture, the previously described behaviors for the voltage are easily observable. When the frequency of the detuning is large, the amplitudes of the oscillations for the voltage phase and amplitude become very small. Also, the larger the amplitude of the detuning the bigger these amplitudes are. In conclusion, for a SRF cavity under dynamic detuning, the behavior of the voltage is crucially linked to the amplitude and the frequency of the detuning compared to the half-bandwidth.

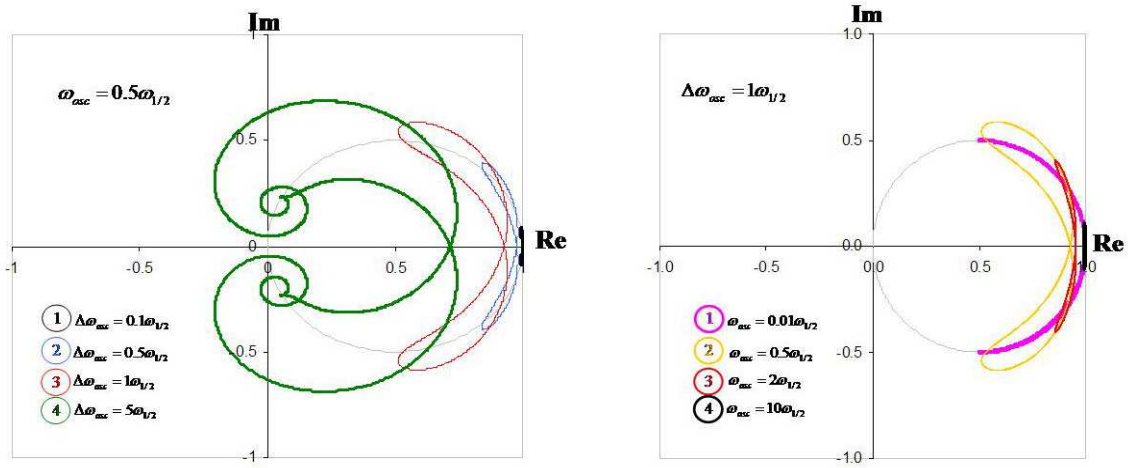

Figure 2.10: Parametric plots of the close trajectory for the voltage in steady state for various sinusoidal detuning conditions.

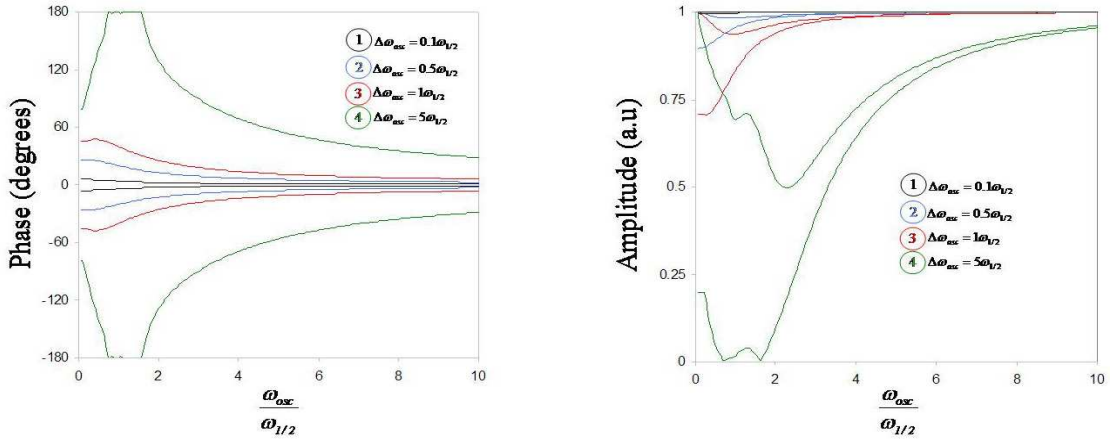

Figure 2.11: Minimum and maximum of the voltage envelope in steady state for various sinusoidal detuning conditions

2.2.3 Other useful interpretations of the voltage equation

In Section 2.2.1, the integral solution for the cavity voltage was calculated from the differential equation written in Eq. (2.5). Instead of solving the differential equation to find the voltage as a function of the current source $\tilde{I}$ and of the detuning $\Delta\omega$, it is possible to transform it to have the current source as a function of the cavity voltage and of the detuning, or to have the detuning as a function of the cavity voltage and of the current source. Both transformations can be of interest. For example, the first one allows the study of different cavity filling schemes and the second implies that the dynamic detuning could be retrieved from the cavity voltage and forward RF power signals (the relation between forward power and RF current amplitude is

$I_{RF} = \sqrt{\frac{8P_g}{R_L}}$). The two transformations and possible applications are presented next.

I Current source as a function of the cavity voltage and of the detuning

From Eq. (2.5) it is easy to obtain

$$\tilde{I}_{RF} = \frac{\left\{\dot{\tilde{V}} - j\tilde{\omega}\tilde{V}\right\}}{R_L\omega_{1/2}} - \tilde{I}_b \tag{2.16}$$

Eq. (2.16) can be useful for example, to obtain the RF forward power to insure the steady state of the cavity voltage when the beam is on, to optimize the cavity parameters $\omega_{1/2}$ and $\Delta\omega_0$, or to study profiles of the feedforward RF source current $\tilde{I}_{RF}(t)$ for different filling schemes of a cavity under dynamic detuning.

I.1) Required RF source ratings to maintain the voltage in steady state

When the beam is on, it is desired to maintain the cavity voltage in steady state. This implies that $\dot{\tilde{V}} = 0$ in Eq. (2.16), and the required RF current $\tilde{I}_{RF}$ to keep the voltage $\tilde{V}$ unchanged is given by

$$\tilde{I}_{RF} = -\frac{j\tilde{\omega}\tilde{V}}{R_L\omega_{1/2}} - \tilde{I}_b \tag{2.17}$$

I.2) Optimization of the cavity parameters in function of the beam current and the synchronous phase

When the beam is on, the necessary ratings for $\tilde{I}_{RF}$ are given by Eq. (2.17). In absence of dynamic detuning, the required RF power to maintain the voltage in steady state can be minimized by choosing appropriate static detuning of the cavity and appropriate Q_{ex}. As demonstrated in Appendix A.5, the values of these parameters are

$$\begin{aligned} Q_{L_{opt}} &= \frac{V}{\frac{r}{Q} I_{b_0} \cos\Phi} \\ \Delta\omega_{opt} &= -\frac{\omega}{2}\frac{\frac{r}{Q} I_{b_0}}{V} \sin\Phi \end{aligned} \tag{2.18}$$

The corresponding RF power is equal to

$$P_{RF_{opt}} = I_{b_0} V \cos\Phi = P_b \tag{2.19}$$

In such case all the forward power is transmitted to the beam and there is no reflected power during the beam on time.

I.3) Additional RF power required for non optimal Q_{ex} and detuning

During the beam on time, the voltage must be kept at a given value. In Section A.5 it is shown that the required RF power to accelerate the beam can be minimized by proper setting of the Q_{ex} and of the detuning of the cavity. Consequently, if

the detuning is not set to such an optimum value, the required RF power increases. The scaling of such additional RF power for non optimal values of the detuning is calculated in Annex A.6 and is given by

$$\frac{\delta P_{RF}}{P_{RF_{opt}}} = \frac{1}{4}\left\{\frac{q^2}{1+q} + \{1+q\}\varepsilon\right\} \tag{2.20}$$

Since the available extra RF power is limited in practice, some limits exists on the tolerable values for the Q_{ex} and the detuning during the beam pulse. These limits are calculable using Eq. (2.20). As two examples, the cases of the medium beta cavity and of the high beta cavity for the SNS are presented. The calculations are done for the cavity having the maximum beam loading in both cases. The H^- beam current is $I_{b_0} = 26\ mA$. The beam power is $Pb = 166\ kW$ for the medium beta cavity and $P_b = 364\ kW$ for the high beta cavity. The results are displayed in Fig. 2.12 and Fig. 2.13.

I.4) Filling schemes for a cavity under dynamic detuning
Eq. (2.16) gives the RF current in function of the voltage and of the detuning. As a direct application, the settings for the RF source current to keep the voltage in steady state during the beam on time was expressed in Eq. (2.17). For the pulsed operation case, it is possible to extend the application and find RF current settings to shape the voltage increase during the turn on transient. In the following, t_{on} will refer to the time when the RF is turned on, t_{inj} to the time when the beam is injected, and t_{end} to the time when the beam pulse ends. The path to raise the voltage from zero to $\tilde{V}_{inj}$ is not unique. For each chosen path and detuning function, the RF current settings are different as given by Eq. (2.16) with the beam current I_b taken equal to zero. Four different possible filling schemes will be presented next.

I.4.a) Linear voltage amplitude and constant voltage phase
This filling scheme gives a very simple analytical expression for the voltage function and insures a tight control of the voltage phase.

$$\tilde{V}(t) = \tilde{V}_{inj}\frac{t}{t_{inj}} \tag{2.21}$$

Using Eq. (2.16), it gives for the RF current

$$\tilde{I}_{RF}(t) = \frac{\tilde{V}_{inj}}{R_L}\frac{\tau_{1/2}}{t_{inj}}\{1 - j\tilde{\omega}t\} \tag{2.22}$$

where $\tau_{1/2} = \frac{1}{\omega_{1/2}}$ and $\tilde{\omega} = \Delta\omega + j\omega_{1/2}$.

I.4.b) Sinusoidal voltage amplitude and sinusoidal voltage phase
This filling scheme allows a smooth approach to the required voltage ratings near the beam injection time.

$$\tilde{V}(t) = \tilde{V}_{inj}\sin\omega_f t e^{j\Phi_{on}\{1-\sin\omega_f t\}} \tag{2.23}$$

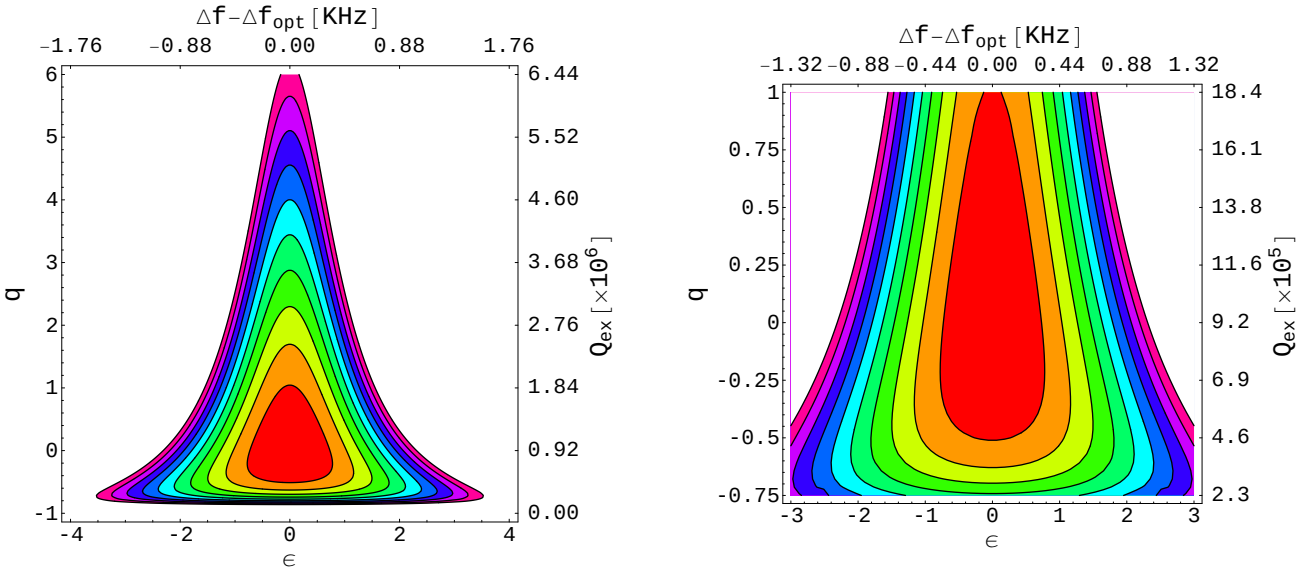

Figure 2.12: Acceptable region for the Q_{ex} and the detuning in the SNS medium beta cavity (ε horizontal axis and q vertical axis). Assuming a total available RF power $P_{RF_{av}} = 410kW$, for a beam current $I_{b_0} = 26mA$, and $P_b = 166kW$, and for a cavity with $V = 6.8\,MV$ and $\frac{r}{Q} = 302\,\Omega$. The optimum values for the Q_{ex} and the detuning are $Q_{L_{opt}} = 9.2\ 10^5$ with corresponding half-bandwidth $f_{1/2_{opt}} = 437Hz$, and $\Delta f_{opt} = 159Hz$. The successive contours starting from the red center region correspond to additional power of 0-10%, 10-20%,... of the available extra RF power. The most outward contour encloses the acceptable limits for the parameters q and ε (enclose the region where the additional power is $\leq$100% of the available power).

where the filling frequency is defined by $\omega_f = \frac{\pi}{2t_{inj}}$ so that the voltage reaches its desired ratings at the injection time. The phase Φ_{on}, corresponding to the excursion of the voltage phase between t_{on} and t_{inj}, is a free parameter. The RF current function associated with the voltage function of Eq. (2.23) is given by

$$\tilde{I}_{RF}(t) = \frac{\tilde{V}_{inj}}{R_L}\frac{1}{\omega_f t_{inj}} e^{j\Phi_{on}\{1-\sin\omega_f t\}}\{\cos\omega_f t\{1 - j\Phi_{on}\sin\omega_f t\} - j\frac{\tilde{\omega}}{\omega_f}\sin\omega_f t\} \quad (2.24)$$

I.4.c) Constant voltage phase and constant RF current amplitude
This filling scheme is hybrid. One constraint is related to the voltage and the other to the RF current. Noting $\tilde{V}(t) = V(t)e^{\Phi_V(t)}$ and $\tilde{I}_{RF}(t) = I_{RF}(t)e^{\Phi_{RF}(t)}$, the constraints can be written as

$$I_{RF}(t) = I_{on} \quad ; \quad \Phi_V(t) = \Phi_{V_{inj}} \quad (2.25)$$

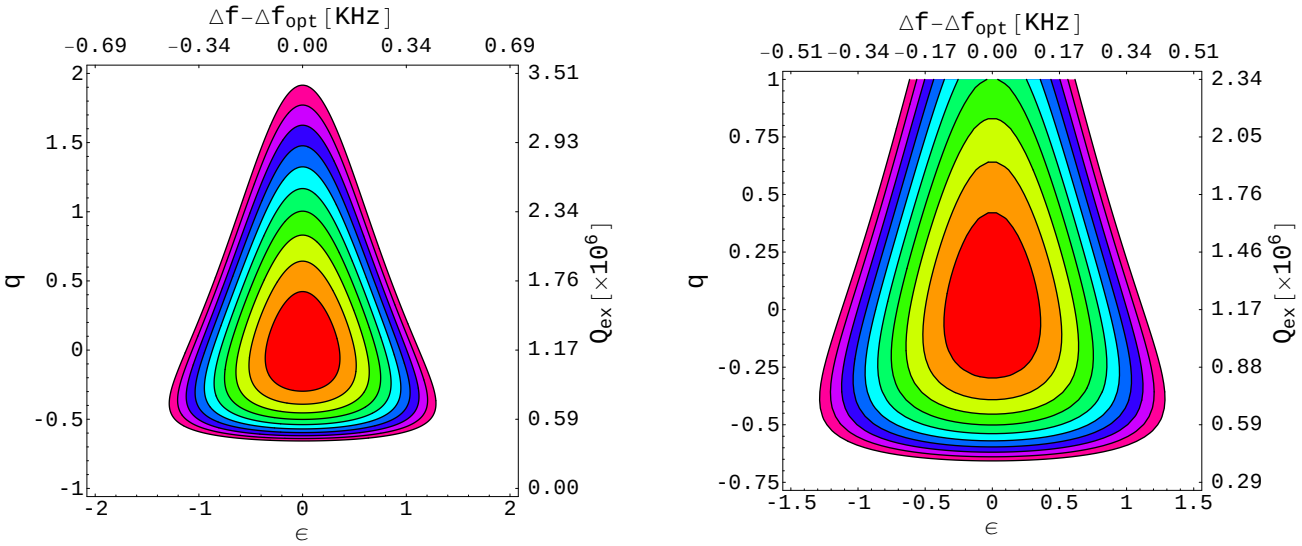

Figure 2.13: Acceptable region for the Q_{ex} and the detuning in the SNS high beta cavity (ε horizontal axis and q vertical axis). Assuming a total available RF power $P_{RF_{av}} = 490\ kW$, for a beam current $I_{b_0} = 26\ mA$, and $P_b = 364\ kW$. The optimum values for the Q_{ex} and the detuning are $Q_{L_{opt}} = 1.2\ 10^6$ with corresponding half-bandwidth $f_{1/2_{opt}} = 343\ Hz$, and $\Delta f_{opt} = 125\ Hz$.

The value of the parameter I_{on} is determined by the constraint that the voltage should reach its amplitude at the time t_{inj}.

I.4.d) Linear RF current amplitude and smooth RF transition at injection
All the previous filling schemes lead to the voltage V_{inj} at the beam injection time. But each of them require a sudden jump in the settings of $\tilde{I}_{RF}$ at that time because these settings, suddenly constrained to keep the voltage in steady state, are in general not continuous at the end of the raising period. It is possible to find a filling scheme that does not present such discontinuities. This means finding some RF current function that satisfies two purposes. First that the voltage reaches its required ratings at t_{inj} and second that the RF current settings are continuous at that time. The continuity criteria can be express by

$$I_{RF}(t_{inj}^-) = I_{RF}(t_{inj}^+) = -\frac{j\tilde{\omega}(t_{inj})\tilde{V}_{inj}}{R_L\omega_{1/2}} - \tilde{I}_b \tag{2.26}$$

where t_{inj}^- and t_{inj}^+ denote times just before and just after t_{inj}. The RF current $\tilde{I}_{RF}(t)$ can be for example chosen as a linear function

$$I_{RF}(t) = \tilde{I}_{RF}(t_{inj}) + \tilde{I}_{on}\{1 - \frac{t}{t_{inj}}\} \tag{2.27}$$

The parameter $\tilde{I}_{on}$ represents the initial value of the RF current and has to be determined so that the voltage at the injection time satisfies its desired ratings. The four filling schemes referenced as a, b, c, and d, for respectively I.4.a), I.4.b), I.4.c), and I.4.d), are illustrated in Fig. 2.14 and Fig. 2.15, in the case of a sinusoidal dynamic detuning function.

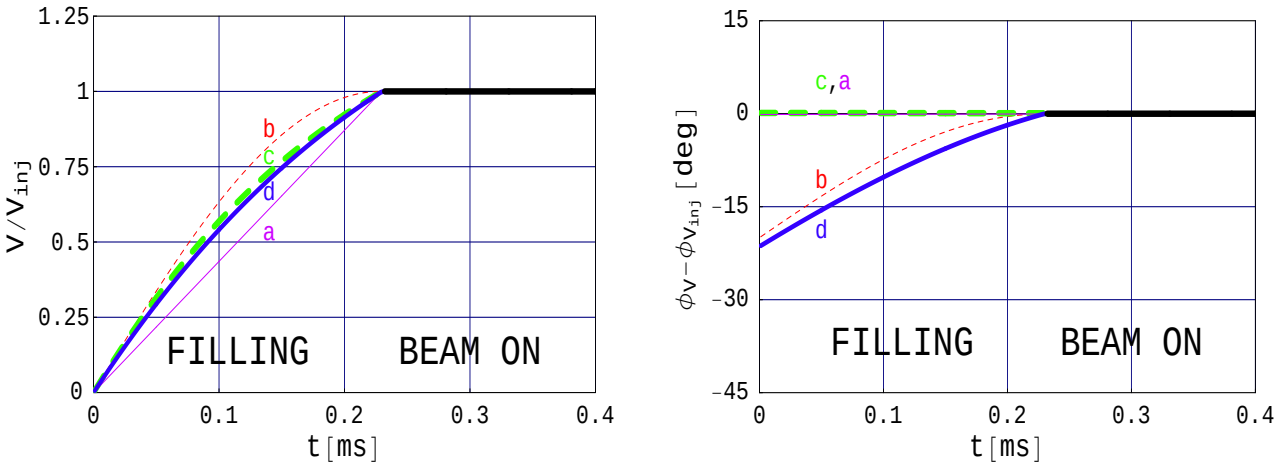

Figure 2.14: Development of the cavity voltage amplitude and phase through time, for different filling schemes (a,b,c,d) in the SNS medium beta cavity. The ratio $\frac{V(t)}{V_{inj}}$ is plotted for the amplitude. This ratio should be equal to one after t_{inj}. The difference $\Phi_V(t) - \Phi_{V_{inj}}$ is plotted for the phase and it should be equal to zero after t_{inj} ($t_{inj} = 230\ \mu s$ here). The beam on time is equal to 1 ms and only a fraction of this time is displayed. A sinusoidal form was used for the dynamic detuning function.

II Detuning in function of the cavity voltage and of the current source

It is possible to modify Eq. (2.5) and write

$$\Delta\omega = -j\omega_{1/2}\left\{1 + \frac{\dot{\tilde{V}}}{\omega_{1/2}\tilde{V}} - \frac{R_L\tilde{I}}{\tilde{V}}\right\} \tag{2.28}$$

$\omega_{1/2}$ and R_L are known parameters. The source current $\tilde{I}(t) = \tilde{I}_{RF}(t) + \tilde{I}_b(t)$ can be obtained from the forward power information and from the beam current informations. $\tilde{V}(t)$ and $\dot{\tilde{V}}(t)$ can be deduced from the pick-up probe signal after proper calibration. Using Eq. (2.28) it is possible to retrieve the detuning $\Delta\omega(t)$ from the measured data. The method to measure the detuning (without beam) by turning off the RF feeding source, monitor the voltage phase evolution $\phi_V(t)$, and equate the cavity detuning to the first derivative of the voltage phase $\Delta\omega(t) = \dot{\phi}_V$, as in [25], is only a particular case of Eq. (2.28). It should be mentioned that the real part of

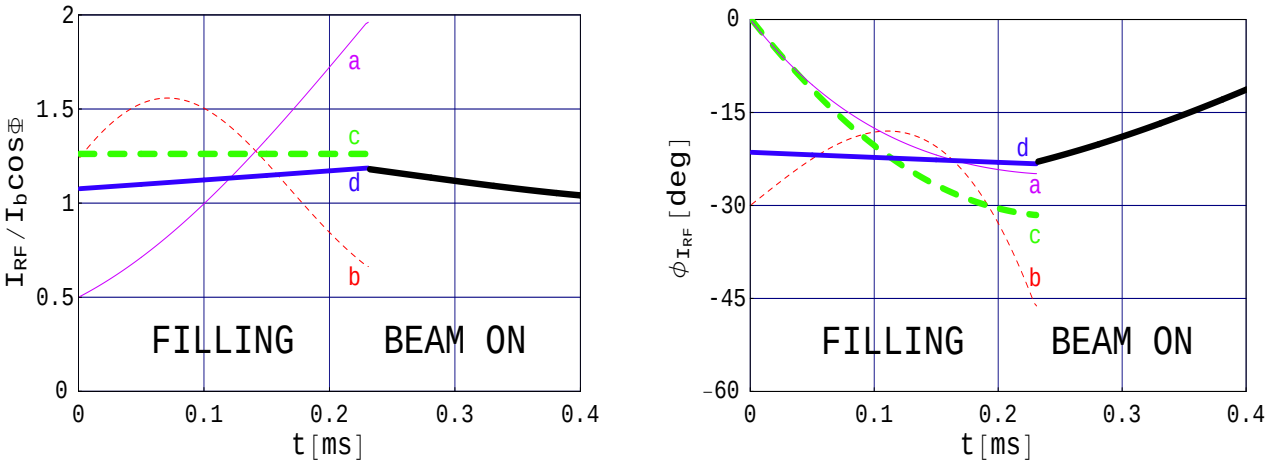

Figure 2.15: RF current amplitude and phase through time for different filling schemes (a,b,c,d) in the SNS medium beta cavity. The ratio $\frac{I_{RF}(t)}{I_b \cos\Phi}$ is plotted for the amplitude. The difference $\Phi_{I_{RF}}(t) - \Phi_{V_{inj}}$ is plotted for the phase. The injection time is $t_{inj} = 230\ \mu s$. The beam on time is equal to 1 ms and only a fraction of this time is displayed. The dynamic detuning function in this example is chosen equal to $\Delta\omega(t) = \omega_{1/2}\{1.3 - 0.9\cos(0.9\omega_{1/2}t)\}$.

the bracket term in Eq. (2.28) should be equal to zero at all time. Eq. (2.28) gives a tool to monitor the dynamic detuning when some voltage signal is available in the cavity. In pulsed operation for example, the cavity has no RF signal between beam pulses and the method can not be applied, unless some small amplitude RF signal is injected during this time. This restriction is not very important since the monitoring of the detuning is primarily of interest during the RF turn on transient and within the beam pulse time period.

2.3 Modeling for the dynamic detuning

In Section 2.2, the first aspect of the modeling of a cavity under dynamic detuning regarding the RF voltage calculation has been presented. The second aspect is the modeling of the cavity frequency detuning itself. The cavity shape deforms under the action of Lorentz forces, piezoelectric forces, or microphonics action (variation in the helium pressure for example). To this mechanical deformation corresponds a variation of the cavity resonance frequency. To estimate the frequency detuning, a mechanical model is necessary. Some mechanical models have been proposed to link the Lorentz forces to the detuning [23, 24]. These models are rather simple and successful approaches to represent experimental results quantitatively by estimating the detuning with ordinary differential equations of the first or second order [32]. The use of mechanical codes also showed interesting results [34] but parameters, particularly for the mechanical damping, can not be accurately known from simulation codes

and need to be adjusted by hand. Other than using extra RF power, some active compensation schemes have been proposed to compensate the effect of the Lorentz detuning [27, 28]. The scheme based on a dynamic adjustement of the frequency by a piezoelectric tuner has been proven to be a viable choice [33, 29]. A first attempt to include the frequency variation generated by the piezoelectric tuner in the modeling process showed good agreement with experimental results [30]. Nevertheless, clear differences between the Lorentz force action and the piezoelectric tuner action were observed experimentally and remain to be clarified [31, 29]. For example, the differences in the phase profile of the respective transfer functions need to be explained. For this purpose, a more qualitative modeling approach is proposed in the following. This model leads to a simple explanation for the difference between the phase profiles of the respective transfer funtions but is also compatible with the simpler modal approach using second order ODE.

2.3.1 Modeling by a vibrating string

The goal is to explain conceptually the main difference between the Lorentz force action and the piezoelectric tuner action. To model the cavity wall by a vibrating string seems an interesting choice because of its relative simplicity and because it contains various aspects of the physics. Firstly, the amplitude of the vibrations are small which is usually assumed in the vibrating string problem. Secondly, a string of finite length with fixed boundary conditions will produce a modal basis equivalent to the mechanical resonances of the cavity. Thirdly, some mode damping can be added to reproduce the attenuation in time of the cavity mechanical mode vibrations. Fourthly, distributed forcing, like the Lorentz forces, or local forcing, like the piezoelectric tuner action, are both possible. Fifthly, the detuning can be connected to the vibrations by integration of the transverse displacement over the longitudinal dimension of the string.

Assuming a string of length l attached at its longitudinal extremities $x = 0$ and $x = l$ so that its transverse displacement $u(x,t)$ at these locations are null at any instant t; $u(0,t) = u(l,t) = 0$. Considering some possible damping forces proportional to the time derivative of the transverse displacement and some driving forces continuously distributed along the string and directed transversely. Assuming also that these driving forces have separable spatial and time dependences. Under these conditions, the transverse motion of the string satisfies a one dimension inhomogeneous damped wave equation.

$$\partial_t^2 u(x,t) + a\partial_t u(x,t) - c^2\partial_x^2 u(x,t) = g(x)h(t) \tag{2.29}$$

where a is the constant damping parameter, c the speed of the wave along the string, and $g(x)h(t)$ the transverse force acting on the string with separated longitudinal and time dependences. The separation between spatial dependence and time dependence is true for the two considered sources of vibrations, Lorentz forces and piezoelectric tuner forces. To complete the model an equivalent of the frequency detuning for the vibrating string should be linked to the transverse displacement. In the case of a cavity, the change in frequency created by a change in the resonator volume is given

by the Slater formulation.

$$\frac{\Delta\omega(t)}{\omega_0} = \frac{\int\limits_{\Delta v_c(t)} \epsilon_0|E|^2 - \mu_0|B|^2\, dv}{\int\limits_{v_c(0)} \epsilon_0|E|^2 + \mu_0|B|^2\, dv} \tag{2.30}$$

where $\Delta\omega$ is the variation of the cavity frequency, ω_0 is the initial frequency of the cavity, and where the quantities depending on the electric and on the magnetic fields should be integrated over the initial volume of the cavity $v_c(0)$ and over the time dependent variation of the cavity volume $\Delta v_c(t)$. In the represention by a vibrating string, the integration over a surface is equivalant to the the integration over a volume. It is assumed that when the string is at its rest position, the dynamic frequency detuning is null. The Eq. (2.30) can be rewritten

$$\Delta\omega(t) = \int\limits_{\Delta s(t)} \frac{\partial\omega}{\partial s}\, ds \tag{2.31}$$

where $\frac{\partial\omega}{\partial s}$ is the frequency detuning sensitivity and $\Delta s(t)$ the variation of the surface occupied by the string in comparison to its rest position as pictured in Fig. 2.16. The electromagnetic fields depend on the position in the resonator but because the

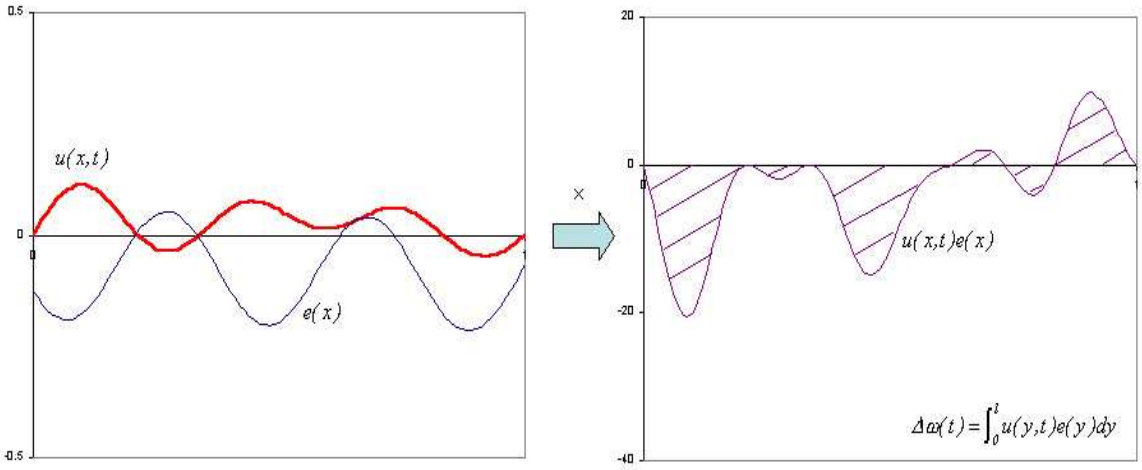

Figure 2.16: Representation of the cavity dynamic detuning process by a vibrating string. The transverse displacement $u(x,t)$ is equivalent to the deformation of the wall. Multiplying by the frequency sensitivity $e(x)$ and integrating along the string gives the detuning $\Delta\omega(t)$.

amplitude of the cavity wall deformations are small, the variation of the field amplitudes in the neighborhood of the cavity surface are negligible. As a consequence, the frequency sensitivity in the string representation can be considered as a function of the longitudinal variable only and not of the transverse displacement. It follows that

the integration over the surface can be replaced by an integration over the longitudinal position. Doing so, the infinitesimal element of surface is decomposed as the transverse displacement times the longitudinal infinitesimal element. Eq. (2.31) can be rewritten as

$$\Delta\omega(t) = \int_0^l u(x,t)e(x)\,dx \tag{2.32}$$

where for convenience $e(x) = \frac{\partial\omega}{\partial s}(x)$. It is important to notice that the function $e(x)$ carries a sign information since from Eq. (2.30), the contributions of the magnetic and electric fields to the frequency detuning, for the same volume variation of a volume, are opposite. Eq. (2.29) and Eq. (2.32) constitute the essence of the vibrating string approach which consists of estimating the detuning in two steps. The first step relates the driving force to the transverse displacement and the second step links the displacement to the frequency detuning. To proceed further, Eq. (2.29) has to be solved. The solution of the wave equation is given in section A.7. The final result shows that the movement of the string can be decomposed on a modal basis and that the transverse displacement associated with each mode has separable spatial and time dependences. The excitation level of a particular mode can be found by projection of the forcing function on the mode spatial shape. The time dependence of each mode is reducible to an ordinary and inhomogenous second order differential equation. The result for the transverse displacement can be used in Eq. (2.32) to find the corresponding detuning. In the next section, it is shown that the model for the detuning can eventually be written as a system of ODEs.

2.3.2 System of ODEs for the detuning

I Solution for the dynamic detuning

It was shown in Section 2.3.1 that the detuning can be obtained from the transverse displacement by integration, as written in Eq. (2.32). Introducing the parameter $z_m = \int_0^l e(x)\sin(K_m x)\,dx$ it follows

$$\begin{aligned}\Delta\omega(t) &= \int_0^l u(x,t)e(x)\,dx \\ &= \sum_m \Big\{ U_m(t) \int_0^l e(x)\sin(K_m x)\,dx \Big\} \\ &= \sum_m z_m U_m(t) \\ &= \sum_m \Delta\omega_m(t)\end{aligned} \tag{2.33}$$

In Eq. (2.33), the total detuning is decomposed to a sum over the detuning associated with each mechanical mode. Using the relation for the m^{th} mechanical mode $\Delta\omega_m(t) = z_m U_m(t)$ in Eq. (A.38) and assuming also that the damping can be different

for each mechanical mode leads to

$$\Delta\ddot{\omega}_m + \frac{\Omega_m}{Q_m}\Delta\dot{\omega}_m + \Omega_m^2\Delta\omega_m = \Omega_m^2\frac{w_m z_m}{\Omega_m^2}h(t) \tag{2.34}$$

where for later convenience, the rigth side has been rewritten into an equivalent form. In conclusion, the qualitative approach to the problem as a vibrating string is compatible with the usual modeling by a system of second order differential equations. The general solution of a second order differential equation is given by Eq. (A.47). Applying it to the parameters of Eq. (A.38) gives

$$\begin{aligned}\Delta\omega_m(t) = \quad & \Delta\omega_{0,m}e^{-\eta_m\Omega_m t}\sin(\mu_m\Omega_m t + \Phi_{0,m}) \\ & + \frac{w_m z_m}{\mu_m\Omega_m}\int_0^t h(t')e^{-\eta_m\Omega_m\{t-t'\}}\sin(\mu_m\Omega_m\{t-t'\})\,dt'\end{aligned} \tag{2.35}$$

where $\Delta\omega_{0,m} = \sqrt{C_m^2 + D_m^2}$, $\Phi_{0,m} = \arctan(\frac{C_m}{D_m})$, $C_m = \Delta\omega_m(0)$, and $D_m = \frac{\Delta\dot{\omega}_m(0)+\eta_m\Omega_m\Delta\omega_m(0)}{\mu_m\Omega_m}$. The first term on the right side of Eq. (2.35) corresponds to the decay of the initial detuning due to the damping. The second term corresponds to the detuning generated by the driving force. It is interesting to note that if the forcing function h is periodic with period T (corresponding to frequency ω), then the steady state detuning is also periodic with the same period. This can be proven by first mentioning that in the steady state, only the second term remains. Then, because $h(t)$ has period T, it is decomposable by a discrete fourier transform into a sum of harmonics of period T. (for example it can be written $h(t) = \sum_{n=0}^{\infty} g_n\cos(n\omega t + \phi_n)$). According to the results of Section A.8, it is shown that any harmonic n of frequency ω will lead, in steady state and for any mode m, to a detuning function of period $n\omega$. Therefore the total detuning obtained by superposition is a sum of periodic functions of period T and its harmonics. In consequence the detuning generated by a periodic function h is also a periodic function of the same period.

II Difference in the coupling to the mechanical modes

In the described mechanical model for the dynamic detuning of a SC cavity, the detuning was shown to satisfy a set of independent second order ODEs. In Eq. 2.34, the driving term is proportional to $w_m z_m$ which is the product of the projection on the m^{th} mechanical mode shape, of the physical driving force and of the frequency sensitivity. In the case of a constant cavity voltage V_{cav}, the generated detuning is static and usually noted $\Delta\omega = -KV_{cav}^2$ where K is called the coupling coefficient (in reality the detuning is commonly expressed with respect to the accelerating field $\Delta\omega = -KE_{cav}^2$, but a linear relation exists between E and V which makes the two forms totally equivalent). From Eq. (2.33) it appears that there is not a unique coupling coefficient but many coupling coefficients $k_m = \frac{w_m z_m}{\Omega_m^2}$ relating the applied force to the different mechanical modes of the cavity structure. These coupling coefficients are simply related to the static coupling coefficient by $-K = \sum_m k_m$. In a cavity operated in CW, the only relevant parameter is the static coupling coefficient K whereas in

pulsed operation, particular attention should also be paid to possible mechanical resonances occuring for modes which are harmonics of the repetition rate. In the case of the Lorentz detuning, the physical force acting on the cavity originates from the radiation pressure $P_{rad} = \frac{1}{4}\{\mu_0|H|^2 - \epsilon_0|E|^2\}$. From the Slater formulation it appears that the frequency sensitivity is actually proportional and of opposite sign to the Lorentz force which in the vibrating string model translates to $g(x) \propto -e(x)$. It follows that for the radiation pressure action $w_m \propto -z_m$ and that all the coupling coefficients k_m are negative. In reality, this assertion is not exactely true because the usual Slater formulation is only valid for the mechanical deformations near the cavity surface but not for geometrical perturbations in the inter cells or in the beam pipe regions as demonstrated in [37]. This consideration will be overlooked here and all the coupling coefficients for the Lorentz forces action will be assumed negative. For convenience it is possible to redefine all the coupling coefficients as positive and add a negative sign to the driving term. Eq. (2.34) is then rewritten as

$$\Delta\ddot{\omega}_m + \frac{\Omega_m}{Q_m}\Delta\dot{\omega}_m + \Omega_m^2\Delta\omega_m = -\Omega_m^2 k_m V^2 \quad ; \quad k_m > 0 \tag{2.36}$$

In contrast, for a cavity driven by a piezoelectric tuner, the driving forces are totally independent of the electromagnetic fields. In consequence, the parameters w_m and z_m are independent and the coupling coefficients $k_m = \frac{w_m z_m}{\Omega_m^2}$ can be positive for some mechanical modes and negative for others. Assuming as a good approximation that the piezoelectric force applied on the cavity is linear with a driving input voltage V_p, the Eq. (2.34) can be written as

$$\Delta\ddot{\omega}_m + \frac{\Omega_m}{Q_m}\Delta\dot{\omega}_m + \Omega_m^2\Delta\omega_m = \Omega_m^2 k_m V_p \tag{2.37}$$

where the coupling coefficients k_m can be of both signs. The qualitive approach of the problem gives a simple insight to the difference between the coupling of the Lorentz force and of the piezoelectric tuner action to the mechanical modes. This consideration is useful when attempting to extract mechanical parameters from measurements with the help of the simulations as done section 2.4.

2.4 Comparison with experimental results from the SNS medium beta prototype cavities

In the previous Sections, the basic constituents of the model for a SRF cavity under dynamic detuning were presented. In this section, results of measurements performed on the SNS medium beta prototype cavities are presented and compared to results of the simulations. Particular emphasis is given to the extraction, from measurements, of the mechanical parameters related to the action of the Lorentz forces and of the piezoelectric tuner forces. This extraction procedure has two purposes, the first one is to show that the model is compatible with measurements, the second one is to have eventually a realistic virtual cavity that allows further study, such as the optimization of the Lorentz detuning compensation using piezoelectric tuners.

2.4.1 Detuning by the Lorentz forces

The equations for the voltage amplitude and phase are much simpler for a cavity operated phase locked (see Section A.9). For example, the voltage amplitude is independent of the detuning and this fact simplifies the extraction of the mechanical parameters associated with the radiation pressure action. As shown by Delayen [38], the cavity can be excited in CW and small modulations of the RF current applied to generate sinusoidal variations of the voltage amplitude which produce in turn sinusoidal variations of the Lorentz forces. The transfer function linking the RF current modulations to the detuning is obtained by fixing the amplitude of the RF current modulations and by sweeping the frequency of these modulations. The amplitude and the phase of the transfer function are displayed in Fig. 2.17. The reconstruction of the mechanical basis is performed using the result of Section A.9.2. As explained in Section A.9.2, the value of the external Q can be deduced from the behavior of the phase of the transfer function and it is found for the considered set of measurements $Q_{ex} = 2.10^6$. The detuning and so the amplitude of the transfer function is proportional to the coupling coefficients as written in Eq. (A.59). The values for the coupling coefficients are scaled using the measured value for the static detuning coefficient (sum of all the modal coupling coefficients as explained previously). It is

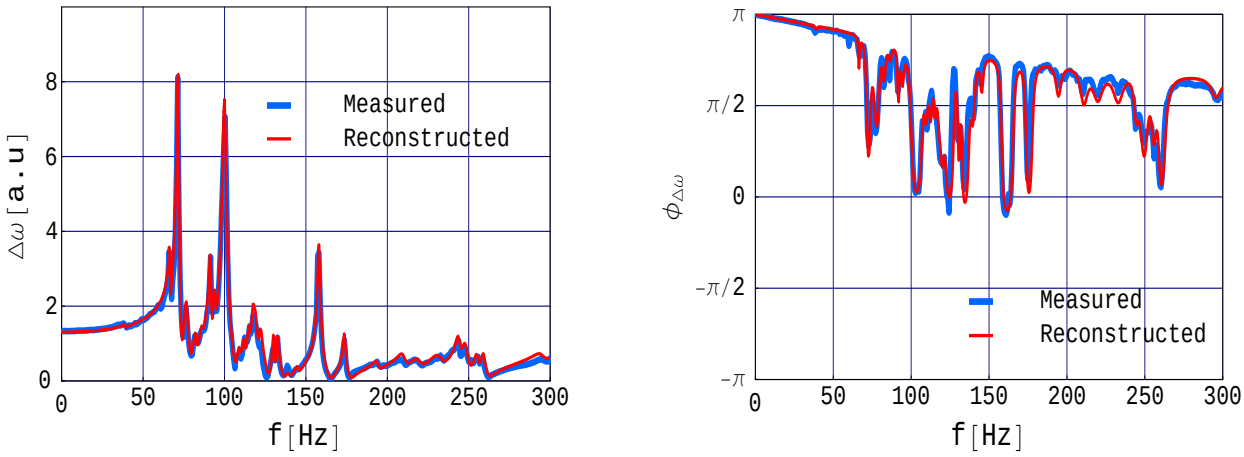

Figure 2.17: Amplitude and phase of the measured [38] and reconstucted transfer function associated with the Lorentz force in the SNS medium beta cavity (Prototype cryomodule cavity #1)

interesting to notice that the amplitude of the transfer function, given by the ratio of the AC components linked to the detuning and to the RF source, is independent of the RF current modulation parameter ϵ. The mechanical parameters of the reconstructed basis are listed in Table 2.1. As expected from the results of Section 2.3.2, all the coupling coefficients linked to the Lorentz force action have the same sign. The transfer function was only measured up to 300 Hz and it appeared during the reconstruction process that a non negligible response of the cavity should be expected above such frequency. Whereas the frequencies and the Q's of higher fre-

quency modes are impossible to determin from the measured data, some information concerning their coupling coefficients can be deduced from the low frequency part of the transfer function. This is because for very low excitation frequencies, the contributions from these unknowns modes add in phase. As a consequence, the sum of the coupling coefficients of the remaining higher frequency modes is known. Also, the modes above and rather close to 300 Hz seriously affect the phase of the transfer function near and below this frequency and some informations about the unknown modes can be determined from this. To reproduce properly the lowest frequency part of the transfer function's amplitude and the highest frequency part of transfer function's phase, a single mode at 320 Hz has been added. This mode is added only to represent the effect of all the modes above 300 Hz and it should therefore not be considered as accurate. It is important to remember that in Eq. (2.36) the variation of the angular frequency is proportional to the square of the accelerating voltage, as opposed to the usual expression of frequency change as a function of the square of the accelerating gradient. Incidentally, the definition of the mechanical mode coupling coefficients are different for both definitions.

Table 2.1: Mechanical parameters for the Lorentz force action in the SNS medium beta prototype cryomodule cavity #1

m	$f_{L,m}$ [Hz]	$Q_{L,m}$	$\frac{k_{L,m}}{2\pi}$ [Hz.MV^{-2}]	m	$f_{L,m}$ [Hz]	$Q_{L,m}$	$\frac{k_{L,m}}{2\pi}$ [Hz.MV^{-2}]
1	39	30	0.05	17	132.6	100	0.21
2	66.4	80	0.34	18	139	50	0.05
3	71.5	50	2.75	19	145	70	0.05
4	76.7	25	1.27	20	158	90	0.85
5	82.4	40	0.26	21	173.7	100	0.26
6	86.5	40	0.16	22	194	50	0.11
7	91.5	80	0.53	23	210	40	0.21
8	94.2	50	0.42	24	219	30	0.21
9	100	40	3.43	25	232	30	0.26
10	109	40	0.26	26	243.9	80	0.21
11	112	50	0.26	27	247.3	30	0.05
12	115	60	0.26	28	248	60	0.32
13	117.6	50	0.53	29	255	80	0.16
14	119	50	0.37	30	259	100	0.16
15	122	50	0.37	31	295	40	0.16
16	130	100	0.21	32	320	30	6.87

2.4.2 Detuning by the piezoelectric tuner

Based on the Telsa's active compensation scheme of the Lorentz detuning, a piezoelectric tuner has succefully been installed and tested on each cavity of a SNS medium beta cryomodule [35]. A series of low power open loop measurements on the cavity # 2 were done to extract the mechanical parameters for the excitation of this cavity by

a piezoelectric tuner and to check the validity of the modeling procedure. Once the mechanical parameters are obtained, it is possible to use them to optimize and/or auto maze the detuning compensation scheme. In the open loop measurement setting, the cavity is excited in CW with a low power generator. The cavity voltage is measured under various dynamic detuning conditions, and the results compared to the simulations. In this experiment, the excited voltage in the cavity is very small and the Lorentz forces are totally negligible.

I Basic excitation of the cavity

As a first mesurement, the basic behavior of the voltage in absence of dynamic detuning is checked and the value of the cavity electromagnetic half-bandwidth is deduced. The cavity is successively excited with different predetuning values. In each case the value of the voltage amplitude is recorded. The measured voltage comes from the signal of the field probe located in the beam pipe region of the cavity, and is therefore not equal to the accelerating voltage. Since a linear relation exists between them and since only relative behavior will be used in the following, no calibration of the field probe is necessary. Three examples of the development in time of the voltage amplitude for different values of the predetuning are presented in Fig. 2.18. From Eq. (2.11), the value of the voltage amplitude in the steady state is equal to $V_{SST}(\Delta\omega_0) = R_L I_0 \left\{1 + \frac{\Delta\omega_0^2}{\omega_{1/2}^2}\right\}^{-1/2}$. Normalizing it with respect to the voltage for the on-resonance case $V_{SST}(0) = V_0 = R_L I_0$ gives $\frac{V_{SST}(\Delta\omega_0)}{V_0} = \left\{1 + \frac{\Delta\omega_0^2}{\omega_{1/2}^2}\right\}^{-1/2}$. For each

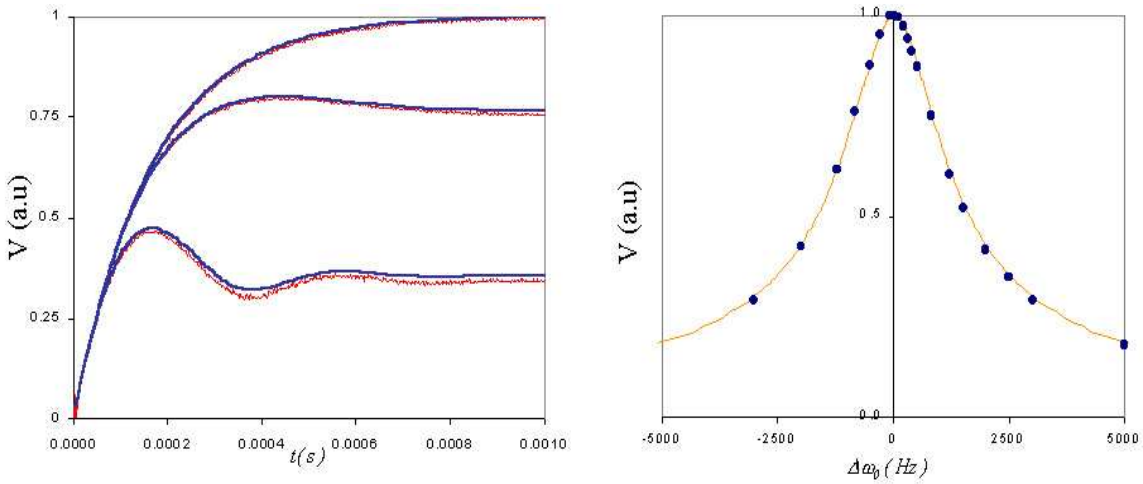

Figure 2.18: On the left, measured (red curve) and simulated (blue curve) development of the cavity voltage for different values of the initial predetuning. On the right, resonance curve of the steady state voltage amplitude (normalized) as a function of the predetuning value. The dots are measured values, the continuous curve is the result from simulations.

predetuning case, the value of the voltage in steady state is recorded and the results are compiled to generate the resonance curve of Fig. 2.18. Since $\frac{V_{SST}(\omega_{1/2})}{V_0} = \frac{1}{\sqrt{2}}$, it is possible to deduce the cavity half-bandwidth value from the amplitude resonance curve, it is found $f_{1/2} = \frac{\omega_{1/2}}{2\pi} = 950$Hz. Using this value, it is possible to compare measured and simulated results. As displayed in Fig. 2.18, the agreement between the measured and the simulated development of the voltage is good and the value of the cavity half-bandwidth will be used in the following simulations.

II Mechanical parameters for the piezoelectric excitation

In the Section 2.4.1 the mechanical parameters in the case of the radiation pressure were investigated using the results of the transfer function linking the modulations of the RF source forward power and the frequency detuning response. In order to extract mechanical parameters, the transfer function linking the piezoelectric input voltage amplitude modulations and the cavity voltage phase response is measured in an open loop setting. The amplitude of the sinusoidal piezoelectric input voltage was equal to 7.6 mV (before amplification) and the frequency of the excitation was swept in the interval [20Hz;600Hz], the corresponding measured transfer function for the voltage phase is presented in Fig. 2.19. The transfer function was measured only up to 600 Hz because no significant mechanical mode was observed above this frequency. But as shown in Section 2.5, the Lorentz detuning in the nominal operation of the SNS medium beta cavity seems to contain non negligible contribution from frequency component higher than 600 Hz and it could in therefore be of interest to use results of the piezoelectric transfer function above this frequency. The transfer functions for the piezoelectric and the Lorentz forces show rather different behaviors. First, the positions of the dominating resonances are not identical (further measurement by JLAB of the piezoelectric transfer function for the cavity #1 confirms this point), which can be a direct consequence of the large differences in the coupling of the piezoelectric action and of the Lorentz forces action to the cavity structure. Second, the phase of the transfer function for the radiation pressure action remains bounded in an interval equal to π whereas for the excitation with the piezoelectric this phase occupies the entire 2π interval. This can be explained by the fact that the coupling coefficient for the piezoelectric action can be of both signs. In Section A.8, it is shown that the phase of the solution to a second order ODE with respect to a harmonic driving term passes from 0 to $-\pi$ as the frequency of the oscillatory excitation is swept from small values to large values compared to the mode frequency. This passage is displayed in Fig. A.7. The transfer function of the piezoelectric shows the phase of the signal $\phi_V(t)$ (cavity voltage phase) with respect to the applied sinusoidal piezoelectric input voltage $V_p(t)$. The driving term for the m^{th} mode is in reality $\Omega_m^2 k_m V_p$. This means that when the coupling coefficient k_m is positive, the phase is within the interval $[0; -\pi]$ when the m^{th} resonance mode is crossed. On the other hand, when k_m is negative, the phase with respect to the driving voltage contains an additionnal π phase shift and the interval for such coupling coefficient is $[-\pi; -2\pi]$. In consequence, the phase of the transfer function can occupy the entire 2π interval. Using the fact that the coupling coefficients can be of both signs, the mechanical basis associated with the

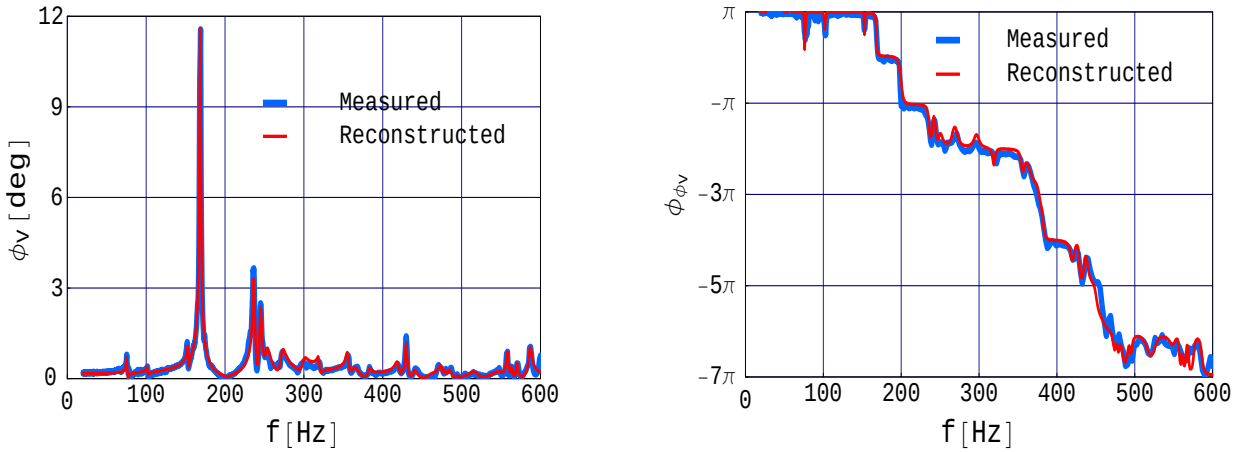

Figure 2.19: Measured and simulated transfer function (amplitude and phase) for the action of the piezoelectric tuner in the SNS medium beta cavity (Prototype cryomodule cavity #2). The input signal is the sinusoidal modulation of the piezoelectric tuner input voltage $V_P(t)$, the output signal is the voltage phase $\phi_V(t)$. The amplitude of the transfer function (on the left) is the ratio of the amplitude of the output signal and the amplitude of the input signal. The phase of the transfer function (on the right) is the phase difference between the output signal and the input signal.

piezoelectric tuner action can be reconstructed from the measured transfer function. This transfer function contains in reality two distinct parts, the first is the excitation of the mechanical modes by the piezoelectric forces which produces a detuning, and the second is the influence of this dynamic detuning on the cavity voltage. Since both aspects are included in the simulations it is possible to use these one to find the mechanical parameters of the modal basis associated to the piezoelectric tuner action. The analytical results of Annex A.3 are used and consequently simplify the reconstruction of the mechanical basis. For the fitting procedure 29 modes are used and their characteristic parameters are presented in Table 2.2. As in the modeling procedure presented in Section 2.3.2, the modes are assumed to be uncoupled and acting in parallel. The resulting simulated transfer function using this modal basis is presented in Fig. 2.19. It is interesting to note that to reproduce the deep notch in amplitude and the phase behavior occuring between 170Hz and 236Hz, it is necessary to add a mode with small negative coupling coefficient around 200Hz. Without it, the notch still exists, since it mainly originates form the interference of the 170Hz and 236Hz modes contributions, but it is less pronounced and the simulated phase would not be correctly reproduced. With the extracted parameters it is possible to predict the detuning and the voltage behavior for any driving piezoelectric tuner input voltage waveform (in reality only Fourier components lower than 600Hz are taken into account in the simulations since the mechanical basis was only reconstructed up to this frequency). As a test, the behavior of the voltage phase is measured

Table 2.2: Mechanical parameters for the piezoelectric action in the SNS medium beta prototype cryomodule cavity # 2

m	$f_{P,m}$ [Hz]	$Q_{P,m}$	$k_{P,m}$ [Hz.mV^{-1}]	m	$f_{P,m}$ [Hz]	$Q_{P,m}$	$k_{P,m}$ [Hz.mV^{-1}]
1	75.5	200	-0.1	16	429.7	250	0.072
2	101.5	80	-0.05	17	440.5	100	0.04
3	152.8	260	-0.07	18	460	30	-0.05
4	168.5	120	-1.3	19	474	130	0.04
5	200	25	0.042	20	479	200	0.015
6	236.5	100	-0.45	21	485	100	0.04
7	245.1	100	-0.3	22	495	200	0.005
8	252.7	40	-0.24	23	517	50	0.06
9	272.6	40	-0.27	24	548	50	0.05
10	299.5	40	-0.15	25	558	250	0.05
11	319	100	0.07	26	563	300	0.015
12	355.5	100	0.1	27	570	300	0.025
13	365.7	40	0.12	28	587	160	0.1
14	383	100	-0.05	29	601.2	250	0.04
15	419	80	0.08				

and simulated for two square waveforms of the piezoelectric input voltage, pulsed at respectively 10Hz and 50Hz. The characteristics of those waveforms and the results from both measurements and simulations are presented in Fig. 2.20 and Fig. 2.21. The agreement between the measured and simulated behaviors of the voltage phase comforts the results obtained for the parameters of the reconstructed mechanical modal basis, validates the modeling approach and shows that the simulations can be used for further investigations. They can for example be used for the study an active compensation scheme of the Lorentz detuning by a piezoelectric tuner as proposed in Section 2.5.

2.5 Study of the compensation of the Lorentz dynamic detuning

The Lorentz detuning in elliptical superconducting cavities can affect the coupling between the resonant cavity and the RF feeding source and be a source of concern in regard of the stability of the accelerating voltage. In pulsed operation, this detuning is dynamic and the frequency of the cavity can change even during the flat top duration of the beam. To compensate this effect, the RF control system can adjust the RF source power amplitude and phase in order to insure the stability of the cavity voltage ratings when the beam is on. It was seen in Section 2.2.3 that such control requires additional RF power which can become a serious issue if the available power margin is not large and/or if the klystron source needs to be operated in its non linear region. Such problems can be overcome by using an active piezoelectric tuning. In

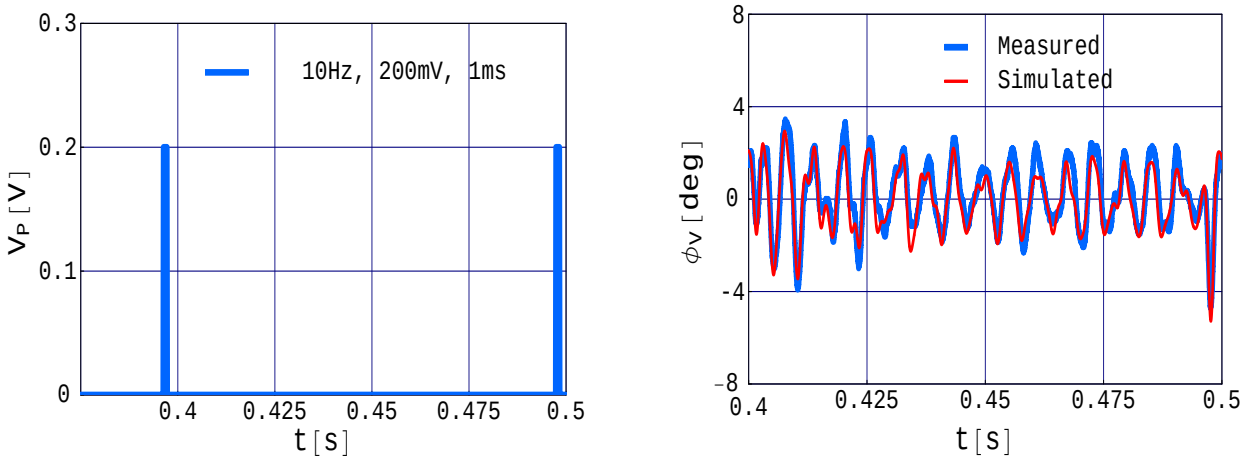

Figure 2.20: Left: Square waveform of the piezoelectric input voltage pulsed at 10 Hz (200 mV before amplification, 1 ms pulse with 100 μs rise and decay time). Right: Measured and simulated (using the reconstructed modal basis) variations of the voltage phase through time. The signal is repeatable 10 Hz.

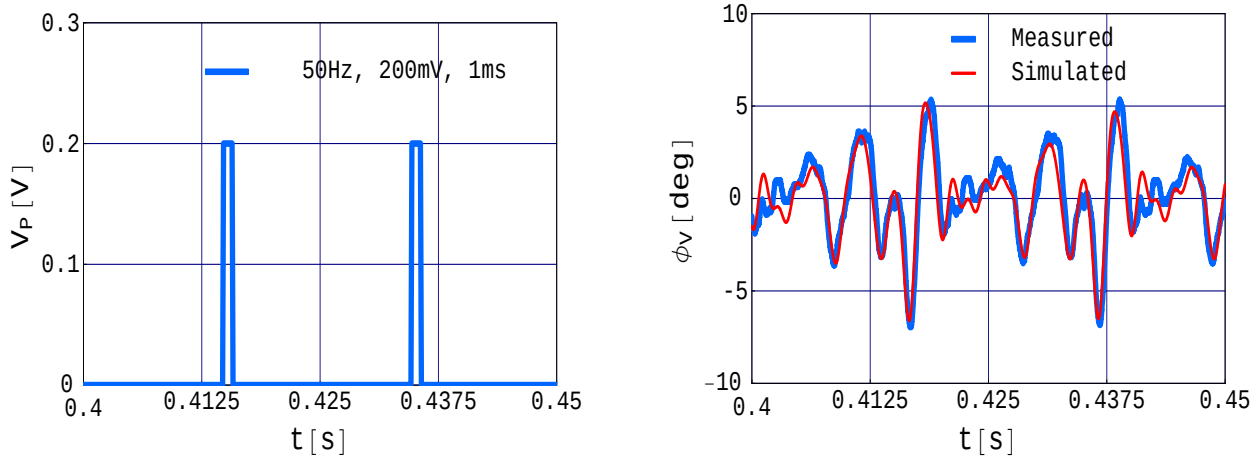

Figure 2.21: Left: Square waveform of the piezoelectric input voltage pulsed at 50 Hz (200 mV before amplification, 1 ms pulse with 100 μs rise and decay time). Right: Measured and simulated (using the reconstructed modal basis) variations of the voltage phase through time. The signal is repeatable 50 Hz.

Section 2.3, the modeling of the detuning was approached qualitatively by viewing the vibrations of the cavity surface as the vibration of a string and it was shown that the detuning could be represented by the superposition of mechanical modes, each mode satisfying a simple second order ODE. Since a sinusoidal excitation of given frequency for the piezo input voltage creates, in the steady state, a sinusoidal detuning of the same frequency, it is possible to consider a compensation scheme using a piezoelectric input voltage signal only composed of harmonics of the repetition rate. This method will be detailed in the following section and applied to the case of the SNS medium beta cavity.

2.5.1 Compensation scheme based on harmonics of the repetition rate

The following method is applicable for the compensation of the Lorentz detuning because in the steady state and for a given cavity voltage development profile, the Lorentz detuning is a periodic function with a period equal to the repetition rate. Calling the Lorentz detuning function $\Delta\omega_L(t)$ and noting the angular frequency associated with the repetition rate ω_{rep}, a discrete fourier transform of the detuning function in the steady state gives only harmonics of ω_{rep}.

$$\Delta\omega_L(t) = \sum_{n=0}^{\infty} \Delta\omega_{L,\,n} \cos(n\,\omega_{rep} t + \phi_{L,n}) \tag{2.38}$$

where $\Delta\omega_{L,\,n}$ and $\phi_{L,n}$ are the amplitude and the phase of the n^{th} harmonic of the repetition rate. To compensate ideally for the Lorentz detuning, the detuning $\Delta\omega_P(t)$ generated by the piezoelectric should be of equal amplitude and opposite sign, $\Delta\omega_P(t) = -\Delta\omega_L(t)$. Since the detuning produced by the piezoelectric can be decomposed on a mechanical basis with each mechanical mode satisfying a second order ODE, and since the driving term for these differential equations are proportional to the input voltage V_P of the piezoelectric tuner, it follows that V_P should also be a function of period equal to ω_{rep}. Taking the discrete Fourier transform of this function, it is possible to write

$$V_P(t) = \sum_{n=0}^{\infty} V_{P,\,n} \cos(n\,\omega_{rep} t + \theta_{P,n}) \tag{2.39}$$

According to Section A.8, such forcing function will produce, in the steady state, a piezoelectric detuning function of the type

$$\Delta\omega_P(t) = \sum_{n=0}^{\infty} \Delta\omega_{P,\,n} \cos(n\,\omega_{rep} t + \phi_{P,n}) \tag{2.40}$$

To compensate exactly for the Lorentz detuning it is necessary to have $\Delta\omega_{P,\,n} = \Delta\omega_{L,\,n}$ and $\phi_{P,n} = \phi_{L,n} + \pi$. From Section A.8, the solution for each harmonic of the

forcing function V_P is obtainable by summation on all the mode contributions. Using the result of Eq. (A.50) gives

$$\Delta\omega_P(t) = \sum_{n=0}^{\infty}\sum_{m=1}^{\infty} V_{P,n}\frac{\Omega_{P,m}}{\omega_n}\frac{k_{P,m}Q_{P,m}}{\sqrt{1+\tan^2\psi_{P,n,m}}}\cos(n\,\omega_{rep}t + \theta_{P,n} + \psi_{P,n,m} - \frac{\pi}{2}) \quad (2.41)$$

where the parameters of the m^{th} mechanical mode related to the piezoelectric action are denoted $\Omega_{P,m}$, $k_{P,m}$, $Q_{P,m}$ and where the phase $\psi_{P,m}$ follows the same definition than in Eq. (A.50). Combining the results of Eq. (2.41) and Eq. (2.40) leads to

$$\begin{aligned}
a_n =& \sum_{m=1}^{\infty}\frac{\Omega_{P,m}}{\omega_n}\frac{k_{P,m}Q_{P,m}}{\sqrt{1+\tan^2\psi_{P,n,m}}}\cos(\psi_{P,n,m} - \frac{\pi}{2}) \\
b_n =& \sum_{m=1}^{\infty}\frac{\Omega_{P,m}}{\omega_n}\frac{k_{P,m}Q_{P,m}}{\sqrt{1+\tan^2\psi_{P,n,m}}}\sin(\psi_{P,n,m} - \frac{\pi}{2}) \\
\Delta\omega_{P,\,n} =& V_{P,n}\sqrt{a_n^2+b_n^2} \\
\phi_{P,n} =& \theta_{P,n} + \arctan(\frac{b_n}{a_n})
\end{aligned} \quad (2.42)$$

It eventually gives for the amplitude and phases of the n^{th} harmonic of the piezoelectric input voltage

$$\begin{aligned}
V_{P,n} =& \frac{\Delta\omega_{L,\,n}}{\sqrt{a_n^2+b_n^2}} \\
\theta_{P,n} =& \phi_{L,n} + \pi - \arctan(\frac{b_n}{a_n})
\end{aligned} \quad (2.43)$$

It should be pointed out that if the transfer function linking the piezoelectric to the cavity detuning is known, the extraction of the mechanical parameters for the piezoelectric tuner action is not required in order to find the coefficients $V_{P,n}$ and $\theta_{P,n}$. For example when the piezoelectric input voltage is of the form $V_P(t) = V_a\sin\omega t$, the induced detuning is of the form $\Delta\omega_P(t) = \Delta\omega_a(\omega)\sin(\omega t + \phi_a(\omega))$. If the the ratio $\frac{\omega_a(\omega)}{V_a}$ and the phase $\phi_a(\omega)$ are known for all the harmonics of the repetition rate, the amplitudes $V_{P,n}$ and the phases $\theta_{P,n}$ of the piezo input voltage needed for the compensation are then given by

$$\begin{aligned}
V_{P,n} =& \frac{\Delta\omega_{L,\,n}}{\Delta\omega_a(n\omega_{rep})}V_a \\
\theta_{P,n} =& \phi_{L,n} + \pi - \phi_a(n\omega_{rep})
\end{aligned} \quad (2.44)$$

The transfer function linking the cavity voltage phase to the input voltage of the piezoelectric tuner is also sufficient, because a simple numerical routine using the results of Annex A.3 can be written to obtain the transfer function linking the cavity detuning and the input voltage of the piezoelectric tuner (such procedure was implicitly done in section 2.4.2).

2.5.2 Illustration of the compensation scheme

Since the primarly goal is to compensate for the Lorentz detuning only when the beam is on, the compensation function need not to be continuously defined through time. When the beam is off, the detuning compensation function can be chosen arbitrarily. Also, the compensation function can be close but not exactly equal and opposite to the Lorentz detuning function. To illustrate the method described in Section 2.5.1, the case of the SNS medium beta cavity will be considered. Measurements performed at JLAB on the SNS medium beta prototype cryomodule cavity #1, showed the Lorentz detuning profile displayed in Fig. 2.22 [29], for a cavity accelerating voltage profile close to the nominal one (shape, amplitude , 60 Hz repetition rate). The detuning was observed to be repeatable at 60 Hz as expected. In Fig. 2.23, the

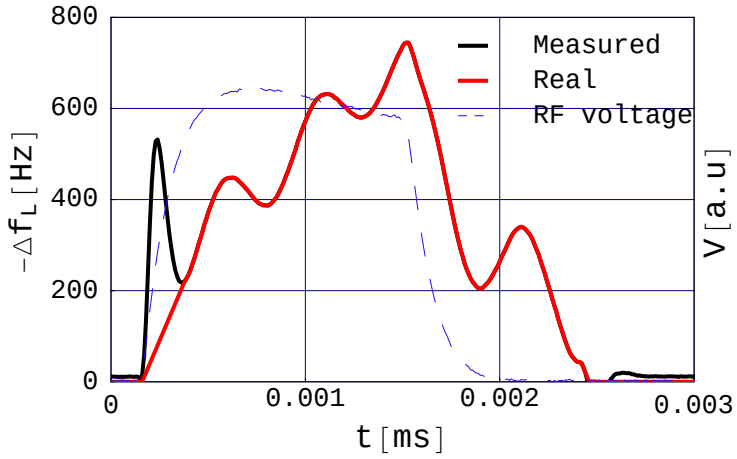

Figure 2.22: Measured [29] Lorentz detuning function in the SNS medium beta prtotype cryomule cavity #1, in pulsed operation close to nominal conditions. The initial part of the measured signal is due to a parasitic signal. The real detuning function is extrapolated and plotted on top of the measured signal.

Lorentz detuning function is null after the RF pulse because the measurement of the detuning was only possible when a RF voltage signal was available in the cavity. As anticipated, the Lorentz force detuning is dynamic and does not exactly follow the RF voltage development. Some high frequency components (higher than a kilohertz) seem to be excited. This is rather surprising because the mechanical damping for such high frequencies was expected to be strong. Such high frequency components are for example much smaller in the Tesla case [33]. Further measurements and understandings will tell if such high frequency components are real or are an artifact of the measurement method. As an example of such an artifact, the initial bump during the RF cavity field development does not correspond to a real detuning but is probably due to a strong transient parasitic term as explained in Appendix A.9.1. This bump is consequently removed from the measured detuning function. The Lorentz detuning function considered in the following is the remaining “Real” part of the measured

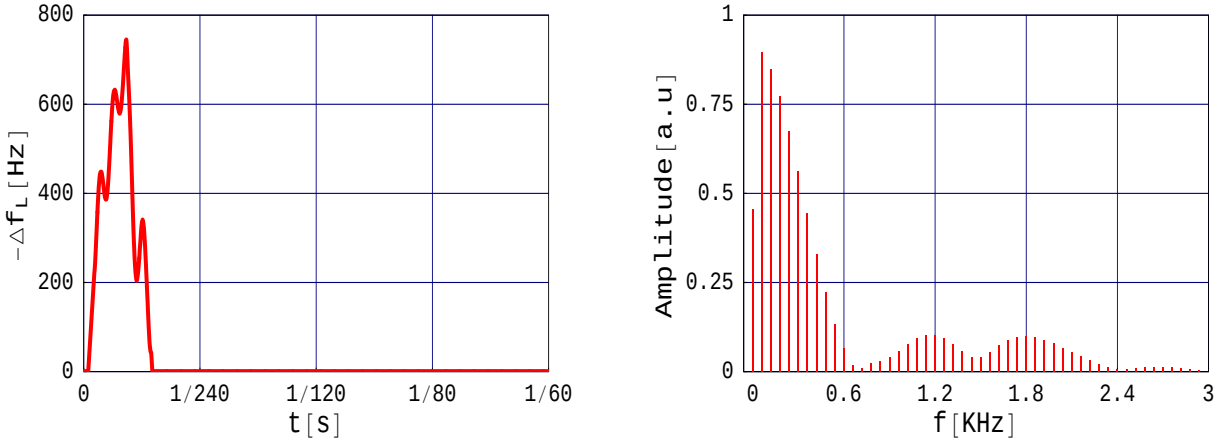

Figure 2.23: Measured Lorentz detuning function $\Delta\omega_L(t)$, for nominal gradient in SNS medium beta prototype cryomodule (periodic 60 Hz) and corresponding amplitude of the discrete fourier components.

signal as illustrated in Fig. 2.23 (the end of the signal corresponding to the end of the RF pulse decay is also smoothed out). Beside the period of time when the beam is on, the detuning function to compensate for can be arbitrarily defined. In the following two different examples will be presented. In the first one, the detuning compensation function will be chosen null between two RF cycles. In the second example, only the part corresponding to the RF turn on transient and the beam pulse duration will be compensated.

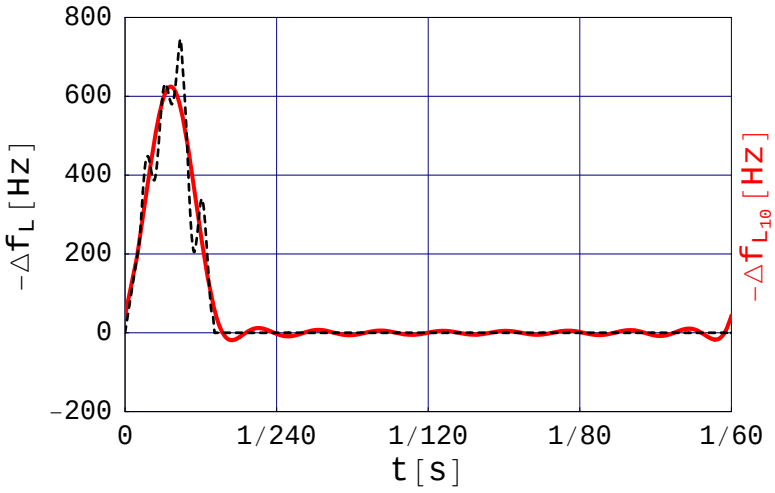

Figure 2.24: Initial measured Lorentz detuning function $\Delta f_L(t)$ and its truncation to the 10^{th} harmonic of 60 Hz, $\Delta f_{L_{10}}(t)$. This truncated function constitutes in the following the function to be compensated by the piezoelectric.

I Null detuning between RF cycles

The Lorentz detuning presented in Fig. 2.24 is null between two RF cycles only because no cavity voltage signal was available during this period of time. Since the compensation method presented in the following requires a continuous detuning function to work on, the measured Lorentz detuning function will first be taken as it is measured, even if the actual unknown detuning within RF cycles is non null. Because the mechanical parameters for the piezoelectric action on the SNS medium beta cavity has only been reconstructed up to 600 Hz, only the first 10 harmonics from the discrete Fourier transform of the Lorentz detuning function will be considered in the following. The continuous function $\Delta\omega_{L_{10}}(t)$ built from these ten components is then attempted to be compensated by finding an adequate profile of the piezoelectric input voltage. The function $\Delta\omega_{L_{10}}(t)$ is illustrated in Fig. 2.24 and its Fourier decomposition (amplitudes $\Delta\omega_{L_{10},n}$ and phases $\phi_{L_{10},n}$) are presented in Fig. 2.25. Using the Eq. (2.43) and the mechanical parameters of Table 2.2, the amplitudes

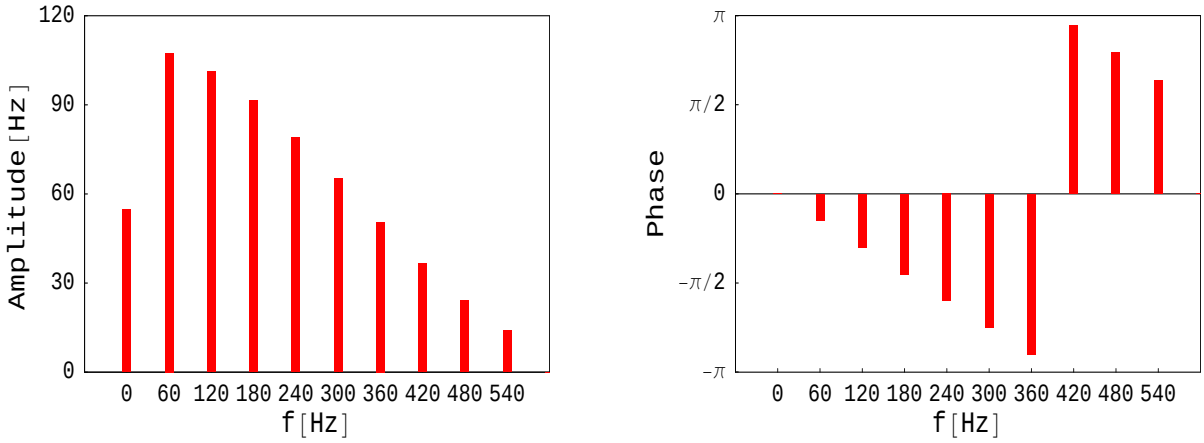

Figure 2.25: Amplitudes $\Delta f_{L_{10},n}$ and phases $\phi_{L_{10},n}$ of the first ten harmonics of the truncated Lorentz detuning function $-\Delta f_{L_{10}}(t)$.

$V_{P,n}$ and the phases $\theta_{P,n}$ for the first ten n harmonics are calculated and displayed in Fig. 2.26. With these results, the piezoelectric input voltage function $V_P(t)$ can be estimated using Eq. (2.39). This function is illustrated in Fig. 2.27. To check the result of the method, the calculated piezoelectric input voltage function $V_P(t)$ can be used as the forcing function for the set of the mechanical equations associated to the piezoelectric action. The developement of the detuning is calculated numerically and is plotted in Fig. 2.28. The transient behavior of the generated detuning is observable at the early time and the steady state behavior is found to satisfy the expectations. To prove this point, the sum $\Delta\omega_{L_{10}}(t) + \Delta\omega_P(t)$ is illustrated in Fig. 2.29. As desired, the compensation is very good and the principle of the compensation scheme using harmonics of the repetition rate is conclusive. In this example, only frequency components lower than 600 Hz were compensated, but the calculations can easily be extended once the mechanical basis, or the transfer function linking the piezoelectric input voltage to the detuning, is known for higher frequencies.

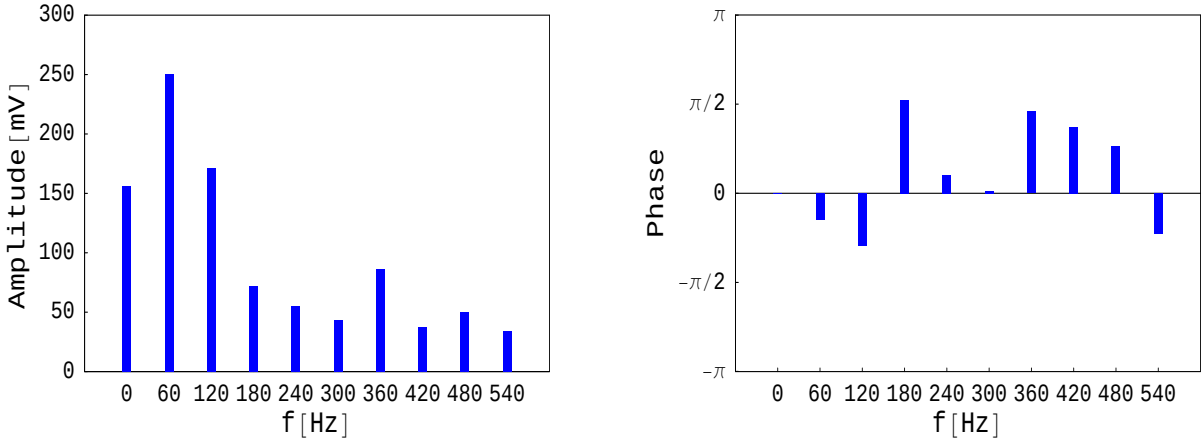

Figure 2.26: Amplitudes $V_{P,n}$ and phases $\theta_{P,n}$ of the first ten harmonics of the piezoelectric input voltage calculated with Eq. (2.43).

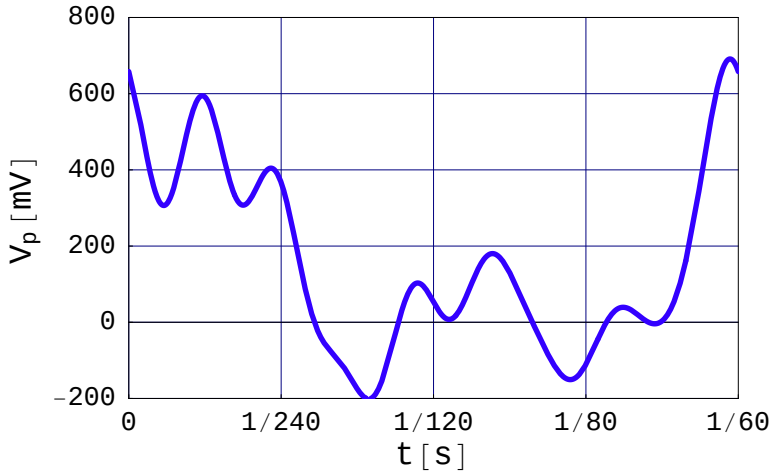

Figure 2.27: Piezoelectric input voltage function $V_P(t)$ (repetitive at 60Hz) for the compensation of the truncated Lorentz detuning function $\Delta\omega_{L_{10}}(t)$.

II Compensation for RF turn on transient and beam pulse duration

In the previous example, the detuning compensation function was chosen null between RF cycles. This choice was totally arbitrary and a slightly different approach will now be presented. The primarly goal of the active compensation using piezoelectric is to reduce as much as possible the dynamic Lorentz detuning within the beam pulse. A second goal would be to compensate for the detuning also during the RF turn on transient, for example to facilitate the task of the RF control system. With such considerations it is possible to focus only on these periods of time and treat the RF decay and gap between RF cycles as free parameters. The previous example was straightforward since the function to compensate for was continuously defined from

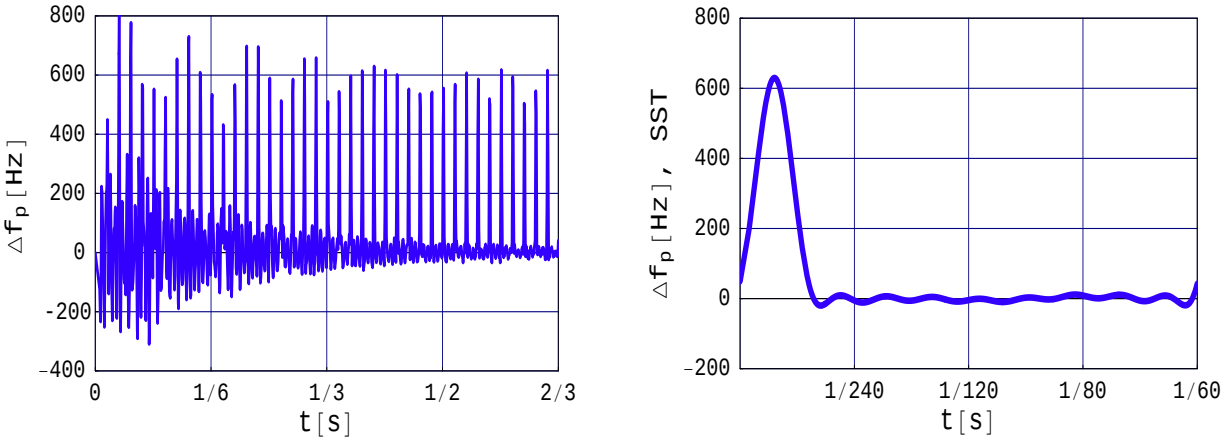

Figure 2.28: Transient and steady state of the detuning $\Delta\omega_P(t)$ generated by the piezoelectric input voltage of Fig. 2.27.

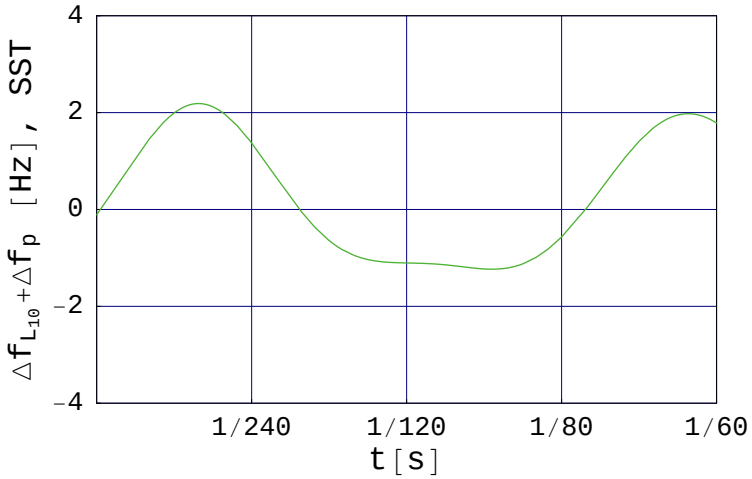

Figure 2.29: Sum of the truncated Lorentz detuning function $\Delta\omega_{L_{10}}(t)$ and of the detuning function generated by the action of the piezoelectric $\Delta\omega_P(t)$. As expected, this sum is close to zero.

the beginning. Restricting the compensation period to the RF turn on transient and the the beam on time requires an additional procedure to obtain a continuous detuning function through time. The benefit of the following approach is to simplify the harmonic content of the detuning compensation function. Doing so allows one to find a simpler piezoelectric input voltage profile which is of practical interest. Looking only at the Lorentz detuning function during the RF turn on transient and the beam on time indicates that a function based on a very few number of harmonics should be sufficient to approximately fit the Lorentz detuning profile over these periods. Using a numerical fitting routine, a function based on a single harmonic (180Hz) would for example be sufficient to approximatly compensate for the Lorentz detuning function. The fiting of this function and its Fourier components are illustrated in Fig. 2.30

and Fig. 2.31 (as mentioned, only a single harmonical component is non null). Using again Eq. (2.43) and the mechanical parameters of Table 2.2, the amplitudes $V_{P,n}$ and the phases $\theta_{P,n}$ for the harmonics are calculated and displayed in Fig. 2.32. The piezoelectric input voltage function $V_P(t)$ built from these Fourier components is illustrated in Fig. 2.33. The detuning (transient and steady state) generated by this piezoelectric input voltage profile is calculated with a numerical routine and the results are presented in Fig. 2.34. The sum with the initial fitted function is checked to be close to zero as illustrated in Fig. 2.35.

The compensation method based on a piezoelectric tuner input voltage composed

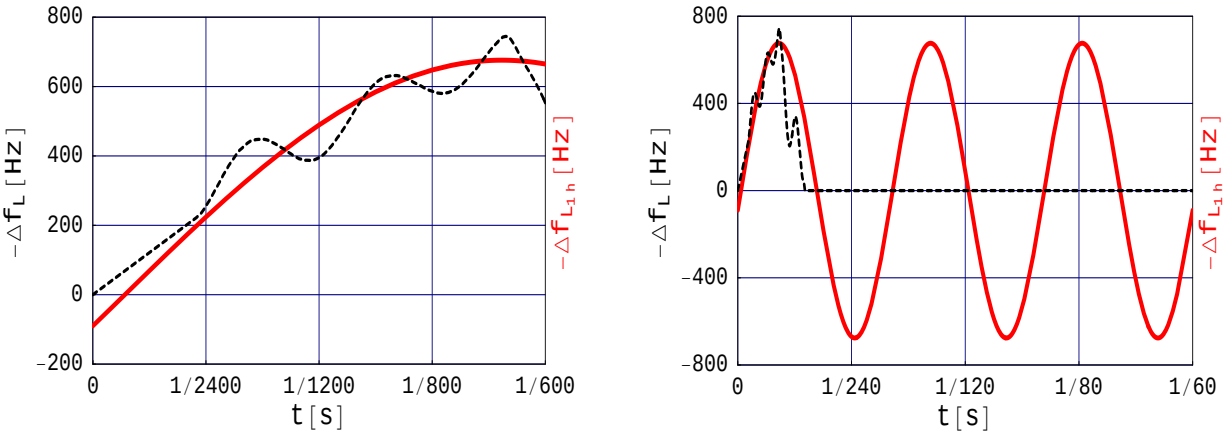

Figure 2.30: Fitting of the detuning function $-\Delta\omega_L(t)$ (RF turn on transient and beam on duration) by projection of only the third harmonic (180 Hz) of the repetition rate. The fitting function $-\Delta\omega_{L_{1h}}(t)$ can be compensated by a piezoelectric input voltage function $V_P(t)$ having the same harmonic.

of the harmonics of the repetition rate was proven to be a possible and attractive scheme. The compensation of the Lorentz detuning does not require the coupling coefficients for the piezoelectric and the Lorentz forces to be equal. The parameters for the harmonics can be found using the reconstructed mechanical basis or the results of the transfer function linking the piezoelectric input voltage to the detuning. In this case only information at the harmonics of the repetition rate are needed. Because the dynamic Lorentz detuning compensation is only desirable during the beam on time and RF turn on transient, a piezoelctric tuner input voltage profile containing only one or a few harmonics of the repetition rate seems possible and of practical interest. Other methods, using different piezoelectric input voltage profiles, such as trapezoidal shape waveforms for example, are also possible but are not as straightforward as the presented method making their optimization more difficult. An advantage of such waveforms is for example their easy programmability using a common pulse generator. A potential difficulty for the compensation using piezoelectric tuners is the possible change of the mechanical spectrum through time (due for example to the change in position of the mechanical tuner). This is a potential source of concern because as observed from the measured transfer functions, the mechanical resonances

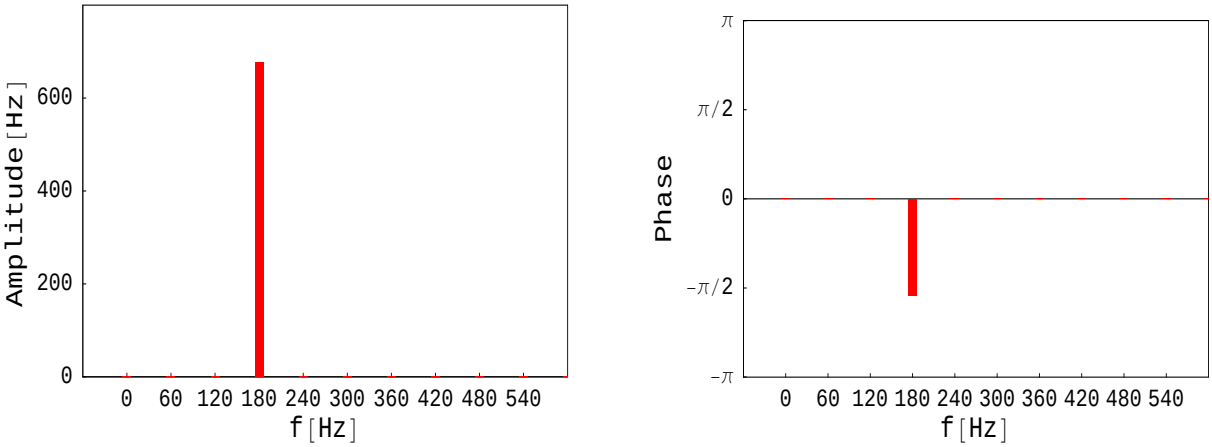

Figure 2.31: Fourier components (amplitudes and phases) of the fiting detuning function $-\Delta\omega_{L_{1h}}(t)$ (see Fig. 2.30). Since only the third harmonic of the repetition rate has been chosen for the fitting, the amplitudes of all the other harmonics are null.

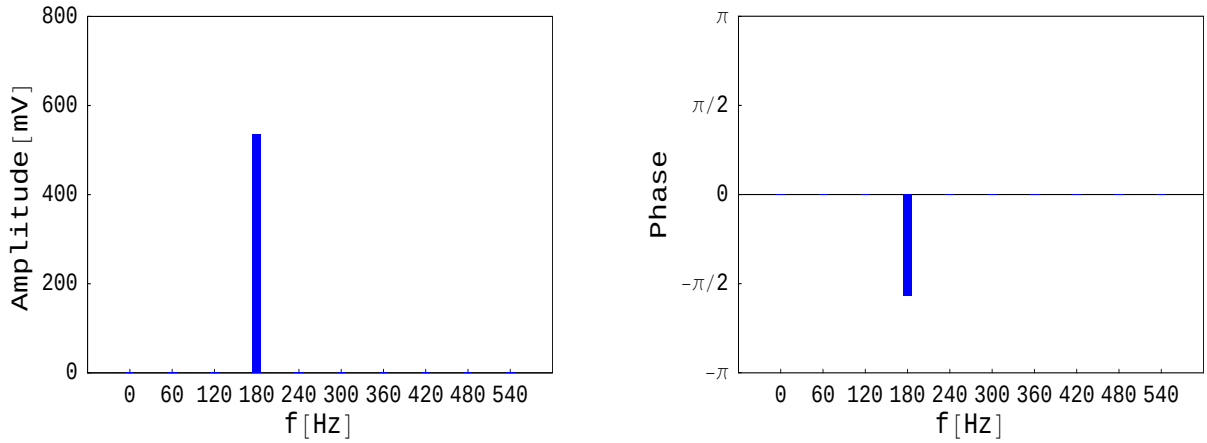

Figure 2.32: Amplitudes $V_{P,n}$ and phases $\theta_{P,n}$ of the first ten harmonics of the piezoelectric input voltage calculated with Eq. (2.43). Only one harmonic is non null since the function to compensate (see Fig. 2.30) contains no other harmonics.

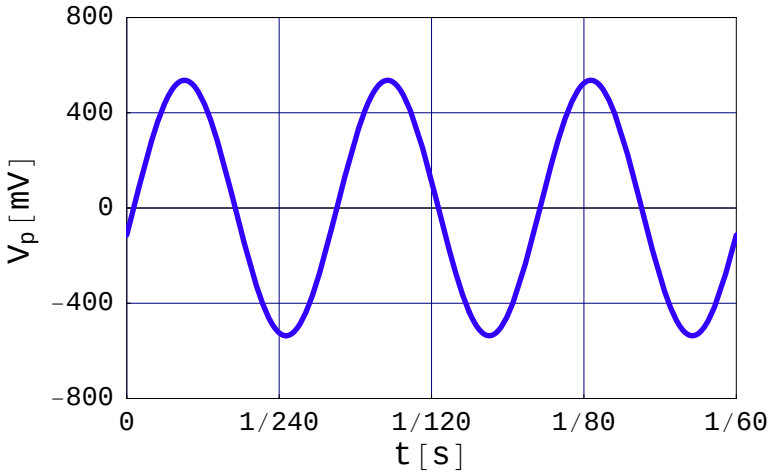

Figure 2.33: Piezoelectric input voltage function $V_P(t)$ (repetitive 60Hz) for the compensation of the detuning function of Fig. 2.30. This function has a much simpler form than the first function displayed in Fig. 2.27.

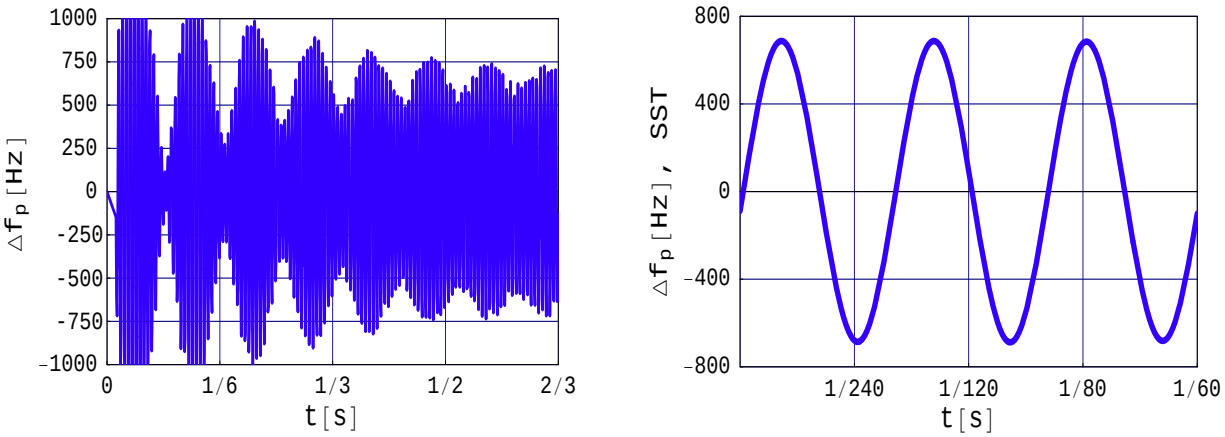

Figure 2.34: Transient and steady state of the detuning $\Delta\omega_P(t)$ generated by the piezoelectric input voltage of Fig. 2.33. In the steady state, the detuning genrated by the piezoelectric is repetitive at 60 Hz and is opposite of the detuning function to compensate, $\Delta\omega_{L_{1h}}(t)$.

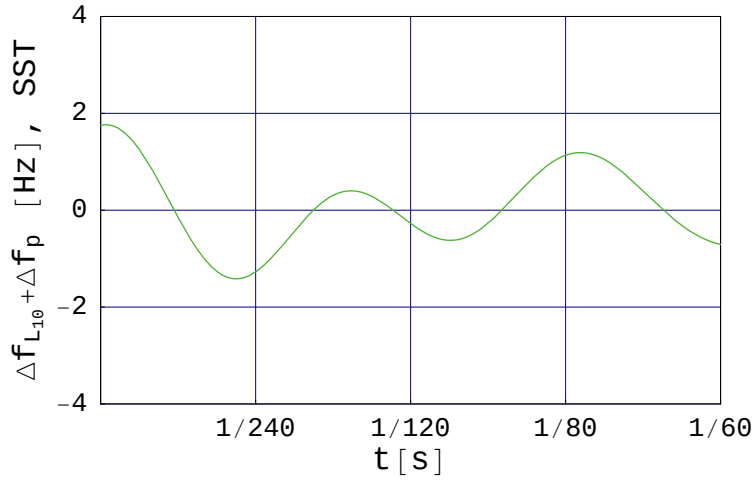

Figure 2.35: Sum of the detuning function $\Delta\omega_{L_{1h}}(t)$ and of the detuning function generated by the action of the piezoelectric $\Delta\omega_P(t)$. As expected, this sum is close to zero.

can be rather narrow. As a simple solution, it would for example be possible to avoid using harmonics of the repetition rate too close to a resonance line in the input voltage function. Therefore, the practicability, the flexibility and the reliability of the presented compensation scheme need to be tested. Since identical superconducting cavities present non negligible differences in their mechanical spectrums, the compensation optimization should be done for each of them. Also, because the cavities of a single cryomodule are possibly mechanically coupled, the optimization of their respective piezoelectric waveforms should not be considered as a totally independent process.

2.6 Conclusion

In this chapter, the issue related to the dynamic Lorentz detuning in SRF cavities was investigated. The modeling for the calculation of the voltage in a cavity under detuning was developed and illustrated to strengthen the understanding of the problem dynamics. Such understanding has for example been beneficial for the extraction of the cavity mechanical parameters from measurements or for identifying possible parasitic signals in these measurements. As a secondary benefit, the effort on the calculations of the voltage lead to interesting insights on the filling of a cavity under dynamic detuning, and to a simple and useful scaling of the required additional RF power when the cavities parameters, Q external and detuning, are varied from their optimum values. It also provided a method to monitor the cavity resonant frequency when some RF signal is available in the cavity. For the modeling of the detuning, a qualitative approach representing the cavity wall vibrations as the vibrations on a string was proposed. This simple analogy is fully compatible with the regular modal basis representation. It naturally lead to a better understanding of the mechanical

coupling coefficients. It was made clear that the usually quoted Lorentz detuning coefficient is in reality the sum of all the coupling coefficients to the different mechanical modes. For this reason it becomes evident that whereas this parameter is the principal figure of merit in a CW operated cavity, its meaning is not as strong in a pulsed case. Instead, the position of the mechanical modes frequencies with respect to the harmonics of the repetition rate, and the values of the modes damping coefficients, are more relevant. Eventually, the difference between the coupling coefficients associated with the Lorentz forces and with the piezoelectric tuner was explained. It was understood that the detuning by the Lorentz forces was a very particular case where the forcing action and its effect on the variation of the cavity frequency always combines to produce coupling coefficients of same sign, for all the mechanical modes of the structure. This result was confirmed by the reconstruction of the mechanical parameters associated to the Lorentz force action using measured data. The extraction of the mechanical parameters for both, Lorentz forces action and peizoelectric tuner action, confirmed the modeling of the system. It also gave the possibility to have a virtual cavity to carry further studies, for example on the compensation of the Lorentz detuning by the piezoelectric tuner. In this study, it was shown that the input voltage waveform using harmonics of the repetition rate was a possible and straightforward method to control and optimize the compensation. Further studies using the same modeling frame are possible. For example, a study on the use of a piezoelectric to compensate for the detuning generated by the microphonics could be of direct interest for machine operated in CW. Also, a study on the time development of the ponderomotive oscillation could be beneficial from the RF control point of view.

Chapter 3

Longitudinal beam dynamics in SRF cavities

A very common practice in linear accelerators (LINAC) is the use of cavities operating in standing waves (SW) like SRF cavities for example [42]. The calculation of the longitudinal dynamics for a particle passing through such an accelerating element is a non-linear coupled problem since the energy gain of a particle depends on the evolution of its phase relative to the RF oscillating field within the element, but the phase itself depends on the evolution of the particle's velocity. In the case of ultrarelativistic particles, the coupling between the evolution of the energy and the evolution of the phase vanishes because the velocity of the particle remains virtually unchanged during the acceleration. To the contrary, this coupling is non negligible when the beta of the particle is changing within the element. When the accelerating cavity is a single cell with a longitudinal electric field symmetric with respect to the geometrical center of the cell and when the beta variation is small, one usually applies the thin lense approximation method [43]. If the element is long, the field non symmetric, and the beta largely varying, the previous treatment can lead to inacuracies. To circumvent these limitations, some approximation methods have been developed where the real non-symmetric field is altered to a symmetric one, where the element is fractioned into successive gaps and where numerical iterations are usually applied to estimate some averaged velocity and phase [44]. Instead of trying to fit to the usual set of equations, it is of interest to try to develop a more general method. This method should pursue three prerequisites: Accuracy, flexibility, and fast computation. A method based on the solution to the non-linear coupled problem by successive analytical iterations has been developed and meets these three prerequisites. As an introduction, the results for the thin lense method based on a linear phase law approximation will be presented. This method will be described for a symmetric field and extended to a non-symmetric one. It will then be used to explain and illustrate some issues pertaining to multicell cavities, field asymetry/tilt, large transit time and longitudinal emittance preservation. The method based on analytical iterations, corresponding to non-linear phase law cases, will then be exposed and discussed. It will be shown for example that the linear phase law approximation corresponds to the results after the second iteration and that the concepts of transit time and average phase can be

adapted to the new method. Finally, using the generality of the analytical results, a powerful semi-analytical method will be derived.

3.1 Longitudinal dynamics with linear phase law approximation

The approximation of a linear phase law leads to simple formulation for the energy gain and for the phase of flight (equivalent to the time of flight expressed in the phase unit of the oscillating RF). Its direct applicability is usually limited to symmetric fields and cases where the beta of the particle is not largely varying. It will nevertheless be shown that it can be extended to non-symmetric fields with minor alterations and will then be used as a first simple method to understand some issues pertaining to the transit time factor, multigap elements, non-symmetric fields, and longitudinal emittance conservation.

3.1.1 Transit time factor and average phase

Assuming an accelerating cavity of resonance frequency ω, where the on-axis longitudinal electric field is $E_z(z,t) = E_z(z)\cos\omega t$, and with its starting longitudinal position z_s and ending position z_e, the energy gain and the phase with respect to the RF oscillating field can be expressed along the longitudinal location z, by the system of coupled integral equations

$$\begin{aligned} \Delta W(z) =& q\int_{z_s}^{z} E_z(s)\cos\phi(s)\,ds \\ \phi(z) =& \phi_{z_s} + \int_{z_s}^{z} k(s)\,ds \end{aligned} \tag{3.1}$$

where $\phi(z_s) = \phi_{z_s}$ is the entrance phase of the particle with respect to the field, and where $k(s)$ depends on the energy of the particle as

$$k(s) = \frac{\omega}{c}\frac{1}{\beta(s)} = \frac{\omega}{c}\frac{1}{\sqrt{1-\gamma^{-2}(s)}} = \frac{\omega}{c}\frac{1}{\sqrt{1-\left[\frac{W_0}{W(s)}\right]^2}} \tag{3.2}$$

with c the speed of light, β the ratio of the particle's velocity and c, W_0 the rest mass energy of the particle and W its total energy. Since the time of flight corresponds to the time taken by a particle to pass from one longitudinal location to an other one, it is convenient to define a corresponding phase of flight measuring this time in comparison to the RF oscillating frequency. The phase of flight is given by $\Delta\phi(z) = \phi(z) - \phi_{z_s}$. The energy gain and the phase of flight at the end of the cavity are $\Delta W(z_e)$ and $\Delta\phi(z_e)$. Approximating the phase law as linear in the calculation of the energy gain,

Eq. (3.1) simplifies to

$$\begin{aligned}\Delta W(z) =& q\int_{z_s}^{z} E_z(s)\cos(\phi_{z_s}+k_{z_s}\{s-z_s\})\,ds\\ \phi(z) =& \phi_{z_s}+k_{z_s}\{z-z_s\}+\int_{z_s}^{z}\Delta k(s)\,ds\end{aligned} \tag{3.3}$$

where $\Delta k(z)=k(z)-k_{z_s}$, with the notation $k_{z_s}=k(z_s)$ (the index z_s will be used for other variables to refer to their values at the entrance of the accelerating gap). This system can be solved by calculating the energy gain function and injecting the result in the phase equation. An elegant manner to solve the integral for the energy gain is to develope the cosine function to separate spatial dependency and phase dependency. This is the essence of the transit time concept first introduced by Panofsky

$$\Delta W(z) = qE_0L\{T_{z_s}(k_{z_s})\cos\phi_{z_s}-S_{z_s}(k_{z_s})\sin\phi_{z_s}\} \tag{3.4}$$

Here L is the length considered, E_0 is the average electric field, $T_{z_s}(k_{z_s})$ and $S_{z_s}(k_{z_s})$ are respectively the cosine and sine transform of the field with z_s taken as reference. The definitions of these parameters are

$$\begin{aligned}L =& z_e-z_s\\ E_0 =& \frac{1}{L}\int_{z_s}^{z_e}|E_z(s)|\,ds\\ T_{z_s}(k_{z_s}) =& \frac{1}{E_0L}\int_{z_s}^{z_e}E_z(s)\cos(k_{z_s}\{s-z_s\})\,ds\\ S_{z_s}(k_{z_s}) =& \frac{1}{E_0L}\int_{z_s}^{z_e}E_z(s)\sin(k_{z_s}\{s-z_s\})\,ds\end{aligned} \tag{3.5}$$

Instead of using the physical entrance phase ϕ_{z_s} it is possible to use an "average" phase Φ and simplify furthermore the form of Eq. (3.4). It writes

$$\Delta W(z_e) = qE_0L\,\overline{T}_{z_s}(k_{z_s})\cos\Phi \tag{3.6}$$

with

$$\begin{aligned}\overline{T}_{z_s}(k_{z_s}) =& \sqrt{T_{z_s}^2(k_{z_s})+S_{z_s}^2(k_{z_s})}\\ \Phi =& \phi_{z_s}+\arctan\frac{S_{z_s}(k_{z_s})}{T_{z_s}(k_{z_s})}\end{aligned} \tag{3.7}$$

For a positively charged particle, the energy gain is maximum when $\Phi=0$, so when $\phi_{z_s}=-\arctan\frac{S_{z_s}(k_{z_s})}{T_{z_s}(k_{z_s})}$. For a negatively charged particle the maximum energy gain is obtainable by a simple π shift of this entrance phase. For simplicity, the following illustrations and discussions will be applied to positively charged particles. The phase Φ is usually refered to as average phase, RF phase, or synchronous phase. In the previous expressions, the phase of flight and consequently all the other results were expressed with respect to the entrance location z_s. This is a natural choice but not

a unique one. Since the phase law for the energy gain calculation in Eq. (3.3) is linear, it can be rewritten with respect to any longitudinal location z_r as $\phi(z) = \phi(z_r) + k_{z_s}\{z - z_r\}$. Using this relation and taking z_r as longitudinal reference for the functions T and S leads to

$$\begin{aligned} T_{z_r}(k_{z_s}) =& \frac{1}{E_0 L}\int_{z_s}^{z_e} E_z(s)\cos(k_{z_s}\{s - z_r\})\,ds \\ S_{z_r}(k_{z_s}) =& \frac{1}{E_0 L}\int_{z_s}^{z_e} E_z(s)\sin(k_{z_s}\{s - z_r\})\,ds \\ \Delta W(z_e) =& qE_0L\{T_{z_r}(k_{z_s})\cos\phi_{z_r} - S_{z_r}(k_{z_s})\sin\phi_{z_r}\} \\ =& qE_0L\,\overline{T}_{z_r}(k_{z_s})\cos\Phi \\ \overline{T}_{z_r}(k_{z_s}) =& \sqrt{T^2_{z_r}(k_{z_s}) + S^2_{z_r}(k_{z_s})} \\ \Phi =& \phi_{z_r} + \arctan\frac{S_{z_r}(k_{z_s})}{T_{z_r}(k_{z_s})} \end{aligned} \tag{3.8}$$

The functions T_{z_r} and S_{z_r} are linked to the previous functions T_{z_s} and S_{z_s} as

$$\begin{aligned} T_{z_r}(k) &= T_{z_s}(k)\cos(k\{z_s - z_r\}) - S_{z_s}(k)\sin(k\{z_s - z_r\}) \\ S_{z_r}(k) &= S_{z_s}(k)\cos(k\{z_s - z_r\}) + T_{z_s}(k)\sin(k\{z_s - z_r\}) \end{aligned} \tag{3.9}$$

With this result it can be simply demonstrated that $\overline{T}_{z_r}(k_{z_s}) = \overline{T}_{z_s}(k_{z_s})$ and conclude that the maximum energy gain is independent of the longitudinal reference used in the definitions. In Fig. 3.1, the functions T and S are plotted as a function of the particle's entrance velocity and for two longitudinal references. These functions are different

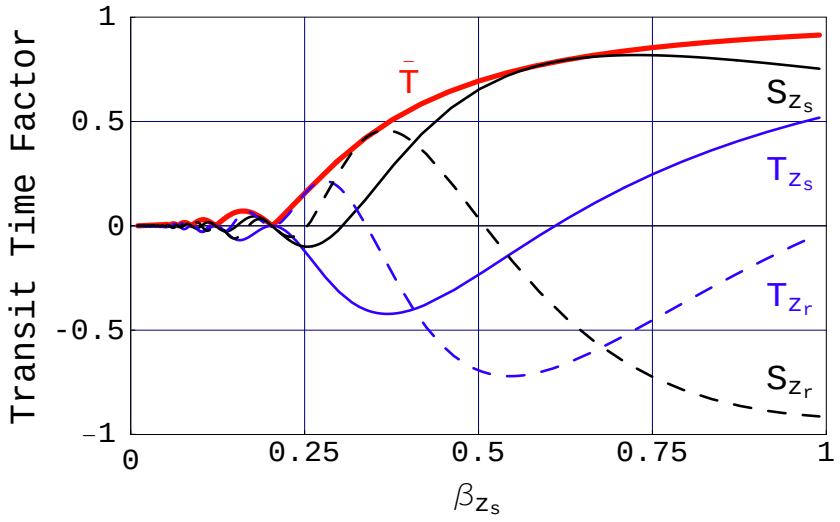

Figure 3.1: T, S, and $\overline{T}$ versus β_{z_s} for a single accelerating gap having a symmetric field profile, and for two different longitudinal references, z_s and $z_r = z_s + \frac{4L}{3}$.

for each longitudinal reference but the associated functions $\overline{T}$ are identical. Because

the phase law is linear it is possible to estimate the phase at the reference location that corresponds to the maximum energy gain by using the result of Eq. (3.7), $\phi_{z_r} = \phi_{z_s} + k_{z_s}\{z_r - z_s\} = -\arctan\frac{S_{z_s}(k_{z_s})}{T_{z_s}(k_{z_s})} + k_{z_s}\{z_r - z_s\}$. For some particular longitudinal locations z_{ec}, the function $S_{z_{ec}}$ becomes null. Using Eq. (3.8) it follows that the physical phase of flight and the average phase at the location z_{ec} are equivalent, $\phi_{z_{ec}} = \Phi$. These points are called electrical centers and their locations usually depend on the particle's entrance velocity. As it is shown in Section B.1, for a gap having a symmetric electric field profile with respect to its middle, the geometrical center $z_{gc} = \frac{z_s+z_e}{2} = z_s + \frac{L}{2}$ is always an electrical center. For this particular case, the accelerating element can efficiently be decomposed in a succession of three simple equivalent elements, a drift space, an infinitely small gap, and a second drift space (this succession of element can be referred to as d-g-d). It will be shown that, if the gap has a non-symmetric field profile with respect to its geometrical middle, the element can still be treated with a d-g-d method, and that the final set of equations for the energy gain and for the phase kick is only slightly different than for the usual symmetric field case.

3.1.2 Drift-gap-drift representation for non-symmetric fields

If the field does not have any particular symmetry, the set of Eq. (B.10) does not apply, nevertheless the d-g-d method presented for symmetric field cases in Annex B.1 can be extended. The development in Annex B.1 was based on a representation of the accelerating element by a succession of a drift space, an infinitesimal gap, and a second drift space, where the location of the gap was exactly at the geometrical center of the element. This particular location is a consequence of the symmetry of the field with respect to the geometrical center and of the linear phase law approximation. When the field does not have such symmetry, the electrical center should be the location where some kicks in energy and phase are applied. If the linear phase law approximation is kept for the calculation of the energy gain, the result of Eq. (3.8) is still valid. However, the result of Eq. (B.5) is changed due to the fact that the function $S_{u_{gc}}$ is not null for a non-symmetric field. This equation can be rewritten in this case as

$$\Delta\phi_{NL}(z_e) = d_\gamma k|_{z_s}\left\{\frac{L}{2}\Delta\gamma(z_e) - \frac{q}{W_0}E_0L\{\quad T'_{u_{gc}}(k_{z_s})\sin(\phi_{z_s} + k_{z_s}\frac{L}{2}) + S'_{u_{gc}}(k_{z_s})\cos(\phi_{z_s} + k_{z_s}\frac{L}{2})\}\right\} \tag{3.10}$$

Since the geometrical center is not the electrical center, the phase $\phi_{z_s} + k_{z_s}\frac{L}{2}$ is not equal to the average phase. Using the linear phase law it is possible to write $\phi_{z_s} + k_{z_s}\frac{L}{2} = \Phi - k_{z_s}\{z_{ec} - z_s\} + k_{z_s}\frac{L}{2}$. Writing $z_{ec} = z_{gc} + u_{ec} = z_s + \frac{L}{2} + u_{ec}$ eventually gives $\phi_{z_s} + k_{z_s}\frac{L}{2} = \Phi - k_{z_s}u_{ec} = \Phi - \Delta\phi_{u_{ec}}$. The parameter u_{ec} corresponds to the longitudinal shift of the electrical center with respect to the geometrical center of the element z_{gc}. The parameter $\Delta\phi_{u_{ec}}$ measures this shift in terms of phase difference. For a symmetric field, u_{ec} and $\Delta\phi_{u_{ec}}$ are null. If the drift-gap-drift is applied with

the gap kicks done at the electrical center location z_{ec}, the Eq. (B.8) is replaced by

$$\begin{aligned}\phi(z_e) &= \phi_{z_s} + \Delta\phi_{drift1} + \Delta\phi_{gap} + \Delta\phi_{drift2} \\ &= \phi_{z_s} + k_{z_s}\{z_{ec} - z_s\} + \Delta\phi_{gap} + \left\{k_{z_s} + d_\gamma k|_{z_s}\Delta\gamma(z_e)\right\}\{z_e - z_{ec}\} \\ &= \phi_{z_s} + k_{z_s}\{\frac{L}{2} + u_{ec}\} + \Delta\phi_{gap} + \left\{k_{z_s} + d_\gamma k|_{z_s}\Delta\gamma(z_e)\right\}\{\frac{L}{2} - u_{ec}\} \\ &= \phi_{z_s} + k_{z_s}L + \Delta\phi_{gap} + d_\gamma k|_{z_s}\Delta\gamma(z_e)\frac{L}{2} - d_\gamma k|_{z_s}\Delta\gamma(z_e)u_{ec}\end{aligned}$$

which, after substracting the linear part $\phi_{z_s} + k_{z_s}L$, gives:

$$\Delta\phi_{NL}(z_e) = \Delta\phi_{gap} + d_\gamma k|_{z_s}\Delta\gamma(z_e)\frac{L}{2} - d_\gamma k|_{z_s}\Delta\gamma(z_e)u_{ec} \tag{3.11}$$

This result must be equivalent to the result of Eq. (3.10) so

$$\Delta\phi_{gap} = d_\gamma k|_{z_s}\left\{-\frac{qE0L}{W0}\{T'_{u_{gc}}(k_{z_s})\sin(\Phi - \Delta\phi_{u_{ec}}) + S'_{u_{gc}}(k_{z_s})\cos(\Phi - \Delta\phi_{u_{ec}})\} + \Delta\gamma(z_e)u_{ec}\right\} \tag{3.12}$$

Using the result of Eq. (3.9) for $z_r = z_{ec}$ allows to find $\Delta\phi_{u_{ec}} = \arctan(\frac{S_{u_{gc}}(k_{z_s})}{T_{u_{gc}}(k_{z_s})})$. Writing

$$\begin{aligned}\Theta_{T,S} = \Delta\phi_{u_{ec}} &= \arctan(\frac{S_{u_{gc}}(k_{z_s})}{T_{u_{gc}}(k_{z_s})}) \\ \Theta_{T',S'} &= \arctan(\frac{S'_{u_{gc}}(k_{z_s})}{T'_{u_{gc}}(k_{z_s})}) \\ \overline{T'} &= \sqrt{T'^2_{u_{gc}} + S'^2_{u_{gc}}}\end{aligned} \tag{3.13}$$

leads for the energy and phase kicks in the gap to

$$\begin{aligned}\Delta W_{gap} &= qE_0L\,\overline{T}\cos\Phi \\ \Delta\phi_{gap} &= \frac{1}{\beta_{z_s}^2\gamma_{z_s}^3}\left\{-\Delta\gamma(z_e)\Theta_{T,S} + \frac{qk_{z_s}E_0L}{W_0}\overline{T'}\sin(\Phi - \Theta_{T,S} + \Theta_{T',S'})\right\}\end{aligned} \tag{3.14}$$

where $\overline{T}$, $\overline{T'}$, $\Theta_{T,S}$, and $\Theta_{T',S'}$ depend on k_{z_s}. The kicks in energy and phase of Eq. (3.14) must be applied at the electrical center. Since its location depends on the particle's entrance velocity, it would be unpractical to carry the calculations for a bunch of particles. For convenience, it is possible to fix a common location where the kicks have to be applied for all the particles. An interesting choice is the geometrical center of the gap. Since u_{ec} represents the difference between the electrical center position and the geometrical center position, the phase kick has to be incremented by $-d_\gamma k|_{z_s}\Delta\gamma(z_e)u_{ec} = \frac{\Delta\gamma(z_e)}{\beta_{z_s}^2\gamma_{z_s}^3}\Theta_{T,S}$. Eq. (3.14) is consequently modified to

$$\begin{aligned}\Delta W_{gap} &= qE_0L\,\overline{T}\cos\Phi \\ \Delta\phi_{gap} &= \frac{qk_{z_s}E_0L}{\beta_{z_s}^2\gamma_{z_s}^3W_0}\overline{T'}\sin(\Phi - \Theta_{T,S} + \Theta_{T',S'})\end{aligned} \tag{3.15}$$

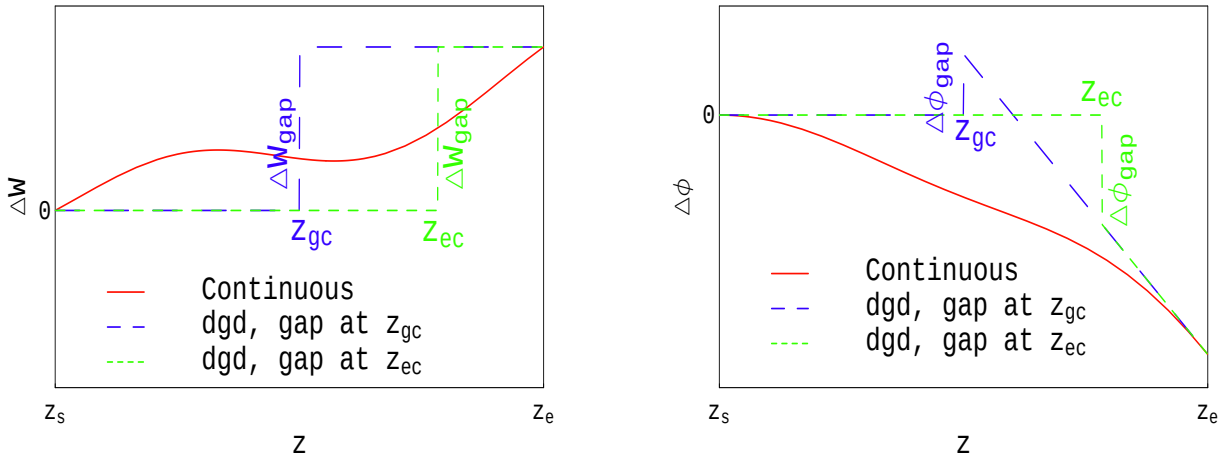

Figure 3.2: Energy gain and phase of flight for a single gap with non-symmetric field. The drift-gap-drift approximation is drawn in dashed line and the continuous functions are plotted in solid lines.

The drift-gap-drift representation for a non-symmetric field is illustrated in Fig. 3.2.

If the field is symmetric with respect to the geometric center, $\Theta_{T,S} = \Theta_{T',S'} = 0$ or π and the result of Eq. (B.10) is retrieved. It should be recalled that the assumptions leading to Eq. (3.15) are a linear phase law approximation for the calculation of the energy gain and a first order truncation in the expansion of the particle's wave vector k as a function of the variation of its energy ΔW. It should also be mentioned that, even if the transformation using Eq. (3.15) has to be made at the geometrical center of the gap for all the particles, the average phase for each particle is still equal to the phase at its corresponding electrical center location, which depends on the particle's entrance velocity. As a consequence, the average phase of a particle depends on both its entrance phase and its entrance velocity. Of course, if the dispersion of entrance velocities in a bunch of particles is small enough, the variation of the electrical center position has a negligible impact. In Annex B.1.1, the general treatment of a bunch of particles using a reference particle is presented in the most general case. Since in the d-g-d method the energy gain can be considered quasi-adaibatic, the Liouville's theorem should be satisfied at least to the first order of the ratio energy gain over entrance energy, and it follows that the area in the longitudinal phase space should be conserved. It is known that the d-g-d representation for an element with symmetric field satisfies this expectation [43]. The verification in the case of a non symmetric element is developed in Annex B.1.2. The result of Eq. (3.15) is applicable to any type of field profile, can be applied to a bunch of particles, and satifies Liouville's theorem. In the following, the d-g-d treatment is also implemented in cases where the non linear part of the phase law is not negligible.

3.1.3 Fractioning of an accelerating element

It was shown that the thin lense method can succefully be applied for any type of accelerating element (single gap or multigap, symmetric or non symmetric field), if the phase of flight of the particle within the entire element can be considered close to linear. For elements with large transit time and/or non negligible variation of the particle's relativistic beta, as for a multicell superconducting cavities for example, the accuracy of the thin lense method should be questioned. Instead of passing such an element at once it is possible to fraction it in a series of consecutive smaller elements and to apply the previous d-g-d method for each of them. The passage from a unique element to a succession of smaller pieces does not pose any difficulty if the entrance parameters β_{zs} and ϕ_{z_s} are known, because the entrance conditions for every successive elements can then be calculated. Unfortunately, the usual intent is to use an average phase for the entire element and such operation can be fairly complex in practice due to the fact that the average phases of the consecutive elements are not independent from one an other and that the locations of their electric centers, and most of the parameters of Eq. (3.14), depend on the entrance velocity of the particle which varies for each consecutive element. To better understand the fractionning process, an example of multicell cavity where the phase law over the entire element is close to linear is first presented. Then, an example where the non-linear part of the phase of law is non negligible is considered and inherent limitations of the thin lense method are emphasized.

I Energy gain in fractionned multicell cavity with linear phase law

As a first example, a cavity of length L, axial electric field gradient E_0, and transit time factor $\overline{T}$, and composed of N cells is considered. Noting for the parameters of the n^{th} cell, L_n, E_n, $\overline{T}_n$, and writing Φ_n the average phase experienced by the particle, gives for the energy gain $\Delta W = q\sum_{n=1}^{N} E_n L_n \overline{T}_n \cos\Phi_n$. Even if the velocity of the particle is considered constant along the entire element, the average phases Φ_n are still depending on each other but the relation between them can be explcitely stated. The cells can oscillate with different phase (π mode case for example) and the particle needs a finite time of flight to pass from the electrical center of a cell to the next. This time of flight depends on the relative position of the electrical centers and on the particle's entrance velocity. Writing the average phase of the cells with respect to the average phase of the first one $\Phi_n = \Phi_1 + \Delta\Phi_n$, where $\Delta\Phi$ takes into

account the two previous effects, allows to write for the energy gain

$$\begin{aligned}
\Delta W =& q\sum_{n=1}^{N} E_n L_n \overline{T}_n \cos(\Phi_1 + \Delta\Phi_n) = qE_0 L \overline{T}_{cav} \cos\Phi_{cav} \\
\tan\Delta\Phi_{tot} =& \frac{\sum_{n=1}^{N} E_n L_n \overline{T}_n \sin\Delta\Phi_n}{\sum_{n=1}^{N} E_n L_n \overline{T}_n \cos\Delta\Phi_n} = \frac{b}{a} \\
\overline{T}_{cav} =& \frac{\sqrt{a^2+b^2}}{E_0 L} \quad ; \quad \Phi_{cav} = \Phi_1 + \Delta\Phi_{tot}
\end{aligned} \tag{3.16}$$

Since the phase of flight has been considered strictly linear, it is understandable that the form of the energy gain for the element treated as a succession of N gaps is fully compatible with the expression of the energy gain for a single gap. The previous result can first be applied to a case where all the gaps are identical and are operating in π mode. In such a case $E_n = E_0$, $L_n = \frac{L}{N}$, and the transit time is the same for all the cells and can be noted $\overline{T}_{cell}$. Also, the average phase difference from a cell to the next is constant and can be written $\Delta\Phi_{cell}$. It follows that $\Delta\Phi_n = (n-1)\Delta\Phi_{cell}$. When the time of flight of the particle to pass from one electrical center to the other is equal to π, which is equivalent to say that the beta of the particle is equal to the geometrical beta of the cells, $\Delta\Phi_{cell}$ is equal to 2π and the average phase Φ_n is the same for all the cells. Using Eq. (3.16) in this particular case gives $\overline{T}_{cav} = \overline{T}_{cell}$ and $\Phi_{cav} = \Phi_1$. This synchronicity between consecutive cells corresponds to the optimum case. Taking more or less than π for the particle to pass from an electrical center to the next leads to a deterioration of the global accelerating efficiency of the cavity. As a direct consequence, the transit time factor for a cavity composed of identical cells is always lower than the one for the single-cell case, for any entrance beta. This can be proven by using Eq. (3.16)

$$\overline{T}_{cav} = \overline{T}_{cell} \frac{\sqrt{\left\{\sum_{n=0}^{N-1} \cos n\Delta\Phi_{cell}\right\}^2 + \left\{\sum_{n=0}^{N-1} \sin n\Delta\Phi_{cell}\right\}^2}}{N} \leq \overline{T}_{cell}$$

This property is illustrated in Fig. 3.3. In this figure, the transit time $\overline{T}_{cav}$ is calculated for cavities with different number of identical cells. The cells used in the example have a geometrical beta equal to 0.61 and a sinusoidal field profile. As expected the transit time corresponding to the single cell case is larger than for the multicell cases. For the single-cell case, the maximum of the transit time function occurs for $beta_{z_s} = 1$. As the number of cells is increased the synchronicity between cells become the preponderant factor and the location of the maximum of the transit time factor moves toward the geometrical beta of the cells.

II Energy gain in fractionned multicell cavity with non-linear phase law

The result of Eq. (3.14) can be used when the phase of flight is close to a linear phase law. If the non linear component of the phase of flight is non negligible the

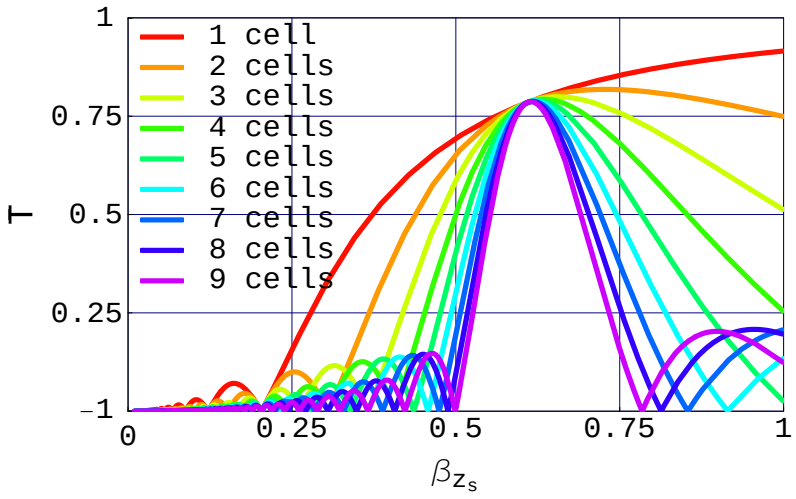

Figure 3.3: Transit time factor as a function of the particle's entrance beta for single-cell and multi-cell cavities (with identical cells of geometrical beta $\beta_{z_s} = 0.61$ and sinusoidal field profile). As the number of cells increases, the maximum of the acceleration progressively passes from $\beta_{z_s} = 1$ to $\beta_{z_s} = 0.61$.

method of fractioning the element into sub-element is possible. It was mentioned that since the velocity and the entrance phase for the consecutive gaps depend on one an other, establishing a global average phase for the entire element is not trivial. Looking deeper into such considerations reveals that the thin lense approximation method is not self-consistent because the initial linear phase law approximation used in the calculations leads to a non-linear phase law as result. In other words, the results for an accelerating element passed at once or fractioned into pieces are not equivalent since for the second one the phase law is linear for each consecutive gap but not for the overall element. As a direct consequence, the definition itself of an overall average phase for a fractioned element has to be clarified. A simple choice is to define that a null average phase for the entire element corresponds to the maximum energy gain. This is consistent with the average phase definition introduced in the thin lense approximation method. As an illustration, an element consituted of six identical and symmetric gaps is considered. The evolution of the energy gain and of the phase of flight are estimated for the cavity passed in a single step and in six steps with each step corresponding to a gap. A numerical iteration process is applied to set the average phase for the fractioned case. Fig. 3.4 reveals inaccuracies in the energy gain and phase of flight obtained from single step calculations, originating from the fact that the linear phase law assumed for the entire element is not precise enough. Fractioning the element into six consecutive steps allow a gain in accuracy but requires the introduction of numerical processes. The energy gain as a function of the average phase for the single step and fractioned element is illustrated in Fig. 3.5. It appears that, if the non-linear component of the phase law is not negligible,

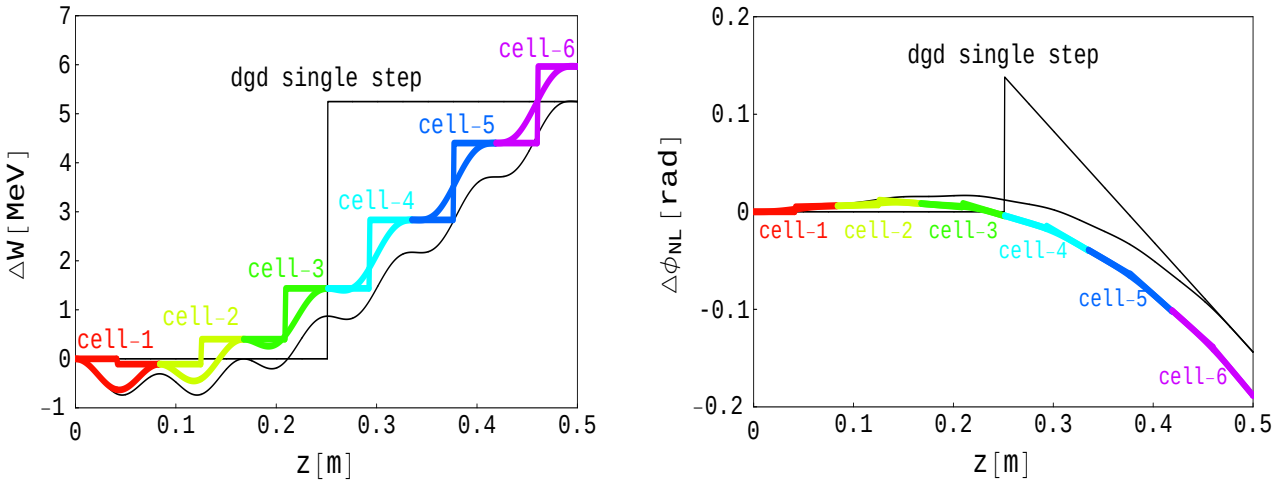

Figure 3.4: Energy gain and non linear phase of flight as a function of the longitudinal position for a H^- particle with $\beta_{z_s} = 0.4$ passing through a 6-cell element of geometrical beta equal to 0.45 and of accelerating gradient $E_0 = 25\ MV/m$. The element is passed at once or fractioned in six consecutive gaps corresponding to the six cells.

the energy gain function seems not to be a simple cosine function of an average phase as written in Eq. (3.15). It will be shown in the Section 3.2.2 that the energy gain and the phase of flight functions can be described, in the general case, with a sum of cosine functions of the entrance phase and its harmonics.

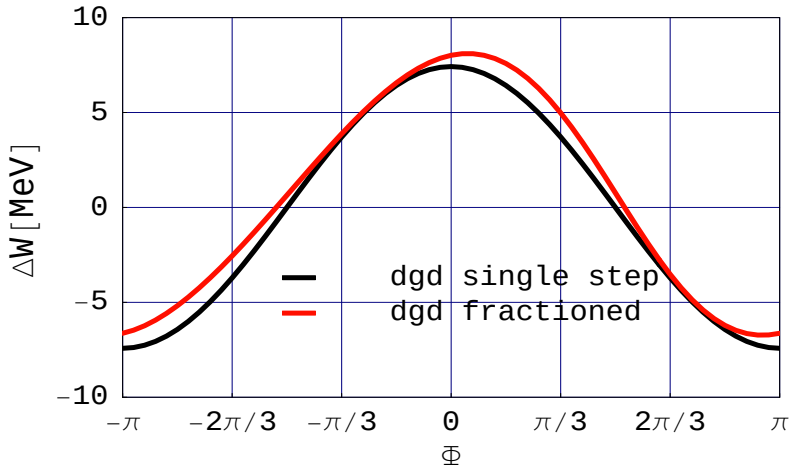

Figure 3.5: Energy gain at the end of the element as a function of the average phase of the single step calculation process. When the non-linear component of the phase of flight is non negligible, the energy gain is not a simple cosine function.

3.2 Longitudinal dynamics with non-linear phase law

3.2.1 Initial considerations

So far, the basic assumption for the calculations of the energy gain and of the phase of flight has been the linearity of the phase law. With such a simplified approach, the initial coupling of Eq. (3.1) between the energy gain and the phase of flight is broken and the thin lense method can be deduced. This is a simple method for the estimation of the energy gain and phase of flight, awhich helps also to understand some issues such as asymmetric field, multicell element, field tilt, and is proven to satisfy Liouville's theorem up to the second order. When the non linear part of the phase of flight is non negligible, the method can lead to some inaccuracies and it was found that the simple cosine dependence of the energy gain function with respect to the entrance phase or average phase was not satisfying. Even if a more precise formulation of the energy gain and phase of flight is not an easy matter, it is possible by simply applying a Fourier expansion to proove that these functions will depend in general on all the other harmonics of the entrance phase. The expansion of a function $f(x)$ with a period $2L$ can be written $f(x) = \frac{a_0}{2} + \sum_{n=1}^{\infty} \{a_n \cos\frac{n\pi x}{L} + b_n \sin\frac{n\pi x}{L}\}$ where a_n and b_n are the Fourier coefficients of the function f. Applying this expansion to the energy gain and the phase of flight, periodic with respect to the variable ϕ_{z_s} allows to write

$$\begin{aligned} \Delta W &= \sum_{n=0}^{\infty} \Delta W_{C_n} \cos n\phi_{z_s} + \Delta W_{S_n} \sin n\phi_{z_s} \\ \Delta\phi &= \sum_{n=0}^{\infty} \Delta\phi_{C_n} \cos n\phi_{z_s} + \Delta\phi_{S_n} \sin n\phi_{z_s} \end{aligned} \tag{3.17}$$

where the indexes C_n and S_n refer to coefficients of functions of the type $\cos n\phi$ and $\sin n\phi$ respectively. The coefficients ΔW_{C_n} , ΔW_{S_n} , $\Delta\phi_{C_n}$, $\Delta\phi_{S_n}$ are functions of the entrance energy and of the field properties but not of the entrance phase. It appears that the thin lense approximation is an estimation of Eq. (3.17) up to the order $n = 1$. In the following, a method based on analytical iterations will be used to solve the initial coupled problem of Eq. (3.1) and higher order terms will be found explicitely.

3.2.2 Solution by analytical iterations

To solve the coupled initial system of Eq. (3.3), the assumption of a linear phase law was made. To go beyond such assumption means introducing some non linearity for the phase law in the calculations. Considering the initial system of Eq. (3.3) and writing the phase of flight as a sum of the linear part and the non linear part, $\phi(z) = \phi_L(z) + \Delta\phi_{NL}(z)$, with $\phi_L(z) = \phi_{z_s} + k_{z_s}(z - z_s)$, allows to rewrite the system

as

$$\begin{aligned} \Delta W(z) =& q \int_{z_s}^{z} E_z(s) \cos(\phi_L(s) + \Delta\phi_{NL}(s))\, ds \\ \Delta\phi_{NL}(s) =& \int_{z_s}^{z} \Delta k(s)\, ds \end{aligned} \tag{3.18}$$

The equations are coupled and can be solved by analytical iterations. A possible starting point is to consider the cavity as a single drift space where the particle does not experience any acceleration. It is possible to note this trivial initial function $\Delta W_0(z) = 0$ and use it in the phase of flight equation, which gives $\Delta\Phi_{NL}(z)_0 = 0$ as a result. The basic idea is to reenter the result of the phase in the energy equation and to progress by successive iteration as displayed in Fig. 3.6. Thus one expects to obtain energy gain and phase of flight functions that converge toward the solution of the initial system. The integral for the energy gain in Eq. (3.18) is not solvable when

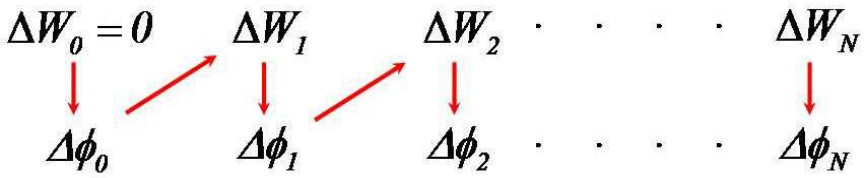

Figure 3.6: The system of coupled equations for the longitudinal dynamics can be approached by an analytical iteration method. As a starting function the gap is considered as a simple drift space

$\Delta\phi_{NL}$ is not of a particular form, therefore cosine function is developed into a Taylor series. The function to integrate for the phase of flight is the variation of the wave number, not the energy gain and this leads to expand also Δk into a Taylor series with respect to ΔW. The system for the i^{th} iteration can be rewritten

$$\begin{aligned} \Delta W_i(z) =& \sum_{n=0}^{\infty} \left\{ \frac{q}{n!} \int_{z_s}^{z} E_z(s)\; d_\theta^n \cos\theta|_{\phi_L(s)}\; \Delta\phi_{i-1}^n(s)\, ds \right\} \\ \Delta\phi_i(z) =& \sum_{n=1}^{\infty} \left\{ \frac{d_W^n k|_{W(z_s)}}{n!} \int_{z_s}^{z} \Delta W_i^n(s)\, ds \right\} \end{aligned} \tag{3.19}$$

To proceed through the iterations some truncations in the series have to be made. The details of the calculations up to three iterations are presented in Appendix B. Using the finding of section 3.2.1, it is of interest to always separate the depedence on the entrance phase from the dependences upon the particle's energy and upon the field characteristics. The solutions written ΔW_2 and $\Delta\phi_2$ obtained after three

iterations can be written under the form

$$\begin{aligned}
\Delta W_2(\beta_{z_s},\phi_{z_s},z,E_z) &= \Delta W_{2,C_0} + \Delta W_{2,C_1}\cos\phi_{z_s} + \Delta W_{2,S_1}\sin\phi_{z_s} \\
&\quad + \Delta W_{2,C_2}\cos 2\phi_{z_s} + \Delta W_{2,S_2}\sin 2\phi_{z_s} \\
&\quad + \Delta W_{2,C_3}\cos 3\phi_{z_s} + \Delta W_{2,S_3}\sin 3\phi_{z_s} \\
\Delta\phi_2(\beta_{z_s},\phi_{z_s},z,E_z) &= \Delta\phi_{2,C_0} + \Delta\phi_{2,C_1}\cos\phi_{z_s} + \Delta\phi_{2,S_1}\sin\phi_{z_s} \\
&\quad + \Delta\phi_{2,C_2}\cos 2\phi_{z_s} + \Delta\phi_{2,S_2}\sin 2\phi_{z_s} \\
&\quad + \Delta\phi_{2,C_3}\cos 3\phi_{z_s} + \Delta\phi_{2,S_3}\sin 3\phi_{z_s}
\end{aligned} \tag{3.20}$$

where all the $\Delta W_{2,C_0}$, $\Delta W_{2,C_1}$, $\Delta W_{2,S_1}$... are functions of all the variables but the entrance phase. The result of Eq. (3.20) is compatible with the expectations of Section 3.2.1. It is worthwhile to normalize the field profile function by the accelerating voltage E_0L and write such a function $k_E(z) = \frac{E_z(z)}{E_0L}$ (since the function has the inverse dimension of a length, it is written k_E as for a wave number). It is then possible to introduce the dimensionless factor $\epsilon = \frac{qE_0L}{W_0}$ and write from the results of Appendix B

$$\begin{aligned}
\frac{\Delta W_{2,C_0}}{W_0} &= a_{0,2}\,\epsilon^2 \quad ; \\
\frac{\Delta W_{2,C_1}}{W_0} &= a_{1,1}\,\epsilon^1 + a_{1,3}\,\epsilon^3 \quad ; \quad \frac{\Delta W_{2,S_1}}{W_0} = b_{1,1}\,\epsilon^1 + b_{1,3}\,\epsilon^3 \\
\frac{\Delta W_{2,C_2}}{W_0} &= a_{2,2}\,\epsilon^2 \quad ; \quad \frac{\Delta W_{2,S_2}}{W_0} = b_{2,2}\,\epsilon^2 \\
\frac{\Delta W_{2,C_3}}{W_0} &= a_{3,3}\,\epsilon^3 \quad ; \quad \frac{\Delta W_{2,S_3}}{W_0} = b_{3,3}\,\epsilon^3 \\
\Delta\phi_{2,C_0} &= c_{0,0}\,\epsilon^0 + c_{0,2}\,\epsilon^2 \quad ; \\
\Delta\phi_{2,C_1} &= c_{1,1}\,\epsilon^1 + c_{1,3}\,\epsilon^3 \quad ; \quad \Delta\phi_{2,S_1} = d_{1,1}\,\epsilon^1 + d_{1,3}\,\epsilon^3 \\
\Delta\phi_{2,C_2} &= c_{2,2}\,\epsilon^2 \quad ; \quad \Delta\phi_{2,S_2} = d_{2,2}\,\epsilon^2 \\
\Delta\phi_{2,C_3} &= c_{3,3}\,\epsilon^3 \quad ; \quad \Delta\phi_{2,S_3} = d_{3,3}\,\epsilon^3
\end{aligned} \tag{3.21}$$

where the dimensionless functions $a_{i,j}$, $b_{i,j}$, $c_{i,j}$, $d_{i,j}$ are only functions of the particle's entrance velocity β_{z_s}, of the longitudinal position z, and of the normalized field profile k_E. The indexes i and j are used to recall that $a_{i,j}$, $c_{i,j}$ and $b_{i,j}$, $d_{i,j}$ are coefficients of $\cos i\phi_{z_s}$ and $\sin i\phi_{z_s}$ respectively, and of ϵ^j. These functions are somehow the generalization of the transit time factor concept in the case of a non linear phase law. The function $c_{0,0} = k_{z_s}\{z - z_s\}$ is the linear part of the phase of flight. To illustrate the results of Eq. (3.20), the same example as in Section 3.1.3 is considered. In Fig. 3.8, the functions a, b, c, and d are plotted with respect to the entrance beta of the particle. Beside the functions $a_{1,1}$, $b_{1,1}$, and $c_{0,0}$, all the other functions decay to zero as the entrance beta approaches one. This is due to the fact that for ultrarelativistic particles the non linear part of the phase of flight is usually totally negligible. Because the geometrical beta of the cells of the cavity in this example is equal to 0.5, all the functions are taking their largest values when the entrance beta is close to 0.5. The dependence of the energy gain and of the non linear phase of flight

on the longitudinal position in the cavity are illustrated in Fig. 3.9. It is observable that as long as the non linear component of the phase of flight remains small, the higher order components of the energy gain function are small. The dependence of the energy gain and of the non linear phase of flight on the entrance phase is pictured in Fig. 3.10. In this figure, the zero order harmonic and the second order harmonic are plotted together.

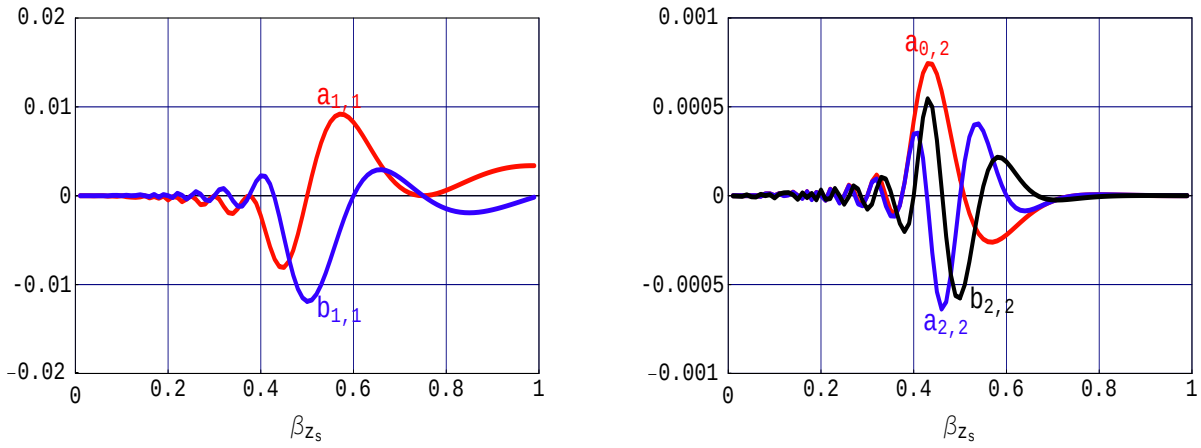

Figure 3.7: Functions $a_{1,1}$, $b_{1,1}$ and $a_{0,2}$, $a_{2,2}$, $b_{2,2}$, as a function of the entrance beta β_{z_s} for a 6-cell superconducting cavity.

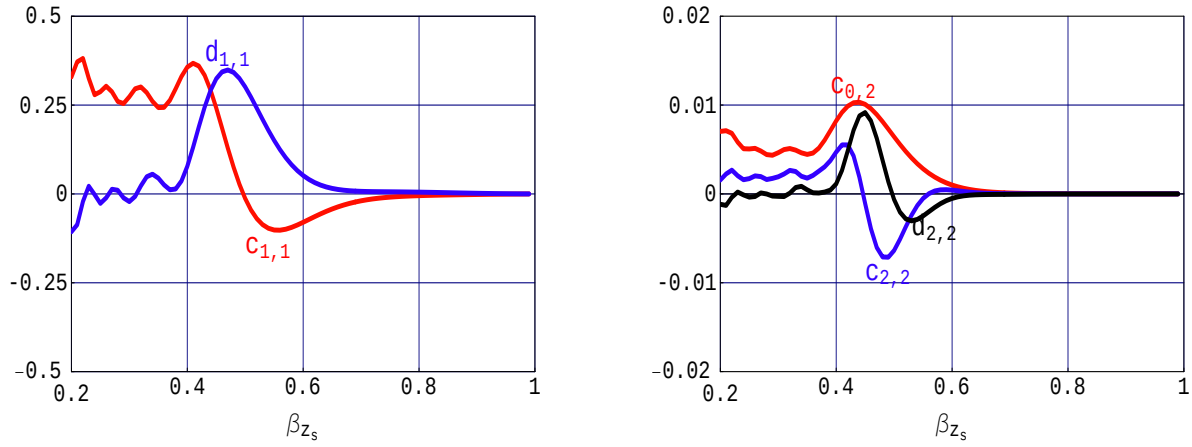

Figure 3.8: Functions $c_{1,1}$, $d_{1,1}$ and $c_{0,2}$, $c_{2,2}$, $d_{2,2}$, as a function of the entrance beta β_{z_s} for a 6-cell superconducting cavity.

The energy gain and the phase of flight in Eq. (3.20) are expressed as a function of the entrance phase. It was pointed out in Section 3.1 that it is a common practice to use an average phase. In Section 3.1.3, it was suggested to define the average phase as null when the energy gain is maximum. This definition can be used in the case of a non linear phase law by finding the value of the entrance phase that maximizes the energy gain. In the linear phase law case this matter was easily solved whereas in the

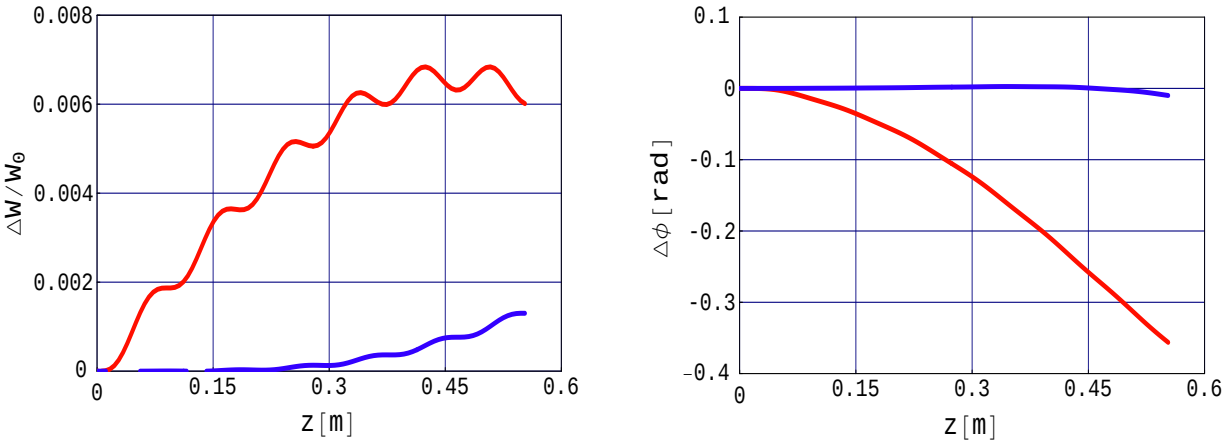

Figure 3.9: Energy gain and non linear phase of flight as a function of the longitudinal position , obtained with the analytical iterative method for a 6-cell superconducting cavity.

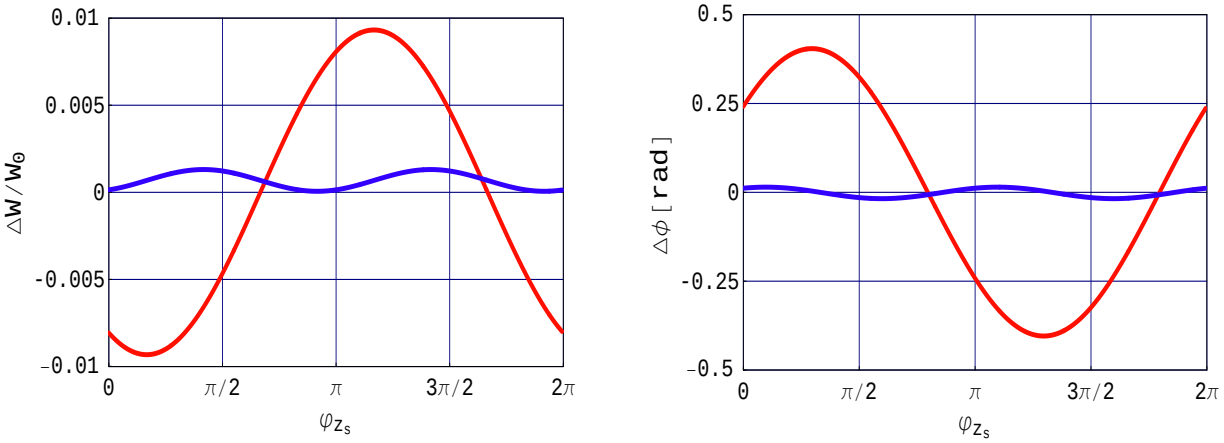

Figure 3.10: Energy gain and non linear phase of flight at the end of a 6-cell superconducting cavity as a function of the entrance phase ϕ_{z_s}, obtained with the analytical iterative method.

non linear phase law case this process is more complicated unless numerical means are used. If the non linearity of the phase of flight is not too large, the problem can be approached by expansion since the entrance phase to be found should be close to the one corresponding to the linear phase law case. First, the energy gain of Eq. (3.20) is rewritten

$$\frac{\Delta W_2}{W_0} = A_0 + A_1\cos(\phi_{z_s}+\phi_1) + A_2\cos(2\phi_{z_s}+\phi_2) + A_3\cos(3\phi_{z_s}+\phi_3) \qquad (3.22)$$

where $A_i = \frac{\sqrt{\Delta W_{2,C_i}^2+\Delta W_{2,S_i}^2}}{W_0}$ and $\tan\phi_i = \frac{\Delta W_{2,S_i}}{\Delta W_{2,C_i}}$. In the previous equation, the entrance phase can be replaced by the average phase $\Phi = \phi_{z_s} + \phi_1 + \Delta\Phi$. The parameter $\Delta\Phi$ represents the difference in the entrance phase that maximizes the

energy gain between the linear phase law case and the non linear phase law case. By definition, the maximum of the energy gain function must occurs at $\Phi = 0$, which implies that the first derivative of this function at this value must vanish. Since it is assumed that $\Delta\Phi$ is a small phase difference, the term proportional to A_3 can be neglected and the first derivative can be treated by expansion. Limiting this expansion to the second order gives an equation of the second power in $\Delta\Phi$

$$\begin{aligned} H\Delta\Phi^2 + I\Delta\Phi - \frac{H}{2} &= 0 \\ \Delta\Phi = \frac{1}{2H}\left\{-I + \sqrt{I^2 + 2H^2}\right\} & \end{aligned} \tag{3.23}$$

with $H = 4A_2 \sin(\phi_2 - 2\phi_1)$ and $I = A_1 + 4A_2 \cos(\phi_2 - 2\phi_1)$. This result is applied to the previous example and illustrated in Fig. 3.11. The few spikes in Fig. 3.11 correspond to the regions where the first order term A_1 is close to zero. It is worthwhile to recall that $\Delta\Phi$ depends on the cavity accelerating voltage E_0L. For example, when the field amplitude is very small, the non linear part of the phase law is negligible and the parameter $\Delta\Phi$ will simply converge to zero.

An analytical approach to the longitudinal dynamics showed that when the phase

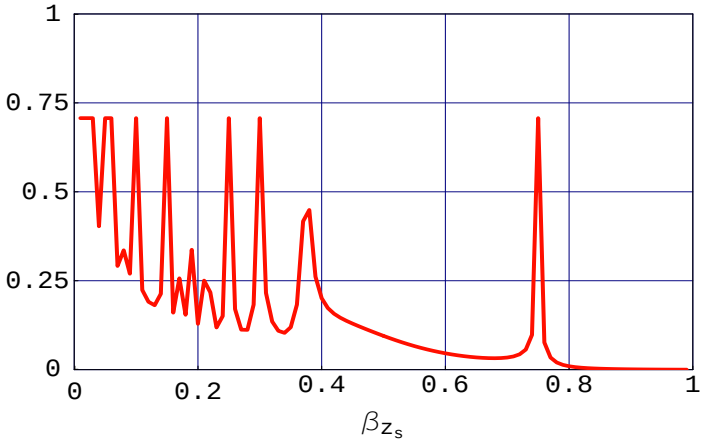

Figure 3.11: $\Delta\Phi$ as a function of the entrance beta. $\Delta\Phi$ depends also on E_0L and converges to zero when the non linear part of the phase law is negligible.

law can not be approximated to linear, the energy gain and the phase of flight can not be expressed as a simple cosine function of the entrance phase or of the average phase, but as a sum of all its harmonics (Eq. (3.20) shows such dependencies up to the third harmonic). As a generalization of the transit time factor concept, the coefficients of each harmonic depend primarly on the entrance beta of the particle. These coefficients were calculated up to the third harmonic of the entrance phase using an analytical iterative method. Furthermore, these coefficients were written under the form of polynomes of the dimensionless parameter ϵ (defined in Annex B, which contains the dependence on the charge and the rest mass energy of the particle,

and on the amplitude of the cavity accelerating voltage. Such a formulation allows efficient computation since the calculated coefficients depend only on the entrance beta of the particle and on the normalized longitudinal field profile. The passage from the entrance phase to an average phase was also approached analytically, which ensures an easy treatment for a bunch of particles. The analytical formulation up to the third harmonic insures fast and accurate calculations if the value of the non linear part of the phase law is not too large. The domain of validity of the formulation can be estimated by saying that in Annex B, the cosine functions are expanded up to the second order of the non linear part of the phase of flight which introduces errors in the order of twenty percent if the non linear part of the phase of flight is about fourty degrees. Because the cosine functions have to be integrated it leads to overall errors roughly half of the previous value. Thus, the corrective terms are expected to be have approximately ten percents error for a non linear phase of fourty degrees. Pursuing the analytical iteration process and calculating the coefficients for higher harmonics of the entrance phase is possible but requires intensive work. Instead of performing all the calculations analytically it will be shown in the next section that the form of the obtained results suggests a more general form valid for any order of the iteration. As a consequence, the very non linear cases can efficiently be approached semi-analytically. The coefficients depending on the entrance beta of the particle and on the field profile can be determined numerically and used in the analytical formulation to obtain the energy gain and the phase of flight for any case.

3.2.3 Semi-analytical method

The results from the analytical iterative method written in Eq. (3.20) and Eq. (3.23) have a rather particular form. It appears that the results could be written in the most general case as

$$\begin{aligned}
\Delta W =& \sum_{n=0}^{\infty} \Delta W_{C_n} \cos n\phi_{z_s} + \Delta W_{S_n} \sin n\phi_{z_s} \\
\Delta \phi =& \sum_{n=0}^{\infty} \Delta \phi_{C_n} \cos n\phi_{z_s} + \Delta \phi_{S_n} \sin n\phi_{z_s} \\
\Delta W_{C_n} =& \sum_{m=n}^{\infty} a_{n,m}\epsilon^m \quad ; \quad \Delta W_{S_n} = \sum_{m=n}^{\infty} b_{n,m}\epsilon^m \\
\Delta \phi_{C_n} =& \sum_{m=n}^{\infty} c_{n,m}\epsilon^m \quad ; \quad \Delta \phi_{S_n} = \sum_{m=n}^{\infty} d_{n,m}\epsilon^m \\
& \begin{cases} a, b, c, d_{m,n} = 0 & \text{for} \quad \text{m+n=odd} \\ a, b, c, d_{m,n} = f(\beta_{z_s}, k_1, z) & \text{for} \quad \text{m+n=even} \end{cases}
\end{aligned} \tag{3.24}$$

The proof that such form is a solution of the initial system of Eq. (3.1) is developed in Appendix B. The benefit of such a formulation is that the dependencies on the various variables are explicitely seperated. The remaining unknown coefficients $a, b, c, d_{m,n}$

are functions of the entrance beta of the particle and of the field profile. Analytical expressions for these coefficients up to the third harmonic have been calculated and can be directly used if the non linear component of the phase law remains below fourty degrees. For cases beyond such a limit, it is possible to carry the analytical iterative process further but this is a heavy task. An other approach is to take benefit of the generality of the formulation of Eq. (3.24) and deduce the values of the a, b, c, d coefficents by numerical means. The introduction of numerical processes is not penalizing since the coefficients are functions of the normalized field profile, which is a given characteristic of the accelerating element, and of the entrance velocity of the particle, allowing therefore their tabulations once and for all. It is interesting to remark that such tabulations are also used for the transit time factors T and S in the d-g-d method. After these coefficients are determined, the computation of the energy gain and of the phase of flight for any particle (charge, rest mass energy), any entrance phase, and any amplitude of the accelerating field, is fast and simple thanks to the analytic formulation of Eq. (3.24). The numerical method to obtain the coefficients in the following is based on a simple and direct numerical integration of the the initial system of equations. Of course, faster processes based for example on fractioning of the element and use of the d-g-d method for the consecutive pieces could efficiently be used as shown in Section 3.1.3. Having a numerical routine that calculates the energy gain and the phase of flight for any input condition allows to estimate the coefficients. A possible process for the extraction of the parameters a, b, c, d is shown below. This method is then applied to a couple of cases and the accuracy of the results is shown to be satisfying compared to the results from a purely numerical routine.

I Procedure to determine the a, b, c, d parameters

The following process is focusing on the extraction of the parameters $a, b, c, d_{m,n}$ of Eq. (3.24) for a given field profile (but free amplitude), given longitudinal position in the cavity (typically the end position z_e of the element), and given entrance beta of the particle (the process can be automized to obtain tables of the coefficients for a desired range of β_{z_s}).
Inspired by the general form of the solution of Eq. (3.24), the parameters can be determined in two successive steps. The first is to use the entrance phase as a varying parameter to determine the coefficients $\frac{\Delta W_{C_n}}{W_0}$, $\frac{\Delta W_{S_n}}{W_0}$, $\Delta\phi_{C_n}$, and $\Delta\phi_{S_n}$, since these coefficients do not depend on ϕ_{z_s}. It is possible to calculate the energy gain and the phase of flight with a purely numerical routine for a given ϵ and different values of ϕ_{z_s}, then perform a discrete Fourier transform on both series of results. The complex numbers for each harmonic of the Fourier transforms are the desired coefficients (the real parts are the coefficients of the cosines, and the imaginary are the coefficients for the sines). This process can then be repeated for various value of ϵ. Since each harmonic coefficient is a polynome of ϵ, as written in Eq. (3.24), a fitting routine allows to find the coefficients $a, b, c, d_{m,n}$ of these polynomes. The number of entrance phases in the first step and the number of ϵ in the second, determine the order up to where the coefficients $a, b, c, d_{m,n}$ will be determined. From the analytical iterative method, it appears that considering equal values for the highest harmonic and the

highest power term of the polynomes makes the most sense. Therefore, if a calculus up to the order N is desired, the coefficients $a, b, c, d_{m,n}$ should be searched such that $m \leq N$ and $n \leq N$.

II Application to two examples

As a first example, the case that was used along the entire chapter will be reconsidered. The number of entrance phases for the runs was fixed to 36 so the discrete Fourier transform gives results up to the 18^{th} harmonic. The results of the discrete Fourier transforms for the energy gain and the phase of flights are presented in Fig. 3.12 for $\epsilon = 0.06$. The results indicate that the coefficients beyond the 7^{th} harmonic are negligible. The polynomes are therefore searched up to the 7^{th} power of ϵ. The $\Delta W_{C_n}, \Delta W_{S_n}$ and $\Delta\phi_{C_n}, \Delta\phi_{S_n}$ coefficients up o the seventh harmonic are illustrated in Figs. 3.13 and 3.14 respectively.In these figures, the dots are the results obtained with the numerical routine and the lines represent the results of the polynomial fitting procedure. The previous results are then used to calculate the energy gain and the

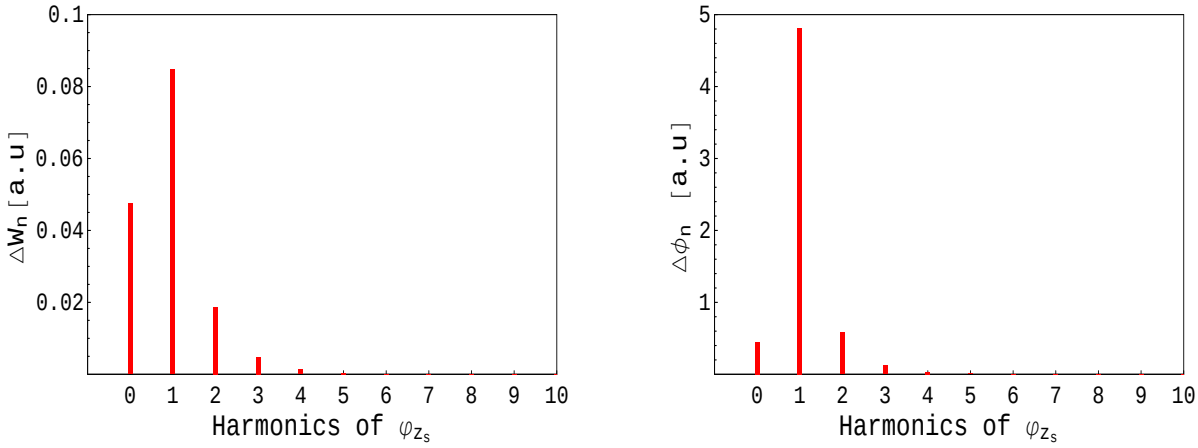

Figure 3.12: Discrete Fourier transforms of the energy gain and of the non linear phase of flight functions for the cavity 1 up to the 10th harmonic of the entrance phase ϕ_{z_s}.

non linear part of the phase of flight for $\epsilon = 0.064$ and various entrance phases. The results are plotted in Fig. 3.15. The agreement with the results of the numerical routine plotted in dots is good which shows the applicability of the semi-analytical method.

As a second example, a 5-cell cavity of geometrical beta equal to 1 is considered for the acceleration of electrons with $\beta_{z_s} = 0.6$. To determin the coefficients of such cavity the same procedure than in the previous case is repeated. First, the field amplitude is fixed so that $\epsilon = 1.5$ and the results of the discrete fourier transforms are presented in Fig. 3.16. In this case also, the coeffcients become negligible after the 7^{th} harmonic, and the fitting polynomes are therefore searched up to the 7^{th} power of ϵ. The $\Delta W_{C_n}, \Delta W_{S_n}$ and $\Delta\phi_{C_n}, \Delta\phi_{S_n}$ coefficients are presented in Figs. 3.17 and 3.18. Examples of energy gain and non linear phase of flight as a function of the

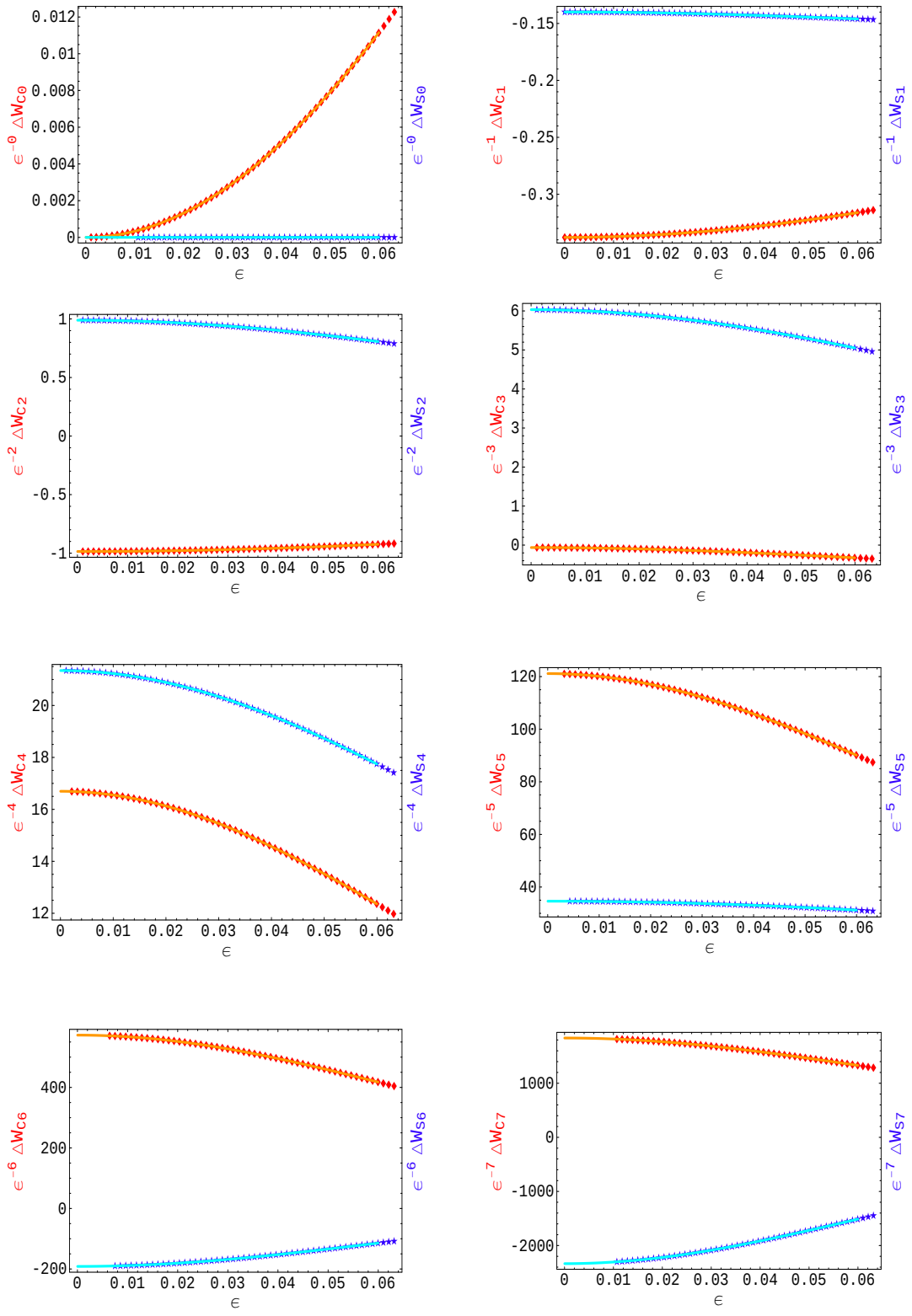

Figure 3.13: coefficients $\frac{\Delta W_{C_n}}{\epsilon^n}$ and $\frac{\Delta W_{S_n}}{\epsilon^n}$ of the n^{th} harmonic for the 0^{th} to the 7^{th} harmonic for the cavity 1.

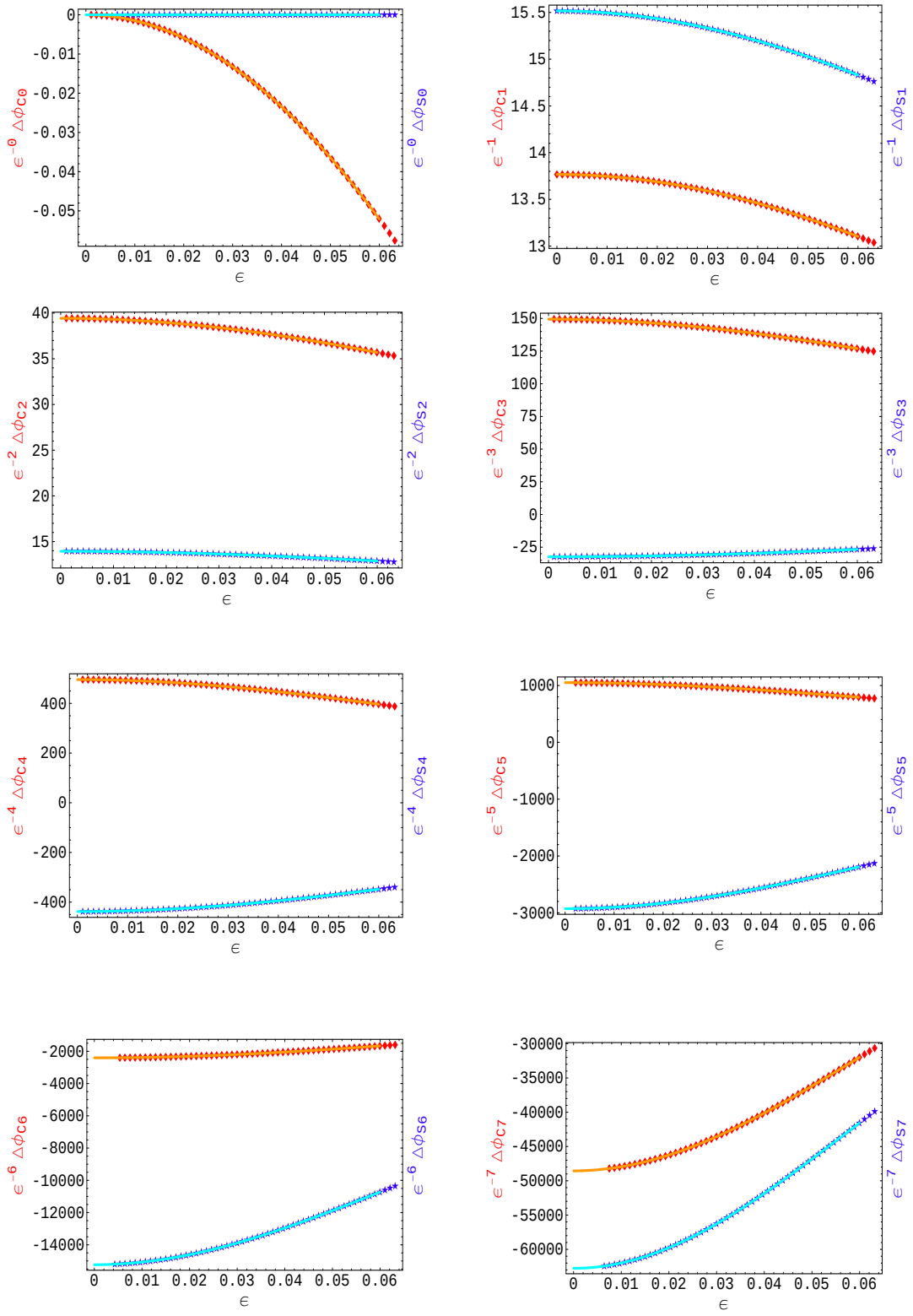

Figure 3.14: coefficients $\frac{\Delta\phi_{C_n}}{\epsilon^n}$ and $\frac{\Delta\phi_{S_n}}{\epsilon^n}$ of the n^{th} harmonic for the 0^{th} to the 7^{th} harmonic for the cavity 1.

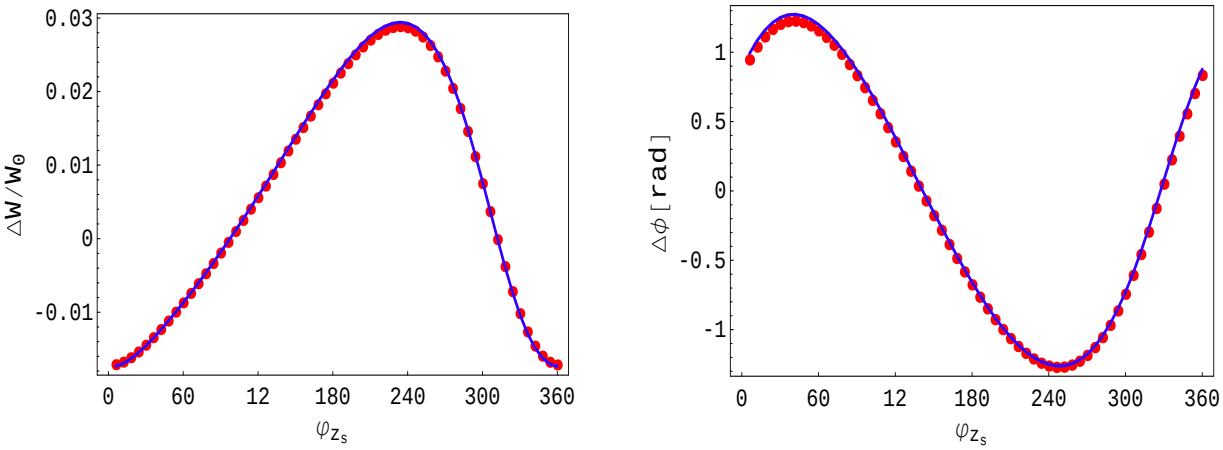

Figure 3.15: Calculation of the energy gain and of the non linear phase of flight for $\epsilon = 0.064$ and various entrance phases for the cavity 1. The agreement with the numerical result (plotted in dots) is satisfying.

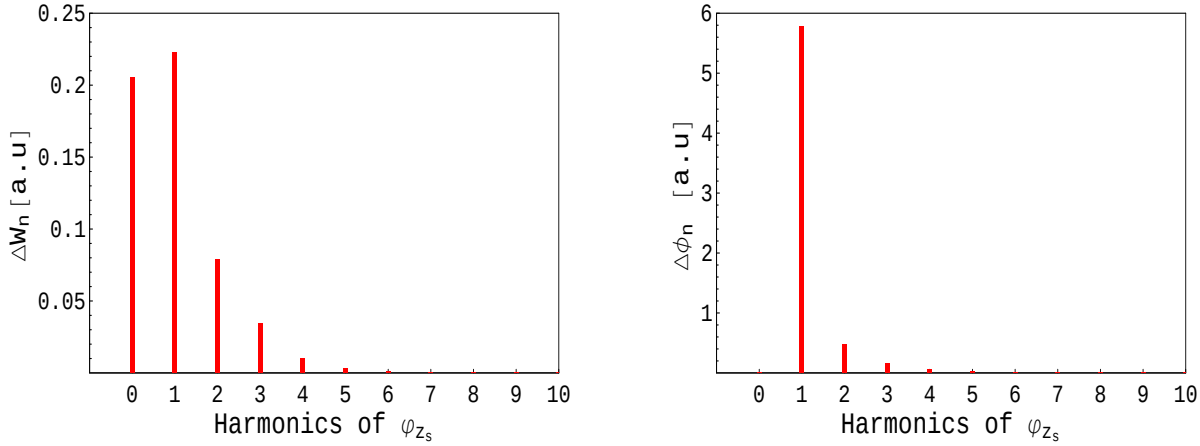

Figure 3.16: Discrete Fourier transforms of the energy gain and of the non linear phase of flight functions for cavity 2. The results appear negligible beyond the 7^{th} harmonic.

entrance phase for $\epsilon = 1.1$ are illustrated in Fig. 3.19. In this example too, the agreement with the results from the numerical routine is good.

3.3 Conclusion

In this chapter the longitudinal beam dynamics in elements where the phase law is non linear was presented. The usual d-g-d method used for linear phase law was reviewed for symmetric field cases and extended to non symmetric ones. It was shown that non linear phase law cases could be approached by fractioning the element into pieces and applying the thin d-g-d method to each of them. Doing so, the usual

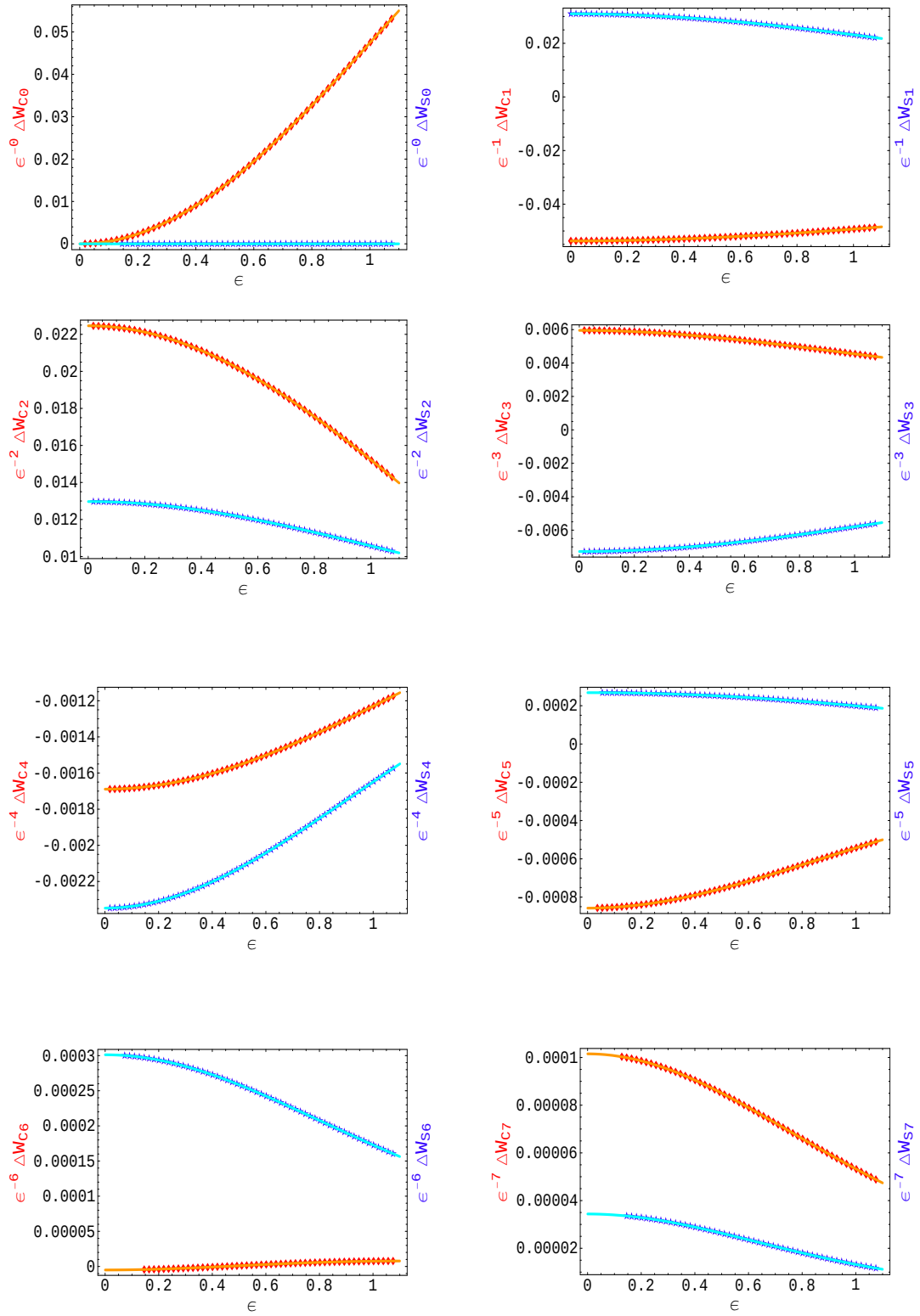

Figure 3.17: Coefficients $\frac{\Delta W_{Cn}}{\epsilon^n}$ and $\frac{\Delta W_{Sn}}{\epsilon^n}$ of the n^{th} harmonic for the 0^{th} to the 7^{th} harmonic for the cavity 2.

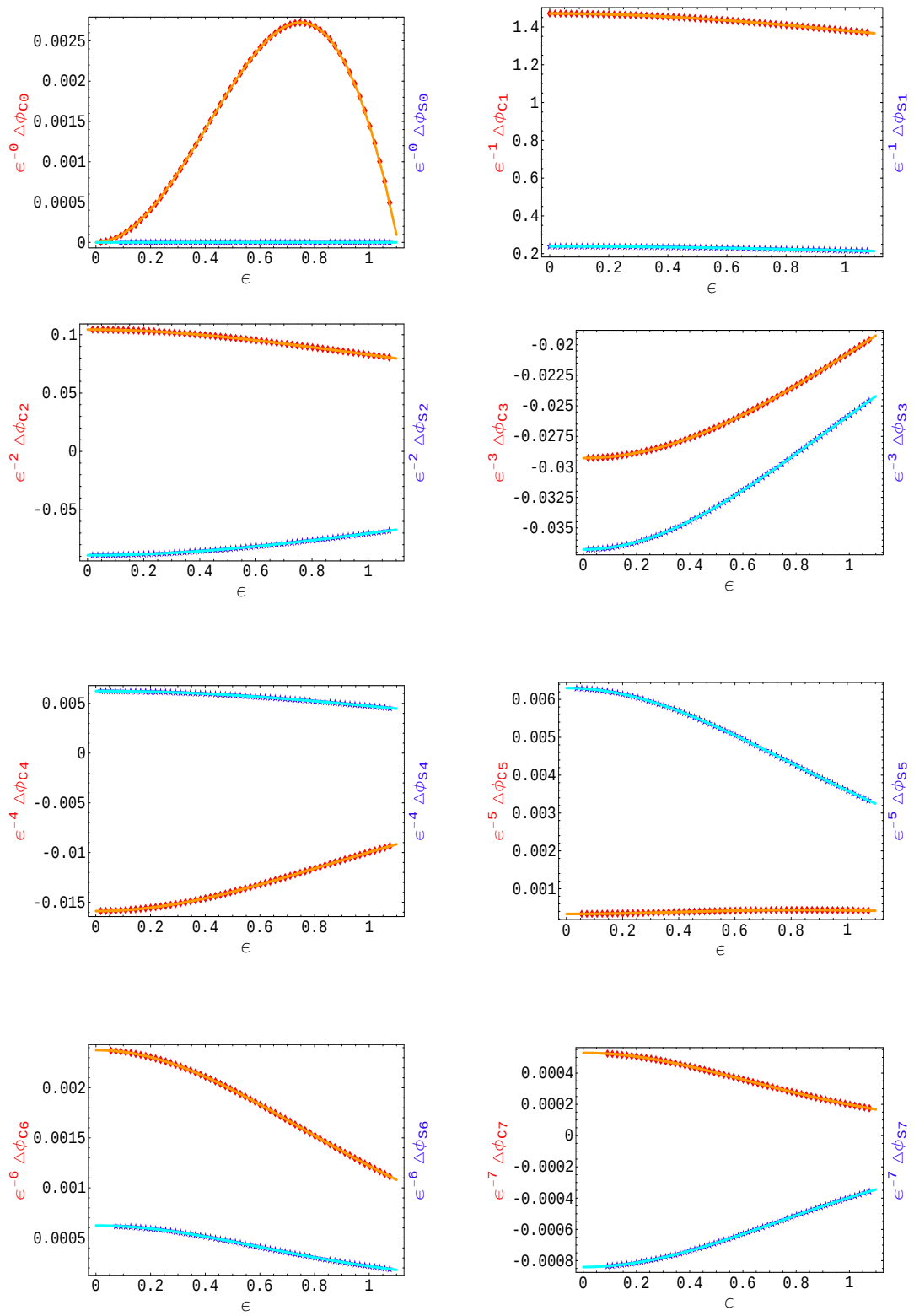

Figure 3.18: coefficients $\frac{\Delta\phi_{C_n}}{\epsilon^n}$ and $\frac{\Delta\phi_{C_n}}{\epsilon^n}$ of the n^{th} harmonic for the 0^{th} to the 7^{th} harmonic for the cavity 2.

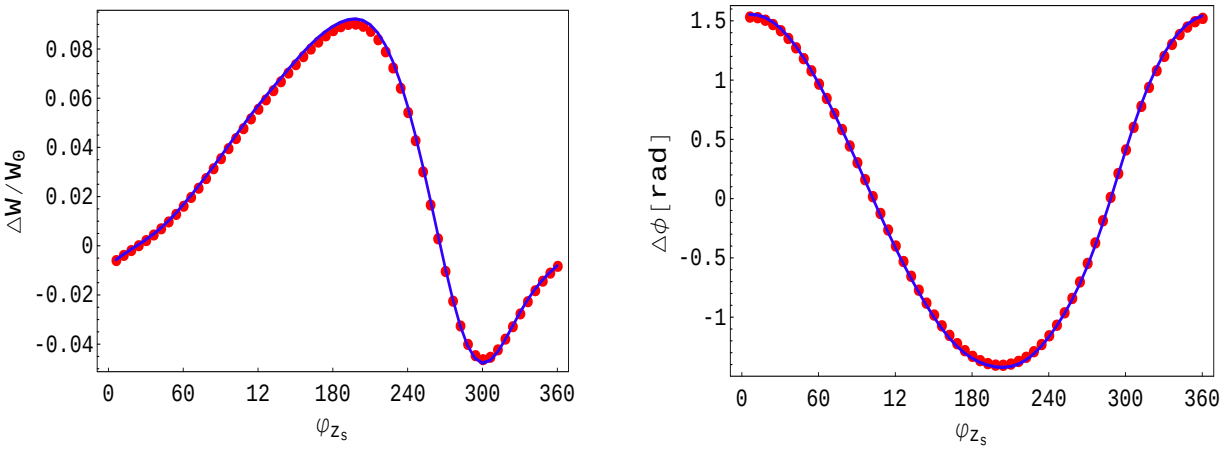

Figure 3.19: Calculation of the energy gain and of the non linear phase of flight for $\epsilon = 1.1$ and various entrance phase for cavity 2. The agreement with the numerical result plotted in dots is satisfying.

concept of average phase had to be defined more clearly, numerical routine were necessary, and the dependence of the final results upon the entrance parameters is lost. A more general method to calculate the longitudinal dynamics, based on analytical iterations was developed. Analytical solutions after three iterations were presented and illustrated. The form of the solutions thus obtained suggest a general formulation for the energy gain and for the phase of flight functions, where the dependence on the different variables can be efficiently separated. It was demonstrated that such a general form was indeed verifying the initial coupled system of integral equations describing the longitudinal dynamics. Although the general form of the solution is known, some of its coefficients are not explicitely known. A semi-analytical method relying on a numerical routine to calculate these coefficients was eventually presented and illustrated for a couple of examples. After determining the coefficients for each case, the analtyical formulation was used and its results successfully compared to the results from a purely numerical routine. The general resolution of the longitudinal dynamics in an accelerating element was only dealing with on-axis particles and therefore, the effect of their transverse position was not considered. For a linear phase law, small transverse displacement, and axis symmetric elements, a corrective term exists in the thin lense approximation method and is obtained by considering the transverse offset constant within the element and by showing that the dependence of the longitudinal field with respect to the transverse position can be expressed using the modified Bessel's function of the zeroth order I_0 [43]. If the offset of the particle is assumed constant, the general form of the results obtained in this chapter can simply be modified by replacing ϵ by $\epsilon I_0(k_{z_s} r_{z_s})$, where r_{z_s} is the initial transverse offset. Also, the effect of an inital angle supposed constant within a cavity was shown to bring a term proportional to the modified Bessel's function of the first order I_1. Such an approach in the non linear phase law context would not be very satifying since large variations of the particle's beta are automatically linked to large variations of the particle's transverse angle. To consider accurately the effect of the transverse

position and angle in the case of a non linear phase law requires to solve a system of six coupled integral equations, where four equations, associated to the calculation of the transverse displacement and of the transverse angles, should be added to the two longitudinal equations.

Appendix A

Dynamic detuning in SRF cavities: Annex

A.1 Verification of the validity of the voltage solution

In Chapter 2 it was asserted that the second order term of the voltage envelope differential equation could be neglected. To show that the voltage given by Eq. (2.10) is, in good approximation, a solution of Eq. (2.4) it is possible to start by differentiating Eq. (2.5)

$$\begin{aligned}\ddot{\tilde{V}}(t) &= R_L\omega_{1/2}\dot{\tilde{I}} + j\dot{\tilde{\omega}}\tilde{V} + j\tilde{\omega}\dot{\tilde{V}} \\ &= R_L\omega_{1/2}\dot{\tilde{I}} + \dot{\tilde{\omega}}\left\{\frac{\dot{\tilde{V}} - R_L\omega_{1/2}\tilde{I}}{\tilde{\omega}}\right\} + j\tilde{\omega}\dot{\tilde{V}} \\ &= \dot{\tilde{V}}\left\{\frac{\dot{\tilde{\omega}}}{\tilde{\omega}} + j\tilde{\omega}\right\} + R_L\omega_{1/2}\left\{\dot{\tilde{I}} - \frac{\dot{\tilde{\omega}}}{\tilde{\omega}}\tilde{I}\right\}\end{aligned}$$

From there follows

$$\frac{1}{2j\omega}\ddot{\tilde{V}} + \dot{\tilde{V}} - j\tilde{\omega}\tilde{V} = \dot{\tilde{V}}\left\{1 + \frac{\dot{\tilde{\omega}}}{2j\omega\tilde{\omega}} + \frac{\tilde{\omega}}{2\omega}\right\} + \frac{R_L\omega_{1/2}}{2j\omega}\left\{\dot{\tilde{I}} - \frac{\dot{\tilde{\omega}}}{\tilde{\omega}}\tilde{I}\right\} - j\tilde{\omega}\tilde{V}$$

It is supposed that the cavity electromagnetic half-bandwidth and the frequency detuning are much smaller than the cavity oscillating frequency, $\omega_{1/2} << \omega$ and $\Delta\omega << \omega$, respectively. It follows that the amplitude of the complex frequency defined as $\tilde{\omega} = \Delta\omega + j\omega_{1/2}$ is much smaller than the cavity frequency, $|\tilde{\omega}| << \omega$. Also, from the assumption that the dynamic detuning contains only slow frequency components compared to the cavity frequency, $|\dot{\Delta\omega}| << |\omega\Delta\omega|$, it is possible to conclude that $|\dot{\tilde{\omega}}| << \omega|\tilde{\omega}|$. The previous statements can be used to write

$$\left|\frac{\dot{\tilde{\omega}}}{2j\omega\tilde{\omega}} + \frac{\tilde{\omega}}{2\omega}\right| << 1$$

Using this fact in the voltage differential equation justifies the following approximation

$$\frac{1}{2j\omega}\ddot{\tilde{V}} + \dot{\tilde{V}} - j\tilde{\omega}\tilde{V} \approx \dot{\tilde{V}} + \frac{R_L\omega_{1/2}}{2j\omega}\Big\{\dot{\tilde{I}} - \frac{\dot{\tilde{\omega}}}{\tilde{\omega}}\tilde{I}\Big\} - j\tilde{\omega}\tilde{V}$$

With Eq. (2.5) it leads to

$$\begin{aligned}\frac{1}{2j\omega}\ddot{\tilde{V}} + \dot{\tilde{V}} - j\tilde{\omega}\tilde{V} &\approx R_L\omega_{1/2}\left\{\frac{\dot{\tilde{I}}}{2j\omega} + \tilde{I}\Big\{1 - \frac{\dot{\tilde{\omega}}}{2j\omega\tilde{\omega}}\Big\}\right\} \\ &\approx R_L\omega_{1/2}\left\{\frac{\dot{\tilde{I}}}{2j\omega} + \tilde{I}\right\}\end{aligned}$$

And because the last condition is that the source current contains only slow frequency components compare to the cavity frequency, $\left|\dot{\tilde{I}}\right| << \left|\omega\tilde{I}\right|$, it finally reduces to

$$\frac{1}{2j\omega}\ddot{\tilde{V}} + \dot{\tilde{V}} - j\tilde{\omega}\tilde{V} \approx R_L\omega_{1/2}\tilde{I} \tag{A.1}$$

This relation proves that when the first order differential equation written in Eq. (2.5) is satisfied, the second order differential equation written in Eq. (2.4) is approximately satisfied. Therefore, the voltage solution of the first order differential equation given by Eq. (2.10) is in good approximation a solution for the initial second order differential equation.

A.2 Voltage as a mapping of the complex frequency

Since the real part of the complex frequency $\tilde{\omega}_0$ is the initial detuning $\Delta\omega_0$ which can take any real value, and since the imaginary part is the constant half-bandwidth $\omega_{1/2}$, all the possible values of the complex frequency $\tilde{\omega}_0$ form a straight line parallel to the real axis in the complex plane. This frequency domain is illustrated in Fig. A.1. For a given set of driving current time function and dynamic detuning time function $\{\tilde{I}, \tilde{\omega}\}$, the cavity voltage can be seen as a time dependent complex transformation of the initial frequency $\tilde{\omega}_0$. This transformation is governed by the Eq. (2.10). An overview of the voltage envelope evolution for a given set of functions $\{\tilde{I}, \tilde{\omega}\}$ can be obtained by applying the transformation to the entire initial complex frequency domain. The result is a time dependent complex mapping. When a map is drawn at a given time t it represents all the possible values of the voltage at that time due to all the possible values of the initial detuning. A map should not be confused with the trajectory in time of the voltage for a particular value of the initial detuning. In all cases, at $t = 0$, the complex map is the zero point if the initial value of the cavity voltage is supposed null. Also, according to Eq. (2.8) the voltage is, regardless of the value of the initial detuning, always initially developing linearly and in phase with the driving current, therefore the map is initially equivalent to a simple point moving away from the origin. With time, the set of functions $\{\tilde{I}, \tilde{\omega}\}$ acts non-uniformly on the frequency domain and the map quickly evolves into a more complex figure. Different example

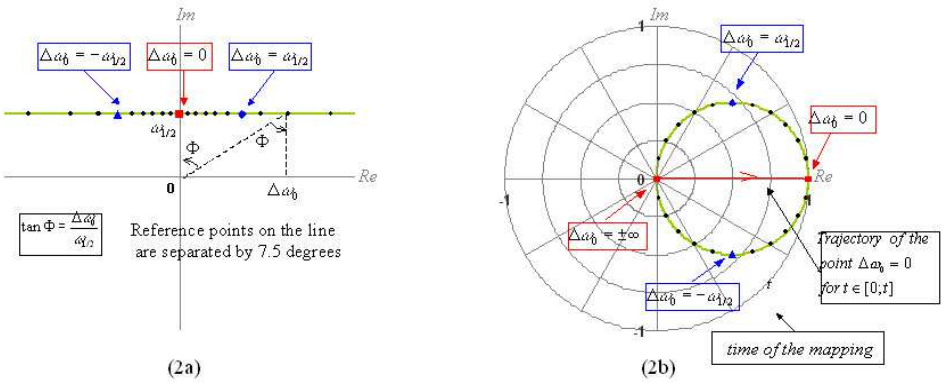

Figure A.1: (2a); The possible domain for the initial frequency $\tilde{\omega}_0$ is a straight line in the complex plane, parallel to the real axis. Some reference points are chosen on the line to facilitate the visualization after the complex transformation. (2b); Complex mapping of the normalized quantity $\frac{\tilde{V}(t)}{R_L \tilde{I}_0}$ at time t . The trajectory of the reference point corresponding to $\Delta\omega_0 = 0$ is drawn as a line with an arrow.

of mappings will be shown using the same visualization model as the one displayed on Fig. A.1. When the amplitude of the driving current is constant through time the mappings will conveniently be done for the normalized quantity $\frac{\tilde{V}(t)}{R_L \tilde{I}_0}$. The time for the mapping will be expressed with respect to the time constant of the cavity, defined as $\tau_{1/2} = \omega_{1/2}^{-1}$.

A.3 Voltage solution for a sine detuning function

From Eq. (2.6) and Eq. (2.10) it follows

$$\tilde{V} - \tilde{V}_{SF} = R_L \omega_{1/2} \int_0^t \tilde{I}(t')\, e^{j\int_{i'}^{t} \tilde{\omega}(t'')dt''}\, dt' \tag{A.2}$$

Considering the case where no voltage is initially present in the cavity, $\tilde{V}_{SF} = 0$, where the current source is constant through time, $\tilde{I}(t) = \tilde{I}_0$, and where the detuning function is a sine function, $\Delta\omega(t) = \Delta\omega_{osc} \sin(\omega_{osc} t + \theta_{osc})$, gives for the voltage

$$\tilde{V}(t) = \omega_{1/2} R_L \tilde{I}_0 \int_0^t e^{j\frac{\Delta\omega_{osc}}{\omega_{osc}}\{\cos(\omega_{osc}t'+\theta_{osc})-\cos(\omega_{osc}t+\theta_{osc})\}} e^{j\tilde{\omega}_0\{t-t'\}} dt'$$

Doing the change of variable $t' \rightarrow u = t - t'$ leads to

$$\tilde{V}(t) = \omega_{1/2} R_L \tilde{I}_0 e^{-j\frac{\Delta\omega_{osc}}{\omega_{osc}}\cos(\omega_{osc}t+\theta_{osc})} \int_0^t e^{j\frac{\Delta\omega_{osc}}{\omega_{osc}}\cos(\omega_{osc}t+\theta_{osc}-\omega_{osc}u)} e^{j\tilde{\omega}_0 u} du$$

It is possible to write $\omega_{osc} t = 2\pi N + \theta$ with N integer. Doing the second change of variable $u \rightarrow \phi = \omega_{osc} u$ brings

$$\tilde{V}(N,\theta) = \frac{\omega_{1/2}}{\omega_{osc}} R_L \tilde{I}_0 e^{-j\frac{\Delta\omega_{osc}}{\omega_{osc}}\cos(\theta+\theta_{osc})} \int_0^{2\pi N+\theta} e^{j\frac{\tilde{\omega}_0}{\omega_{osc}}\phi} e^{j\frac{\Delta\omega_{osc}}{\omega_{osc}}\cos(\theta+\theta_{osc}-\phi)} d\phi \tag{A.3}$$

It is now useful to decompose the integral as a sum on successive entire periods plus a fraction of a period

$$\tilde{V}(N,\theta) = \frac{\omega_{1/2}}{\omega_{osc}} R_L \tilde{I}_0 e^{-j\frac{\Delta\omega_{osc}}{\omega_{osc}}\cos(\theta+\theta_{osc})} \left\{ \sum_{n=0}^{N-1} \left(\int_{2\pi n}^{2\pi(n+1)} e^{j\frac{\tilde{\omega}_0}{\omega_{osc}}\phi} e^{j\frac{\Delta\omega_{osc}}{\omega_{osc}}\cos(\theta+\theta_{osc}-\phi)} d\phi \right) + \int_{2\pi N}^{2\pi N+\theta} e^{j\frac{\tilde{\omega}_0}{\omega_{osc}}\phi} e^{j\frac{\Delta\omega_{osc}}{\omega_{osc}}\cos(\theta+\theta_{osc}-\phi)} d\phi \right\} \tag{A.4}$$

using the following definitions and relations

$$\sigma = \frac{\Delta\omega_{osc}}{\omega_{osc}} \qquad \tilde{\psi} = \psi_r + j\psi_i \qquad \psi_r = \frac{\Delta\omega_0}{\omega_{osc}} \qquad \psi_i = \frac{\omega_{1/2}}{\omega_{osc}} \tag{A.5}$$

$$\int_{2\pi n}^{2\pi(n+1)} e^{j\frac{\tilde{\omega}_0}{\omega_{osc}}\phi} e^{j\frac{\Delta\omega_{osc}}{\omega_{osc}}\cos(\theta+\theta_{osc}-\phi)} d\phi = e^{j2\pi n\tilde{\psi}} \int_0^{2\pi} e^{j\tilde{\psi}\phi} e^{j\sigma\cos(\theta+\theta_{osc}-\phi)} d\phi$$

$$\tilde{a}_{\tilde{\psi},N} = \sum_{n=0}^{N-1} e^{j2\pi n\tilde{\psi}} = \sum_{m=1}^{N} e^{j2\pi(m-1)\tilde{\psi}} = \frac{1-e^{j2\pi N\tilde{\psi}}}{1-e^{j2\pi\tilde{\psi}}}$$

$$\tilde{b}_{\tilde{\psi},N} = e^{j2\pi N\tilde{\psi}}$$

$$\tilde{S}_\theta(\varphi) = \int_0^{\varphi} e^{j\tilde{\psi}\phi} e^{j\sigma\cos(\phi-\theta-\theta_{osc})} d\phi$$

Eq. (A.4) is equivalent to

$$\tilde{V}(N,\theta) = R_L \tilde{I}_0 \psi_i e^{-j\sigma\cos(\theta+\theta_{osc})} \left\{ \tilde{a}_{\tilde{\psi},N} \tilde{S}_\theta(2\pi) + \tilde{b}_{\tilde{\psi},N} \tilde{S}_\theta(\theta) \right\} \tag{A.6}$$

The steady state for the voltage $\tilde{V}_{SST}(\theta)$ is obtained by taking the limit of Eq. (A.6) when $N \to \infty$. Using the limits $lim_{N\to\infty}\tilde{a}_{\tilde{\psi},N} = \frac{1}{1-e^{j2\pi\tilde{\psi}}}$ and $lim_{N\to\infty}\tilde{b}_{\tilde{\psi},N} = 0$ leads for the steady state to

$$\tilde{V}_{SST}(\theta) = R_L \tilde{I}_0 \frac{\psi_i}{1-e^{j2\pi\tilde{\psi}}} e^{-j\sigma\cos(\theta+\theta_{osc})} \tilde{S}_\theta(2\pi) \tag{A.7}$$

This equation shows that the voltage envelope in the steady state is a periodic function of frequency ω_{osc}, since it depends only on θ but not on the integer N anymore. To evaluate the voltage of Eq. (A.6) or Eq. (A.7) requires to solve the complex integral $\tilde{S}_\theta$. In the most general case it is not an easy matter due to the complex exponential term. Nevertheless an approximation is possible when the amplitude of the detuning oscillatory function is not too large compare to its frequency. In such case, the rotary exponential term $e^{j\sigma\cos(\phi-\theta+\theta_{osc})}$ can efficiently be expanded into Taylor's serie. Using $e^x = \sum_{n=0}^{\infty} \frac{1}{n!} x^n$ it gives

$$\tilde{S}_\theta(\varphi) = \sum_n \int_0^{\varphi} e^{j\tilde{\psi}\phi} \frac{\{j\sigma\}^n}{n!} \cos^n(\theta+\theta_{osc}-\phi)\, d\phi \tag{A.8}$$

But the cosines elevated to a power can be decomposed with

$$\begin{aligned}\cos^{2n-1} x &= \frac{1}{2^{2\{n-1\}}}\sum_{k=0}^{n-1}\left\{\binom{2n-1}{k}\cos(\{2n-2k-1\}x)\right\}\\ \cos^{2n} x &= \frac{1}{2^{2n}}\left\{\binom{2n}{n}+\sum_{k=0}^{n-1}\left\{2\binom{2n}{k}\cos(\{2n-2k\}x)\right\}\right\}\end{aligned} \tag{A.9}$$

From Eq. (A.8) and Eq. (A.9) it is possible to write

$$\tilde{S}_\theta(\varphi) = \sum_n \tilde{P}_n(\sigma)\int_0^\varphi e^{j\tilde{\psi}\phi}\cos(n\{\phi-\theta-\theta_{osc}\})\,d\phi \tag{A.10}$$

where the $\tilde{P}_n(\sigma)$ are polynomes of σ. The coefficients of these polynomes are calculated and presented in Table A.1 using a decomposition of the exponentiel at the 10th order which is satisfying for $\sigma < 5$. In the case of dynamic detuning induced by the action of Lorentz forces or a piezoelectric, this decomposition will usually be enough but if needed the expansion can be pursued to a higher order.

Table A.1: Polynomes $\tilde{P}_n(\sigma)$ for the decomposition of $e^{j\sigma\cos(\phi-\theta+\theta_{osc})}$ up to n=10

$\tilde{P}_n(\sigma)$	$\frac{\sigma^0}{0!}$	$j\frac{\sigma^1}{1!}$	$\frac{\sigma^2}{2!2^1}$	$j\frac{\sigma^3}{3!2^2}$	$\frac{\sigma^4}{4!2^3}$	$j\frac{\sigma^5}{5!2^4}$	$\frac{\sigma^6}{6!2^5}$	$j\frac{\sigma^7}{7!2^6}$	$\frac{\sigma^8}{8!2^7}$	$j\frac{\sigma^9}{9!2^8}$	$\frac{\sigma^{10}}{10!2^9}$
$\tilde{P}_0$	1	0	-1	0	3	0	-10	0	35	0	-126
$\tilde{P}_1$	0	1	0	-3	0	10	0	-35	0	126	0
$\tilde{P}_2$	0	0	-1	0	4	0	-15	0	56	0	-210
$\tilde{P}_3$	0	0	0	-1	0	5	0	-21	0	84	0
$\tilde{P}_4$	0	0	0	0	1	0	-6	0	28	0	-120
$\tilde{P}_5$	0	0	0	0	0	1	0	-7	0	36	0
$\tilde{P}_6$	0	0	0	0	0	0	-1	0	8	0	-45
$\tilde{P}_7$	0	0	0	0	0	0	0	-1	0	9	0
$\tilde{P}_8$	0	0	0	0	0	0	0	0	1	0	-10
$\tilde{P}_9$	0	0	0	0	0	0	0	0	0	1	0
$\tilde{P}_{10}$	0	0	0	0	0	0	0	0	0	0	-1

The remaining integrals of Eq. (A.10) are now solvable with

$$\int e^{ax}\cos(bx+c)\,dx = \frac{e^{ax}}{a^2+b^2}\{a\cos(bx+c)+b\sin(bx+c)\}$$

where x is real. Applying this relation in Eq. (A.10) leads to

$$\begin{aligned}\tilde{S}_\theta(\varphi) = \sum_n \frac{\tilde{P}_n(\sigma)}{-\tilde{\psi}^2+n^2}\Big\{&e^{j\tilde{\psi}\varphi}\{j\tilde{\psi}\cos(n\{\varphi-\theta-\theta_{osc}\})+n\sin(n\{\varphi-\theta-\theta_{osc}\})\}\\ &-\{j\tilde{\psi}\cos(n\{\theta+\theta_{osc}\})-n\sin(n\{\theta+\theta_{osc}\})\}\Big\}\end{aligned} \tag{A.11}$$

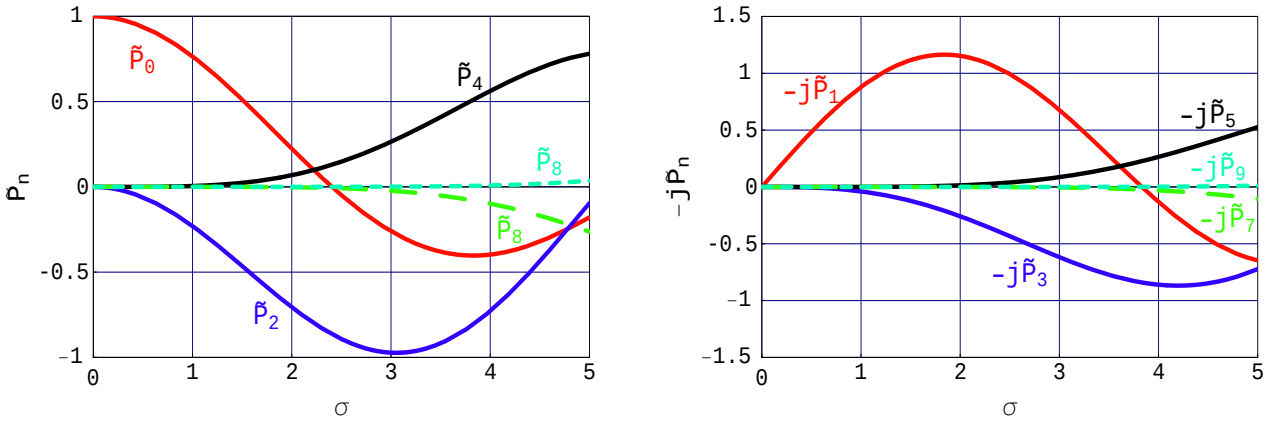

Figure A.2: Polynomes $\tilde{P}_n(\sigma)$. P_n is real for n even and imaginary for n odd.

An important factor for the voltage solution is $\tilde{S}_\theta(2\pi)$, using Eq. (A.11) it writes

$$\tilde{S}_\theta(2\pi) = \sum_n \frac{-\tilde{P}_n(\sigma)}{-\tilde{\psi}^2 + n^2}\{1 - e^{2\pi j\tilde{\psi}}\}\{j\tilde{\psi}\cos(n\{\theta+\theta_{osc}\}) - n\sin(n\{\theta+\theta_{osc}\})\} \tag{A.12}$$

Considering the case with no initial detuning so that $\psi_r = 0$ and inserting in Eq. (A.7) gives for the steady state voltage

$$\begin{aligned}\tilde{V}_{SST}(\theta) &= R_L\tilde{I}_0 e^{-j\sigma\cos(\theta+\theta_{osc})}\sum_n \tilde{P}_n(\sigma)\frac{\psi_i}{{\psi_i}^2+n^2}\begin{bmatrix}\psi_i\cos(n\{\theta+\theta_{osc}\})+\\ n\sin(n\{\theta+\theta_{osc}\})\end{bmatrix} \\ &= R_L\tilde{I}_0 e^{-j\sigma\cos(\theta+\theta_{osc})}\sum_n \tilde{P}_n(\sigma)\cos\theta_n\cos(n\{\theta+\theta_{osc}\}-\theta_n)\end{aligned} \tag{A.13}$$

with $\tan\theta_n = \frac{n}{\psi_i}$. The previous treatment is suited for any case with $\sigma < 5$ and any values of ψ_i which covers almost the entire range of practical interest, but when the frequency ω_{osc} of the detuning function is much lower than the electromagnetic half-bandwidth $\omega_{1/2}$ so that $\psi_i \gg 1$, the limitation on the value of parameter σ can be too restrictive. For such a particular case, it is convenient to restart from the definition of the integral $\tilde{S}_\theta(2\pi)$ written in Eq. (A.5) and note that the real exponential term under the integral decays very fast within the interval of integration. As a consequence, the slower complex exponential term $e^{j\sigma\cos(\phi-\theta-\theta_{osc})}$ can be approximated by Taylor

expansion around $\phi = 0$.

$$\begin{aligned}\tilde{S}_\theta(2\pi) = &\int_0^{2\pi} e^{j\tilde{\psi}\phi} e^{j\sigma\cos(\phi-\theta-\theta_{osc})} d\phi \\ \approx &e^{j\sigma\cos(\theta+\theta_{osc})} \int_0^{2\pi} e^{j\tilde{\psi}\phi} e^{j\phi\sigma\sin(\theta+\theta_{osc})} d\phi \\ = &e^{j\sigma\cos(\theta+\theta_{osc})} \left[\frac{e^{j\tilde{\psi}\phi} e^{j\phi\sigma\sin(\theta+\theta_{osc})}}{j\{\tilde{\psi} + \sigma\sin(\theta+\theta_{osc})} \right]_{\phi=0}^{\phi=2\pi} \\ \approx &\frac{e^{j\sigma\cos(\theta+\theta_{osc})}}{j\{\tilde{\psi} + \sigma\sin(\theta+\theta_{osc})}\end{aligned} \tag{A.14}$$

Using this result in Eq. A.7, and noting that for $\psi_i \gg 1$ it is possible to do the approximation $\frac{1}{1-e^{j2\pi\tilde{\psi}}} \approx 1$, eventually gives for the steady state voltage

$$\tilde{V}_{SST}(\theta) = R_L \tilde{I}_0 \frac{\omega_{1/2}}{\tilde{\omega}_0 + \Delta\omega_{osc}\sin(\theta+\theta_{osc})} \tag{A.15}$$

The result of Eq. (A.15) is equivalent to the solution for a static detuning, see Eq. (2.11), where the initial detuning is replaced by the sum of the initial detuning and the dynamic detuning. This simple result is due to the fact that the variations of the detuning function are very slow compare to the electromagnetic time constant $\tau_{1/2}$, which means that the cavity voltage has always enough "time " to reach its static steady state value for all the values of the detuning. At the opposite, when the detuning is very fast so that $\psi_i \ll 1$, the voltage can not follow the rapid variations of the detuning function and an average effect occures. When ψ_i is small, all the term of the sum in Eq. (A.13) are small except for the term $n = 0$. In consequence, for $\psi_i \ll 1$ the voltage is approximately given by

$$\tilde{V}_{SST}(\theta) = R_L \tilde{I}_0 e^{-j\sigma\cos(\theta+\theta_{osc})} \tilde{P}_0(\sigma) \tag{A.16}$$

From Eq. (A.16) it concludes that for fast detuning the amplitude remains approximately constant through time and that the phase oscillate in quadrature with the detuning function.

In this section, an approximate solution for the voltage of a cavity under sinusoidal detuning was developed. An important parameter for this solution was found to be the ratio of the amplitude and frequency of the sinusoidal detuning function. The voltage solution contains parameters that depends on this factor, and calculations of these coefficients were done to cover most of the cases of interest. Particular cases, when the frequency of the detuning function is much smaller or much larger than the cavity half-bandwidth, were also presented. The analytical expression for the solution of the voltage can for example be of interest in the reconstruction of the cavity mechanical basis parameters as done in section 2.4.2, or in the investigation of the ponderomotive oscillation phenomenon.

A.4 Semi-analytical scheme to solve general cases of dynamic detuning

Other than for particular cases of dynamic detuning and RF current functions, the voltage integral formulation is not solvable analytically. Because the variations of the cavity frequency are slow, it is possible to efficiently treat the dynamic detuning in a semi-analytical manner. The basic idea is to approximate the continuous integration of Eq. (2.10) by a discrete summation over successive time intervals Δt where analytical results can be applied. Some situations where analytical solutions are obtainable are shown in Section 2.2.2. The simplest choice for a semi-analytical scheme is to consider the source current and the cavity frequency constant during a time interval. The dynamic detuning is then represented by a succession of frequency steps, between two steps the frequency and the current source are approximated as constant and the analytical solution of Eq. (2.11) is used for the calculation of the voltage envelope. The discrete version of this formula with a time interval Δt can be written as

$$\begin{aligned}\tilde{V}[t+\Delta t] &= \tilde{V}_{SF}[t+\Delta t] + \tilde{V}_I[t+\Delta t] \\ &= \tilde{V}[t]e^{j\tilde{\omega}[t+\frac{\Delta t}{2}]} + R_L\tilde{I}[t+\frac{\Delta t}{2}]\frac{j\omega_{1/2}}{\tilde{\omega}[t+\frac{\Delta t}{2}]}\{1-e^{j\tilde{\omega}[t+\frac{\Delta t}{2}]\Delta t}\}\end{aligned} \tag{A.17}$$

where to optimize the accuracy the values of the detuning and of the driving current are taken in the middle of the time interval $[t;\, t+\Delta t]$. When a frequency increment $\delta\omega$ is applied, the immediate voltage envelope variations are of the same order than $\frac{\delta\omega}{\omega_c}$. Since this ratio is very small compared to unity, the voltage envelope can be approximated as constant. In other words, the change of the cavity frequency has a negligible immediate effect on the voltage envelope $\tilde{V}$ and affects only its first derivative $\dot{\tilde{V}}$. It follows that the value of the voltage envelope at the end of a time interval constitutes the initial condition of the source free voltage for the next time interval. With the new values of the cavity frequency and of the initial source free voltage, the calculations for the following time interval can be performed. The process is repeated until the total period of time is covered. The basic representation of the semi-analytical method is illustrated in Fig. A.3. For each time interval, the voltage is obtained by summation of the source free voltage and of the driven voltage as in Eq. (A.17). The introduction of a numerical process raises a concern on the accuracy for the calculations. As an example a sinusoidal detuning case is considered and displayed in Fig. A.4. The voltage behavior is accurately represented even for rather large time interval. In conclusion, the semi-anlytical method offers a simple and flexible manner to calculate the voltage in any situation.

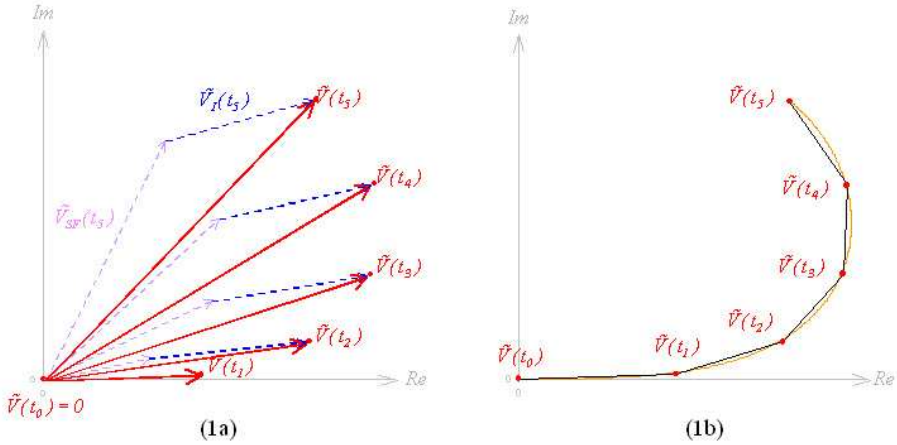

Figure A.3: Semi-analytic method. (a) The voltage is calculated analytically within a time interval by superposition of the source free voltage $\tilde{V}_{SF}$ and of the driven voltage $\tilde{V}_I$. (b) The discrete successive values of the voltage are showed over the continuous analytical solution line.

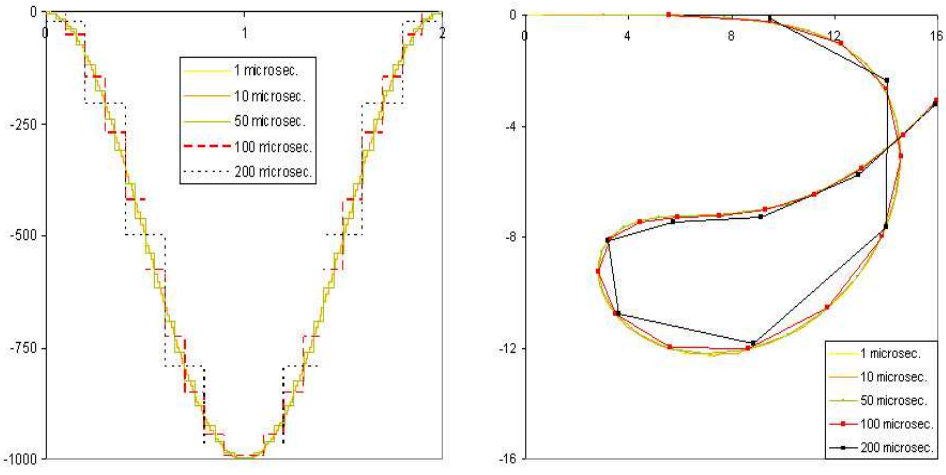

Figure A.4: Accuracy. (a) The continuous detuning function is discretized in a succession of detuning steps (time in ms for the horizontal axis, and detuning in Hz for the vertical axis) (b) Evolution in time of the voltage (Real and imaginary part, arbitrary unit)

A.5 Optimization of the Q_{ex} and of $\Delta\omega$ as a function of the cavity voltage and the beam current

In Section 2.2.3 the equation for the RF source current needed to maintain the voltage in steady state during the beam on period was given by

$$\tilde{I}_{RF} = -\frac{j\tilde{\omega}\tilde{V}}{R_L\omega_{1/2}} - \tilde{I}_b \tag{A.18}$$

Introducing the normalized detuning $\tilde{\rho} = \rho e^{j\phi_\rho} = \frac{\tilde{\omega}}{\omega_{1/2}} = \frac{\Delta\omega}{\omega_{1/2}} + j$, Eq. (2.17)gives

$$\tilde{I}_{RF} = -j\frac{\tilde{\rho}\tilde{V}}{R_L} - \tilde{I}_b \tag{A.19}$$

In the following the notations $\tilde{V} = Ve^{\phi_V}$, $\tilde{I}_b = I_b e^{\phi_b}$, and $\tilde{I}_{RF} = I_{RF}e^{\phi_{RF}}$ will be used. Dividing Eq. (A.19) by $-\tilde{I}_b$ and taking the modulus yields

$$\frac{I_{RF}}{I_b} = |1 + \frac{\rho V}{R_L I_b} e^{j\{-\frac{\pi}{2}+\phi_\rho+\Phi\}}| \tag{A.20}$$

where $\Phi = \pi + \phi_V - \phi_b$ is the chosen average accelerating phase for the beam. Introducing the shorthand dimensionless parameter $\nu_b = \frac{V}{R_L I_b}$ and taking the square of the Eq. (A.20) gives

$$\begin{aligned}\frac{I_{RF}^2}{I_b^2} =& \big\{1 + \nu_b\{\cos\Phi + \frac{\Delta\omega}{\omega_{1/2}}\sin\Phi\}\big\}^2 + \big\{\nu_b\{\sin\Phi - \frac{\Delta\omega}{\omega_{1/2}}\cos\Phi\}\big\}^2 \\ =& \{1 + \nu_b^2 + 2\nu_b\cos\Phi\} + \nu_b\frac{\Delta\omega}{\omega_{1/2}}\{2\sin\Phi + \nu_b\frac{\Delta\omega}{\omega_{1/2}}\}\end{aligned} \tag{A.21}$$

Minimizing the required RF power with respect to the value of the detuning is equivalent to searching for the value $\Delta\omega_{opt}$ that makes null the derivative of Eq. (A.21) with respect to $\Delta\omega$. It follows

$$\begin{aligned}\nu_b\{2\sin\Phi + \nu_b\frac{\Delta\omega_{opt}}{\omega_{1/2}}\} + \nu_b^2\frac{\Delta\omega_{opt}}{\omega_{1/2}} &= 0 \\ \Delta\omega_{opt} &= -\frac{\omega_{1/2}}{\nu_b}\sin\Phi\end{aligned}$$

Using $I_b = 2I_{b_0}$ and $R_L = \frac{1}{2}\frac{r}{Q}Q_L = \frac{1}{4}\frac{r}{Q}\frac{\omega}{\omega_{1/2}}$, the value of the detuning that minimizes the required RF power is

$$\Delta\omega_{opt} = -\frac{\omega}{2}\frac{\frac{r}{Q}I_{b_0}}{V}\sin\Phi \tag{A.22}$$

Eq. (A.22) gives the value for the detuning that minimizes the RF power in function of the cavity voltage and the beam current. This value is independent of the Q_{ex} of the

cavity. When the beam is accelerated with a null synchronous phase, it is optimal to set the cavity on resonance. However, if the synchronous phase is non null the cavity should be adequately detuned to minimize the required RF power. Assuming that Eq. (A.22) is satified, using it in Eq. (A.21), and recalling that $I_{RF} = \sqrt{\frac{8P_{RF}}{R_L}}$ leads to

$$P_{RF} = \frac{I_b^2}{8}\Big\{\{R_L + \frac{V^2}{R_L I_b^2} + 2\frac{V}{I_b}\cos\Phi\} - R_L\sin^2\Phi\Big\} \tag{A.23}$$

The value of the Q_{ex} that minimizes the required RF power makes the derivative of Eq. (A.23) with respect to R_L equal to zero, namely:

$$1 - \left\{\frac{V}{R_L I_b}\right\}^2 - \sin^2\Phi = 0$$

$$\cos^2\Phi = \left\{\frac{V}{R_L I_b}\right\}^2$$

It follows, assuming Φ between $-\frac{\pi}{2}$ and $\frac{\pi}{2}$

$$R_L = \frac{V}{I_b\cos\Phi} \tag{A.24}$$

Using $I_b = 2I_{b_0}$ and $R_L = \frac{1}{2}\frac{r}{Q}Q_L = \frac{1}{4}\frac{r}{Q}\frac{\omega}{\omega_{1/2}}$ it is possible to write the optimum value of Q_L as

$$Q_{L_{opt}} = \frac{V}{\frac{r}{Q}I_{b_0}\cos\Phi} \tag{A.25}$$

It should be mentioned that the value of Q_L is found independent of $\Delta\omega$ because it was assumed that the cavity detuning satisfied Eq. (A.22). If no such assumption was made, the optimum Q_L would depend on $\Delta\omega$. Using the results of Eq. (A.24) in Eq. (A.23) gives the minimum RF power $P_{RF_{opt}}$ required to maintain the cavity voltage in steady state when the beam is on

$$P_{RF_{opt}} = I_{b_0}V\cos\Phi = P_b \tag{A.26}$$

The result of Eq. (A.26) means that for optimum values of Q_L and $\Delta\omega$, the minimum required power is simply equal to the power extracted by the beam. The results of Eq. (A.26) can be used to find

$$\rho = \frac{1}{\cos\Phi} \qquad ; \qquad \phi_\rho = \Phi + \frac{\pi}{2} \tag{A.27}$$

These results will be used in the following.

A.6 Additional RF power for non optimized Q_{ex} and $\Delta\omega$

In Section A.5 it was shown that the power required to accelerate a beam can be minimized by choosing the appropriate external Q and detuning for the cavity. If

both of these parameters are not optimum, the required RF power is larger. Scaling of such power increases will be presented next. Coming back to Eq. (A.21) and using $I_{RF} = \sqrt{\frac{8P_{RF}}{R_L}}$ gives

$$P_{RF} = \frac{1}{8} R_L I_b^2 \{1 + \nu_b^2 + 2\nu_b \cos\Phi\} + \nu_b \frac{\Delta\omega}{\omega_{1/2}} \{2\sin\Phi + \nu_b \frac{\Delta\omega}{\omega_{1/2}}\} \tag{A.28}$$

but writing $\Delta\omega = \Delta\omega_{opt} + \delta\omega$ it follows

$$\begin{aligned}
\nu_b \frac{\Delta\omega}{\omega_{1/2}} \{2\sin\Phi + \nu_b \frac{\Delta\omega}{\omega_{1/2}}\} &= -\sin\Phi \frac{\Delta\omega}{\Delta\omega_{opt}} \{2\sin\Phi - \sin\Phi \frac{\Delta\omega}{\Delta\omega_{opt}}\} \\
&= -\sin^2\Phi \frac{\Delta\omega}{\Delta\omega_{opt}} \{2 - \frac{\Delta\omega}{\Delta\omega_{opt}}\} \\
&= -\sin^2\Phi \{1 + \frac{\delta\omega}{\Delta\omega_{opt}}\}\{1 - \frac{\delta\omega}{\Delta\omega_{opt}}\} \\
&= -\sin^2\Phi \{1 - \{\frac{\delta\omega}{\Delta\omega_{opt}}\}^2\}
\end{aligned}$$

using $R_L = R_{L_{opt}} + \delta R_L$, $Q_L = Q_{L_{opt}} + \delta Q_L$, and $q = \frac{\delta R_L}{R_{L_{opt}}} = \frac{\delta Q_L}{Q_{L_{opt}}}$ leads to

$$\nu_b = \frac{V}{R_L I_b} = \frac{V}{R_{L_{opt}} I_b} \frac{1}{1+q} = \cos\Phi \{1 - \frac{q}{1+q}\}$$

Using these results in Eq. (A.28) and writing $\varepsilon = \frac{\delta\omega}{\omega_{1/2_{opt}}}$ gives

$$\begin{aligned}
P_{RF} =& \frac{1}{8} R_L I_b^2 \{1 + \cos^2\Phi \{1 - \frac{q}{1+q}\}^2 + 2\cos^2\Phi \{1 - \frac{q}{1+q}\} - \sin^2\Phi + \sin^2 \{\frac{\delta\omega}{\Delta\omega_{opt}}\}^2\} \\
=& \frac{1}{2} R_L I_b^2 \cos^2\Phi \{1 - \frac{q}{1+q} + \frac{1}{4}\{\frac{q}{1+q}\}^2 + \frac{1}{4}\tan^2\Phi \{\frac{\delta\omega}{\Delta\omega_{opt}}\}^2\} \\
=& \frac{1}{2} R_{L_{opt}} I_b^2 \cos^2\Phi \{1+q\}\{1 - \frac{q}{1+q} + \frac{1}{4}\{\frac{q}{1+q}\}^2 + \frac{1}{4}\varepsilon^2\} \\
=& P_b + P_b\{\{-\frac{q}{1+q} + \frac{1}{4}\{\frac{q}{1+q}\}^2 + \frac{1}{4}\varepsilon^2\} + q\{\frac{1}{1+q} + \frac{1}{4}\{\frac{q}{1+q}\}^2 + \frac{1}{4}\varepsilon^2\}\} \\
=& P_b + P_b \frac{1}{4}\left\{\frac{q^2}{1+q} + \{1+q\}\varepsilon\right\}
\end{aligned}$$

Noting that $\delta P_{RF} = P_{RF} - P_b$ we get:

$$\frac{\delta P_{RF}}{P_b} = \frac{1}{4}\left\{\frac{q^2}{1+q} + \{1+q\}\varepsilon\right\} \tag{A.29}$$

Eq.(A.29) expresses the necessary additional RF power required for non optimum external Q and detuning. It is possible to plot the result in a 3D plot as in Fig. A.5. As done in Section 2.2.3, the result of Eq. (A.29) is usefull to determin some tolerable limits for the Q_{ex} and for the detuning of the cavity, when the available

RF power is known. An efficient way to spot a region in the parameter space $\{\varepsilon, q\}$ that corresponds to a given additional amount of RF power is to use contour plot as displayed in Fig. A.6. In this illustration, the parameter region corresponding to an additional RF power lower than 100 percent of the minimum required RF power is identified. In practical cases, the available additional RF power is known and the previous contour plot technique can be used to determin the acceptable region for the external Q and the detuning. Several examples are presented in section 2.2.3 based on the SNS SC cavities parameters.

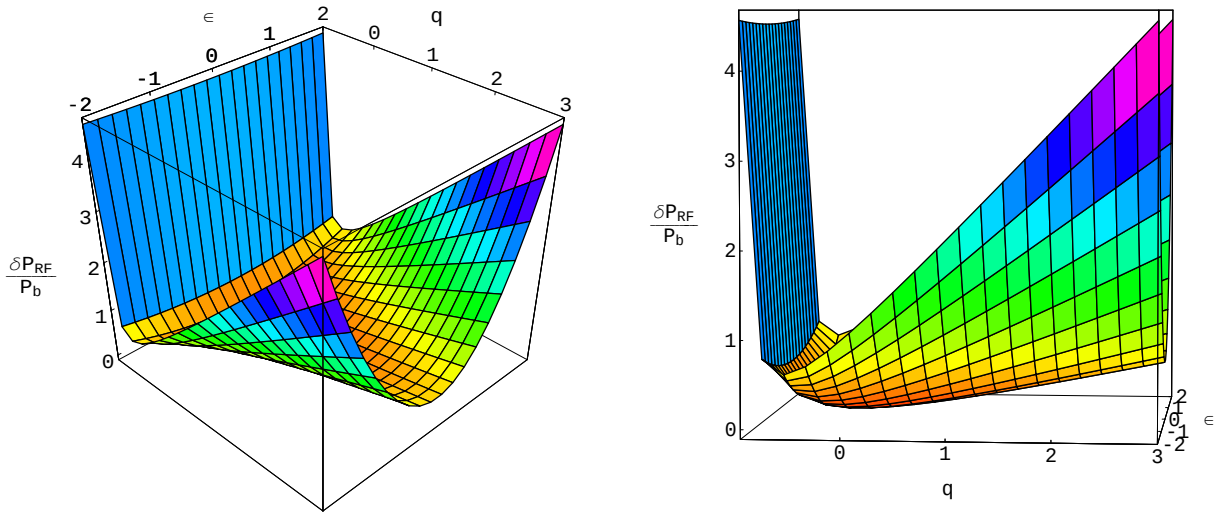

Figure A.5: Required additional RF power for non optimum external Q and detuning. The plotted variables are $\frac{\delta P_{RF}}{P_b}$, $q = \frac{\delta Q_L}{Q_{L_{opt}}}$, and $\varepsilon = \frac{\delta\omega}{\omega_{1/2_{opt}}}$.

A.7 Solution to the wave equation

In section 2.3.1, the modeling for the cavity vibration was approached using a simple vibrating string. To solve the string problem requires to solve the traditional wave equation written in Eq. (2.29). The solution process is presented in this section. Considering first the homogeneous part of Eq. (2.29) and searching its solution under the separable form $u(x,t) = \alpha(x)\beta(t)$ leads to

$$\alpha(x)\ddot{\beta}(t) + a\alpha(x)\dot{\beta}(t) - c^2\ddot{\alpha}(x)\beta(t) = 0$$

Dividing by $\alpha\beta$ and separating the time and spatial components gives

$$\frac{\ddot{\beta} + a\dot{\beta}}{\beta} = \frac{c^2\ddot{\alpha}}{\alpha} \tag{A.30}$$

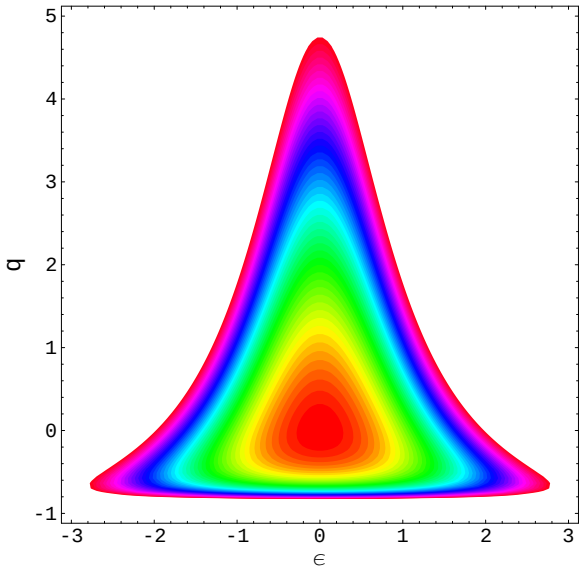

Figure A.6: Example of a contour plot showing the parameter region corresponding to an additional RF power smaller than 100 percent of the minimum required RF power.

To satisfy this equation requires that the left and the right side functions be equal to the same constant, noted $-\Omega^2$. The Eq. (A.30) is then equivalent to a system of two homogeneous ordinary differential equations

$$\begin{cases} \ddot{\alpha} + K^2\alpha = 0 \\ \ddot{\beta} + \frac{\Omega}{Q}\dot{\beta} + \Omega^2\beta = 0 \end{cases} \tag{A.31}$$

where $K = \frac{\Omega}{c}$ and where, for convenience, the damping parameter is introduced with $a = \frac{\Omega}{Q}$. The general solution of the spatial equation is

$$\alpha(x) = A\cos(Kx) + B\sin(Kx)$$

Using the boundary conditions for the string leads to the appearance of spatial modes satisfying

$$\alpha_n(x) = B\sin(K_n x) \tag{A.32}$$

with the conditions $K_n = n\frac{\pi}{l}$ and n is an integer. For each value of K_n corresponds a pulsation $\Omega_n = K_n c$. Using this relation in Eq. (A.31) it is possible to write the solution of the time differential equation as

$$\beta_n(t) = e^{-\eta\Omega_n t}\{C_n\cos(\mu\Omega_n t) + D_n\sin(\mu\Omega_n t)\} \tag{A.33}$$

with the parameters $\mu = \frac{1}{2Q}$ and $\mu = \sqrt{1-\eta^2}$, and where the coefficients C_n and D_n depend on the initial conditions of the transverse displacement. The total displacement is given by summation over the modes

$$u(x,t) = \sum_n u_n(x,t) = \sum_n \alpha_n(x)\beta_n(t) \tag{A.34}$$

Since the solution of the homogeneous part of the Eq. (2.29) can be decomposed on a spatial modal basis, it is of interest to decompose the driving force on such a basis.

$$g(x)h(t) = \sum_n v_n(t)\sin(K_n x) \tag{A.35}$$

The contribution of the driving force to a particular spatial mode can be found by projecting both sides of Eq. (A.35) onto a vector of the spatial modal basis

$$\int_0^l g(x)h(t)\sin(K_m y)\,dy = \sum_n \int_0^l \sin(K_n y)\sin(K_m y)\,dy$$

using the orthogonality property of the spatial modal basis $\int_0^l \sin(K_n)\sin(K_m)\,dy = \frac{\delta(K_m - K_n)}{2}$ leads for the time dependent coefficient to

$$\begin{aligned} v_m(t) &= h(t)\frac{2}{l}\int_0^l g(x)\sin(K_m y)\,dy \\ &= w_m h(t) \end{aligned} \tag{A.36}$$

The parameter w_m can be understood as the projection of the driving force on the m^{th} vector of the spatial basis. Assuming that the solution of the inhomogeneous equation has a form decomposable on the spatial basis,

$$u(x,t) = \sum_m U_m(t)\sin(K_m x) \tag{A.37}$$

and replacing in Eq. (2.29) leads to

$$\ddot{U_m} + \frac{\Omega_m}{Q}\dot{U_m} + \Omega_m^2 U_m = w_m h(t) \tag{A.38}$$

Eq. (A.37) is an ordinary inhomogeneous second order equation that can be solved using the superposition principle as shown in Section A.8. To obtain the solution for the total transverse displacement of the vibrating string, the solution to Eq. (A.38) can be inserted in Eq. (A.37). The wave equation for the transverse displacement is solved and the result is usable for the estimation of the detuning.

A.8 Solution of an ordinary second order differential equation

Considering the a system representable by an ordinary second order differential equation

$$\ddot{x}(t) + \frac{\omega}{Q}\dot{x}(t) + \omega^2 x(t) = \omega^2 f(t) \tag{A.39}$$

The homogeneous part of Eq. (A.39) has for general solution

$$x = x_1 e^{j\tilde{\omega}_1 t} + x_2 e^{-j\tilde{\omega}_1^* t} \tag{A.40}$$

with $\eta = \frac{1}{2Q}$, $\mu = \sqrt{1-\eta^2}$, and $\tilde{\omega}_1 = \omega(\mu + j\eta)$. The two coefficients x_1 and x_2 are obtained from the initial conditions $x(0)$ and $\dot{x}(0)$. To solve the inhomogeneous part of Eq. (A.39) the principle of superposition can be applied. First it is possible to consider a driving function $\omega^2 f$ only applied for a infinitesimal amount of time dt. When the driving force is applied, the second derivative takes the value $\ddot{x} = f$. Using the definition of the second derivative it is possible to write that after dt, the first derivative has changed by an amount

$$d\dot{x} = \omega^2 f dt \tag{A.41}$$

The change of x is of second order and can therefore be neglected. Since the driving was only an impulse, the system is now undriven and its behavior is given by the homogeneous part of Eq. (A.39). The initial conditions are given by

$$\begin{cases} x(dt) = 0 \\ \dot{x}(dt) = \omega^2 f dt \end{cases} \tag{A.42}$$

The solution of the homogeneous equation is written in Eq. (A.40). The initial conditions of Eq. (A.42) leads for the coefficients to

$$\begin{cases} x_1 = \frac{\omega f}{2j\mu} dt \\ x_2 = -x_1 \end{cases}$$

The solution for this driving impulse is

$$x = \frac{\omega f}{2j\mu} \left\{ e^{j\tilde{\omega}_1 t} - e^{-j\tilde{\omega}_1^* t} \right\} \tag{A.43}$$

Coming back to the initial problem, the driving function f can be seen as a succession of impulses. The superposition principle can be applied and the particular solution to Eq. (A.39) is given by the convolution integral

$$x = \int_0^t \frac{\omega f(t')}{2j\mu} \left\{ e^{j\tilde{\omega}_1 \{t-t'\}} - e^{-j\tilde{\omega}_1^* \{t-t'\}} \right\} dt' \tag{A.44}$$

The general solution is now obtained by summing the results of Eq. (A.40) and Eq. (A.44)

$$x = x_1 e^{j\tilde{\omega}_1 t} + x_2 e^{-j\tilde{\omega}_1^* t} + \int_0^t \frac{\omega f(t')}{2j\mu} \left\{ e^{j\tilde{\omega}_1 \{t-t'\}} - e^{-j\tilde{\omega}_1^* \{t-t'\}} \right\} dt' \tag{A.45}$$

where x_1 and x_2 are related to the initial conditions by

$$\begin{aligned} x_1 &= \frac{1}{2} \left\{ \frac{-j}{\mu} \left\{ \frac{\dot{x}(0)}{\omega} + \eta x(0) \right\} + x(0) \right\} \\ x_2 &= \frac{1}{2} \left\{ \frac{j}{\mu} \left\{ \frac{\dot{x}(0)}{\omega} + \eta x(0) \right\} + x(0) \right\} \end{aligned} \tag{A.46}$$

Another possible manner to write Eq. (A.45) is

$$\begin{aligned} x = e^{-\eta\omega t}\big\{x(0)\cos(\mu\omega t) + \frac{1}{\mu\omega}\{\dot{x}(0) + \eta\omega x(0)\}\sin(\mu\omega t)\big\} \\ + \frac{\omega}{\mu}\int_0^t f(t')e^{-\eta\omega\{t-t'\}}\sin(\mu\omega\{t-t'\})\,dt' \end{aligned} \tag{A.47}$$

A.8.1 Solution for a constant forcing $f(t) = f_0$

Considering null input conditions so that $x_1 = x_2 = 0$ and introducing the function $f(t) = f_0$ in Eq. (A.45) gives

$$\begin{aligned} x &= \frac{\omega f_0}{2j\mu}\int_0^t \big\{e^{j\tilde{\omega}_1\{t-t'\}} - e^{-j\tilde{\omega}_1^*\{t-t'\}}\big\}\,dt' \\ &= \frac{\omega f_0}{2j\mu}\Big\{\frac{j}{\tilde{\omega}_1}\big\{1 - e^{j\tilde{\omega}_1 t}\big\} + \frac{j}{\tilde{\omega}_1^*}\big\{1 - e^{-j\tilde{\omega}_1^* t}\big\}\Big\} \end{aligned}$$

Noting $\tilde{\omega}_1 = |\tilde{\omega}_1|e^{j\Phi_1} = \omega e^{j\Phi_1}$ it follows

$$\begin{aligned} x &= \frac{\omega f_0}{2\mu}\Big\{\frac{2\cos\Phi_1}{\omega} - \frac{1}{\omega}\big\{e^{j\tilde{\omega}_1 t - \Phi_1} + e^{-j\tilde{\omega}_1^* t + \Phi_1}\big\}\Big\} \\ &= \frac{\omega f_0}{2\mu}\Big\{\frac{2\mu}{\omega} - \frac{e^{-\eta\omega t}}{\omega}\big\{e^{j\mu\omega t - \Phi_1} + e^{-j\mu\omega t + \Phi_1}\big\}\Big\} \end{aligned}$$

Finally it leads to

$$x = f_0\Big\{1 - \frac{1}{\mu}e^{-\eta\omega t}\cos(\mu\omega t - \Phi_1)\Big\} \tag{A.48}$$

In the steady state this quantity will be equal to $x_{SST} = f_0$.

A.8.2 Solution for a complex exponential forcing $f(t) = f_0 e^{j\tilde{\omega}_0 t}$

With null input conditions so that $x_1 = x_2 = 0$ and the driving function $f(t) = f_0 e^{j\tilde{\omega}_0 t}$, Eq. (A.45) becomes

$$\begin{aligned} x &= \frac{\omega f_0}{2j\mu}\int_0^t \big\{e^{j\tilde{\omega}_1 t}e^{j\{\tilde{\omega}_0 - \tilde{\omega}_1\}t'} - e^{-j\tilde{\omega}_1^* t}e^{j\{\tilde{\omega}_0 + \tilde{\omega}_1^*\}t'}\big\}\,dt' \\ &= \frac{\omega f_0}{2j\mu}\Big\{\frac{-j}{\tilde{\omega}_0 - \tilde{\omega}_1}\{e^{j\tilde{\omega}_0 t} - e^{j\tilde{\omega}_1 t}\} + \frac{j}{\tilde{\omega}_0 + \tilde{\omega}_1^*}\{e^{j\tilde{\omega}_0 t} - e^{-j\tilde{\omega}_1^* t}\}\Big\} \end{aligned}$$

Rearranging it gives

$$x = -\frac{\omega f_0}{2\mu}\Big\{e^{j\tilde{\omega}_0 t}\big\{\frac{1}{\tilde{\omega}_0 - \tilde{\omega}_1} - \frac{1}{\tilde{\omega}_0 + \tilde{\omega}_1^*}\big\} - \frac{e^{j\tilde{\omega}_1 t}}{\tilde{\omega}_0 - \tilde{\omega}_1} + \frac{e^{-j\tilde{\omega}_1^* t}}{\tilde{\omega}_0 + \tilde{\omega}_1^*}\Big\} \tag{A.49}$$

In the case where $\tilde{\omega}_0$ is real, the forcing function has a constant amplitude equal to f_0 and in the steady state, Eq. (A.49) leads to

$$x_{SST} = f_0 Q\frac{\omega}{\omega_0}\frac{e^{j\psi}}{\sqrt{1+\tan^2\psi}}e^{j\{\omega_0 t - \frac{\pi}{2}\}} \tag{A.50}$$

with $\tan\psi = Q(\frac{\omega}{\omega_0} - \frac{\omega_0}{\omega})$. On resonance $\omega_0 = \omega$ and from Eq. (A.50), $x_{SST} = f_0 Q$. Some typical behaviors for the amplitude of x and for the phase ψ as a function of the ratio $\frac{\omega_0}{\omega}$ are plotted in Fig. A.7, for a few values of the damping parameter Q.

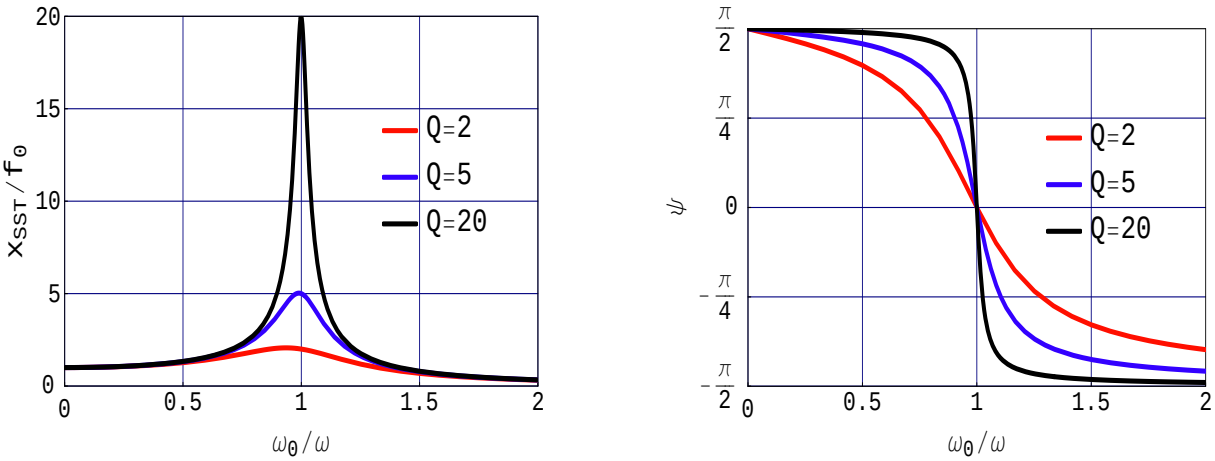

Figure A.7: Amplitude and phase of a driven oscillator, in function of the frequency ratio $\frac{\omega_0}{\omega}$, in the case of $\tilde{\omega_0}$ real.

A.9 Cavity in phase locked operation

When a SC cavity is dynamically detuned, its matching to the RF is varying. It was seen in Section 2.2 that to ensure the development of the voltage and its stability, the RF source ratings had to be controled or the dynamic detuning had to be actively compensated. A possible way to fill a cavity under dynamic detuning is the phase locked loop configuration [38]. A phase locked loop is a feedback loop designed to keep the phase between the RF source and the cavity voltage at a given constant value. The filling pattern of a cavity is determined by the setting of this phase and is independent of the dynamic variation of the cavity frequency. This can simply be proven by first writing the complex voltage envelope $\tilde{V}$ and the complex driving current $\tilde{I}$ as real amplitudes time complex exponentials where both are possibly varying in time: $\tilde{V} = Ve^{j\Phi_{\tilde{V}}}$ and $\tilde{I} = Ie^{j\Phi_{\tilde{I}}}$. Differentiating the relation for the voltage gives $\dot{\tilde{V}} = \{\dot{V} + j\dot{\Phi}_{\tilde{V}}V\}e^{j\Phi_{\tilde{V}}}$. Introducing these equations in Eq. (2.5) leads to

$$\dot{V} + j\{\dot{\Phi}_{\tilde{V}} - \tilde{\omega}\}V = \omega_{1/2}R_L I e^{j\{\Phi_{\tilde{I}} - \Phi_{\tilde{V}}\}} \tag{A.51}$$

Coming back to the definition of the complex frequency $\tilde{\omega} = \Delta\omega + j\omega_{1/2}$ and separating the real part from the imaginary part in Eq. (A.51) give the system of coupled differential equations

$$\begin{cases} \dot{V} + \omega_{1/2}V = \omega_{1/2}R_L I\cos(\Phi_{\tilde{I}} - \Phi_{\tilde{V}}) \\ \{\dot{\Phi}_{\tilde{V}} - \Delta\omega\}V = \omega_{1/2}R_L I\sin(\Phi_{\tilde{I}} - \Phi_{\tilde{V}}) \end{cases} \tag{A.52}$$

In the case of a phase locked loop, the phase difference between the RF current source and the cavity voltage is kept constant through time, and it is interesting to define a phase loop parameter $\theta_l = \Phi_{\tilde{I}} - \Phi_{\tilde{V}}$. From Eq. (A.52) it is possible to find the solution for the voltage amplitude and for the voltage phase

$$\begin{cases} V(t) = V_0 e^{-\omega_{1/2} t} + \omega_{1/2} R_L \cos\theta_l \int_0^t I(t') e^{-\omega_{1/2}\{t-t'\}}\, dt' \\ \dot{\Phi}_V(t) = \Delta\omega(t) + \frac{\omega_{1/2} R_L I(t) \sin\theta_l}{V(t)} \end{cases} \tag{A.53}$$

The time dependences are explicitely written and as mentioned before, the voltage amplitude is independent of the detuning. As a consequence the complexity of the coupled system of the voltage differential equations and the mechanical differential equations is greatly reduced. Another interesting fact is that the voltage amplitude development profile depends only of the RF current function. For example, in the case of a constant RF current, $I(t) = I_0$, and an initially null voltage

$$V(t) = R_L I_0 \cos\theta_l \{1 - e^{-\omega_{1/2} t}\}$$

The value of the phase loop parameter θ_l plays the role of a simple coefficient as displayed in Fig. A.9. In the particular case where the phase loop is set to zero, $\theta_l = 0$, Eq. (A.53) simplifies to

$$\begin{cases} V(t) = V_0 e^{-\omega_{1/2} t} + \omega_{1/2} R_L \int_0^t I(t') e^{-\omega_{1/2}\{t-t'\}}\, dt' \\ \dot{\Phi}_V(t) = \Delta\omega(t) \end{cases} \tag{A.54}$$

Thus, when $\theta_l = 0$, the value of the detuning can simply and straightforwardly be derived from the measurement of the voltage phase. If the phase loop is not equal to zero, some parasitic signal can appear in the measurements of the detuning, see Section A.9.1, and the detuning is not strictly equal to the derivative of the voltage phase anymore.

A.9.1 Parasitic measurement for a non zero phase loop

Assuming the phase between the RF current source and the cavity voltage exactly equal to zero is a rather ideal case, particularly during the RF turn on transient. In practice this phase can have some small value. From Eq.(A.53) it is possible to write

$$\dot{\Phi}_V(t) = \Delta\omega(t) + \frac{\omega_{1/2} R_L I(t) \sin\theta_l}{V(t)} \tag{A.55}$$

When the phase loop is equal to zero, the derivative of the voltage phase is exactly equal to the detuning. In this case, it is possible to obtain the value of the detuning from the cavity voltage signal. But when the phase loop is not equal to zero, the second term of the rigth side of Eq. (A.55) is a parasitic signal that can be large, when the RF source is on, particularly if the voltage is small like during the RF turn on transient. To illustrate the possible effect of such term in a measurement, a case is simulated for a pulsed current and a sinusoidal dynamic detuning function. The current is supposed to raise quickly from zero to a constant value, the phase loop is

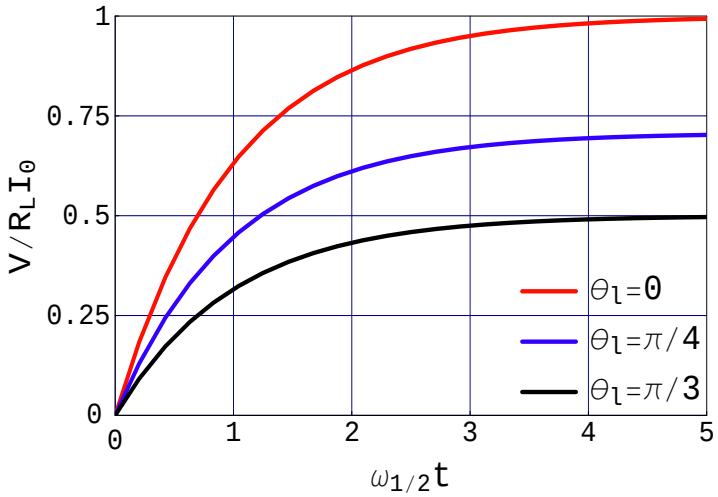

Figure A.8: In a phase locked loop, the voltage amplitude development profile depends on the current function, the phase loop parameter θ_l only acts as a global multiplication coefficient.

supposed to raise from zero to 2 degrees at the beginning of the pulse. The voltage development and result for Eq. (A.55) is displayed in Fig. A.9. In Fig. A.9, the real detuning funtion is also plotted in dashed line. As expected, the parasitic term is strong at the transient, and a discrepancy between the real detuning value and the derivative of the voltage phase is observable when the voltage is small. Such a parasitic signal can be observed in the measured Lorentz detuning profile displayed in Section 2.5.

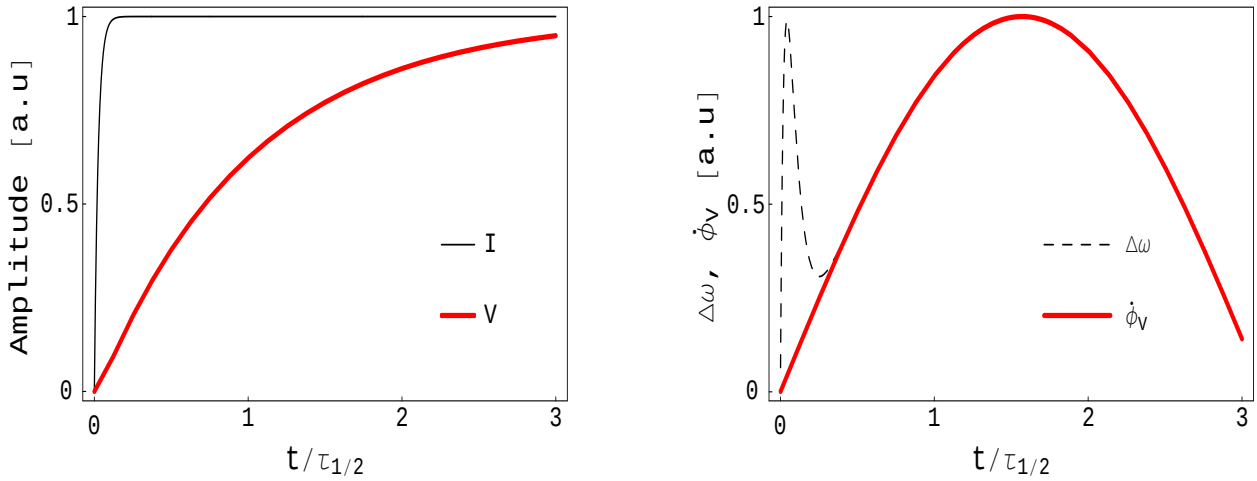

Figure A.9: Simulated effect of the parasitic term of Eq. (A.55) for a non null phase loop. In the transient region, when the voltage is small, $\dot{\Phi}_V$ is non equal to $\Delta\omega$.

A.9.2 Small modulation of the RF current source in CW operation

To generate the transfer function associated with the radiation pressure action, the cavity can be driven in CW with a constant forwarded power having small RF modulations. Considering an initially empty cavity, driven in a phase locked loop by a source current of the form

$$I(t) = I_0\{1 + \epsilon \sin(\omega_{mod} t)\} \tag{A.56}$$

where ϵ is a small parameter and ω_{mod} the frequency of the modulations, gives using Eq. (A.53)

$$\begin{aligned} V(t) &= \omega_{1/2} R_L I_0 \cos\theta_l \int_0^t \{1 + \epsilon \sin(\omega_{mod} t')\} e^{-\omega_{1/2}\{t-t'\}}\, dt' \\ &= \omega_{1/2} R_L I_0 \cos\theta_l \Big\{ \frac{1}{\omega_{1/2}} \{1 - e^{-\omega_{1/2} t}\} + \frac{\epsilon}{\omega_{mod}^2 + \omega_{1/2}^2} \big\{ \omega_{mod} e^{-\omega_{1/2} t} \\ &\qquad - \omega_{mod} \cos(\omega_{mod} t) + \omega_{1/2} \sin(\omega_{mod} t) \big\} \Big\} \end{aligned}$$

In the steady state, the voltage will be equal to

$$V_{SST}(t) = R_L I_0 \cos\theta_l \{1 + \epsilon \cos\phi_{mod} \sin(\omega_{mod} t + \phi_{mod})\} \tag{A.57}$$

where $\tan\phi_{mod} = \frac{-\omega_{mod}}{\omega_{1/2}}$. Basically, the modulations of the source current induce sinusoidal modulations of the voltage, in phase for low modulation frequencies compared to the electromagnetic bandwidth, and in quadrature for high modulation frequencies. As shown in section A.3 for very fast modulations of the cavity resonant frequency, very fast modulations of the RF current have a negligible impact on the voltage (the term $\cos\phi_{mod}$ becomes very small when $\omega_{mod} \gg \omega_{1/2}$). Taking the square of the voltage, neglecting the term of second order in ϵ, and noting the static part of the voltage associated with the value of the phase loop as $V_l = R_L I_0 \cos\theta_l$ gives

$$V_{SST}^2(t) \approx V_l^2 \{1 + 2\epsilon \cos\phi_{mod} \sin(\omega_{mod} t + \phi_{mod})\} \tag{A.58}$$

Inserting this result in the Eq. (2.36) and using the results of Eq. (A.50) leads to the steady state value of the detuning for the m^{th} mechanical mode

$$\Delta\omega_{m,SST}(t) = -k_m V_l^2 \{1 + 2\epsilon \cos\phi_{mod} Q_m \frac{\Omega_m}{\omega_{mod}} \frac{\sin(\omega_{mod} t + \phi_{mod} + \psi_m - \frac{\pi}{2})}{\sqrt{1 + \tan^2\psi_m}}\} \tag{A.59}$$

where $\tan\psi_m = Q_m(\frac{\omega_m}{\omega_{mod}} - \frac{\omega_{mod}}{\omega_m})$. This result is used in section 2.4.1 for the reconstruction of the mechanical basis parameters associated with the radiation pressure action.

Appendix B

Longitudinal dynamics in SRF cavities: Annex

B.1 Drift-gap-drift representation for symmetric field

For an element having a symmetric electric field profile, it is of interest to perform the change of variable $u = s - z_{gc} = s - z_s - \frac{L}{2}$ in Eq. (3.8). Doing so, the starting of the element is changed from z_s to $u_s = -\frac{L}{2}$, the middle of the element from z_{gc} to $u_{gc} = 0$, and the end of the element from z_e to $u_e = \frac{L}{2}$. The electric field function is conveniently written $E_u(u) = E_z(u - z_{gc})$. Using the geometrical center of the gap $u_{gc} = 0$ as the longitudinal reference for the calculations of T and S leads to

$$\begin{aligned} T_{u_{gc}}(k_{z_s}) =& \frac{1}{E_0 L} \int_{-\frac{L}{2}}^{\frac{L}{2}} E_u(u) \cos(k_{z_s} u)\, du \\ S_{u_{gc}}(k_{z_s}) =& \frac{1}{E_0 L} \int_{-\frac{L}{2}}^{\frac{L}{2}} E_u(u) \sin(k_{z_s} u)\, du \end{aligned} \tag{B.1}$$

For a symmetrical field $E_u(-u) = E_u(u)$, the integral S is null, and the geometrical center is the electrical center for any beta of the particle. For an antisymmetric field $E_u(-u) = -E_u(u)$ the integral T is null. Using Eq. (3.8) it follows that the phase at the geometrical center is in quadrature compare to the average phase, $\phi_{u_{gc}} = \Phi + \frac{\pi}{2}$. In this case it is possible to redefine the average phase by doing the transformation $\Phi + \frac{\pi}{2} \rightarrow \Phi$. With this change of variable, the energy gain is maximum when the average phase is equal to $\frac{\pi}{2}$. The energy gain and the average phase for a symmetric or antisymmetric field are given by

$$\begin{aligned} &\begin{cases} \Delta W(z) &= q E_0 L\, T_{u_{gc}}(k_{z_s}) \cos\Phi \\ \Phi &= \phi_{u_{gc}} \end{cases} \\ &\begin{cases} \Delta W(z) &= q E_0 L\, S_{u_{gc}}(k_{z_s}) \sin\Phi \\ \Phi &= \phi_{u_{gc}} \end{cases} \end{aligned} \tag{B.2}$$

The energy gain has been calculated under the approximation of a linear phase law. This result can be inserted in the expression of the phase in Eq. (3.3). From this equation, the phase of flight can be separated in a sum of a linear component and a non-linear component $\Delta\phi = \Delta\phi_l + \Delta\phi_{NL}$. The linear part is simply $\Delta\phi_l(z) = k_{z_s}\{z - z_s\}$ and the non linear part, linked to the variation of the particle's energy, is written

$$\begin{aligned}\Delta\phi_{NL}(z_e) =& \int_{z_s}^{z_e} \Delta k(z)\, dz \\ \approx& d_\gamma k|_{z_s} \int_{z_s}^{z_e} \Delta\gamma(z)\, dz\end{aligned} \tag{B.3}$$

where the expansion of the variation of k wih respect to the variation of γ has been truncated to the first order. This is a valid approximation only if the variations of the particle's beta are small compare to its entrance value β_{z_s}. The function $\Delta\gamma$ is obtained from Eq. (3.3)

$$\Delta\gamma(z) = \frac{q}{W_0} \int_{z_s}^{z} E_z(s) \cos(\phi_{z_s} + k_{z_s}\{s - z_s\})\, ds \tag{B.4}$$

If the field is symmetric with respect to its geometric center, the change of variables $z \to x = z - z_{gc} = z - z_s - \frac{L}{2}$, respectively $s \to u = s - z_{gc} = s - z_s - \frac{L}{2}$ are made for convenience in Eq. (B.3), respectively Eq. (B.4). It gives

$$\begin{aligned}\Delta\phi_{NL}(z_e) =& d_\gamma k|_{z_s} \int_{-\frac{L}{2}}^{\frac{L}{2}} \Delta\gamma(x + z_s + \frac{L}{2})\, dx \\ \Delta\gamma(x + z_s + \frac{L}{2}) =& \frac{q}{W_0} \int_{-\frac{L}{2}}^{x} E_u(u) \cos(\phi_{z_s} + k_{z_s}\frac{L}{2} + k_{z_s}u)\, du\end{aligned} \tag{B.5}$$

where the function E_u was defined previously. The first integral of Eq. (B.5) can be solved by part.

$$\begin{aligned}\Delta\phi_{NL}(z_e) =& d_\gamma k|_{z_s} \left\{ \left[x\Delta\gamma(x + z_s + \frac{L}{2}) \right]_{-\frac{L}{2}}^{\frac{L}{2}} - \int_{-\frac{L}{2}}^{\frac{L}{2}} x\Delta\gamma'(x + z_s + \frac{L}{2})\, dx \right\} \\ =& d_\gamma k|_{z_s} \left\{ \frac{L}{2}\Delta\gamma(z_e) - \frac{q}{W_0} \int_{-\frac{L}{2}}^{\frac{L}{2}} xE_u(x) \cos(\phi_{z_s} + k_{zs}\frac{L}{2} + k_{z_s}x)\, dx \right\} \\ =& d_\gamma k|_{z_s} \left\{ \frac{L}{2}\Delta\gamma(z_e) + \frac{q}{W_0} \sin(\phi_{z_s} + k_{zs}\frac{L}{2}) \int_{-\frac{L}{2}}^{\frac{L}{2}} xE_u(x) \sin(k_{z_s}x)\, dx \right\} \\ =& d_\gamma k|_{z_s} \left\{ \frac{L}{2}\Delta\gamma(z_e) - \frac{q}{W_0} E_0 L T'_{u_{gc}}(k_{z_s}) \sin\Phi \right\}\end{aligned} \tag{B.6}$$

where from Eq. (B.1) it was obatined that $T'_{u_{gc}}(k_{z_s}) = -\frac{1}{E_0 L} \int_{-\frac{L}{2}}^{\frac{L}{2}} xE_u(x) \sin(k_{z_s}x)\, dx$, and using the fact that for a symmetric field, the average phase is equal to the physical

phase at the geometrical center $\Phi = \phi_{z_s} + k_{z_s}\frac{L}{2}$. From Eq. (3.3), Eq. (B.2) and Eq. (B.6), it is possible to write the energy gain and the phase of flight for an accelerating element having a symmetrical field.

$$\begin{aligned} \Delta W(z_e) &= qE_0 L\, T(k_{z_s}) \cos\Phi \\ \phi(z_e) &= d_\gamma k|_{z_s} \left\{ \frac{L}{2}\Delta\gamma(z_e) - \frac{q}{W_0} E_0 L T'(k_{z_s}) \sin\Phi \right\} + \phi_{z_s} + k_{z_s}\{z_e - z_s\} \end{aligned} \tag{B.7}$$

where for convenience it is here implied that $T(k) = T_{u_{gc}}(k)$. These longitudinal transformations give the energy gain and the phase of flight for the entire accelerating gap. Using the idea of Lapostolle [45], the element can conveniently be redefined as a succession of three elements. A drift space from the longitudinal entrance z_s to the middle of the gap z_{gc}, an infinitesimal gap where kicks in energy and phase are applied, and a second drift space from the middle to the end of the element z_e. The total energy gain and phase of flight are given by summation over the three consecutive transformations. During the drifts, the energy of a particle is unchanged and its phase of flight linear. If the kick in energy of Eq. (B.7) is applied at the middle of the element, the phase of flight in the drift-gap-drift representation is given by

$$\begin{aligned} \phi(z_e) &= \phi_{z_s} + \Delta\phi_{drift1} + \Delta\phi_{gap} + \Delta\phi_{drift2} \\ &= \phi_{z_s} + k_{z_s}\frac{L}{2} + \Delta\phi_{gap} + \left\{k_{z_s} + d_\gamma k|_{z_s}\Delta\gamma(z_e)\right\}\frac{L}{2} \end{aligned} \tag{B.8}$$

Since this result should be equivalent to the result of Eq. (B.7), it gives the expression for the kick in phase that has to be applied in the middle.

$$\Delta\phi_{gap} = -d_\gamma k|_{z_s} \frac{q}{W_0} E_0 L T'(k_{z_s}) \sin\Phi \tag{B.9}$$

With $d_\gamma k|_{z_s} = -\frac{k_{z_s}}{\beta_{z_s}^2 \gamma_{z_s}^3}$, the gap transformations can eventually be written as

$$\begin{aligned} \Delta W_{gap} &= qE_0 L\, T(k_{z_s}) \cos\Phi \\ \Delta\phi_{gap} &= \frac{qk_{z_s} E_0 L}{\beta_{z_s}^2 \gamma_{z_s}^3 W_0} T'(k_{z_s}) \sin\Phi \end{aligned} \tag{B.10}$$

The drift-gap-drift representation is illustrated in Fig. B.1. The previous development is valid for a gap with symmetric field. If the gap is not symmetric the kick in phase in Eq. (B.9) is not correct. Also, if the accelerating element is long and the variation of the particle's beta non negligible, its accuracy is questionable.

B.1.1 Transformation using a reference particle

In Eq. (3.15), the average phase depends on the entrance velocity and entrance phase, it is in consequence different for every particle of a bunch. It is possible to express all these different average phases with respect to the average phase Φ_{rp} of

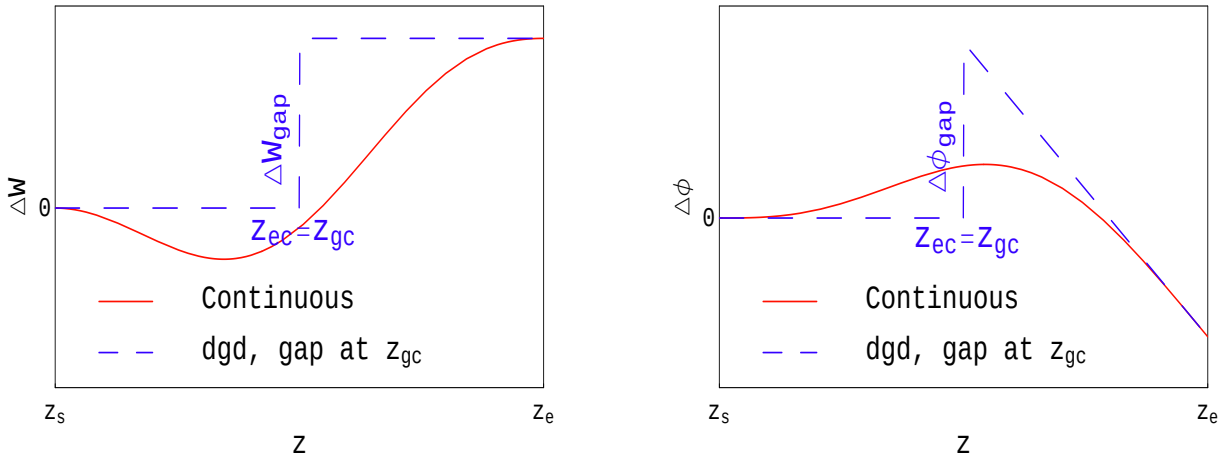

Figure B.1: Energy gain and phase of flight for a single gap with symmetric field. The drift-gap-drift approximation is drawn in dashed line and the continuous functions are plotted in solid lines.

a reference particle (rp) in the bunch. To distinguish between the reference particle and all the other particles, the index rp will be used. For example, the electrical center position of the reference particle will be written $z_{rp,ec}$. Also, the difference of any value with respect to the corresponding reference particle's one will be written using the δ symbol. For example, the average phase of a particle can be written $\delta\Phi = \Phi - \Phi_{rp}$. Since the phase law is supposed linear, the average phase difference generated by a dispersion in the particle's entrance phases and entrance velocities is $\delta\Phi = \delta\phi_{z_s} + \delta k_{z_s}\{\frac{L}{2} + u_{ec,rp}\} + k_{z_s}\delta u_{ec}$. The transformation using the reference particle's average phase is given by

$$\begin{aligned} \Delta W_{gap} &= qE_0 L\,\overline{T}\cos(\Phi_{rp} + \delta\Phi) \\ \Delta\phi_{gap} &= \frac{qk_{z_s}E_0 L}{\beta_{z_s}^2\gamma_{z_s}^3 W_0}\overline{T'}\sin(\Phi_{rp} + \delta\Phi - \Theta_{T,S} + \Theta_{T',S'}) \end{aligned} \tag{B.11}$$

In Eq. (B.11) the average phase Φ_{rp} can now be treated as a free parameter and can be understood as the usual average phase quoted for the acceleartion of a bunch in a cavity. This suppose that the reference particle is chosen as representative of the bunch. A common practice is to define a virtual particle having an entrance energy equal to the average entrance energy of the bunch and a entrance phase equal to the average entrance phase of the bunch. Considering a bunch of N particles

$$\begin{aligned} W_{z_s,rp} &=< W_{bunch} >= \sum_{n=1}^{N} W_{z_s,n} \\ \phi_{z_s,rp} &=< z_{bunch} >= \sum_{n=1}^{N} \phi_{z_s,n} \end{aligned} \tag{B.12}$$

B.1.2 Liouvillian character of the transformation

According to Liouville's theorem, the area in the phase-space coordinates $(\delta W, \delta\phi)$ should be conserved. It has been shown that the longitudinal transformation of the drift-gap-drift representation satisifes this theorem up to the second order for an element with longitudinal electric field symmetric with respect to the geometrical center. [43]. Such verification should be done in the case of a non-symmetric element. For this, the Jacobian determinant of the functions $\delta W_f(\delta W_i, \delta\phi_i)$ and $\delta\phi_f(\delta W_i, \delta\phi_i)$ has to be calculated and found close to the unity. The Jacobian determinant is given by

$$\frac{\partial(\delta W_f, \delta\phi_f)}{\partial(\delta W_i, \delta\phi_i)} = |J| = \begin{vmatrix} \dfrac{\partial\, \delta W_f}{\partial\, \delta W_i} & \dfrac{\partial\, \delta\phi_f}{\partial\, \delta W_i} \\ \dfrac{\partial\, \delta W_f}{\partial\, \delta\phi_i} & \dfrac{\partial\, \delta\phi_f}{\partial\, \delta\phi_i} \end{vmatrix} \tag{B.13}$$

where the indexe i respectively f refers to a value before respectively after the transformation. The energy gain and the phase of flight for the transformation are noted as before ΔW and $\Delta\phi$. In the phase space coordinates it leads to $\delta W_f = \delta W_i + \delta\Delta W$ and $\delta\phi_f = \delta\phi_i + \delta\Delta\phi$ which gives for the determinant

$$|J| = \begin{vmatrix} 1 + \dfrac{\partial\,(\delta\Delta W)}{\partial\, \delta W_i} & \dfrac{\partial\,(\delta\Delta\phi)}{\partial\, \delta W_i} \\ \dfrac{\partial\,(\delta\Delta W)}{\partial\, \delta\phi_i} & 1 + \dfrac{\partial\,(\delta\Delta\phi)}{\partial\, \delta\phi_i} \end{vmatrix} = \begin{vmatrix} 1+\epsilon_{11} & \epsilon_{12} \\ \epsilon_{21} & 1+\epsilon_{22} \end{vmatrix} \tag{B.14}$$

For a drift space of length L, the particles experience no energy gain so $\delta\Delta W = 0$ and the phase of flight is linear so $\delta\Delta\Phi = L\delta k_i$. It follows that $\epsilon_{11} = \epsilon_{22} = \epsilon_{21} = 0$. ϵ_{21} is not null but the determinant of the Jacobian matrix is exactly equal to one, which means that the transformation for a drift space is Liouvillian. To insure the Liouvillain character for the drift-gap-drift transformation it must be proven that the determinant is also close to unity for the gap transformation given in Eq. (B.11). Using the Taylor's theorem of the mean at the first order gives for a function of two variables $f(x_0+\delta x, y_0+\delta y) - f(x_0, y_0) \approx \delta x \frac{\partial f}{\partial x}(x_0, y_0) + \delta y \frac{\partial f}{\partial y}(x_0, y_0)$. Using this result for the functions ΔW_{gap} and $\Delta\phi_{gap}$ leads to

$$\begin{aligned} \delta\Delta W_{gap}(\delta W_i, \delta\phi_i) =& \Delta W_{gap}(W_{i,rp} + \delta W_i, \phi_{i,rp} + \delta\phi_i) - \Delta W_{gap}(W_{i,rp}, \phi_{i,rp}) \\ =& \left.\frac{\partial\Delta W_{gap}}{\partial\delta W_i}\right|_{rp} \delta W_i + \left.\frac{\partial\Delta W_{gap}}{\partial\delta\phi_i}\right|_{rp} \delta\phi_i \\ \delta\Delta\phi_{gap}(\delta W_i, \delta\phi_i) =& \Delta\phi_{gap}(W_{i,rp} + \delta W_i, \phi_{i,rp} + \delta\phi_i) - \Delta\phi_{gap}(W_{i,rp}, \phi_{i,rp}) \\ =& \left.\frac{\partial\Delta\phi_{gap}}{\partial\delta W_i}\right|_{rp} \delta W_i + \left.\frac{\partial\Delta\phi_{gap}}{\partial\delta\phi_i}\right|_{rp} \delta\phi_i \end{aligned}$$

Using the relations

$$\begin{aligned}
\overline{T} &\approx \overline{T}_{rp} + \overline{T}'_{rp} d_\gamma k \, \frac{\delta W_i}{W_0} \\
\overline{T'} &\approx \overline{T'}_{rp} + \overline{T'}'_{rp} d_\gamma k \, \frac{\delta W_i}{W_0} \\
\Theta_{S,T} &\approx \Theta_{S,T,rp} + \Theta'_{S,T,rp} d_\gamma k \, \frac{\delta W_i}{W_0} \\
\Theta_{S',T'} &\approx \Theta_{S',T',rp} + \Theta'_{S',T',rp} d_\gamma k \, \frac{\delta W_i}{W_0} \\
\delta\phi_i &= \delta\phi_{z_s} + \delta k_{z_s} \frac{L}{2} \\
\delta\Phi &\approx \delta\phi_i + \Theta'_{S,T,rp} d_\gamma k \, \frac{\delta W_i}{W_0}
\end{aligned} \tag{B.15}$$

gives

$$\begin{aligned}
\delta\Delta W_{gap}(\delta W_i, \delta\phi_i) =& q E_0 L \left\{ \begin{array}{rr} d_\gamma k \{ -\overline{T}\Theta'_{T,S} \sin\Phi_{rp} + \overline{T}' \cos\Phi_{rp} \} \dfrac{\delta W_i}{W_0} \\ -\overline{T}\sin\Phi_{rp} \quad \delta\phi_i \end{array} \right\} \\
\delta\Delta\phi_{gap}(\delta W_i, \delta\phi_i) =& -\frac{q}{W_0} E_0 L d_\gamma k \left\{ \begin{array}{rr} \left\{ \begin{array}{l} (\overline{T'} d_\gamma k)' \sin(\Phi_{rp} - \Theta_{T,S} + \Theta_{T',S'}) \\ + \overline{T'}\Theta'_{T',S'} d_\gamma k \cos(\Phi_{rp} - \Theta_{T,S} + \Theta_{T',S'}) \end{array} \right\} \dfrac{\delta W_i}{W_0} \\ \overline{T'}\cos(\Phi_{rp} - \Theta_{T,S} + \Theta_{T',S'}) \quad \delta\phi_i \end{array} \right\}
\end{aligned} \tag{B.16}$$

where all the functions depending on the energy $(d_\gamma k, T, S, \overline{T}, \Theta_{S,T}, T', S'...)$ are evaluated for the reference particle energy at the entrance of the gap $W_{i,rp} = W_{z_s,rp}$, and where the prime denotes as before a derivation with respect to k. With Eq. (B.16) it is possible to calculate the value of the Jacobian for the gap transformation. This one satisfies the Liouville's theorem up to the second order if $\epsilon_{11} + \epsilon_{22} = 0$. With $\cos\arctan x = \frac{1}{\sqrt{1+x^2}}$, $\sin\arctan x = \frac{x}{\sqrt{1+x^2}}$, $\Theta'_{S,T} = \frac{TS' - ST'}{\overline{T}^2}$ it writes

$$\begin{aligned}
\epsilon_{11} + \epsilon_{22} =& -\frac{q}{W_0} E_0 L d_\gamma k \left\{ \overline{T'}\cos(\Phi_{rp} - \Theta_{T,S} + \Theta_{T',S'}) + \overline{T}\Theta'_{S,T}\sin\Phi_{rp} - \overline{T}'\cos\Phi_{rp} \right\} \\
=& -\frac{q}{W_0} E_0 L d_\gamma k \left\{ \begin{array}{l} \overline{T'}\{ \dfrac{TT' + SS'}{\overline{TT'}}\cos\Phi_{rp} + \dfrac{ST' - S'T}{\overline{TT'}}\sin\Phi_{rp} \} \\ + \overline{T}\dfrac{-ST' + S'T}{\overline{T}^2}\sin\Phi_{rp} - \dfrac{TT' + SS'}{\overline{T}}\cos\Phi_{rp} \end{array} \right\} \\
=& 0
\end{aligned} \tag{B.17}$$

In conclusion, the drift-gap-drift transformation for non-symmetric field satisifies the Liouville's theorem up to the second order. This result apply for any type of non-symmetric longitudinal field profile. For example, in the case of a multicell superconducting cavity, the end-cells field profile are non-symmetric due to the large field

extension of the field lines into the beampipe region, also the amplitude of the field in each cell of the cavity can be different creating a global field unbalance and shifting the electrical center away from the geometrical center. Fig. B.2 illustrates the conservation of the longitudinal phase space area for an on-axis field profile of the type $E_z(s) = E_m \sin k_m s + \phi_{asym}$ where ϕ_{asym} is a parameter introducing a field asymetry. As expected the quantity $\epsilon_{11}\epsilon_{22} - \epsilon_{12}\epsilon_{21}$ is found close to zero.

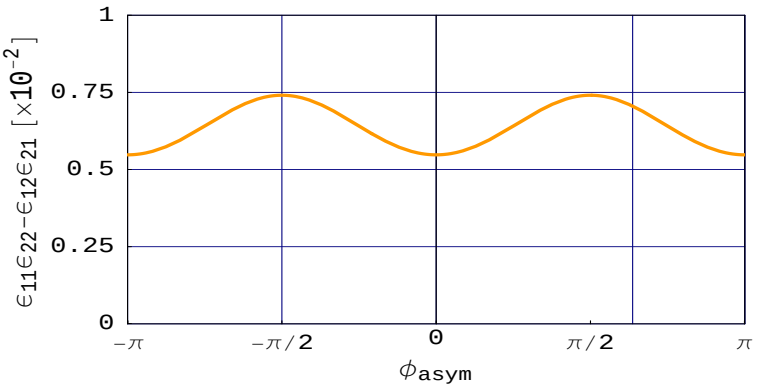

Figure B.2: $\epsilon_{11}\epsilon_{22}-\epsilon_{21}\epsilon_{12} < 1$ for a non-symmetric field profile. The parameter ϕ_{asym} controls the extent of the asymetry. For $\phi_{asym} = 0$ the field is symmetric, and for $\phi_{asym} = +/-\pi$ the field is asymmetric.

B.2 Analytic iterations for the longitudinal dynamics in accelerating cavities

The initial system of coupled integral equations for the longitudinal dynamics of Eq. (3.1) has been transformed to a system of integral equations written in Eq. (3.19) solvable by iteration. It is assumed that the successive energy gain and phase of flight functions obtained from the iteration process converge toward the solutions of the initial system of equations. Three analytical iterations have explicitely been performed and the results are shown next. It appears that the iterative process becomes rapidly a heavy process and that going to further order become increasingly difficult. But, carrying the calculations give interesting insights and allows to deduce a rather general analytical form for the solutions of the inital system of equations. The validity of this solution is demonstrated in section B.3. Eventually, a semi-analytical calculation scheme combining the knowledge of the form for the solution to a numerical routine to calculate unknown parameters allows to calculate the longitudinal dynamics even in cases where the phase of flight is strongly non-linear (see section 3.2.3).

B.2.1 First iteration: ΔW_0 and $\Delta\Phi_0$

For the first analytical iteration, the particle is supposed to experience no acceleration which implies that its velocity remains unchanged through the entire cavity. Since

$\Delta\Phi(z)$ is the difference between the total phase of flight and its linear part, it follows immediately

$$\begin{aligned} \Delta W_0(z) &= 0 \\ \Delta\Phi_0(z) &= 0 \end{aligned} \tag{B.18}$$

B.2.2 Second iteration: ΔW_1 and $\Delta\Phi_1$

I $\Delta W_1(z)$

For the second analytical iteration, The result of $\Delta\Phi_0(z)$ written in Eq. (B.18) is reentered in Eq.(3.19), it follows

$$\Delta W_1(z) = \sum_{n=0}^{\infty}\Big\{\frac{q}{n!}\int_{z_s}^{z} E_z(s)\partial_\theta^n \cos\theta|_{\theta=\phi_L(s)}{\Delta\Phi_0}^n\, ds\Big\} \tag{B.19}$$

The only non-nul term is for $n = 0$, leading to

$$\begin{aligned} \Delta W_1(z) &= q\int_{z_s}^{z} E_z(s)\cos(\phi_{z_s} + k_{z_s}\{s - z_s\})\, ds \\ &= q\sum_{m=1}^{M}\int_{z_s}^{z} E_m\cos(k_m s + \phi_m)\cos(\phi_{z_s} + k_{z_s}\{s - z_s\})\, ds \\ &= q\sum_{m=1}^{M}\Delta W_{1,m}(z) \end{aligned}$$

where the definition $\Delta W_{1,m}(z) = \int_{z_s}^{z} E_m\cos(k_m s + \phi_m)\cos(\phi_{z_s} + k_{z_s}\{s - z_s\})\, ds$ is implied and where the longitudinal electric field is decomposed into a discrete sum of M cosine functions $E_z(z) = \sum_{m=1}^{M} E_m\cos(k_m z + \phi_m)$ .Carrying the integration for the $\Delta W_{1,m}(z)$ it follows, using $\cos a\cos b = \frac{1}{2}\{\cos(a+b) + \cos(a-b)\}$

$$\begin{aligned} \Delta W_{1,m}(z) = \frac{q}{2}E_m\int_{z_s}^{z}\{&\cos(\{k_m + k_{z_s}\}s + \phi_m + \phi_{z_s} - k_{z_s}z_s) \\ &+ \cos(\{k_m - k_{z_s}\}s + \phi_m - \phi_{z_s} + k_{z_s}z_s)\}\, ds \\ = \frac{q}{2}E_m\Big\{&\frac{\sin(\{k_m + k_{z_s}\}z + \phi_m + \phi_{z_s} - k_{z_s}z_s)}{k_m + k_{z_s}} \\ &+ \frac{\sin(\{k_m - k_{z_s}\}z + \phi_m - \phi_{z_s} + k_{z_s}z_s)}{k_m - k_{z_s}} \\ &- \frac{\sin(k_m z_s + \phi_m + \phi_{z_s})}{k_m + k_{z_s}} \\ &- \frac{\sin(k_m z_s + \phi_m - \phi_{z_s})}{k_m - k_{z_s}}\Big\} \end{aligned} \tag{B.20}$$

where it assumed that the denominators are not null. It is useful to introduce the notations

$$\begin{aligned} S(K;\Theta;K') &= \frac{\sin\Big(\big\{\sum_{i=1}^{I} k_i\big\}z + \sum_{j=1}^{J}\theta_j\Big)}{\sum_{l=1}^{L} k'_l} \\ C(K;\Theta;K') &= \frac{\cos\Big(\big\{\sum_{i=1}^{I} k_i\big\}z + \sum_{j=1}^{J}\theta_j\Big)}{\sum_{l=1}^{L} k'_l} \end{aligned} \tag{B.21}$$

with $K = \sum_{i=1}^{I} k_i$, $\Theta = \sum_{j=1}^{J}\theta_j$, and $K' = \sum_{i=1}^{I} k'_i$. Using these relations, it is possible to write Eq. (B.20) under the form

$$\Delta W_1(z) = \Delta W_{1C}(z)\cos\phi_{z_s} + \Delta W_{1S}(z)\sin\phi_{z_s} \tag{B.22}$$

With the definitions and relations

$$\begin{aligned} \Delta W_{1C}(z) &= \sum_{m=1}^{M}\Delta W_{1C,m}(z) \\ \Delta W_{1S}(z) &= \sum_{m=1}^{M}\Delta W_{1S,m}(z) \\ \Delta W_{1C;m}(z) &= \frac{q}{2}E_m\sum_{\mu=1}^{4} S(K_{1C;m,\mu},\Theta_{1C;m,\mu},K'_{1C;m,\mu}) \\ \Delta W_{1S;m}(z) &= \frac{q}{2}E_m\sum_{\mu=1}^{4} C(K_{1S;m,\mu},\Theta_{1S;m,\mu},K'_{1S;m,\mu}) \end{aligned} \tag{B.23}$$

and where the K, Θ and K' are conveniently written under a vector format

$$K_{1C;m,\mu}\begin{pmatrix} k_m + k_{z_s} \\ k_m - k_{z_s} \\ 0 \\ 0 \end{pmatrix} \quad \Theta_{1C;m,\mu}\begin{pmatrix} \phi_m - k_{z_s}z_s \\ \phi_m + k_{z_s}z_s \\ \phi_m + k_m z_s \\ \phi_m + k_m z_s \end{pmatrix} \quad K'_{1C;m,\mu}\begin{pmatrix} +k_m + k_{z_s} \\ +k_m - k_{z_s} \\ -k_m - k_{z_s} \\ -k_m + k_{z_s} \end{pmatrix} \tag{B.24}$$

$$K_{1S;m,\mu}\begin{pmatrix} k_m + k_{z_s} \\ k_m - k_{z_s} \\ 0 \\ 0 \end{pmatrix} \quad \Theta_{1S;m,\mu}\begin{pmatrix} \phi_m - k_{z_s}z_s \\ \phi_m + k_{z_s}z_s \\ \phi_m + k_m z_s \\ \phi_m + k_m z_s \end{pmatrix} \quad K'_{1S;m,\mu}\begin{pmatrix} +k_m + k_{z_s} \\ -k_m + k_{z_s} \\ -k_m - k_{z_s} \\ +k_m - k_{z_s} \end{pmatrix} \tag{B.25}$$

II $\Delta\Phi_1(z)$

The phase slip $\Delta\Phi_1$ is obtained using the results of ΔW_1.

$$\Delta\Phi_1(z) = \sum_{n=1}^{\infty}\Big\{\frac{\partial_W^n k(W)|_{W=W(z_s)}}{n!}\int_{z_s}^{z}\Delta W_1^n(s)\,ds\Big\} \tag{B.26}$$

The following calculations will be limited to the indexes $n = 1, 2$ (which is sufficient to insure accuracy in many cases)

$$\begin{aligned}\Delta\Phi_1(z) &\approx -\frac{k_{z_s}}{\beta_{z_s}^2\gamma_{z_s}^3}\frac{1}{W_0}\int_{z_s}^{z}\Delta W_1(s)\,ds + \frac{3k_{z_s}}{\beta_{z_s}^4\gamma_{z_s}^4}\frac{1}{2W_0^2}\int_{z_s}^{z}\Delta W_1(s)^2\,ds \\ &= \quad \Delta\Phi_{1a}(z) \quad + \quad \Delta\Phi_{1b}(z)\end{aligned} \tag{B.27}$$

where W_0 is the mass energy of the considered particles. The result of Eq. (B.22) is used for the estimation of the integrals.

$$\int_{z_s}^{z}\Delta W_1(s)\,ds = \cos\phi_{z_s}\int_{z_s}^{z}\Delta W_{1C}(s)\,ds + \sin\phi_{z_s}\int_{z_s}^{z}\Delta W_{1S}(s)\,ds \tag{B.28}$$

and

$$\begin{aligned}\int_{z_s}^{z}\Delta W_1(s)^2\,ds = \quad & \cos^2\phi_{z_s}\int_{z_s}^{z}\Delta W_{1C}(s)^2\,ds + \sin^2\phi_{z_s}\int_{z_s}^{z}\Delta W_{1S}(s)^2\,ds \\ & + 2\cos\phi_{z_s}\sin\phi_{z_s}\int_{z_s}^{z}\Delta W_{1C}(s)\Delta W_{1S}(s)\,ds \\ = \quad & \frac{1}{2}\Big\{\int_{z_s}^{z}\Delta W_{1C}(s)^2\,ds - \int_{z_s}^{z}\Delta W_{1S}(s)^2\,ds\Big\} \\ & + \frac{1}{2}\Big\{\int_{z_s}^{z}\Delta W_{1C}(s)^2\,ds + \int_{z_s}^{z}\Delta W_{1S}(s)^2\,ds\Big\}\cos 2\phi_{z_s} \\ & + \int_{z_s}^{z}\Delta W_{1C}(s)\Delta W_{1S}(s)\,ds\sin 2\phi_{z_s}\end{aligned} \tag{B.29}$$

To solve the integrals of Eq. (B.28) it is necessary to have the results of the following integrals

$$\begin{aligned}\int_{z_s}^{z}S(K;\Theta;K')\,ds &= C(K;\Theta;-KK') + C(0;\Theta+Kz_s;KK') \\ \int_{z_s}^{z}C(K;\Theta;K')\,ds &= S(K;\Theta;KK') + S(0;\Theta+Kz_s;-KK')\end{aligned} \tag{B.30}$$

In the particular case where $K = 0$, the previous integrals become

$$\begin{aligned}\int_{z_s}^{z}S(0;\Theta;K')\,ds &= \{z-z_s\}S(0;\Theta;K') \\ \int_{z_s}^{z}C(0;\Theta;K')\,ds &= \{z-z_s\}C(0;\Theta;K')\end{aligned} \tag{B.31}$$

It is worthy to point out that since $C(K;\Theta;K') = S(K;\Theta+\frac{\pi}{2};K')$, having the result for the function S provides easily the result for the function C and vice-versa. To solve the integrals of Eq. (B.29) it is necessary to have the results of the following integrals

$$\begin{aligned}\int_{z_s}^{z} S(K_1;\Theta_1;K_1')S(K_2;\Theta_2;K_2')\,ds = \\ \frac{1}{2}\big\{&S(K_1-K_2;\Theta_1-\Theta_2;\{K1-K2\}K_1'K_2') \\ &+S(0;\Theta_1-\Theta_2+\{K1-K2\}z_s;-\{K1-K2\}K_1'K_2') \\ &+S(K_1+K_2;\Theta_1+\Theta_2;-\{K1+K2\}K_1'K_2') \\ &+S(0;\Theta_1+\Theta_2+\{K1+K2\}z_s;\{K1+K2\}K_1'K_2')\big\}\end{aligned} \tag{B.32}$$

$$\begin{aligned}\int_{z_s}^{z} C(K_1;\Theta_1;K_1')C(K_2;\Theta_2;K_2')\,ds = \\ \frac{1}{2}\big\{&S(K_1-K_2;\Theta_1-\Theta_2;\{K1-K2\}K_1'K_2') \\ &+S(0;\Theta_1-\Theta_2+\{K1-K2\}z_s;-\{K1-K2\}K_1'K_2') \\ &+S(K_1+K_2;\Theta_1+\Theta_2;\{K1+K2\}K_1'K_2') \\ &+S(0;\Theta_1+\Theta_2+\{K1+K2\}z_s;-\{K1+K2\}K_1'K_2')\big\}\end{aligned} \tag{B.33}$$

$$\begin{aligned}\int_{z_s}^{z} S(K_1;\Theta_1;K_1')C(K_2;\Theta_2;K_2')\,ds = \\ \frac{1}{2}\big\{&C(K_1-K_2;\Theta_1-\Theta_2;-\{K1-K2\}K_1'K_2') \\ &+C(0;\Theta_1-\Theta_2+\{K1-K2\}z_s;\{K1-K2\}K_1'K_2') \\ &+C(K_1+K_2;\Theta_1+\Theta_2;-\{K1+K2\}K_1'K_2') \\ &+C(0;\Theta_1+\Theta_2+\{K1+K2\}z_s;+\{K1+K2\}K_1'K_2')\big\}\end{aligned} \tag{B.34}$$

Eq. (B.32), Eq. (B.33), Eq. (B.34) are valid in all cases but when $K_1 = K_2$. For this particular case it writes

$$\begin{aligned}\int_{z_s}^{z} S(K_1;\Theta_1;K_1')S(K_1;\Theta_2;K_2')\,ds = \\ \frac{1}{2}\big\{&\{z-z_s\}C(0;\Theta_1-\Theta_2;K_1'K_2') \\ &+S(2K_1;\Theta_1+\Theta_2;-2K_1K_1'K_2') \\ &+S(0;\Theta_1+\Theta_2+2K_1z_s;2K_1K_1'K_2')\big\}\end{aligned} \tag{B.35}$$

$$\begin{aligned}\int_{z_s}^{z} C(K_1;\Theta_1;K_1')C(K_1;\Theta_2;K_2')\,ds = \\ \frac{1}{2}\big\{&\{z-z_s\}C(0;\Theta_1-\Theta_2;K_1'K_2') \\ &+S(2K_1;\Theta_1+\Theta_2;2K_1K_1'K_2') \\ &+S(0;\Theta_1+\Theta_2+2K_1z_s;-2K_1K_1'K_2')\big\}\end{aligned} \tag{B.36}$$

$$\int_{z_s}^{z} S(K_1;\Theta_1;K_1')C(K_1;\Theta_2;K_2')\,ds = \frac{1}{2}\big\{\{z-z_s\}S(0;\Theta_1-\Theta_2;K_1'K_2') + C(2K_1;\Theta_1+\Theta_2;-2K_1K_1'K_2') + C(0;\Theta_1+\Theta_2+2K_1z_s;+2K_1K_1'K_2')\big\} \tag{B.37}$$

Coming back to Eq. (B.27) and Eq. (B.28) and using the results of Eq. (B.30) gives

$$\Delta\Phi_{1a}(z) = \Delta\Phi_{1aC_1}(z)\cos\phi_{z_s} + \Delta\Phi_{1aS_1}(z)\sin\phi_{z_s} \tag{B.38}$$

where

$$\Delta\Phi_{1aC_1}(z) = -\frac{k_{z_s}}{\beta_{z_s}^2\gamma_{z_s}^3}\frac{1}{W_0}\frac{q}{2}\sum_{m=1}^{M}E_m\Big\{\sum_{\mu=1}^{2}\{C(K_{1C;m,\mu};\Theta_{1C;m,\mu};-K_{1C;m,\mu}K'_{1C;m,\mu})+ C(0;\Theta_{1C;m,\mu}+K_{1C;m,\mu}z_s;K_{1C;m,\mu}K'_{1C;m,\mu})\}+ \sum_{\mu=3}^{4}C(0;\Theta_{1C;m,\mu};K'_{1C;m,\mu})\{z-z_s\}\Big\} \tag{B.39}$$

$$\Delta\Phi_{1aS_1}(z) = -\frac{k_{z_s}}{\beta_{z_s}^2\gamma_{z_s}^3}\frac{1}{W_0}\frac{q}{2}\sum_{m=1}^{M}E_m\Big\{\sum_{\mu=1}^{2}\{S(K_{1S;m,\mu};\Theta_{1S;m,\mu};+K_{1S;m,\mu}K'_{1S;m,\mu})+ S(0;\Theta_{1S;m,\mu}+K_{1S;m,\mu}z_s;-K_{1S;m,\mu}K'_{1S;m,\mu})\}+ \sum_{\mu=3}^{4}S(0;\Theta_{1S;m,\mu};K'_{1S;m,\mu})\{z-z_s\}\Big\} \tag{B.40}$$

The first part $\Delta\Phi_{1a}(z)$ of the function $\Delta\Phi_1(z)$ has been calculated, to estimate $\Delta\Phi_{1b}(z)$, three integrals are preliminary calculated. For the first of them, some simplifying notations are used

$$\begin{aligned} K_1 &= K_{1C;m,\mu} \quad \Theta_1 = \Theta_{1C;m,\mu} \quad K_1' = K'_{1C;m,\mu} \\ K_2 &= K_{1C;n,\nu} \quad \Theta_2 = \Theta_{1C;n,\nu} \quad K_1' = K'_{1C;n,\nu} \end{aligned} \tag{B.41}$$

Using these parameters, it writes for the first preliminary integral

$$\int_{z_s}^{z}\Delta W_{1S}(s)^2\,ds = \frac{q^2}{2^3}\sum_{m=1}^{M}\sum_{n=1}^{M}\sum_{\mu=1}^{4}\sum_{\mu=1}^{4}E_mE_n\times \begin{bmatrix} S(K_1+K_2;\Theta_1+\Theta_2;-\{K_1-K_2\}K_1'K_2') + \\ S(0;\Theta_1+\Theta_2+\{K_1+K_2\}z_s;\{K_1-K_2\}K_1'K_2') + \\ \begin{cases} \begin{bmatrix} S(K_1-K_2;\Theta_1-\Theta_2;\{K_1-K_2\}K_1'K_2') + \\ S(0;\Theta_1-\Theta_2+\{K_1-K_2\}z_s;-\{K_1-K_2\}K_1'K_2') \end{bmatrix} & \text{if } K_1\neq K_2 \\ \{z-z_s\}C(0;\Theta_1-\Theta_2;K_1'K_2') & \text{if } K_1=K_2 \end{cases} \end{bmatrix} \tag{B.42}$$

For the second integral, the parameters are redefined by

$$\begin{aligned} K_1 &= K_{1S;m,\mu} \qquad \Theta_1 = \Theta_{1S;m,\mu} \qquad K_1' = K_{1S;m,\mu}' \\ K_2 &= K_{1S;n,\nu} \qquad \Theta_2 = \Theta_{1S;n,\nu} \qquad K_1' = K_{1S;n,\nu}' \end{aligned} \tag{B.43}$$

Using these parameters for the second integral gives

$$\begin{aligned} \int_{z_s}^{z} \Delta W_{1C}(s)^2 \, ds = \frac{q^2}{2^3} \sum_{m=1}^{M} \sum_{n=1}^{M} \sum_{\mu=1}^{4} \sum_{\mu=1}^{4} E_m E_n \times \\ \left[\begin{array}{l} S(K_1 + K_2; \Theta_1 + \Theta_2; + \{K_1 - K_2\} K_1' K_2') + \\ S(0; \Theta_1 + \Theta_2 + \{K_1 + K_2\} z_s; - \{K_1 - K_2\} K_1' K_2') + \\ \left\{ \begin{array}{ll} \left[\begin{array}{l} S(K_1 - K_2; \Theta_1 - \Theta_2; \{K_1 - K_2\} K_1' K_2') + \\ S(0; \Theta_1 - \Theta_2 + \{K_1 - K_2\} z_s; - \{K_1 - K_2\} K_1' K_2') \end{array} \right] & \text{if } K_1 \neq K_2 \\ \{z - z_s\} C(0; \Theta_1 - \Theta_2; K_1' K_2') & \text{if } K_1 = K_2 \end{array} \right. \end{array} \right] \end{aligned} \tag{B.44}$$

For the third and last preliminary integral, the following definitions apply

$$\begin{aligned} K_1 &= K_{1C;m,\mu} \qquad \Theta_1 = \Theta_{1C;m,\mu} \qquad K_1' = K_{1C;m,\mu}' \\ K_2 &= K_{1S;n,\nu} \qquad \Theta_2 = \Theta_{1S;n,\nu} \qquad K_1' = K_{1S;n,\nu}' \end{aligned} \tag{B.45}$$

Using these parameters leads to

$$\begin{aligned} \int_{z_s}^{z} \Delta W_{1S}(s) \Delta W_{1C}(s) \, ds = \frac{q^2}{2^3} \sum_{m=1}^{M} \sum_{n=1}^{M} \sum_{\mu=1}^{4} \sum_{\mu=1}^{4} E_m E_n \times \\ \left[\begin{array}{l} C(K_1 + K_2; \Theta_1 + \Theta_2; - \{K_1 - K_2\} K_1' K_2') + \\ C(0; \Theta_1 + \Theta_2 + \{K_1 + K_2\} z_s; + \{K_1 - K_2\} K_1' K_2') + \\ \left\{ \begin{array}{ll} \left[\begin{array}{l} C(K_1 - K_2; \Theta_1 - \Theta_2; - \{K_1 - K_2\} K_1' K_2') + \\ C(0; \Theta_1 - \Theta_2 + \{K_1 - K_2\} z_s; + \{K_1 - K_2\} K_1' K_2') \end{array} \right] & \text{if } K_1 \neq K_2 \\ \{z - z_s\} S(0; \Theta_1 - \Theta_2; K_1' K_2') & \text{if } K_1 = K_2 \end{array} \right. \end{array} \right] \end{aligned} \tag{B.46}$$

Coming back to Eq. (B.27) and Eq. (B.29) it is possible to write

$$\begin{aligned} \Delta\Phi_{1b}(z) = \; & \Delta\Phi_{1bC_0}(z) \\ & + \Delta\Phi_{1bC_2}(z) \cos 2\phi_{z_s} + \Delta\Phi_{1bS_2}(z) \sin 2\phi_{z_s} \end{aligned} \tag{B.47}$$

with the following definitions

$$\begin{aligned} \Delta\Phi_{1bC_0}(z) &= \frac{k_{z_s}}{\beta_{z_s}^4 \gamma_{z_s}^4} \frac{3}{4W_0^2} \Big\{ \int_{z_s}^{z} \Delta W_{1C}(s)^2 \, ds + \int_{z_s}^{z} \Delta W_{1S}(s)^2 \, ds \Big\} \\ \Delta\Phi_{1bC_2}(z) &= \frac{k_{z_s}}{\beta_{z_s}^4 \gamma_{z_s}^4} \frac{3}{4W_0^2} \Big\{ \int_{z_s}^{z} \Delta W_{1C}(s)^2 \, ds - \int_{z_s}^{z} \Delta W_{1S}(s)^2 \, ds \Big\} \\ \Delta\Phi_{1bS_2}(z) &= \frac{k_{z_s}}{\beta_{z_s}^4 \gamma_{z_s}^4} \frac{3}{2W_0^2} \int_{z_s}^{z} \Delta W_{1C}(s) \Delta W_{1S}(s) \, ds \end{aligned} \tag{B.48}$$

Explicit solutions for these functions can be found by using the results of Eq. (B.42), Eq. (B.44), and Eq. (B.46). Combining the results of Eq. (B.38) and Eq. (B.47) it is eventually possible to write

$$\begin{aligned}\Delta\Phi_1(z) = \;& \Delta\Phi_{1C_0}(z) \\ &+ \Delta\Phi_{1C_1}(z)\cos\phi_{z_s} + \Delta\Phi_{1S_1}(z)\sin\phi_{z_s} \\ &+ \Delta\Phi_{1C_2}(z)\cos 2\phi_{z_s} + \Delta\Phi_{1S_2}(z)\sin 2\phi_{z_s}\end{aligned} \tag{B.49}$$

where the indexes a and b were dropped. With the previous relations it is easy to see that if an average electric field is defined as $E_0 = \frac{1}{|z-z_s|}\int_{z_s}^{z}|E_z(s)|\,ds$, then the functions $\Delta\Phi_{1C_1}(z)$, and $\Delta\Phi_{1S_1}(z)$ are proportional to $\frac{qE_0}{W_0}$, but the functions $\Delta\Phi_{1C_0}(z)$, $\Delta\Phi_{1C_2}(z)$, and $\Delta\Phi_{1S_2}(z)$ are proportional to $\frac{q^2E_0^2}{W_0^2}$. The result of Eq. (B.49) contains only cosine functions up to the second order in ϕ_{z_s} because the initial summation of Eq. (B.26) has been truncated to this order. Without such trunction, Eq. (B.49) could be found of the form

$$\Delta\Phi_1(z) = \sum_{n=0}^{\infty}\Delta\Phi_{1C_n}(z)\cos n\phi_{z_s} + \Delta\Phi_{1S_n}(z)\sin n\phi_{z_s} \tag{B.50}$$

B.2.3 Third iteration: ΔW_2 and $\Delta\Phi_2$

For the third analytical iteration, The result of $\Delta\Phi_1(z)$ is reentered in Eq.(3.19).

$$\Delta W_2(z) = \sum_{n=0}^{\infty}\Big\{\frac{q}{n!}\int_{z_s}^{z}E_z(s)\partial_\theta^n\cos\theta|_{\theta=\phi_L(s)}{\Delta\Phi_1}^n\,ds\Big\} \tag{B.51}$$

Truncating again at the second order it follows

$$\begin{aligned}\Delta W_2(z) =& \Delta W_1(z) + q\int_{z_s}^{z}E_z(s)\sin(\phi_{z_s}+k_{z_s}\{s-z_s\})\Delta\Phi_1(s)\,ds \\ &- q\int_{z_s}^{z}E_z(s)\cos(\phi_{z_s}+k_{z_s}\{s-z_s\})\Delta\Phi_1^2(s)\,ds \\ =& \Delta W_1(z) + \Delta W_{2a}(z) + \Delta W_{2b}(z)\end{aligned} \tag{B.52}$$

To calculate $\Delta W_{2a}(z)$, the expression of Eq. (B.49) for $\Delta\Phi_1(s)$ is used. It writes

$$\Delta W_{2a}(z) = q\int_{z_s}^{z}E_z(s)\sin(\phi_{z_s}+k_{z_s}\{s-z_s\})\Delta\Phi_1(s)\,ds \tag{B.53}$$

Because the function $\Delta\Phi_1(s)$ contains some terms proportional to E_0 and higher order terms proportional to E_0^2, it is worthy to split the previous equation in two parts, $\Delta W_{2a}(z) = \Delta W_{2a,1}(z) + \Delta W_{2a,2}(z)$ with respectively

$$\begin{aligned}\Delta W_{2a,1}(z) = q\int_{z_s}^{z}E_z(s)\sin(\phi_{z_s}+k_{z_s}\{s-z_s\})\times \\ \{\Delta\Phi_{1C_1}(s)\cos\phi_{z_s} + \Delta\Phi_{1S_1}(s)\sin\phi_{z_s}\}\,ds\end{aligned} \tag{B.54}$$

and

$$\begin{aligned}\Delta W_{2a,2}(z) = q\int_{z_s}^{z} E_z(s)\sin(\phi_{z_s} + k_{z_s}\{s - z_s\})\times \\ \{\Delta\Phi_{1C_0}(s) + \Delta\Phi_{1C_2}(s)\cos 2\phi_{z_s} + \Delta\Phi_{1S_2}(s)\sin 2\phi_{z_s}\}\, ds\end{aligned} \tag{B.55}$$

Developing the sine function in Eq. (B.54), it is possible to write

$$\begin{aligned}\Delta W_{2a,1}(z) =& \Delta W_{2a,1C_0}(z) \\ & \Delta W_{2a,1C_2}(z)\cos 2\phi_{z_s} + \Delta W_{2a,1S_2}(z)\sin 2\phi_{z_s}\end{aligned} \tag{B.56}$$

with the following definitions

$$\Delta W_{2a,1C_0}(z) = \frac{q}{4}\sum_{m=1}^{M} E_m \left[\begin{array}{l} \displaystyle\int_{z_s}^{z}\{S(K_1;\Theta_1;1) + S(K_2;\Theta_2;1)\}\Delta\Phi_{1C_1}(s)\, ds \\ \displaystyle + \int_{z_s}^{z}\{S(K_1;\Theta_1+\frac{\pi}{2};1) + S(K_2;\Theta_2+\frac{\pi}{2};1)\}\Delta\Phi_{1S_1}(s)\, ds\end{array}\right] \tag{B.57}$$

$$\Delta W_{2a,1C_2}(z) = \frac{q}{4}\sum_{m=1}^{M} E_m \left[\begin{array}{l} \displaystyle\int_{z_s}^{z}\{S(K_1;\Theta_1;1) + S(K_2;\Theta_2;1)\}\Delta\Phi_{1C_1}(s)\, ds \\ \displaystyle - \int_{z_s}^{z}\{S(K_1;\Theta_1+\frac{\pi}{2};1) + S(K_2;\Theta_2+\frac{\pi}{2};1)\}\Delta\Phi_{1S_1}(s)\, ds\end{array}\right] \tag{B.58}$$

$$\Delta W_{2a,1S_2}(z) = \frac{q}{4}\sum_{m=1}^{M} E_m \left[\begin{array}{l} \displaystyle\int_{z_s}^{z}\{S(K_1;\Theta_1;1) + S(K_2;\Theta_2;1)\}\Delta\Phi_{1S_1}(s)\, ds \\ \displaystyle + \int_{z_s}^{z}\{S(K_1;\Theta_1+\frac{\pi}{2};1) + S(K_2;\Theta_2+\frac{\pi}{2};1)\}\Delta\Phi_{1C_1}(s)\, ds\end{array}\right] \tag{B.59}$$

From Eq. (B.57) to Eq. (B.59), $K_1 = k_{z_s} + k_m$, $K_2 = k_{z_s} - k_m$, $\Theta_1 = \phi_m - k_{z_s} z_s$, and $\Theta_2 = -\phi_m - k_{z_s} z_s$. The integrals in these same equations are of three types

$$\begin{aligned} I_1 =& a\int_{z_s}^{z} S(K_1;\Theta_1;K_1')\, ds \\ I_2 =& \int_{z_s}^{z} S(K_1;\Theta_1;K_1')S(K_2;\Theta_2;K_2')\, ds \\ I_3 =& b\int_{z_s}^{z} S(K_1;\Theta_1;K_1')\{z - z_s\}\, ds\end{aligned} \tag{B.60}$$

The two first types were already met before and their solutions are given in Eq. (B.30) and Eq. (B.32), the solution to I_3 is

$$I_3 = b\begin{bmatrix} S(0;\Theta_1 + K_1 z_s; -K_1^2 K') + S(K_1;\Theta_1;K_1^2 K_1') + \\ C(K_1;\Theta_1;K_1 K_1')\{z - z_s\}\end{bmatrix} \tag{B.61}$$

Using these results it is possible to write

$$\int_{z_s}^{z} S(K_\mu;\Theta_\mu;K'_\mu)\begin{bmatrix} a+ \\ b\{z-z_s\}+ \\ C(K_\nu;\Theta_\nu;K'_\nu)\end{bmatrix} ds = \left[\begin{array}{l} a\begin{bmatrix} C(K_\mu;\Theta_\mu;-K_\mu K'_\mu)+ \\ C(0;\Theta_\mu+K_\mu z_s;-K_\mu K'_\mu)\end{bmatrix}+ \\ b\begin{bmatrix} C(K_\mu;\Theta_\mu;K_\mu K'_\mu)\{z-z_s\}\}+ \\ S(K_\mu;\Theta_\mu;K_\mu^2 K'_\mu)+ \\ S(0;\Theta_\mu+K_\mu z_s;-K_\mu^2 K'_\mu)\end{bmatrix}+ \\ \frac{1}{2}\left\{\begin{array}{l}\begin{bmatrix} C(K_\mu-K_\nu;\Theta_\mu-\Theta_\nu;-\{K_\mu-K_\nu\}K'_\mu-K'_\nu)+ \\ C(0;\Theta_\mu-\Theta_\nu+\{K_\mu-K_\nu\}z_s;-\{K_\mu-K_\nu\}K'_\mu-K'_\nu) \\ C(K_\mu+K_\nu;\Theta_\mu+\Theta_\nu;-\{K_\mu+K_\nu\}K'_\mu-K'_\nu)+ \\ C(0;\Theta_\mu+\Theta_\nu+\{K_\mu+K_\nu\}z_s;-\{K_\mu+K_\nu\}K'_\mu+K'_\nu)\end{bmatrix} \text{ if } K_\mu\neq K_\nu \\ \begin{bmatrix} S(0;\Theta_\mu-\Theta_\nu;-\{K_\mu-K_\nu\}K'_\mu-K'_\nu)+ \\ C(K_\mu+K_\nu;\Theta_\mu+\Theta_\nu;-\{K_\mu+K_\nu\}K'_\mu-K'_\nu)+ \\ C(0;\Theta_\mu+\Theta_\nu+\{K_\mu+K_\nu\}z_s;-\{K_\mu+K_\nu\}K'_\mu+K'_\nu)\end{bmatrix} \text{ if } K_\mu=K_\nu\end{array}\right.\end{array}\right] \tag{B.62}$$

with the previous result it is now possible to solve Eq. (B.58) and Eq. (B.59). All the results have been showed explicitely so far. Nevertheless, the increasing weight of the calculations makes their display difficult. The remaining calculations for the remaining part ΔW_{2b}, as written in Eq. (B.52), of the energy gain function ΔW_2 were carried but will not be explicitely reported here. Also,Same for the calculations of the phase of flight $\Delta\Phi_2$. Instead, the general form of their results is presented.

$$\begin{aligned} \Delta W_2 = \Delta W_{2,C_0} &+ \Delta W_{2,C_1}\cos\phi_{z_s} + \Delta W_{2,S_1}\sin\phi_{z_s} \\ &+ \Delta W_{2,C_2}\cos 2\phi_{z_s} + \Delta W_{2,S_2}\sin 2\phi_{z_s} \\ &+ \Delta W_{2,C_3}\cos 3\phi_{z_s} + \Delta W_{2,S_3}\sin 3\phi_{z_s} \\ \Delta\phi_2(\beta_{z_s},\phi_{z_s},z,E_z) = \Delta\phi_{2,C_0} &+ \Delta\phi_{2,C_1}\cos\phi_{z_s} + \Delta\phi_{2,S_1}\sin\phi_{z_s} \\ &+ \Delta\phi_{2,C_2}\cos 2\phi_{z_s} + \Delta\phi_{2,S_2}\sin 2\phi_{z_s} \\ &+ \Delta\phi_{2,C_3}\cos 3\phi_{z_s} + \Delta\phi_{2,S_3}\sin 3\phi_{z_s} \end{aligned} \tag{B.63}$$

The various coefficients depend on the amplitude of the accelerating field E_0L, on the electric charge q, on the entrance beta β_{z_s}, and on the field profile, and on the longitudinal position z. More explicit dependences with respect to the first two of

these variables are of particular interest. It is found

$$\begin{aligned}
\Delta W_{2,C_0} &= f_1 \{qE_0L\}^2 \quad ; \\
\Delta W_{2,C_1} = f_2 \{qE_0L\}^1 + f_3 \{qE_0L\}^3 \quad &; \quad \Delta W_{2,S_1} = f_4 \{qE_0L\}^1 + f_5 \{qE_0L\}^3 \\
\Delta W_{2,C_2} &= f_6 \{qE_0L\}^2 \quad ; \quad \Delta W_{2,S_2} = f_7 \{qE_0L\}^2 \\
\Delta W_{2,C_3} &= f_8 \{qE_0L\}^3 \quad ; \quad \Delta W_{2,S_3} = f_9 \{qE_0L\}^3 \\
\Delta \phi_{2,C_0} = g_1 \{qE_0L\}^0 + g_2 \{qE_0L\}^2 \quad &; \\
\Delta \phi_{2,C_1} = g_3 \{qE_0L\}^1 + g_4 \{qE_0L\}^3 \quad &; \quad \Delta \phi_{2,S_1} = g_5 \{qE_0L\}^1 + g_6 \{qE_0L\}^3 \\
\Delta \phi_{2,C_2} &= g_7 \{qE_0L\}^2 \quad ; \quad \Delta \phi_{2,S_2} = g_8 \{qE_0L\}^2 \\
\Delta \phi_{2,C_3} &= g_9 \{qE_0L\}^3 \quad ; \quad \Delta \phi_{2,S_3} = g_{10} \{qE_0L\}^3
\end{aligned} \tag{B.64}$$

The functions f and g, have been calculated explicitely, for example the function f_1 can be deduced from Eq. (B.48). The results of Eq. (B.63) and Eq. (B.64) have rather particular forms. Based on these reaults, an analytical form for the general solution of the the initial system of coupled integral equations can be found. Details on this issue are developed in Section B.3.

B.3 General form of the solution

The coupled system of equations can be written, using Eq. (3.19)

$$\begin{aligned}
\frac{\Delta W_i(z)}{W_0} = \quad & \epsilon \sum_{n=0}^{\infty} \Big\{ \int_{z_s}^{z} \frac{k_E(s)}{n!}\, d_\theta^n \cos\theta|_{\phi_L(s)}\, \Delta\phi_{i-1}^n(s)\, ds \Big\} \\
\Delta \phi_i(z) = \quad & \sum_{n=1}^{\infty} \Big\{ \frac{d_\gamma^n k|_{\gamma(z_s)}}{n!} \int_{z_s}^{z} \left(\frac{\Delta W_i(s)}{W_0} \right)^n ds \Big\}
\end{aligned} \tag{B.65}$$

In chapter 3, the solution to the initial coupled system of integral equation was approached by analytical iterations. The detail of the calculation up to three iterations is given in section B.2. From the results it appeared that the solution would be of the form

$$\begin{aligned}
\frac{\Delta W}{W_0} &= \sum_{n=0}^{\infty} A_{2n} \cos 2n\phi_{z_s} + B_{2n} \sin 2n\phi_{z_s} \\
&\quad + A_{2n+1} \cos(2n+1)\phi_{z_s} + B_{2n+1} \sin(2n+1)\phi_{z_s} \\
\Delta\phi &= \sum_{n=0}^{\infty} C_{2n} \cos 2n\phi_{z_s} + D_{2n} \sin 2n\phi_{z_s} \\
&\quad + C_{2n+1} \cos(2n+1)\phi_{z_s} + D_{2n+1} \sin(2n+1)\phi_{z_s} \\
&\quad with \begin{cases} A, B, C, D_{2n} = & \sum\limits_{m=2n}^{\infty} a, b, c, d_{2n,2m} \epsilon^{2m} \\ A, B, C, D_{2n+1} = & \sum\limits_{m=2n+1}^{\infty} a, b, c, d_{2n+1,2m+1} \epsilon^{2m+1} \end{cases}
\end{aligned} \tag{B.66}$$

The functions A, B, C and D are polynomes of even or odd powers of the parameter ϵ. For instance, the few first even polynomes for the functions A can be more explicitely written

$$\begin{aligned} A_0 = &\ a_{0,0}\epsilon^0 + a_{0,2}\epsilon^2 + a_{0,4}\epsilon^4 + ... \\ A_2 = &\ a_{2,2}\epsilon^2 + a_{2,4}\epsilon^4 + ... \\ A_4 = &\ a_{4,4}\epsilon^4 + ... \end{aligned}$$

To assert that the energy gain and the phase of flight functions can be written under the forms of Eq. (B.66) means that these forms should be invariant under the analytical iterative process. To proove this point, it is interesting to point out two remarkable properties of the solution forms written in Eq. (B.66). The first one is that all the terms of the energy gain and of the phase of flight functions are polynomes of even, respectively odd, powers of ϵ multiplying a cosine or a sine function of an even, respectively odd, harmonic of the entrance phase ϕ_{z_s}. It is therefore impossible to find some crossing terms such as $\epsilon^3 \cos 2\phi_{z_s}$ or $\epsilon^4 \sin \phi_{z_s}$. The second property is that the lowest power of a polynome is never lower than the harmonic it is multiplying. For instance, it is not possible to find some terms such as $\epsilon^2 \cos 4\phi_{z_s}$ or $\epsilon^3 \sin 9\phi_{z_s}$. Having strengthened out these two properties it is possible to demonstrate that the functions $\frac{\Delta W}{W_0}$ and $\Delta\phi$ elevated to any integer power will keep such properties. For sake of simplicity, a polynome of the even/odd powers of ϵ will be called an even/odd polynome and will be noted P_{even}/P_{odd}. Also, the cosine or sine function of an even/odd harmonic of the entrance phase ϕ_{z_s} will be refered to as an even/odd harmonic and noted for both functions H_{even}/H_{odd}. Any functions supposed to be a linear combination

Table B.1: Properties of the inner product of polynomes P of ϵ, and of harmonics H of ϕ_{z_s}.

$\times$	P_{even}	P_{odd}
P_{even}	P_{even}	P_{odd}
P_{odd}	P_{odd}	P_{even}

$\times$	H_{even}	H_{odd}
H_{even}	H_{even}	H_{odd}
H_{odd}	H_{odd}	H_{even}

of even polynomes multiplying even harmonics and odd polynomes multiplying odd harmonics is of the form $\sum P_{even}H_{even} + P_{odd}H_{odd}$. Considering the product of two such functions gives, using the multiplcation rules of Table B.1, a third function of the same form. The first property is then preserved after multiplication. The second property is also conserved. For example, multiplying $\epsilon^m \cos^i \phi$ and $\epsilon^n \cos^j \phi$, with the initial assumptions $m \geq i$ and $n \geq j$, gives $\epsilon^{m+n} \cos^{i+j} \phi$. The cosine function can be linearized $\cos^K \phi = \sum_{k \leq K} c_k \cos k\phi$ (where c_k are constant coefficients). This means that the highest harmonic of the linearized cosine function is $i + j$. Eventually, the second property is preserved through multiplication because $m + n \geq i + j$. In consequence, if the energy gain function and the phase of flight are functions of the form as given in Eq. (B.66), any of their power is too. An other important point is that if a function satisfies the two properties, its integration over the longitudinal variable will preserve them since neither the parameter ϵ nor the entrance phase ϕ_{z_s} depends

on the longitudinal variable. Now, if after the i^{th} iteration, the function $\frac{\Delta W_i}{W_0}$ has the form exposed in Eq. (B.66), then the function $\Delta\phi_i$ will be of a similar form because, according to Eq. (B.65), the i^{th} iteration for the phase of flight is obtained by integration of all the powers of $\frac{\Delta W_i}{W_0}$, and both, elevation to any power and integration over the longitudinal variable, preserve this form as mentionned before. To finish the demonstration it must be shown that reinjecting $\Delta\phi_i$ leads also to a function $\frac{\Delta W_{i+1}}{W_0}$ of equivalent form. From Eq. (B.65), the necessary clarification concerns the multiplication, for any integer n, of the n^{th} power of $\Delta\phi_i$ by $\epsilon\, d_\theta^n \cos\theta|_{\phi_L(s)}$, which depends on both ϵ and ϕ_{z_s} (it is here useful to remember that the linear phase of flight is given by $\phi_L(z) = \phi_{z_s} + k_{z_s}\{z - z_s\}$). But $\epsilon\, d_\theta^n \cos\theta|_{\phi_L(s)}$ is of the form $P_{odd}H_{odd}$ for any integer n. Multiplying it by $\Delta\phi^n$ will therefore give, according to Table B.1, a function $\frac{\Delta W_{i+1}}{W_0}$ of the expected form. It finally concludes that the solution form of the Eq. (B.66) is invariant under the iterative process and is in consequence a valid solution of the initial set of coupled integral equations.

Whereas explicit formulations for the energy gain function and for the phase of flight function were developed in Annex B.2, their applicability is limited to cases where the non linear part of the phase of flight is approximately below fourty degrees. In contrary, The general form for the solutions of the energy gain and of the phase of flight written in Eq. (B.66) can be used to develop a semi-analytic method of calculations which can be applied to cases with larger non linearity but which has non explicit dependences (with respect to the particle's entrance beta and field profile). The semi-analytic method and its illustration is presented in Section 3.2.3.

Bibliography

[1] H. Padamsee, J. Knobloch, T. Hays, RF Superconductivity for accelerators, John Wiley & Sons, New-York (1998)

[2] Sang-ho Kim, Marc Doleans, and Yoon Kang "Efficient Design Scheme of Superconducting Cavity," Proceedings of Linear Accelerator Conference 2000 (LINAC2000), pp.923-925, Monterey, California, 21st-25th, August, 2000

[3] P. Kneisel et al., "Superconducting Prototype Cavities for the Spallation Neutron Source (SNS) Project," Proceedings of Particle Accelerator Conference 2001 (PAC2001), pp. 484-486, Chicago, Illinois, 18th-22nd, June 2001

[4] J. Billen and L. Young, "POISSON SUPERFISH," LA-UR-96-1834 (2000)

[5] C. Reece et al., "Improvement of the Operational Performance of SRF Cavities via In Situ Helium Processing and Waveguide Vaccum Processing," Proceedings of Particle Accelerator Conference 1997 (PAC97), 3P034, Vancouver, B.C., Canada, 12th-16th, May 1997

[6] Ph. Bernard et al., 5th Workshop on RF Superconductivity, Hamburg,Germany, 1995

[7] E. Kako et al., "Improvement of Cavity Performance by Electropolishing in the 1.3 GHz Nb Superconducting Cavities," Proceedings of Particle Accelerator Conference 1999 (PAC1999), New-York City, New-York, March 29th-April 2nd, 1999

[8] B. Visentin et al., "the Cavity Heating: A Cure against the High Accelerator Field Q0 Drop," 9th Workshop on RF Superconductivity, Santa Fe, New Mexico, USA, 1999

[9] C. Antoine et al., "Alternative Approaches for Surface Treatment of Nb Superconducting Cavities," 9th Workshop on RF Superconductivity, Santa Fe, New Mexico, USA, 1999

[10] G. Ciovati and al., "Superconducting Prototype Cavities for the Spallation Neutron Source (SNS) Project," Proceedings of the 8th European Particle Accelerator Conference , Paris, 3rd-7th, June 2002

[11] P. Balleyguier, "External Q Studies for APT SC-Cavity Couplers," Proceedings of Linear Accelerator Conference 1998 (LINAC98), pp.133-135, Chicago, Illinois, 23rd-28th, August, 1998

[12] C. Yinghua, J. Sekutowicz, W. Yixiang, "A Different Tuning Method for Accelerating Cavities," DESY M-89-11, DESY, (1989)

[13] D. Jeon et al., "Cumulative beam break-up study of the Spallation Neutron Source Linac," Nuclear Instruments and Methods in Physics Research A 495 (2002) 85-94

[14] S. Kim, M. Doleans, D. Jeon, R. Sundelin, "Higer-order-mode (HOM) power in elliptical superconducting cavities for intense pulsed proton accelerators," Nuclear Instruments and Methods in Physics Research A 492 (2002)1-10

[15] G. Ciovati and al., "Superconducting Prototype Cavities for the Spallation Neutron Source (SNS) Project," Proceedings of Particle Accelerator Conference 2001 (PAC2001), Chicago, Illinois, 18th-22nd, June 2001

[16] Ansys user's manual, eleventh Edition, Ansys release 5.6, SAS IP, Inc., 1999

[17] L. Kravchuk, G. Romanov, S. Tarasov "Multipactoring Code for 3D Accelerating Structures," Proceedings of Linear Accelerator Conference 2000 (LINAC2000), pp. 821-823, Monterey, California, 21st-25th, August 2000

[18] L. Kravchuk, G. Romanov, S. tarasov, "Multipacting Analysis Possibility for the SNS Accelerator System Cavities," SNS ASD Technical Note-AP-68, May 2002

[19] E. Somersalo et al., "Computational Methods for Analysing Electron Multipacting in RF Structures," Particle Accelerators 59, 107 (1998)

[20] S. Kim, P. Kneisel, R. Sundelin, "Multipacting Analysis Possibility for the SNS Accelerator System Cavities," SNS ASD Technical Note-AP-63, 2002

[21] P.B Wilson, "High Energy Electron Linacs: Applications to Storage Ring RF Systems and Linear Coliiders," SLAC-PUB-2884, (1987)

[22] B.W Zotter, Impedances and Wakes in High-Energy Particle Accelerators, World Scientific Publishing Co. Pte. Ltd, Singapore (1998)

[23] A. Mosnier, "Dynamic Measurements of the Lorentz Forces on a MACSE cavity," DESY Print TESLA 93-09, DESY, (1993)

[24] N. Ouchi et al., "Superconducting Cavity Development for High Intensity Proton Linac in JAERI," 9th Workshop on RF Superconductivity, Santa Fe, New Mexico, USA, 1999

[25] T. Schilcher, "Vector Sum Control of Pulsed Accelerating Fields in Lorentz Force Detuned Superconducting Cavities," Thesis, DESY, August 1998

[26] J. Tuckmantel, "Control Instabilities in a Pulsed Multi-Cavity RF System with a Vector Sum Feedback (a Mathematical Analysis)," SL-Note-2001-023 HRF, CERN, june 2001

[27] M. Liepe, W.D. Moeller, and S.N. Simrock, "Dynamic Lorentz Force Compensation with a Fast Piezoelectric Tuner," Proceedings of Particle Accelerator Conference 2001 (PAC2001),pp. 1074-1076, Chicago, Illinois, 18th-22nd, June 2001

[28] Y. Kang, M. Tiefenback, P. Chevstov, "Reactive RF Tuning for Compensation of a Detuned Accelerating Cavity," Proceedings of Linear Accelerator Conference 2002 (LINAC2002), TH456, Gyeongju, 19th-23rd, August 2002

[29] J. Delayen et al., "Results of the Cryogenic Testing of the SNS Prototype Cryomodule," Proceedings of Linear Accelerator Conference 2002 (LINAC2002), TU476, Gyeongju, 19th-23rd, August 2002

[30] M. Doleans, S. Kim, "Analytical and Semi-analytical Expressions for the Voltage in a Cavity under Dynamic Detuning," Proceedings of Linear Accelerator Conference 2002 (LINAC2002), TH430, Gyeongju, 19th-23rd, August 2002

[31] L Lilje et al., "Characteristics of a Fast Piezo-tuning Mechanism for Superconducting Cavities," Proceedings of the 8th European Particle Accelerator Conference , Paris, 3rd-7th, June 2002

[32] N. Ouchi, E. Chishiro, C. Tsukishima, and K. Mukugi, "Pulsed SC Proton Linac," Proceedings of Linear Accelerator Conference 2000 (LINAC2000), pp. 683-687, Monterey, California, 21st-25th, August 2000

[33] S. Simrock , "Lorentz Force Compensation of Pulsed SRF Cavities," Proceedings of Linear Accelerator Conference 2002 (LINAC2002), WE204, Gyeongju, 19th-23rd, August 2002

[34] H. Gassot, "Mechanical Instability of Radiofrequency Superconducting Cavities and Cavity Passif Stiffening," Proceedings of the 8th European Particle Accelerator Conference , Paris, 3rd-7th, June 2002

[35] S. Smee, "Piezo Tuner Design,"Presentation at the Spallation Neutron Source Project Accelerator System Advisory Committee Review, Oak Ridge, 12th-14th, February 2002

[36] R. Stassen et al., "Superconductive Activities at COSY FZJ," SRF workshop, KEK, 6th-11th, September 2001

[37] M. Ferrario, "Slater's Theorem for Magnetic mirror Boundary perturbations," TESLA Note 93-44, Desy Print, December 1993

[38] J. Delayen, "Self Excited loop," LLRF workshop, JLAB, 25th-27th, April 2001

[39] H. Gassot, "Etude de la stabilite mecanique des cavites supraconductrices et de la methode de rigidification par projection thermique de cuivre," Thesis, Universite Paris Sud/Paris XI, January 2001

[40] S. Simrock et al., "First Demonstration of Microphonic Control of a Superconducting Cavity with a Fast Piezoelectric Tuner," Proceedings of Particle Accelerator Conference 2003 (PAC2003), ROAA004, Portland, Oregon, 12th-16th, May 2003

[41] M. Doleans, Sang-ho Kim, "Analytical and semi-analytical formalism for the voltage and the current sources of a superconducting cavity under dynamic detuning," Nuclear Instruments and Methods in Physics Research A 496 (2003) 51-63

[42] P. Lapostolle, M. Weiss, "Formulae and Procedures Useful for the Design of Linear Accelerators," CERN-PS-2000-001(DR), Geneva, Switzerland, January 2000

[43] T. Wangler, Principles of RF Linear Accelerators, John Wiley & Sons, New-York (1998)

[44] H. Takeda, J. H. Billen, "Recent Developments in the Accelerator Design Code PARMILA," Proceedings of Linear Accelerator Conference 1998 (LINAC98), pp.156-158, Chicago, Illinois, 23rd-28th, August, 1998

[45] P. Lapostolle, "Introduction à l'Etude des Accélérateur Linéaire," CERN Yellow Report 66-20, Geneva, June 1966

[46] N. Holtkamp, "Status of the SNS Project," Proceedings of Particle Accelerator Conference 2003 (PAC2003), MOAL003, Portland, Oregon, 12th-16th, May 2003